Additive Manufacturing of WC-Co Cermets using Composite Powders

Mohaimen Habeeb Makki Al-Thamir, BSc, MSc

Thesis submitted for the degree of Doctor of Philosophy (PhD)

Department of Mechanical, Materials, and Manufacturing Engineering

University of Nottingham, UK

November 2020

Acknowledgements

This thesis would never see the light without the grace of almighty Allah. I sincerely thank the Ministry of Higher Education and Scientific Research in Iraq for sponsoring my PhD study.

I am obliged to express my deepest gratitude to my supervisors; Prof. Adam Clare, Prof. Richard Hague, Prof. D.G. McCartney, and Dr. Marco Simonelli. Their guidance, patience, and support are too much to thank.

I gratefully acknowledge the help of Mr. Stuart Branston, Mr. Mark Hardy, Dr. Nigel Neate, Dr. Hannah Constantin, Dr. Elisabeth Steer, Mr. Alexander Jackson-Crisp, and all other laboratories staff.

My sincere thanks go to Dr. Xianghui and Mr. Peifeng for their help in tribology tests.

Special thanks to all my friends and colleagues for their help and encouragement especially Dr. Kamaal Al-Hamdani.

I wished if my father and my mother are alive to say there are no words can express how I am grateful to you. I miss you every single day and for ever.

I would like to thank my brothers and sister for their passions and encouragements during my PhD journey.

Finally, my special thanks to my wife (Marwa). I much appreciate her standing by me, patience, and taking full responsibility looking after our children in the absence of me during more than three years of this study. She is a great gem. I am grateful to the precious gifts in my life; my son (Ibrahim) and my daughters (Fatimah and Maryam).

Thank you all.

Publication

Published paper

A journal paper has been published from the current research work as shown below.

- M. Al-Thamir, D.G. McCartney, M. Simonelli, R. Hague, A. Clare, Processability of Atypical WC-Co Composite Feedstock by Laser Powder-Bed Fusion, Materials 13(1) (2020) 50.

Abstract

Cermets are defined as “Composite materials consisting of two constituents, one being either an oxide, carbide, boride, or similar inorganic compound, and the other a metallic binder”. Cermets based on tungsten carbide -cobalt (WC-Co), in both sintered and coatings forms, are extensively used in the fabrication of engineering components that require excellent wear resistance. The excellent wear properties of sintered cutting tools arise because WC-Co cermets give a compromise between toughness, provided by the metal matrix (Co), and the hardness of the ceramic (WC) phase. However, in overlay coatings, a reaction between WC and Co during deposition can degrade their wear performance from the ideal one of WC in a ductile Co matrix.

Additive manufacturing (AM) technologies such as laser powder bed fusion (L-PBF) or laser direct energy deposition (DED-L) can provide significant design flexibility in the manufacture of cutting tools. However, there are significant challenges in processing WC-Co materials when melting of the Co binder phase is involved. The effect of process parameters needs to be fully understood and optimised to avoid cracks, pores, and excessive reaction between the WC and Co phases during manufacture. In the present study, a novel type of WC_M-12 wt.% Co powder, prepared by a “satelliting” method, was employed in both L-PBF and DED-L studies; WC_M represents the commercially available mixed carbide with the tradename Spherotene®. In addition, a commercially available plasma densified WC-Co feedstock with a smaller particle size and higher Co (17 wt.%) content was also examined in the L-PBF process.

In this study and for the first time, it is now possible to produce applicable WC-Co feedstock for AM using the simple manually prepared satelliting method.

Abstract

In DED-L, single clads were fabricated. The results demonstrated stable depositions, uniform distribution of WC_M particles in the matrix, good bonding with the substrate, and an almost full density matrix. These aspects can show the applicability of this feedstock to produce high quality coatings. To define an appropriate process map, two hypothesises were employed. The first one compromised between linear energy density and powder feed rate. The second one used effective energy density versus powder deposition density. The results showed that the second approach is more representative to the melt pool physics. Also, a high WC_M dissolution increased the microhardness and wear resistance of the multitrack deposited coatings.

In L-PBF, the processability of the satellited WC_M-12 wt.% Co feedstock was investigated. Melting trials were undertaken to evaluate the consolidation behaviour of single tracks within a single layer. Also, the evolution of surface morphology of single layers and multilayers was studied. A continuous and relatively uniform single-track morphology was obtained. This has led to a relatively smooth single layer without cracks or matrix pores. However, increasing the numbers of layers increased cracks significantly. The plasma densified WC-17 wt.% Co powder was used in a different L-PBF machine of a relatively large laser spot size. Uniform cubic samples without distortions were fabricated in a process window. However, all samples revealed microcracks and open pores on the as-laser-scanned surfaces.

List of abbreviations and symbols

Abbreviations

AM	Additive manufacturing
bcc	Body-centred-cubic
BSE	Back scattered electrons
CAD	Computer aided design
CDM	Cool-down mechanism
CNC	Computer numerically controlled
DED-L	Laser direct energy deposition
EDX	Energy dispersive X-ray
fcc	Face-centred-cubic
HAZ	Heat affected zone
hcp	Hexagonal closed packed
HIP	Hot isostatic pressing
HVOF	High velocity oxy fuel
LAM	Laser additive manufacturing
L-PBF	Laser-powder bed fusion
MMC	Metal matrix composite
OM	Optical microscope
SEM	Scanning electron microscopy
SLM	Selective laser melting
TGM	Thermal gradient mechanism
XRD	X-ray diffraction

Symbols used in mathematical equations

A_c	Clad area above substrate (mm^2)
A_s	Substrate melted area (mm^2)
C_{Co}	Specific heat capacity of Co (J/g/K)

List of abbreviations and symbols

C_e	Effective specific heat capacity (J/g/K)
c_p^p	Specific heat capacity of a powder particle (J/g/K)
C_{WC}	Specific heat capacity of WC (J/g/K)
D_E	Deposition efficiency (%)
D_L	Laser spot diameter (mm)
D_m	Melt pool depth (µm)
D_P	Powder nozzle diameter (mm)
D_r	Dilution ratio (%)
E_v	Volumetric energy density considering the hatch distance (J/mm³)
F_g	Flow rate of the carrier gas (mm³/s)
r_p	Powder particle radius (mm)
T_m	Melting temperature (K)
T_o	Initial powder temperature (K)
T_p	Powder particle temperature (K)
V_{Co}	Volume fraction of Co in the feedstock
V_{dis}	Dissolution ratio of WC_M volume (%)
v_p	Powder particle velocity (mm/s)
V_{WC}	Volume fraction of WC in the feedstock
W_m	Melt pool width (µm)
α_e	Effective thermal diffusivity (m²/s)
α_p	Laser absorption coefficient of a powder particle
α_{th}	Coefficient of thermal expansion (m/m/K)
η_{Co}	Laser absorption coefficient of Co (%)
η_e	Effective laser absorption coefficient
η_{WC}	Laser absorption coefficient of WC
λ_{Co}	Thermal conductivity of Co (W/m/K)
λ_e	Effective thermal conductivity (W/m/K)
λ_{WC}	Thermal conductivity of WC (W/m/K)
ρ_{Co}	Effective material density of Co (kg/m³)
ρ_e	Effective material density (kg/m³)

List of abbreviations and symbols

ρ_p	Particle density (kg/m³)
ρ_{WC}	Effective material density of WC (kg/m³)
Δl	Particle-laser flight distance (mm)
d	laser beam diameter (mm)
E	Effective energy density (J/mm²)
FRI	Flow rate index
h	Hatch distance (mm)
M	Constant (m^{-1})
N	Constant (m^{-1})
P	Laser power (W)
PDD	Powder deposition density (g/mm²)
PFR	Powder feed rate (g/min)
q	Laser power density (W/mm²)
r	Melt pool dimension (mm)
SI	Stability index
t	Powder layer thickness (mm)
V	Scanning speed in (mm/min) or (m/s)
VED	Volumetric energy density considering laser spot size (J/mm³)
λ	Thermal conductivity (W/m/K)
ξ	Melt pool dimension in the direction of the laser scanning (m)

Table of contents

List of figures

List of figures

List of figures

List of figures

List of figures

List of figures

List of figures

List of figures

List of figures

List of tables

List of tables

List of tables

1. Introduction

1.1 Background and problems definition

Cermets are defined as, “Composite materials consisting of two constituents, one being either an oxide, carbide, boride, or similar inorganic compound, and the other a metallic binder”. Cermets based on tungsten carbide-cobalt (WC-Co) are extensively used in the fabrication of engineering components that require excellent wear resistance. Sintered WC-Co based materials are used extensively in industry as cutting tools. WC-Co overlay coatings (an early example of additive manufacturing by thermal spraying or laser cladding) are used to protect engineering components from abrasion, sliding, fretting, and erosion resistance. The excellent wear properties of sintered cutting tools arise because WC-Co cermets give a compromise between toughness, provided by the metal matrix (Co), and the hardness of the ceramic (WC) phase. However, in overlay coatings or in other processes involving melting of the cobalt phase a reaction between WC and Co during deposition can degrade their wear performance from the ideal one of WC in a ductile Co matrix.

Additive manufacturing (AM) technologies such as laser powder bed fusion (L-PBF) (also referred to as selective laser melting (SLM)) or laser direct energy deposition (DED-L) (also known as laser cladding or laser additive manufacture) can provide significant design flexibility in the manufacture of cutting tools and other parts used for cutting applications. However, there are significant challenges in processing WC-Co materials when melting of the Co binder phase is involved. The effect of process parameters on microstructure formation and mechanical performance needs to be fully understood and parameters need to be optimised to avoid cracks, pores, and excessive reaction between the WC and Co phases during manufacture.

1.2 Research hypothesis

The integrity of WC-Co materials in laser additive manufacturing (LAM) faces several challenges such as inhomogeneous microstructure, undesirable phase formation, cracking during manufacture, and development of porosity. WC grains are typically in the micron size range and so have a relatively large surface area per unit volume. This increases the kinetics of dissolution during laser processing when the cobalt phase is melted resulting in the formation of secondary brittle carbides which consume the cobalt phase and increase cracking susceptibility. In addition, depletion or uneven growth of WC grains can also happen between melt pools due to this dissolution effect. To potentially address this problem, relatively large WC_M particles (45 – 125 μm) (where WC_M is a commercially available multiphase carbide with the trade name Spherotene®) will be combined with small Co particles (1 – 3 μm) by using a satelliting method to achieve the following:

- Enhancing the flowability of the composite powder compared to one that is simply blended: The satelliting of smaller Co particles on the surfaces of larger WC_M particles can reduce the free motion of Co particles and then the inter-particle friction inside the feedstock.
- Obtaining a high satelliting efficiency as smaller Co particles can effectively decorate the surfaces of WC_M. This can also maintain a uniform distribution of WC_M particles inside the feedstock and then in the microstructure.
- Reducing the surface area per unit volume of WC_M particles thus the extent of dissolution.

1.3 Aim and objectives of the research

In this research, the overall aim can be divided into two fields. First, the deposition behaviours of simply blended and satellited WC_M-12 wt.% Co powders will be

investigated in DED-L (which will also be referred to as laser cladding throughout the thesis). Secondly, the consolidation behaviours of the satellited WC_M-12 wt.% Co and commercially available plasma densified WC-17wt.% Co powders will be investigated in L-PBF. Higher Co content can help to increase material ductility and then reduce cracking propensity. In addition, the size distribution of the plasma densified powder is 15 – 45 µm. This can increase powder packing density. Also, it allows using a lower powder layer thickness. As a result, a higher material density can be obtained. Thus, the specific objectives of this research are as follow:

A- DED-L (laser cladding) specific objectives

- To compare the deposition behaviour of single clads produced from blended and satellited composite powders seeking for crack-free, pore-free, continuous, and well bonded single clads.
- To investigate the effects of laser power, scanning speed, and powder feed rate on clad microstructures and geometrical characteristics.
- To produce multitrack clad layers to investigate the effect of overlapping between tracks on the microstructure and then on wear resistance.

B- L-PBF specific objectives

In L-PBF, two powders will be used: satellited WC_M-12 wt.% Co powder and plasma densified WC-17 wt.% Co powder. The specific objectives of these two materials are as the following:

1- The specific objectives of using satellited WC_M-12 wt.% Co powder

- To fabricate crack-free, pore-free, continuous, and well bonded single tracks using a range of energy density values.

- To investigate the effects of energy density and the number of consolidated layers on the evolution of surface morphology and microstructure of single layers and multi layers components.

2- The specific objectives of using plasma densified WC-17 wt.% Co powder

- To fabricate crack-free, pore-free, and uniform cubic samples.
- To investigate the effects of laser power and scanning speed in a process window on the surface morphology, and cracking tendency.

1.4 Proposed methodology

The overall research methodology can be divided into two main parts: DED-L methodology and L-PBF methodology.

1.4.1 DED-L methodology

The suggested methodology for DED-L experiments is summarized by the following steps:

1- Preparation of blending and satelliting WC_M-12 wt.% Co powders.
2- Studying the deposition behaviour of single tracks.
3- Performing a multi-level full factorial design of experiments method using the satellited powder to discover the deposition trend.
4- Studying the impact of process parameters on melt pool characteristics, deposition efficiency, and WC_M dissolution.
5- Determining the appropriate process map to represent the relationship between process parameters and clads qualities.
6- Investigating the mechanical performance of multitrack coatings including the microhardness, friction coefficient, and wear resistance.

1.4.2 L-PBF methodology

Two machines were used with a different feedstock in each one. Firstly, the Realizer SLM-50 will be used with satelliting WC_M-12 wt.% Co powder. A relatively small powder batch can be used in this machine to perform the experiments. The suggested methodology is explained step-by-step as:

1- Preparation of satelliting WC_M – 12 wt.% Co powder.
2- Estimation of the melt pool size by using the Rosenthal equation to find out the likely values of laser power and scanning speed that can be used to produce a suitable melt pool for a given powder.
3- Fabrication of single tracks on a single powder layer to examine the possibility of obtaining a continuous track without cracks and pores using the predicted values of laser power and scanning speed.
4- Systematically expanding the process parameters to study the impact of energy density on consolidation behaviour of single tracks including melt pool geometry.
5- Fabrication of single layers and multilayers to monitor the consolidation behaviour in the initial building stages.
6- Studying the impact of energy density and the number of consolidated layers on surface morphology, cracking tendency, and microstructure.

Secondly, Renishaw AM 125 will be used with plasma densified WC-17 wt.% Co powder. This machine has a laser spot size of more than 3 times that of Realizer SLM-50. Besides a lower particle size of WC-17 wt.% Co powder, this enables the laser to effectively accommodate powder particles and homogenize the temperature within a given layer thickness. Thus, smoother surface morphology containing less intensity of

cracks and pores and then high-density builds are expected. The methodology is explained by the following steps:

1- Commercially available plasma densified WC-17 wt.% Co powder will be examined.
2- Estimation of the melt pool size by using the Rosenthal equation to find out the likely values of laser power and scanning speed that can be used to produce a suitable melt pool for a given powder.
3- Examining the possibility of obtaining a continuous, crack-free, and uniform topography single walls using the predicted values of laser power and scanning speed.
4- Fabrication of uniform cubic samples without distortions in a process window of laser power and scanning speed to show the consolidation behaviour in a systematic approach.
5- Studying the impact of energy density on surface morphology and cracking tendency.
6- Studying the microstructural characteristics.

1.5 Thesis structure

The thesis includes 6 chapters. The chapters flow presents as the following:

- Chapter 1 provides the research background and problems, hypothesis to potentially address these problems, proposed methodology, and general outlines of the thesis.
- Chapter 2 discusses a relevant literature review in both DED-L and L-PBF fields. This includes the contributions, difficulties, and opportunities extracted from previous research works regrading laser additive manufacturing of WC-

Co materials. Based on this, the research goals are defined after identifying the gaps in the literature.

- Chapter 3 shows the materials, equipment, experiments, and characterisation procedures followed to carry out this research. It also includes the morphology, particles size distribution, and flowability investigations of the WC_M, Co, blending WC_M- 12 wt.% Co, and satelliting WC_M-12 wt.% Co powders. The morphology and particles size distribution analyses can indicate the satelliting efficiency. The flowability comparisons indicate the deposition behaviour of the blending and satelliting powders.
- Chapter 4 reports the DED-L results. This includes (1) deposition behaviour of the blending and satelliting powders, (2) a multilevel full factorial design of experiments to show the deposition trend including melt pools characteristics, deposition efficiency, and WC_M dissolution using the satelliting powder, (3) appropriate process map to represent the relationship between process parameters and clads qualities, and (4) the microstructure and mechanical properties of multitrack coatings.
- Chapter 5 discusses the L-PBF consolidation behaviour of (1) single tracks, single layers, and multilayers produced using the satelliting WC_M-12 wt.% Co powder, (2) a single wall and cubic samples produced using plasma densified WC- 17 wt.% Co powder, and (3) the potential reasons behind the differences between the predicted widths of melt pools by the Rosenthal equation and the experimental tracks widths.
- Chapter 6 summarizes the overall conclusions of this research and proposes future works that can be expanded from the current DED-L and L-PBF results.

2. Literature review

2.1.Introduction

This chapter presents a review of relevant literature related to research work reported in this thesis. The chapter is divided into 9 sections. Section one gives an introduction about the laser additive manufacturing (LAM) technologies including direct laser deposition (DED-L) and laser-powder bed fusion (L-PBF) with a brief history of the employed materials. Section two discusses the metal matrix composites fabricated by DED-L. This also includes the operation of DED-L systems, the evolution of powder temperature while transferring in the laser beam, the mechanism of track formation, the effects of process parameters on track formation, and the common defects in laser cladding materials. The metallurgy and properties of WC-based composites are given in section three. Previous work on laser cladding of WC-based composites is discussed in section four. This also includes the main factors which affect WC dissolution. The operation of L-PBF system is explained in section five. After that, previous work on L-PBF of WC-Co composites is detailed in section six. Then, the basic WC-Co powder preparation methods are given in section seven. Later, a novel powder preparation method ‘satelliting’ is shown in the next section. Finally, the chapter ends with a summary of main points in the literature. The summary also highlights the gaps found in DED-L and L-PBF sections which are used to direct the research work included in this thesis.

2.2. Laser Additive Manufacturing Technology

Laser additive manufacturing (LAM) technology encompasses a number of processes and two of the main ones are directed energy deposition with a laser (DED-L) and laser-powder bed fusion (L-PBF). The product is built track-by-track and layer-by-

layer directly from computer aided design (CAD) data. LAM provides design flexibility to produce complex parts of near-net-shape and rapid manufacturing has the potential to reduce time and costs. The feedstock can be either powder or wire in DED-L whilst it is powder in L-PBF. The metallurgical mechanism depends on melting the feedstock during laser processing. Although DED-L and L-PBF share the same material additive philosophy, each process has different laser-powder interaction mechanisms. The powder is fed into a melt pool generated by the laser beam in DED-L whereas in L-PBF, the powder is pre-placed on powder bed before laser scanning. This can result in different track geometry, microstructure, and phase formation even with the same feedstock alloy due to different heating and cooling thermal cycles [1]. DED-L has a capability to manufacture parts, repair and rebuild worn or damaged parts, and to deposit wear resistant coatings [2]. L-PBF on the other hand has the capability to only manufacture parts. It also has a smaller melt pool and layer thickness in which leads to a smaller spatial resolution than that produced by DED-L [3]. To date, metals, ceramics, and polymers have all been produced using both DED-L and L-PBF techniques.

In recent years, L-PBF has attracted extensive attention for the fabrication of near net shape metallic alloy parts such as Al-based alloys [4-6], Ti-based alloy [7-9], Ni-based alloys [10, 11], and stainless steel alloys [12, 13].

DED-L differs from L-PBF in that it was first employed some 40 years ago to deposit protective coatings on the surfaces of metallic alloys for surface engineering applications. Its use to build 3D parts has evolved more recently and can be traced back some 25 years to the laser engineering net shape (LENS) process.

Although both processes use a powder feedstock, the laser-powder interaction mechanisms in L-PBF are very different from those found in laser cladding.

The following sections will provide a more detailed review of processes and materials relevant to the present thesis.

2.3.Laser cladding of metal-ceramic composites

Hardfacing coatings have been widely used to increase the service life of a component [14]. Since the 1980s, DED-L (often referred to as laser cladding) was used to process different types of powders. The alloy powders were based on a wide range of alloys such as Co, Fe, Ni, Al, stainless steel, and tool steel [15-20] . As a surface engineering technology, the major objective of DED-L is to create high-performance surface properties on relatively inexpensive and easily to process base materials to provide components with wear, corrosion, and oxidation resistance [21].

Metal matrix composites (MMC) provides an optimum combination of ductile metallic matrix with harder and stiffer particles. This enhances the mechanical properties over unreinforced metallic alloy [22]. MMC can be divided into two categories: in-situ and ex-situ materials. In-situ MMC is developed by chemical reactions between the initial constituents of the feedstock completely melted in the melt pool [2]. It results in new hard phases dispersed in the solidified material. This provides the possibility of obtaining microstructures suitable for functionally graded materials to improve the wear resistance. Table 2.1 gives a review of in-situ hard particles produced by DED-L processing using various types of composite powders on various substrates.

Table 2.1: In-situ MMCs produced by DED-L technique using different types of composite powders on various substrates.

Feedstock powder	Particle size (µm)	Substrate	In-situ formed hard particles	Results outlines
Al-TiO_2 [23]	Al = 7 – 100 TiO_2 = ~ 1	N/A	Al_2O_3	Promising approach to produce functionally graded materials
Ni/Al + TiC [24]	Ni/Al = 49 – 75 TiC= ≤74	Mild steel	Fine TiC	Producing TiC-reinforced NiAl matrix composite coatings
B_4C-TiNi [25]	Ti = 20 – 50 Ni = 20 – 30 B_4C = 20 – 50	Ti-alloy	TiB TiB_2 TiB_2+TiC	The microhardness and wear resistance of the coatings were 4.6 and 2 times, respectively, that of the TC4 substrate
Ti-C-Cr-CeO_2-Fe [26]	75 – 150	Low carbon steel	VC TiVC2	The microhardness values of the composite coatings were more than 4 times than that of the low carbon steel substrate
TiB_2-Ti6Al4V [27]	TiB2 = 5 – 50 Ti6Al4V = < 300	Ti6Al4V	TiB	Improving the yield and ultimate strengths as well as the microhardness values

Ni-C-TiN-CeO_2 [28]	Ni = 40 – 100 C = 10 – 20 TiN = 1 – 10 CeO_2 = 40	Ti6Al4V	Ti (C, N)	CeO2 increased the precipitation rate of Ti (C, N) particles which in turn improved the wear resistance of the coatings
B_4C-C [29]	B4C = 44 – 46 C = 40 – 45	Ti6Al4V	TiC, TiB TiN TiB_2	The microhardness and wear resistance of the coating reached up to 4 times that of the Ti6Al4V substrate
W-C-Ni [30]	N/A	Mild steel	WC	The microhardness of the coating reached up to 755 HV and the volume fraction of WC was 71%

On the other hand, ex-situ MMCs materials are produced by pre-mixing of ceramic particles with metallic powder acting as structural and matrix material, respectively. Different powder preparation methods can be used to produce the composite powders such as mechanical mixing (simply blending), ball milling, spray drying, chemically coating, and agglomerating and sintering [31-35]. Uniform microstructures without cracks or pores can be obtained by melting the matrix powder of the lowest melting point without completely melting all the initial feedstock constituents such as that followed in the in-situ MMCs. The ceramics particles can be carbides, oxides, or borides. The matrix can be pure metal or alloy powder. Table 2.2 lists various ex-situ

MMCs produced by DED-L using different types of composite powders (ceramics with metallic powders) on various substrates.

Table 2.2: Ex-situ MMCs materials produced by DED-L technique using different types of powders on various substrates.

Feedstock constituents				
Ceramic powder and type	**Matrix powder and type**	**Particle size (µm)**	**Substrate**	**Results outlines**
WC (carbide)	Ni (pure metal)	WC = 40 – 150 Ni = 40 – 100	Tool steel	The clad wear resistance was 5 – 10 times higher than that of the substrate [36]
SiC (carbide)	Al-Si (alloy)	SiC = 26.2 (median) Al-Si = 71 (median)	Aluminium alloy	The coating enhanced the corrosion resistance [37]
Al_2O_3 (oxide)	304 stainless steel (alloy)	45 – 100	45 steel	Improving the corrosion resistance, wear resistance, and microhardness [38]
TiB_2 (boride)	Ti6Al4V (alloy)	TiB_2 = 10 (median) Ti6Al4V = 108 (median)	Ti6Al4V	The elastic modulus was improved by 27% as compared to that of Ti6Al4V [39]

Al_2O_3 (oxide)	Ti (metal)	N/A	Ti6Al4V	The clad improved the corrosion resistance of the substrate [40]
TiC (carbide)	Al (metal)	Al: 15-45 TiC: < 5	Aluminium alloy	The clad improved microhardness and wear resistance [41]
SiC (carbide)	316L stainless (alloy)	316L: 45-60 SiC: 25-40	Mild steel	The microhardness and wear resistance are proportional to SiC fraction [42]

2.3.1. Operation of laser cladding

Laser cladding with powder can be operated in different configurations: (1) the blown powder can be side fed, blown coaxially, or pre-placed on the part to be clad, (2) the part to be coated can be mounted on a computer numerically controlled (CNC) bed or a robot, and (3) the laser source can be a fixed or moving head. Common industrial lasers are fibre lasers, CO_2 lasers, Nd:YAG laser, and diode laser [43]. Considering the 2-kW laser cladding machine at the University of Nottingham, the laser beam profile and corresponding spot size change significantly by changing the laser focus distance: a top-hat profile with ~1 mm laser spot diameter can be obtained at focus whilst a Gaussian profile with 3.1 mm laser spot diameter was observed at 20 mm out-of-focus [39]. Figure 2.1 shows a schematic representation of the side powder fed-CNC bed configuration which was the type used in the present project. The powder is fed from the lateral nozzle feeder using an inert gas (such as argon or nitrogen) to prevent oxidation. The powder stream interacts with the laser before reaching the

substrate surface. Both the laser and powder stream are focused on the same area at which the laser beam melts the powder and the substrate surface to generate a melt pool. By moving the substrate, the laser and powder continuously scan the substrate and a track is formed.

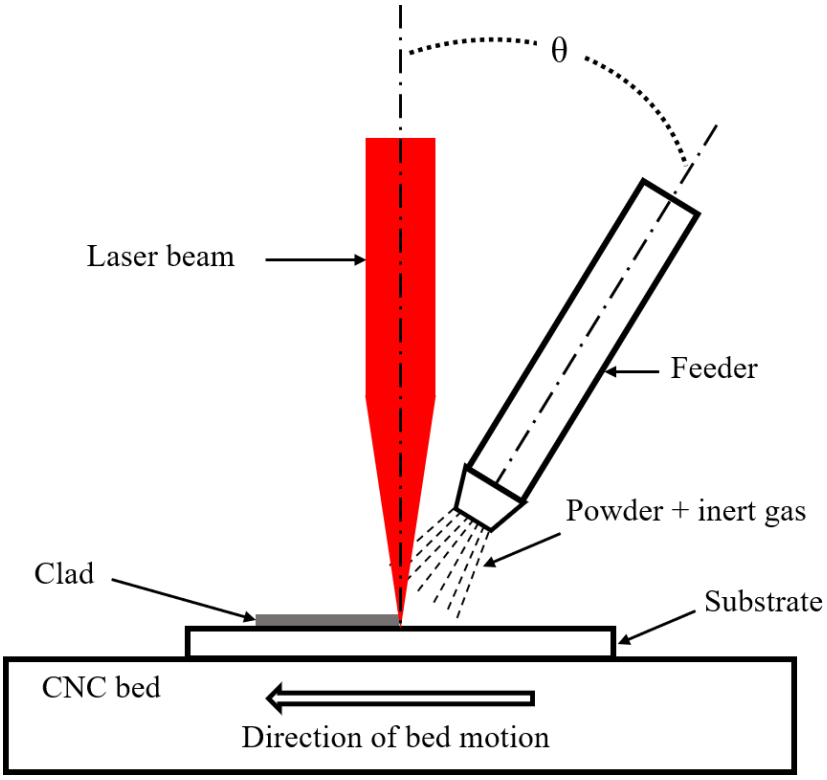

Figure 2.1: Schematic representation of side powder fed direct laser cladding.

2.3.2. Substrate and particle heating during laser cladding

The temperature of melt pool in laser cladding can reach up to 2000 °C in a very short laser dwelling time of 4 – 12 ms [44]. And the cooling rate can be more than 1000 °C/s [45]. When studying the process, it is necessary to know how the particle temperature can develop while passing through the laser beam. The incident energy in the laser beam will lead to particle heating, substrate heating, and some will be reflected from the powder stream.

Qi et al. [46] used a simple heat balance equation to estimate the powder temperature during laser cladding as given in Eq.2.1.

$$q\,\alpha_p \pi\, r_p^2 \frac{\Delta l}{v_p} = \frac{4}{3}\,\pi\, r_p^3\, \rho_p\, c_p^p\, \Delta T \qquad (2.1)$$

where q = attenuated laser power density, α_p = laser absorption coefficient of a powder particle, r_p = particle radius, Δl = particle-laser flighting distance, v_p = particle velocity, ρ_p = particle density, c_p^p = specific heat capacity of the particle, and ΔT = temperature rise of the particle. The attenuation represents the shadowing effect of the powder stream on the incident energy density. This indicates the total effect of both the absorption of laser by powder particles and the reflection of laser from the powder particles surfaces. And depending on the process conditions, the material of high laser absorption coefficient can absorb significant amount of heat while passing through the laser beam resulting in possibility of powder melting. In this trend, the recent study showed that a portion of the powder (steel was considered of a 100 µm particle size) can be molten and even vaporized when the laser power range was 500 – 1000 W for the particle velocity of less than 1.5 m/s. To maintain powder deposition efficiency, the evaporation of the powder should be avoided. It has been shown that melting of nickel-chromium alloy powder (60 µm mean particle size) can occur at laser power of less than 750 W and particle velocity of less than 0.5 m/s [47]. However, the substrate was not melted due to insufficient energy density, thus, weak metallurgical bonding was formed between the deposited track and the substrate. This can help to indicate the required energy density at a given powder velocity/feed rate to melt the powder and the substrate and then to form a satisfied track.

For an incident energy density, the attenuated ratio and then powder deposition efficiency depends on three factors: powder feed rate, powder size, and laser-powder

interaction distance. Tabernero et al. [48] showed that the energy attenuation is proportional to powder feed rate and can reach to more than 13%. Also, the powder of smaller particle size absorbs more energy as compared to that of larger particle size, thus, increases the attenuation. Moreover, it has been shown that the attenuation ratio increased up to 21% by increasing the laser-powder interaction distance [46]. This can reach to more than 50% resulting in a low powder catchment efficiency due to a low substrate heating [49]. Thus, to enhance catchment efficiency of a given powder size, the optimization between the delivered energy density and powder feeding density is a must.

2.3.3. Mechanism of clad track formation in DED-L

The laser cladding process should fabricate a uniform and continuous track which is as wide as the laser spot size [50]. The key point for a successful DED-L processing is the generation of the melt pool since it contributes to the initiation of the track deposition [51] and then the powder catchment efficiency [52]. Figure 2.2 shows a schematic representation to melt pool and internal fluid flow during laser processing. If the melt pool is not formed, powder particles can ricochet from the substrate surface and lost [53].

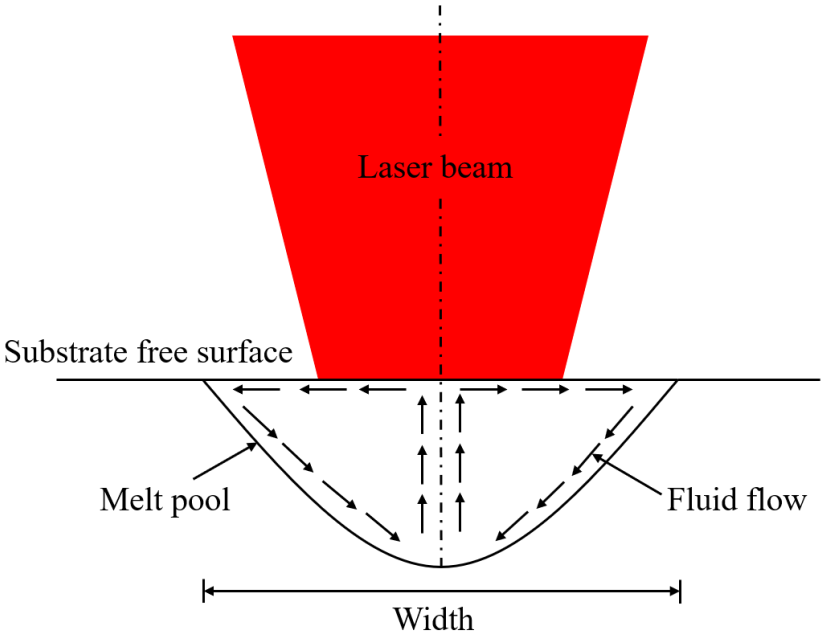

Figure 2.2: Schematic representation of laser generated melt pool showing possible internal fluid flow.

Initially, the substrate area irradiated by the laser beam heats up rapidly. At a sufficiently high energy density, a thin layer of the substrate surface melts. Powder entering in the melt pool is heated and its mass is added to the melt pool. In the case of a pure metal or alloy, the powder will be melted and fully incorporated into the melt pool. This process is driven by laser heating and conduction in the solid. However, convection occurs inside the melt pool, driven by a surface tension gradient between the centre (lower) and the periphery (higher) of the melt pool due to the difference in energy distribution of the laser beam (highest at the centre) [54, 55]. This induces a thermocapillary flow directed from low surface tension (centre) to high surface tension (periphery) of the melt pool which results in radially outward flow. However, at a high oxygen concentration, the surface tension increases with temperature which can cause radially inward flow from the periphery to the centre of the melt pool. The internal flow enhances heat transfer to the substrate and then contributes to the growth of the

melt pool which can extend beyond the laser irradiated area [53]. By moving the laser, the liquid material starts to solidify at the rear of the melt pool and then a track is formed on the substrate along the laser-powder scanning path. The typical cross sectional track geometry is shown schematically in Figure 2.3.

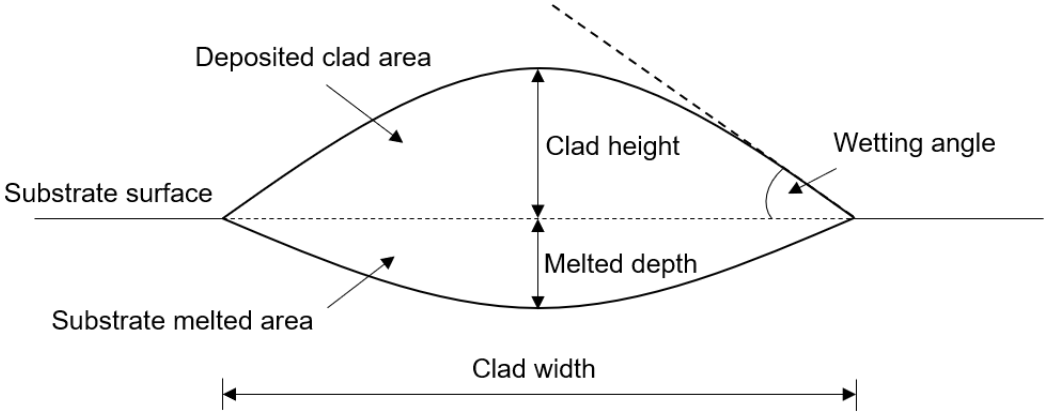

Figure 2.3: Schematic representation of typical laser track transverse cross section showing its geometrical characteristics.

The degree of the substrate melted area to the total clad area represents the dilution ratio (D_r) as given in Eq.2.2 [56].

$$D_r = \frac{\text{Substrate melted area}}{\text{Deposited clad area} + \text{substrate melted area}} \times 100\% \qquad (2.2)$$

Too low a dilution can result in a weak metallurgical bonding between the clad and the substrate. Too high a dilution can significantly change the cladding composition and so it is undesirable for high-quality clads. For a well-bonded clad, suitable clad geometry should be obtained. The clad geometry is determined by the applied process parameters. This will be explained in the next section.

2.3.4. Effect of process parameters on track formation

DED-L processing involves a large number of factors which can affect the quality and properties of the laser cladding tracks [52]. These include (1) laser wave-length, (2) powder properties (such as particle size, morphology, optical, and thermo-physical properties), (3) substrate (optical, metallurgical, thermo-physical properties), and (4) operating parameters (laser power, spot size, beam shape, scanning speed, powder feed rate, and substrate pre-heating). For a given laser and material, the evolution of melt pool and then microstructure can be determined by three main factors: laser power, scanning speed, and powder feed rate.

The prior knowledge of the likely ranges of process parameters that can be used to produce high quality clads can save time and resources during initial experiments [57]. To date, different approaches have been tried to represent the relationship between process parameters and clads qualities. In this trend, Erfanmanesh et al. [58] used two main parameters; laser power versus the ratio of powder feed rate/scanning speed to define a processing window for the most applicable working zone for a WC-12 Co system. However, controlling of DED-L process is complicated due to the potential effect of one variable on the effective laser-powder residence time. It is well known that changing scanning speed can affect the laser dwelling time and then the energy input to melt pool [59]. Thus, the above approach cannot represent the physics of the laser-powder interaction in the melt pool. This indicates the importance to developing suitable compile parameters to represent the overall effects of laser power, scanning speed, and powder feed rate on the clads properties. Dass et al. [60] used linear energy density (laser power/scanning speed) versus powder feed rate values to compare the responses of different materials. However, the potential impact of scanning speed on the amount of delivered powder to melt pool has not been considered. Thus, the actual

laser-powder interaction behaviour cannot be described. Bax et al. [61] reported the behaviour of Inconel 718 single clads using laser power values versus powder feed rate values at two scanning speed values: 500 mm/min and 1000 mm/min. It suggests multi process window at each level of scanning speed. This strategy cannot provide a clear vision to the applicable working zone considering a full range of process parameters. Moreover, Emamian et al. [62] used two combined parameters; effective energy density (E) and powder deposition density (PDD) to show the properties of Fe-TiC composite clads. E was defined as the delivered energy by the laser beam to the melt pool per unit area (Eq.2.3). On the other hand, the scanning speed, powder feed rate, and powder nozzle diameter determine the powder deposition density (PDD). This represents the amount of powder delivered from the feeder system to melt pool per unit area (Eq.2.4).

$$E = \frac{P}{VD_L} \qquad [J/mm^2] \qquad (2.3)$$

$$PDD = \frac{PFR}{VD_L}\frac{D_L^2}{D_p^2} \qquad [g/mm^2] \qquad (2.4)$$

where P is the laser power (W), V is the scanning speed (mm/s), D_L is the laser spot diameter (mm), PFR is the powder feed rate (g/s), D_p is the powder feeder diameter (mm).

The above two equations can provide a suitable controlling of process parameters. To fabricate an optimal clad quality, the tracks should bring to certain geometrical features [47]. Figure 2.4 shows schematic representations of four main possibilities for the impact of energy density and powder deposition density on melt pool geometry. A low energy density results in a low deposition rate due to insufficient energy to melt the powder and the substrate (Figure 2.4a). High laser power and/or low scanning speed

provide a high energy density which allows laser to penetrate deeper into substrate (high dilution) at a relatively low powder feeding as shown in Figure 2.4b [63]. This behaviour is also undesirable as it can largely change the composition of the clad and then the mechanical/tribological properties. A high energy density also increases track width [64]. A careful setting of energy and powder feeding density can give a suitable deposition rate with good metallurgical bonding to the substrate (Figure 2.4c). Nonetheless, increasing the powder feed rate increases the clad height and decreases substrate melted area as illustrated in Figure 2.4d [63].

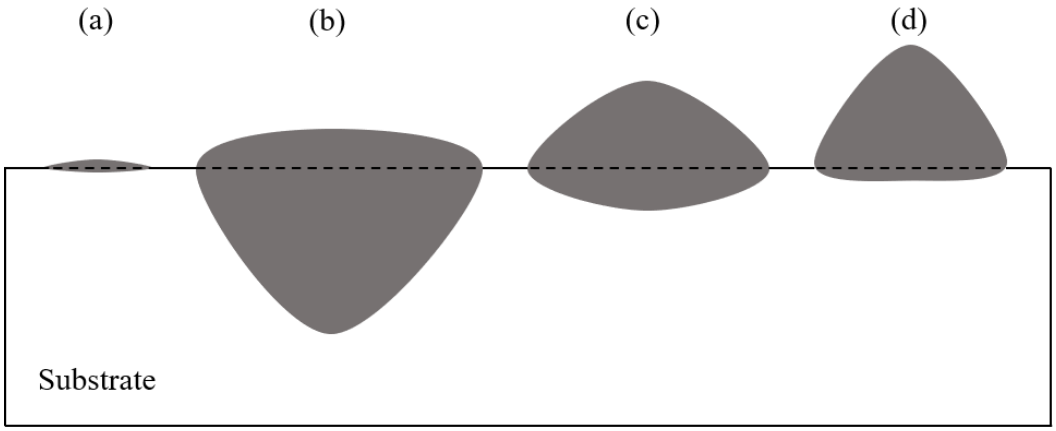

Figure 2.4: Schematic representations of the effects of energy and powder feeding density on the evolution of melt pool geometry: (a) = low energy + low powder feeding: (b) = high energy + low powder feeding: (c) = moderate energy + moderate powder feeding: (d) = moderate energy + high powder feeding.

2.3.5. Meso-scale structural features of clads – cracks, pores inclusions

The main defects in the laser clads can be divided into two groups: defects in single phase alloys and defects in metal matrix composites. In single phase alloys the main defect is the inhomogeneous microstructure consisting of different morphologies such as columnar dendrites, cluster of cells, and equiaxed grains which can vary from the

clad-substrate interface to the top surface of the clad due to different thermal fields [15, 18]. Uncontrollable formation of various phases due to chemical reaction of the involved elements is another defect [65]. Moreover, evaporation of some powder elements and pores can occur which decreases the strength of the clad [16, 17]. Nonetheless, cracks can also occur during laser cladding [66].

In metal matrix composites, cracking is the main defect due to the presence of hard phase particles which decrease material ductility [67, 68]. In addition, porosity is another defect [69].

The mechanisms of cracking and porosity formations in DED-L processing of different powders are explained as follow. Zhou et al. [66] reported two types of cracks in Ni-based alloy: solidification cracks and liquation cracks. The solidification cracks occur within the melt pool. When laser melts the substrate, the melt pool tends to expand. When laser is removed, cooling starts, and the heated material begins to shrink which is restrained by the surrounded material resulting in residual stresses. When these stresses exceed the ultimate tensile strength of the material at a given temperature, cracks can form. The liquation cracks are generally reported to occur in the heat affected zone (HAZ) away from the melt pool where the material is heated to a lower than its overall liquidus temperature. Due to melting of some low melting point compounds, liquid films are formed in HAZ at the grains boundaries which act as crack initiation sites when the induced thermal stresses are large enough. This type of cracking is likely to occur in the single-phase alloys due to a lower melting point as compared to that of ceramic particles.

On the other hand, the residual porosity can be attributed to gas entrapment. The possible sources of enclosed gas can be gases entrapped between powder particles,

gases contained within powder particles, and evaporation of metals [45]. Also, high cooling rate during solidification results in insufficient time to the gas to completely escape from the melt pool. Moreover, Ng et al. [70] showed that the gas bubbles in the melt pool are driven by the Marangoni convection flow which was in order of 5 times higher than the flotation effect. This can contribute to pores distribution and enhance gas retention. Nonetheless, insufficient energy density leads to regions of un-melted powder near the substrate or between adjacent tracks which appear as voids [60]. The optimization between the energy density and powder feeding density can be a key point to reduce porosity formation.

2.4.Metallurgy and properties of WC-based composite materials (cermets)

The cermet is a term created to link between ceramic and metal into one word to describe a composite. This mixture keeps the properties of the ceramic and metal. The mixtures based upon carbides as the hard phase are called hardmetals or cemented carbides. These materials are utilized as bulk parts or coatings. Conventionally, liquid phase sintering (LPS) and thermal spraying (TS) are typically used to produce bulk and coating hardmetals, respectively [71-73]. LPS involves the sintering of a mixed and compressed powder mixture at elevated temperature. TS is performed by depositing a coating on to the surface by for example high velocity oxy-fuel or air plasma spraying. The feedstock for TS is normally WC-Co powder with 12 or 17 wt.% Co which has been agglomerated and sintered or plasma densified. In the field of additive manufacturing, L-PBF has the potential to manufacture bulk parts of complex shape. On the other hand, DED-L can produce WC-Co coatings of low porosity with good metallurgical bonding to a substrate, and small dilution ratio [74, 75].

The cermet consisting of tungsten carbide (WC) and cobalt (Co) exhibits excellent wear resistance at elevated temperatures up to 500 °C [76, 77]. Thus, this composite

material is widely utilized in numerous applications such as automotive and aerospace manufacturing, oil and gas drilling, mining, geothermal energy exploration, construction, and other industries where extreme wear resistance is required [77, 78]. Co is a common metal matrix with a content ranging from 3-30 wt.% [58, 79]. Ni and Fe are the most common alternatives/added elements to Co to enhance the mechanical properties. The wetting of the liquid metal on the surface of solid WC particle is an important parameter for cermet processing [80]. It has been shown that Co is better wetting WC grains than Ni which in turn better than Fe [81]. This resulted in a lower porosity in WC-Co liquid phase sintered parts.

WC has a hexagonal closed packed (hcp) crystal structure. It has high hardness, excellent thermal stability, low thermal expansion coefficient, good oxidation resistance, high density, and high melting point.

The W-C binary phase diagram is shown in Figure 2.5 and reveals a number of other WC based phases can form in the system, for example W_2C.

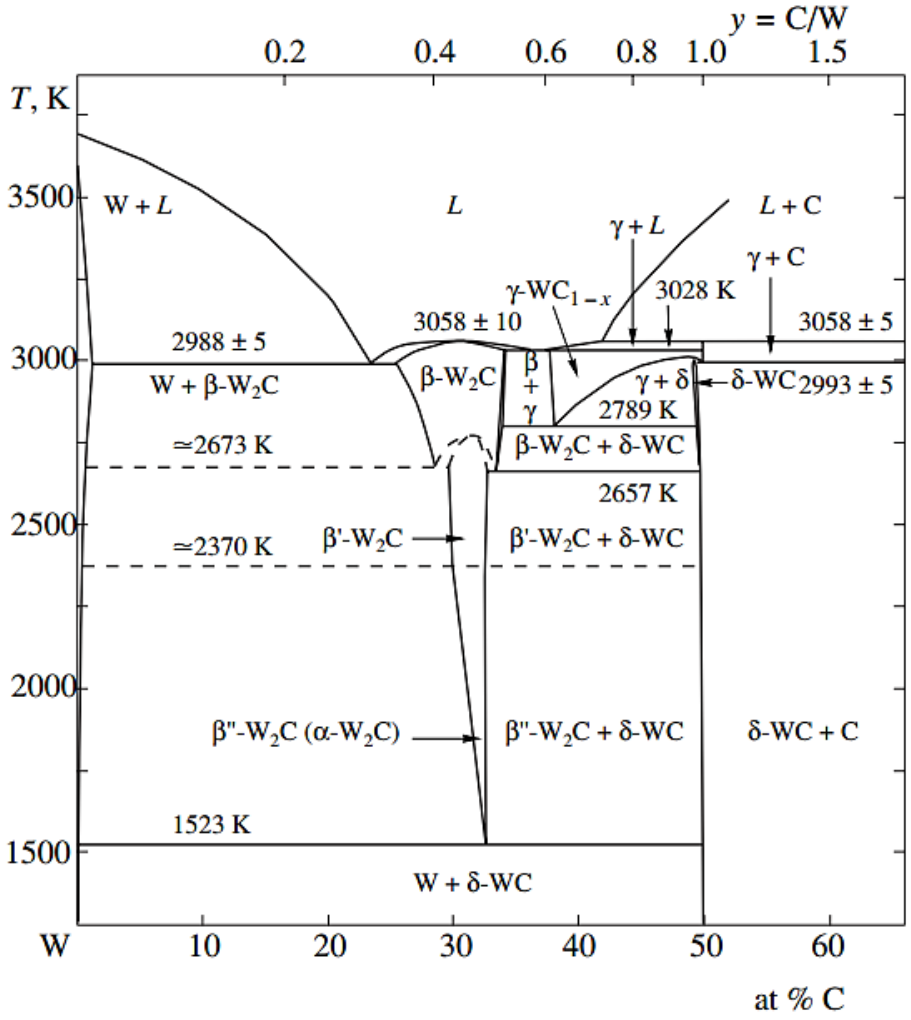

Figure 2.5: Binary phase diagram of the W-C system: the values in the upper horizontal axis (y) represent the ratios of C atomic % to the W atomic % [43].

At equilibrium, Co exhibits a hexagonal close packed (hcp) crystal structure at room temperature but transforms to the face centred cubic (fcc) from above 427 °C [82]. The thermophysical properties of WC and Co are given in Table 2.3.

Table 2.3: Thermophysical properties of WC and Co [83].

Properties	Unit	WC	Co
Density	Kg/m^3	15800	8900
Melting point	°C	2687	1495
Thermal conductivity	W/m/K	84	100
Coefficient of thermal expansion	m/m/K	4.3	14
Hardness	HRA	93	67

Figure 2.6 shows the phase diagram of the W-C-Co system calculated at 12 wt.% Co [71]. The focusing is on important two-phase region WC+ FCC where FCC represents the cobalt. It indicates the favourable carbon content denoted by vertical dashed lines, and solid red "p" and "q" lines showing the maximum and minimum melting temperature of the Co in the system, respectively. The solubility of WC in Co strongly depends upon the temperature. The solid solubility of W and C in Co are inversely related. W solubility in Co increases by decreasing C and has a range of 2 – 15 wt.% at about 1250 °C. On the other hand, typical C solubility in Co has a range of 0 – 0.2 wt.% at elevated temperatures with higher values at lower W levels. Increasing carbon content leads to the formation of graphite. Carbon deficiency leads to the crystallization of M_6C and $M_{12}C$ which are also referred as η-carbide phases. The narrow carbon window indicates a more difficult to avoiding either η-phases or graphite. Excessive heat input during manufacturing by liquid phase sintering leads to partial melting of WC and the formation of η phases. Due to their brittleness, these phases are considered detrimental to wear resistance as they decrease the fracture toughness [71]. For high performance, a large proportion of WC particles should be retained in a Co-rich matrix.

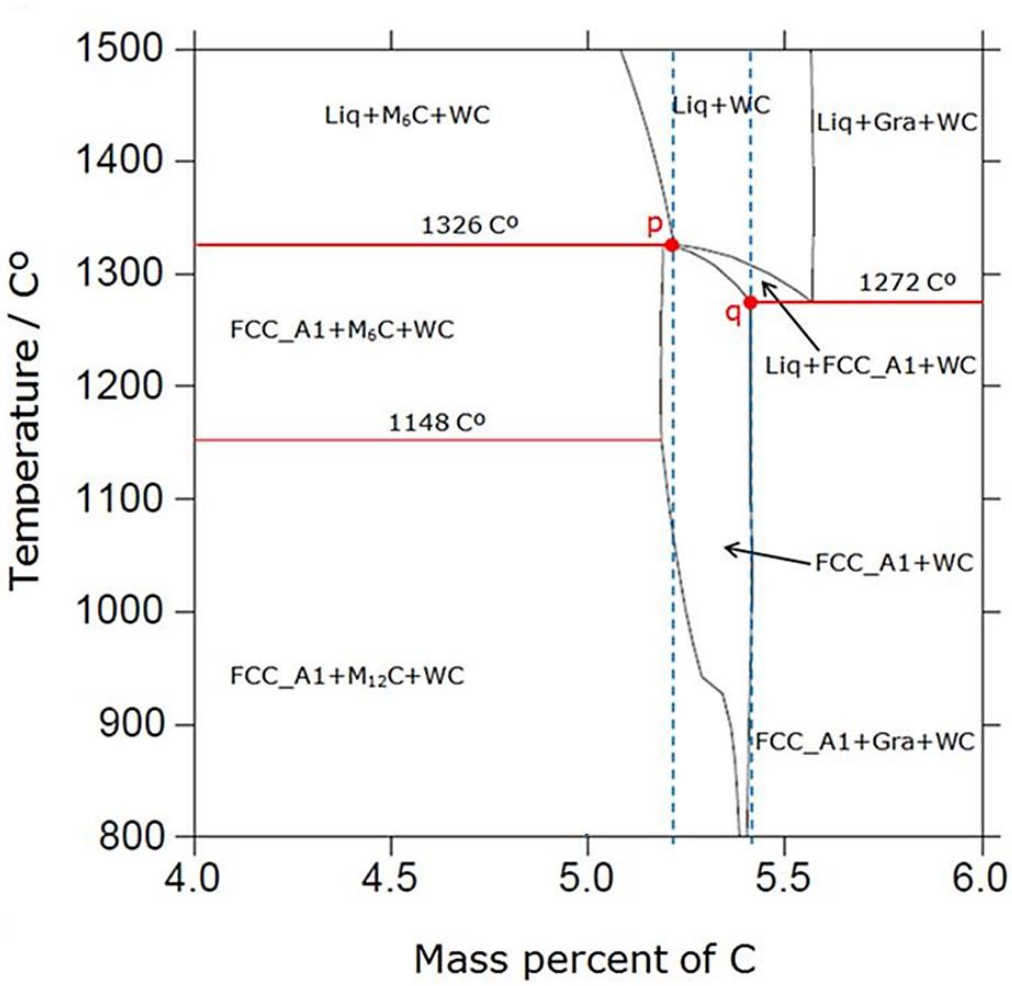

Figure 2.6: Phase diagram of the W-C-Co system calculated at 12 wt.% Co: FCC + WC indicates the favourable composition: FCC refers to cobalt: the vertical blue dashed lines indicate the favourable carbon content range: the p and q solid red lines define the maximum and minimum melting temperatures of the cobalt in the system, respectively [71].

2.5.Experimental observations on laser cladding of WC-Co cermets

To date, several studies have been reported in relation to the fabrication of WC-Co using DED-L. This can overcome some of the disadvantages of manufacturing of WC-Co in conventional sintering technique, e.g. significant coarsening of WC particles, long processing time, and expensive machining costs for parts in complex shapes [13]. However, a non-uniform microstructure with the formation of phases such as W_2C and η carbides is the dominant problem along with cracking and porosity formation within the clad layer.

Studies on the deposition of WC-Co based laser clad layers have mainly involved investigating the effect of changes in process parameters on microstructure formation and properties such as wear or corrosion resistance.

Cadenas et al. [76] used WC-Co (83-17) wt.% powder with an average grain size of 39 µm to fabricate coatings on AISI HI43 steel using power density, scanning speed, and powder feed rate ranges of (6000 – 18000 W/cm²), (200 – 800 mm/min), and (5 – 20 g/min), respectively. Besides pores and cracks, it showed that there were places in the cross-sectional area where WC has dissolved completely. For a high-performance coating, high content of WC particles must be retained.

The nano sized and even few micron sized WC particles have a relatively high surface area per unit volume which can enhance heat absorption and then dissolving extent. The dissolution of these particles can result in uneven WC grain growth during laser processing due to re-melting effect in overlapping regions between melt pools. In addition, the interaction between dissolved W and C elements and the molten Co produces η carbides. Besides this, W_2C phase has also been observed using WC-10 wt.% Co powder in a size range of 45-90 µm [79]. The presence of these brittle phases

can decrease the ductility and then material toughness. Moreover, significant variation in the microstructure containing fine and coarse WC grains between the deposited layers has been observed (Figure 2.7). The variation in microstructure can cause significant variations in the hardness across the coating thickness [84]. This can affect the stability of wear resistance.

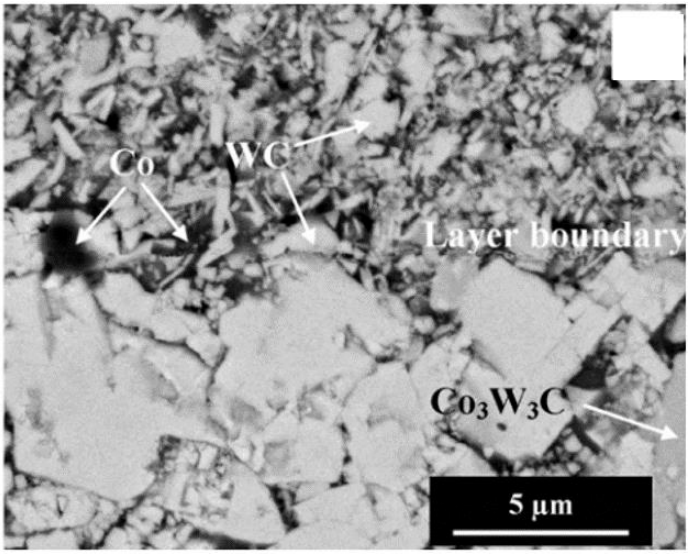

Figure 2.7: SEM/BSE image of WC-10 wt.% Co thick wall laser clad showing alternating microstructure between deposited layers [79].

On the other hand, the effect of process parameters on porosity has not been fully understood. For instance, Balla et al. [85] observed that increasing the energy input from 350 W to 450 W has led to decrease the porosity ratio from (2-3%) to (1-2%) when a cast and crushed WC-12 wt.% Co powder of 45-75 µm particle size has been used. While Erfanmanesh et al. [58] investigations showed a different behaviour; it appeared that by keeping the scanning speed and powder feed rate at 4 mm/s and 100 mg/s, respectively, increasing the laser power from 150 W to 300 W has led to increase the porosity ratio from 0.4% to 11.81% where agglomerated WC-12 wt.% Co powder

in a size range of 15-45 μm has been used to fabricate single clads. However, no clear trend was observed in the other variations of process parameters.

In all previous studies, the size of WC particles used in the composite powders can range from nano-sized to a micron. The impact of particle morphology, particle size, WC content, and substrate pre-heating on the WC dissolution has not been reported. These aspects, as well as energy input, will be discussed in the next section using micro-sized WC particles with different metal matrices.

2.5.1. WC dissolution during laser cladding

In general, the results of a number of studies show that WC dissolution is driven by four factors namely: energy input, WC particle morphology, WC particles size distribution, and substrate pre-heating. These factors will now be considered.

Although the increase of WC particle size can lead to decrease the surface area and then heat absorption, a completely dissolution of WC particles can happen at excessive energy density. On the other hand, decreasing the energy density can lead to retain WC particles, however, pores can increase. For instance, Amado et al. [69] used NiCr-WC (60-40 wt.%) alloy powder. The powder is presented in Figure 2.8a. It shows spherical and irregular blocky morphology of the WC and NiCr powders, respectively. The size distribution of the WC powder was 40-160 μm. Single tracks were deposited on low carbon steel. Cracks and pores were observed in the analysed tracks. Besides these defects, the microstructure reveals an absence of WC particles in the core of some clads produced at a high energy density (Figure 2.8b). A slower solidification rate in the cladding core gives sufficient time to WC particles to dissolve. By decreasing the energy density (laser power/scanning speed), a more uniform distribution of WC particles was obtained as shown in Figure 2.8c. However, pores cannot be eliminated.

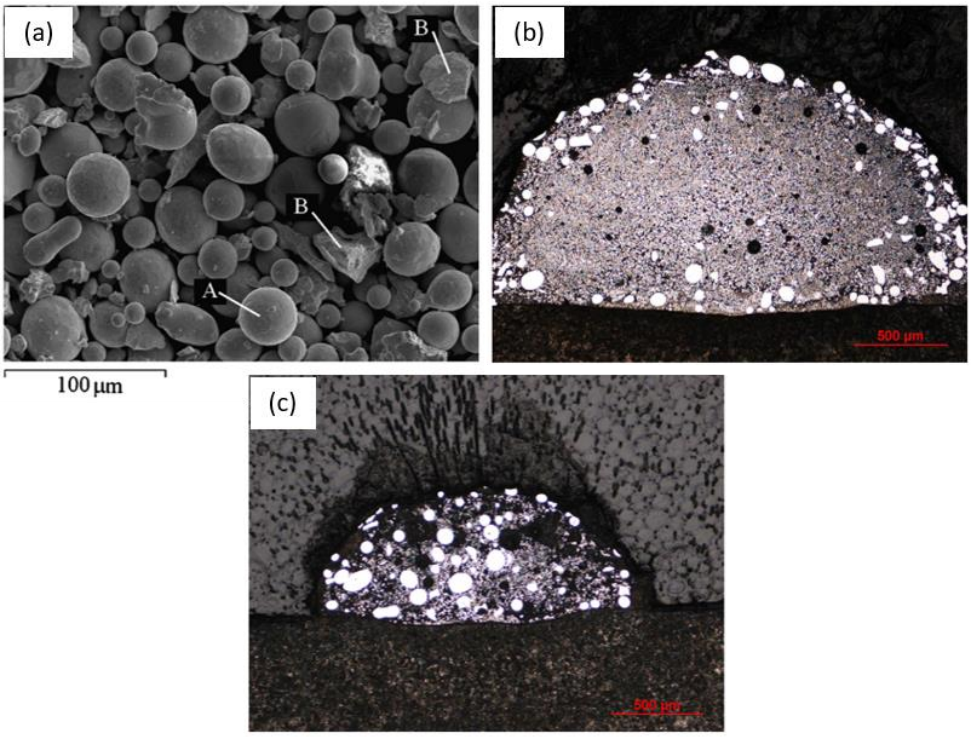

Figure 2.8: (a)-micrograph of composite powder showing WC (A) and NiCr (B) particles, (b)-single clad cross section produced at laser power, scanning speed, and powder feed rate of 1100 W, 5 mm/s, and 0.36 g/s, respectively, showing no WC particles in the cladding core, (c)- single clad cross section produced at laser power, scanning speed, and powder feed rate of 700 W, 7 mm/s, and 0.36 g/s, respectively, showing a relatively uniform distribution of WC particles and pores [69].

The dissolution of carbide particles can form interface shell with the matrix as shown in Figure 2.9. It shows two morphologies: carbide A with interface and carbide B without interface. Such phenomenon (carbide-matrix interface) can produce a strong metallurgical bonding between the WC particle and the matrix, thus, reducing the probability of WC pulling out during a tribological contact.

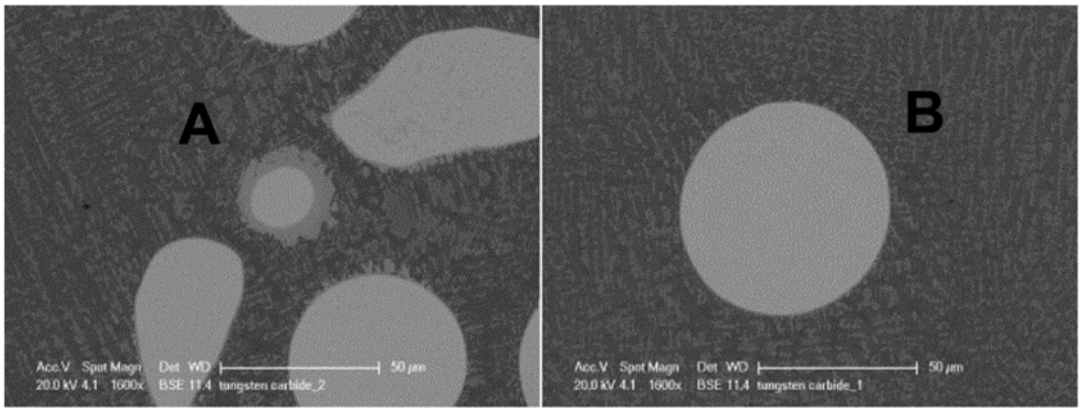

Figure 2.9: Microstructures produced by laser cladding of WC with Co-based alloy powders showing two morphologies of carbides: A with (left), and B without (right) interface shell [86].

Nonetheless, the dissolved W and C elements from carbide particles can disperse into melt pool following Marangoni convection flow. Due to interacting with molten metal matrix, new carbides in a dendritic structure can be formed after the solidification. Increasing the dissolution extent of carbide particles increases the formation of dendritic morphology. The formation of dendritic morphology due to precipitation of Ni_2W_4C carbide in the Ni matrix has been reported by Huang et al. [36] as presented in Figure 2.10. This can consume the matrix phase resulting in a low ductility and then high cracking susceptibility.

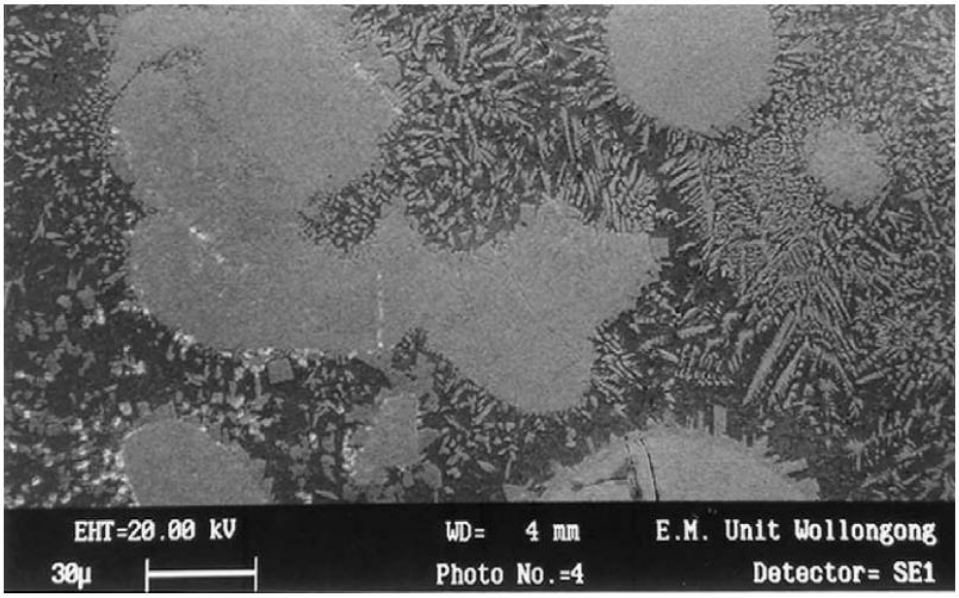

Figure 2.10: Microstructure of a clad layer produced from a powder mixture of WC-Ni-Al showing dendritic structure around WC particles in light colour [36].

Besides energy density, the shape and size of WC particles can play an important role on WC dissolution and then evolution of microstructure. Janicki et al. [87] showed that spherical WC particles can reduce the WC dissolution ratio by ~ 7% as compared to irregular particles. Spherical morphology minimizes the contact area with the molten pool and then reduces the absorbed heat. On the other hand, Leunda et al. [88] used two spherical WC powders in sizes of 10 – 45 µm and 45 – 125 µm to prepare two mixtures with NiCr powder for laser cladding. The mixtures had the same composition of (WC-NiCr) (60-40 wt.%). It was observed that coating produced from a mixture containing (10-45 µm) carbides had two distinct regions: more concentrated WC particles, and depleted bands in the overlaps between adjacent tracks. Smaller particles have a larger surface area per unit volume which can absorb more energy during laser processing. This increases WC dissolution especially in the overlapping zones where re-melting has taken place. In comparison, coatings fabricated using the larger WC size (45 – 125 µm) gave a uniform carbide distribution inside the matrix as shown in

Figure 2.11. However, unless a careful setting of energy input, a completely dissolution of carbide particles can occur [69].

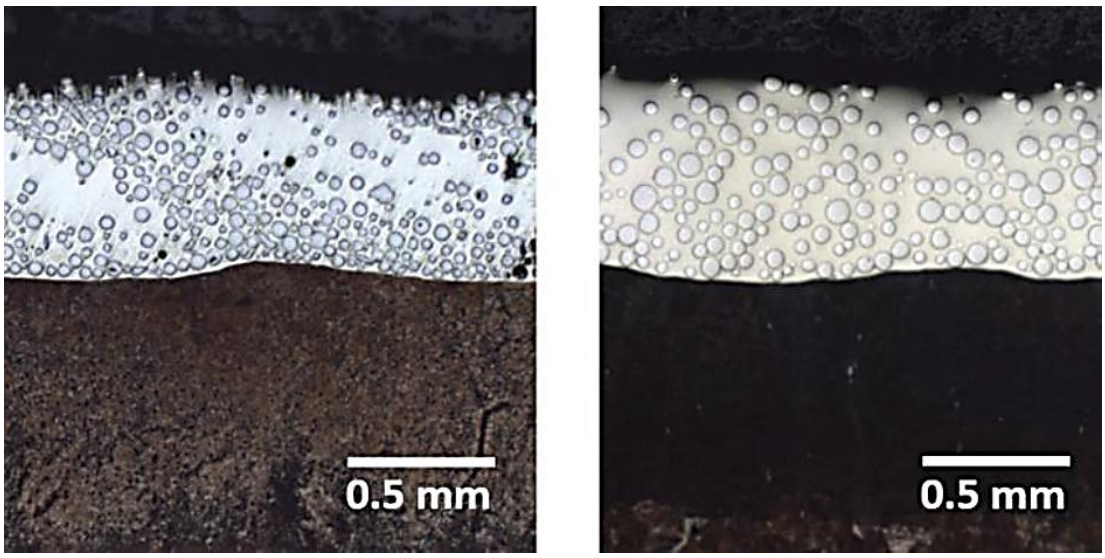

Figure 2.11: Cross sections of NiCr matrix coatings produced with spherical WC 10-45 µm powder size (left) showing carbide depletion zones, and spherical WC 45-125 µm powder size (right) showing a uniform carbide distribution [88].

In addition to the above three factors (energy density, WC particle morphology and WC particle size), few studies have been reported about the effect of substrate pre-heating condition on WC dissolution. A conflict has raised between WC dissolution and cracking. It has been reported that pre-heating the substrate to 400 °C can increase the dissolution of carbides due to increasing the average temperature experienced by the melt pool during the cladding process [86]. On the other hand, another approach showed that crack-free WC-based coatings cannot be produced by laser cladding without preheating the substrate to 300 °C, however, the retained WC volume has decreased as compared to non-preheated samples [36]. The non-cracking behaviour has been attributed to the reduction in cooling rate at preheating condition which diminishes the induced thermal stresses [89].

As a result, appropriate substrate pre-heating condition, thermal cycle (considering both the time required to deposit a new overlapped single track and overlapping ratio), and process parameters for high-quality WC-Co clads cannot be confirmed. Also, no representative processing window to the relationship between process parameters and the desired clad quality was confirmed. Moreover, no suitable WC-Co mixture for DED-L processing has been confirmed. However, the DED-L literature indicates that using a spherical WC particle morphology within a particular particle size range can minimise WC dissolution. This presents an opportunity to investigate/confirm the impact of feedstock constituents on the microstructure. On the other hand, the impact of Co particle morphology, Co particles size distribution, and Co content in the feedstock has not been reported. Thus, more research needs to be done to cover these gaps of knowledge.

2.6.Operation of laser-powder bed fusion

In laser-powder bed fusion (L-PBF) technology (also known as selective laser melting (SLM)), complex parts can be fabricated by melting layers of powder. The process starts by defining a CAD model to the part to be fabricated. The model is sliced into thin layers using a special software. Build supports are also defined which can constitute many layers depending on build geometry. Then, the sliced model with supports is uploaded to the L-PBF machine. The process parameters are explained schematically in Figure 2.12. These include laser power, scanning speed, hatch distance (which determines the overlapping ratio and then affects the overall thermal cycle), and powder layer thickness. The combined effect is represented by volumetric energy density as given in Eq.2.5 [90].

$$E_v = \frac{P_L}{v_s\, h_s\, I_z} \qquad J/mm^3 \qquad (2.5)$$

where P_L, v_s, h_s, and I_z are laser power (W), scanning speed (mm/s), hatch distance (mm), and powder layer thickness (mm), respectively. When the laser is applied, a track is formed along the laser scanning path from the melted powder. Each layer consists of multi-overlapped tracks. The process is repeated layer-by-layer until the required part is completely built.

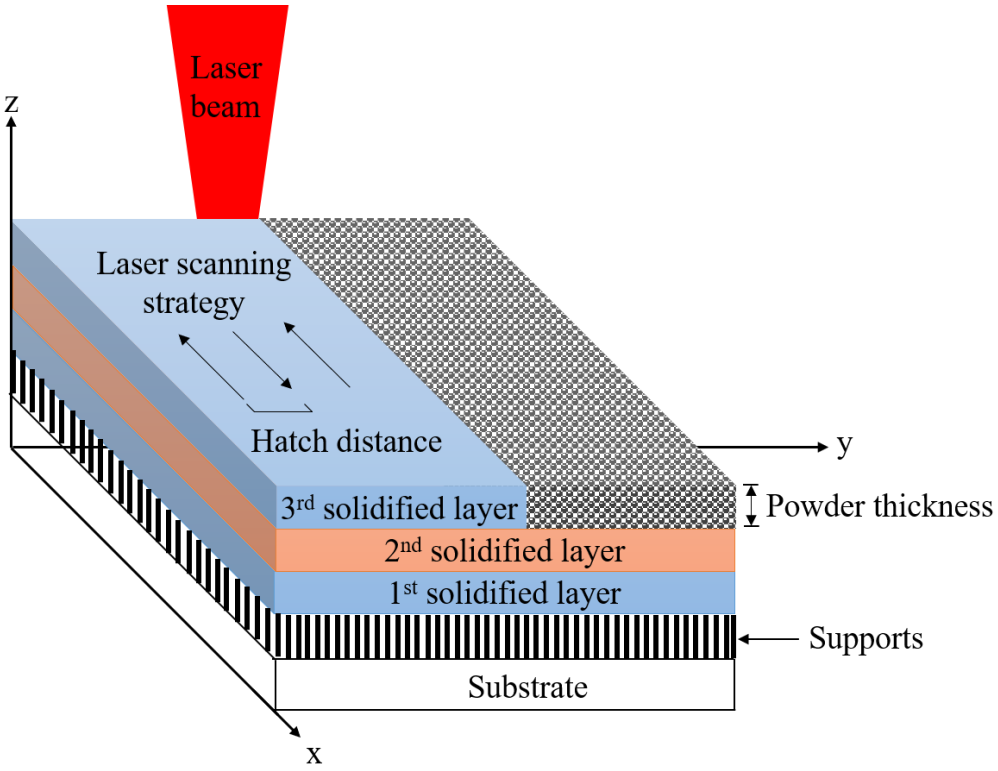

Figure 2.12: Schematic representation of L-PBF process parameters.

2.7.Previous work on laser-powder bed fusion of WC-Co cermets

To date, few studies reported about the processing of WC-Co in L-PBF. The response can be affected by four main factors: energy density, Co content in the feedstock, powder morphology, and sample temperature. The way in which these factors affect the development of L-PBF micro and meso-structures are reviewed.

The impact of energy density on WC-Co solidification reveals a clear conflict: high energy encourages cracks and Co evaporation, whilst low energy increases porosity. In addition, the inhomogeneous microstructure is another pronounced defect. In this trend, Uhlmann et al. [90] used WC-17 Co powder to produce multilayers samples. All samples revealed a tendency to cracking regardless the process parameters used as shown in Figure 2.13. At high energy densities, the cracks run more continuously than at low ones. Decreasing the energy density led to increase porosity.

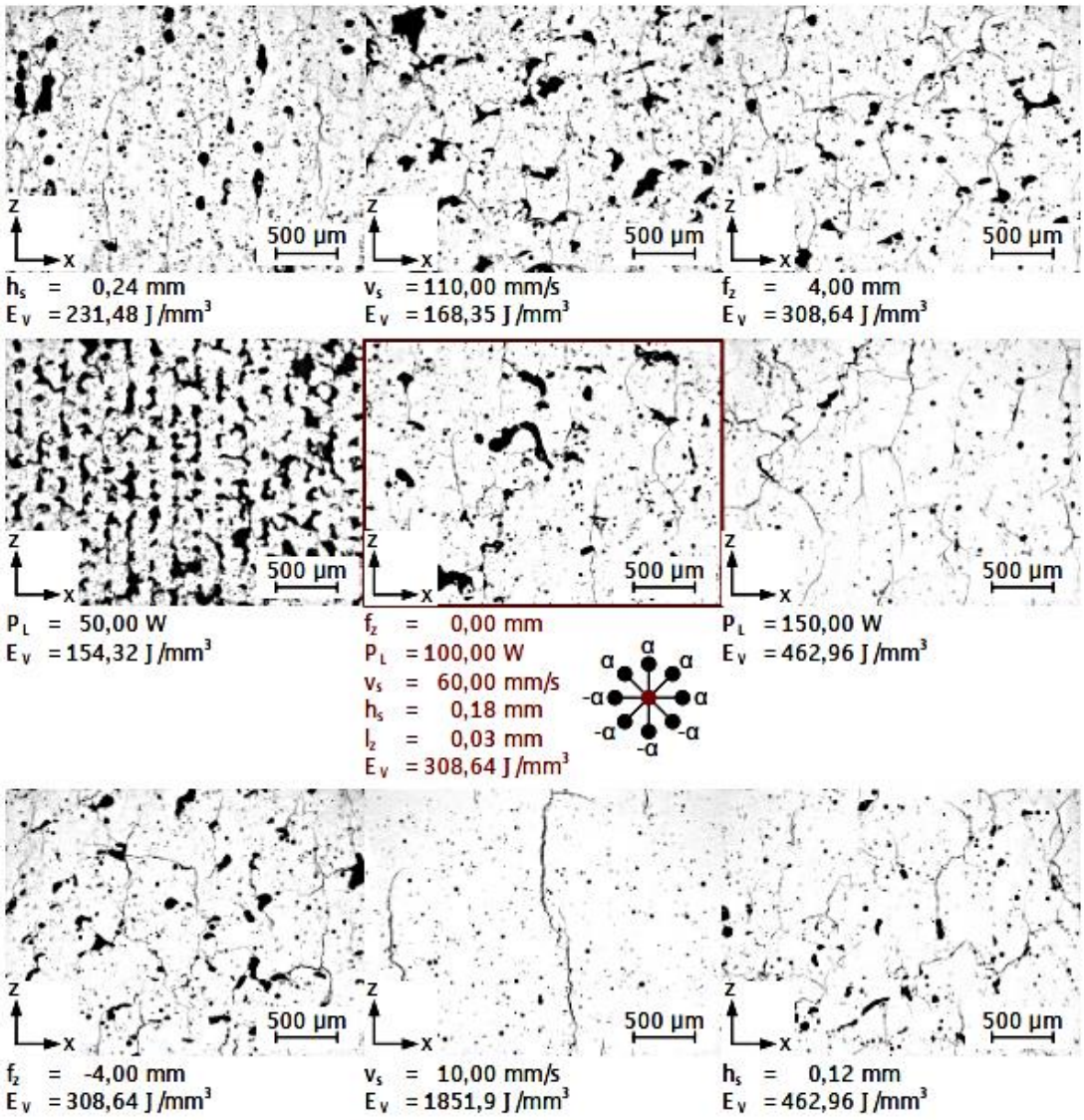

Figure 2.13: The effect of volumetric energy density on cracks and porosity formations of WC-17 Co multilayers specimens produced by L-PBF technology [90].

The conflict between the cracking and porosity with respect to energy input has been clearly shown by Schwanekamp et al. [91] using two size distributions of agglomerated WC-12 Co powders: 10-25 µm and 22-45 µm as presented in Figure 2.14. It shows that porosity decreases by increasing the specific energy (volumetric energy density) until 1250 J/mm³. Then, the porosity starts to increase after this limit. The cracking ratio reveals an opposite trend. The fine powder presents a relatively lower porosity and less cracking tendency as compared to coarse powder. Fine powder bed can enhance laser absorptivity and then temperature homogeneity. This can lead to release thermal stresses and then cracking propensity. Also, a higher powder packing density can be achieved using smaller particle size which results in increasing the build density.

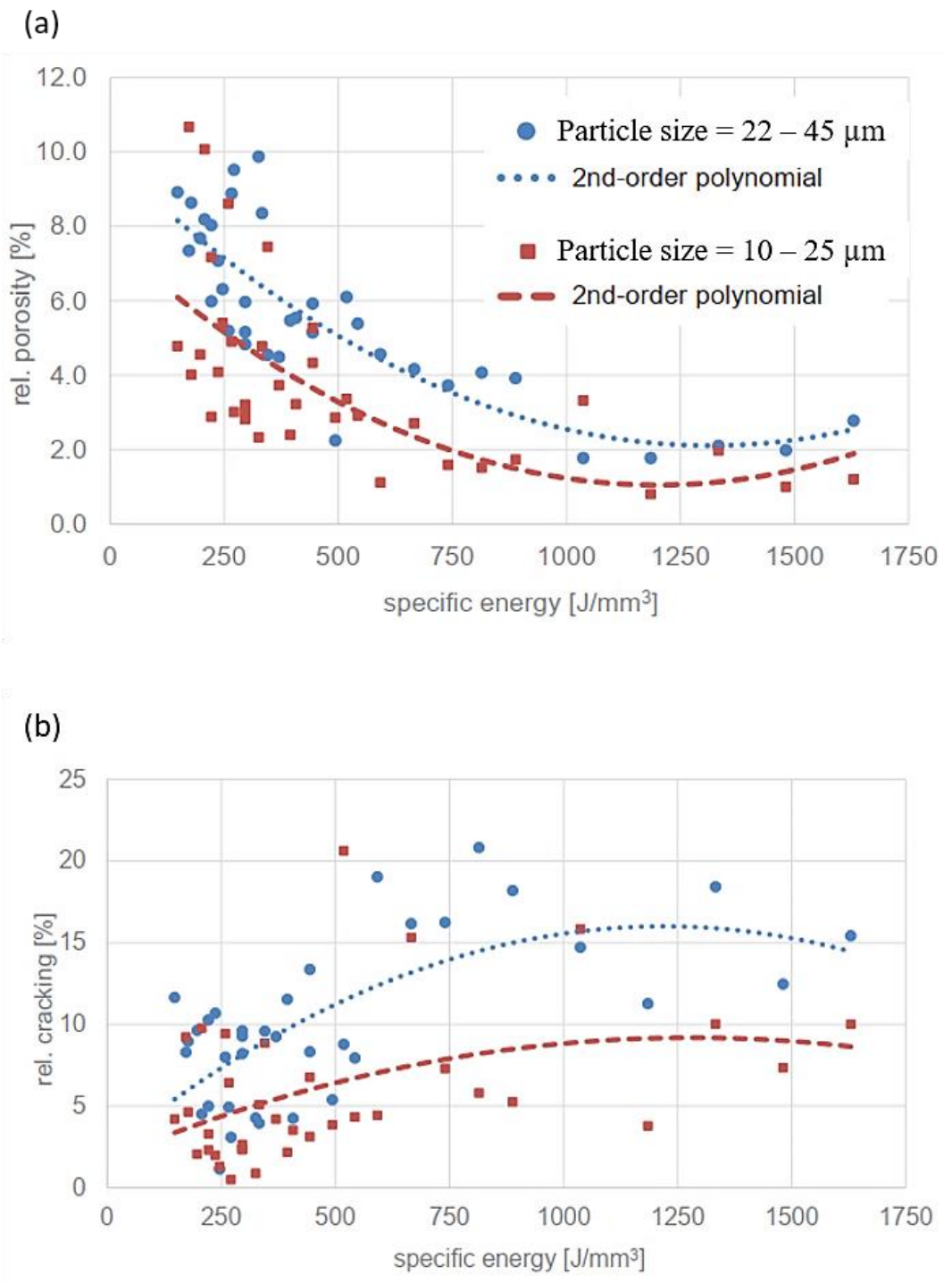

Figure 2.14: The effect of specific energy (volumetric energy density) on (a) relative porosity and (b) relative cracking of WC-12 Co parts produced by L-PBF using fined-grained (10 – 25 µm) and coarse-grained (22 – 45 µm) powders [91].

Besides cracks and pores, inhomogeneous microstructure due to different sizes of WC grains is a dominant phenomenon in WC-Co materials produced by L-PBF as

presented in Figure 2.15. Moreover, it showed that high energy density produces extremely low free Co content of 1% (as compared to 17 wt.% Co in the feedstock) resulting in enormous material embrittlement. During laser processing, finer WC particles can absorb more energy due to a larger surface area resulting in a high likelihood to be dissolved. The dissolved W and C elements are re-precipitated on the surfaces of nearby larger WC particles, thus, giving rise to WC grain growth. During the building state, the upper part of a previously solidified layer is subjected to re-melting cycle when a new layer is formed. This leads to coarsening of WC grains in the re-melting zone. As a result, WC grains appear cyclically fine and coarse throughout the build height. The Marangoni convection flow can also influence in-track segregation of submicron or even micron WC size.

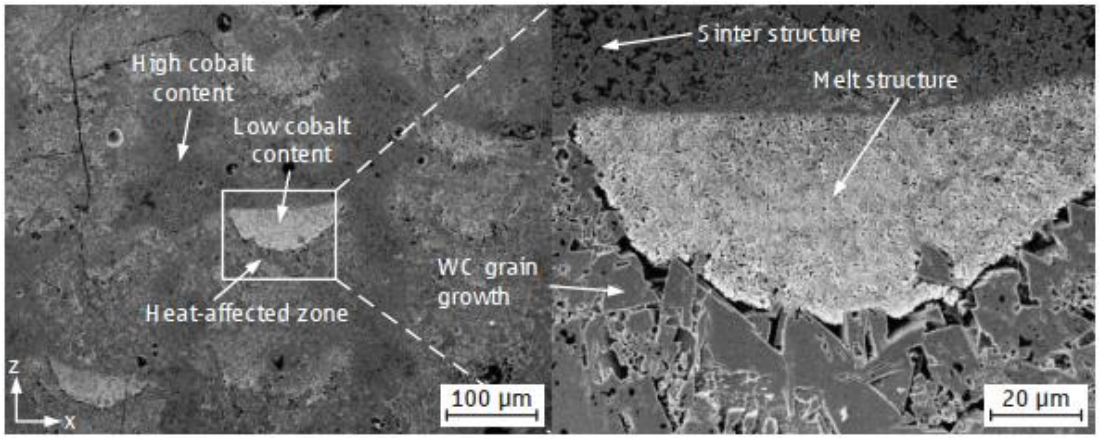

Figure 2.15: Inhomogeneous microstructure produced at high volumetric energy density showing different Co concentrations and WC grain growth [90].

The alternative microstructure, as well as cracks and pores, has also been observed by Campanelli et al. [92] using WC10Co4Cr powder. It has been shown that the inhomogeneity of microstructure has led to a large variance in hardness up to 600 HV

[91]. For cutting tool applications, such variance is extremely undesirable. Nonetheless, Domashenkov et al. [93] showed the formation of new W_2C and W_2Co_4C carbides when two types of WC- 12 Co powders were used: nanostructured (WC size = 10 $\pm$ 3 nm) and conventional powder (WC size = 56 $\pm$ 6 nm). These are brittle phases which can increase cracking susceptibility. Moreover, no residual free Co was detected by XRD investigations. To reduce the re-melting effect, using a large WC size distribution can provide a solution to these phenomena by reducing WC dissolution. This can lead to a uniform microstructure and to less fractions of new formed brittle carbides and then to a less cracking propensity.

Besides energy density, the effect of Co content in the feedstock on WC-Co solidification can be evaluated from cracking point of view. In this trend, Khmyrov et al. [94] showed that using a Co content of 6 wt.% can help to retain WC particles after laser processing. However, no residual free Co was detected by XRD investigation. Increasing the Co content to 50 wt.% has led to completely dissolution of WC particles. Another reseach showed that this Co fraction presented high cracking suceptibility due to formation of brittle W_3Co_3C phase and only a mixture containing 75 wt.% Co can be used to produce single layers without cracks as shown in Figure 2.16 [95].

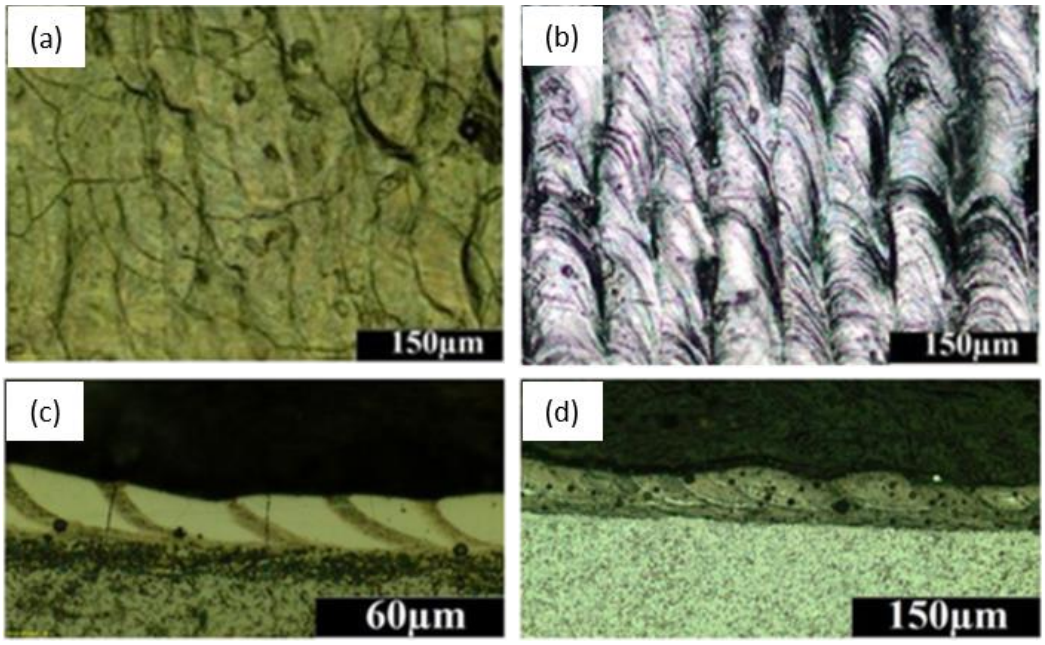

Figure 2.16: Surface morphology of single layers fabricated by L-PBF at the same process parameters: (a) WC-Co (50-50 wt.%) showing cracks, (b) WC-Co (25-75 wt.%) showing crack-free, and corresponding cross sections (c), and (d), respectively [95].

Nonetheless, the effect of Co content in the feedstock on porosity formation has been studied. Fortunato et al. [96] reported the pores sizes in two Co contents: 11 and 17 wt.%. It showed that, although hot isostatic pressing (HIP) was carried out, the lower Co has led to three types of pores: A (< 10 µm), B (10 – 25 µm), and C (> 50 µm). While only type A was detected in the higher Co content. As a result, a clear conflict can be indicated: low Co can lead to retain WC, but with large pore size: high Co can lead to high WC dissolution, but with low pore size. Interestingly, crack free WC-Co has been produed using 6 wt.% Co as shown in Figure 2.17 [97]. This was because of using a nano-sized Co with average particle size of 40 nm with larger WC (average particle size = 400 nm). Nanosized Co has a relatively larger surface area per unit volume which can result in a lower melting temperature than that of micron powder. Reducing the melting point decreases the dissolving extend of WC particles and then the formations of brittle phases.

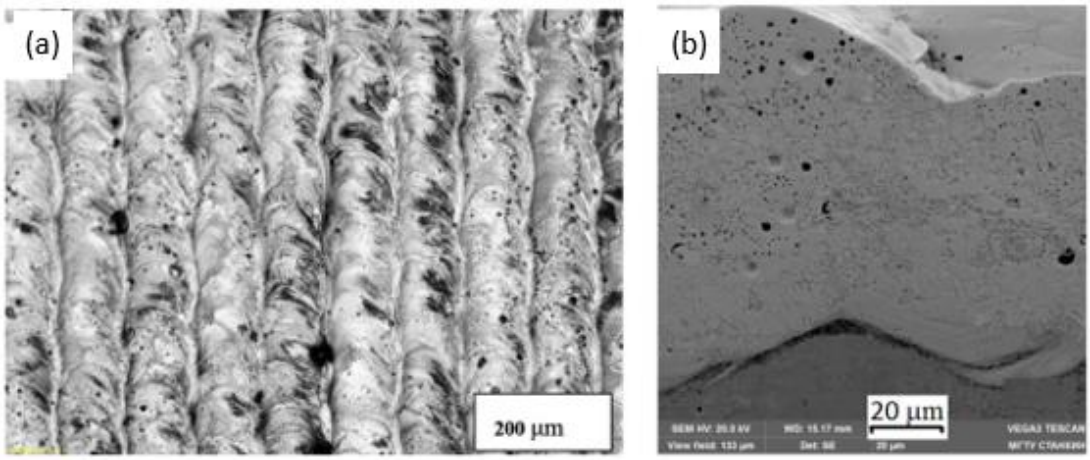

Figure 2.17: Crack free multilayer WC-Co (94-6 wt.%) sample produced by L-PBF using nanosized Co powder showing (a) surface morphology and (b) cross section [97].

The above approach can represent an opportunity to use fine Co particles to reduce WC dissolution. However, higher content of nanosized Co can increase the viscosity of the composite powder and then reduce its flowability. Poor flowability can lead to non-unifrom powder layer thickness and then to inconsistent solidification which encourages balling.

In addition to energy density and Co content, the feedstock morphology can also affect the WC-Co solidification behaviour. This can be indicated from the powder packing density. Chen et al. [98] used two WC-20 Co powders of the same composition: A in a spherical shape (mean particle size = 21 µm) and B in irregular shape (mean particle size = 41 µm). A relative density of 96% without cracks was obtained from A. Pores and cracks with a relative density of 86% were observed in the material produced from B. Spherical particles with smaller size can (1) increase powder packing density and (2) enhance energy absorption and then temperature homogenization within the melt pool. These aspects can lead to increase material density and reduce cracks. However,

no similar results were observed in the previous studies when comparable powders were employed.

Finally, the effect of sample building temperature on material cracking was evaluated. Solidification cracks caused by thermal stresses can initiate in WC-Co system due to thermal expansion/shrinkage movement during heating/cooling cycle [99]. Keeping the sample temperature at a high level during the building stage can release the induced thermal stresses and then cracking tendency. Schwanekamp et al. [91] showed that using multiple laser scanning strategy with a small time step of 15 seconds between laser exposures can reduce cracking by ~ 4% and the porosity by 6% as compared to the time step of 250 seconds. However, re-scanning strategy can also generate residual stresses in the fabricated parts [100]. On the other hand, Fries et al. [101] reported that using a high pre-heating temperature of 900 °C has led to produce crack free samples with porosity ratio between 2-5% from WC-17 Co powder. Free Co and new W_2C phase were also detected by XRD results. However, uneven distribution of WC grains is observed in the microstructure. The presence of fusible Co (melting point = 1495 °C) can cause partial powder sintering during powder spreading and then interrupt the manufacturing process [93]. Thus, more research needs to be done to confirm the reliability of the recent strategy.

As a result, appropriate laser scanning strategy and pre-heating condition cannot be confirmed. Also, likely ranges of process parameters and energy density that can be used to produce high-quality WC-Co parts have not been advised. Moreover, no suitable WC-Co mixture for L-PBF processing has been confirmed. However, the L-PBF literature revealed an opportunity to use fine Co particles in combination with a relatively large WC particles to fabricate crack free samples. This indicates the impact of WC-Co mixture design on the solidification behaviour.

2.8.WC-Co powder preparation methods

The performance of metal matrix composite depends on the ability to (1) disperse the reinforcement in the metal matrix, (2) maintain the structural integrity after material synthesis, and (3) produce matrix-reinforcement interface [102]. High performance materials can be obtained through the selection of three fundamentals: reinforcement phase, matrix phase, and powder production method [103].

Four main methods are used to prepare the WC-Co powders. The first one is ball-milling. Its procedure based on cold-welding, crushing, and refining the ingredients by the collision of hard balls in a planetary machine [104]. The initial powder particles are in micron size. During milling, Co is deformed and fractured, and WC is mainly fractured. The fractured particles agglomerate to produce nanostructured composite powder of irregular morphology. However, it leads to induce internal stresses in WC particles [105].

The second method is fused and crushing. It involves mixing and melting of initial powder components in furnaces. After cooling, the resulted block is crushed by various ways: hammer mills, stamping mills, jaw crushers, and gyratory crushers. This gives dense, blocky, and angular composite particles [106]. However, undesirable η- phases, e.g. Co_3W_3C, are commonly produced due to high densification temperature [107].

The third method is agglomeration and sintering. WC and Co powders are mixed with water, solvent, and organic binder. After spray-drying and subsequent sintering, porous WC-Co agglomerates are produced [101].

Electrodeposition coating is the fourth way. It is performed in an electrolyte cell at a constant temperature. Before processing, WC particles are chemically degreased and activated to make it easy to be coated by Co [108]. In laser processing, this

configuration ensures that laser radiation is preferentially absorbed by Co material which is to be melted [109].

The above methods can produce homogenous WC-Co powders containing a uniform distribution of WC particles which is essential for a uniform microstructure and then high-quality material. However, preparations depended mechanical work or thermal processing can induce residual stresses and produce undesirable phase changing. In addition, the costs of these methods are inevitably high [103]. Thus, developing a new strategy to produce the WC-Co powder is important.

2.9.Satelliting powder preparation method

An innovation powder preparation method 'satelliting' was used to successfully deposit materials using different techniques: cold spray, DED-L, and L-PBF [23, 110-113]. It involves coating of a larger parent particle with smaller satellite particles using polyvinyl alcohol as a binder [Patent Application No. 15/022 344].

In cold spray, it has been reported that satelliting of TiC (< 5 μm) with spherical Al (15 – 45 μm size range) has led to increase the capturing efficiency of smaller particles by 7 times as compared to that of simply blending feedstock [110].

In DED-L, it has been shown that using this method has led to produce homogenous microstructure containing a uniform distribution of TiB2 reinforcements ($<$ 3 μm) in the AlSi10Mg matrix (15 – 45 μm) [111]. Similar trend has been observed by another research when Mo (~3 μm) was used to reinforce Ti matrix (100 – 150 μm) [112].

On the other hand, a better flowability has been observed in the satelliting Ti-6Al-4V as compared to simply blending feedstock [113]. This can be attributed to homogenous distribution of powder particles in the satelliting feedstock. Consequently, consistent flow rate in DED-L and uniform powder layers in L-PBF can be achieved which are

essential characteristics for high quality materials. However, comparable densities were produced by L-PBF.

As a result, the satelliting method can represent an effective route to fabricate a desired microstructure without changing the mechanical properties and chemical composition of the initial constituents. In addition, it can be simply performed using a low-cost apparatus.

2.10. Summary of the literature review

The literature review of laser additive manufacturing of WC-Co system was divided into two fields: DED-L and L-PBF. The basic WC-Co powder preparation methods were also discussed. The overall summary and gaps detected are given below.

a) DED-L review:

The DED-L literature review showed that:

- The non-uniform microstructure due to dissolution of WC particles faced the integrity of WC-Co clads.
- Excessive energy input has led to completely dissolution of WC particles of 40 – 160 µm size range.
- The impact of process parameters on porosity formation has not been fully understood.
- Clads fabricated by using spherical WC particles in a size range of (45 – 125 µm) gave a uniform WC distribution inside the matrix, less porosity, and less WC dissolution as compared to the size range of 10 – 45 µm.
- A conflict has raised with respect to pre-heating of the substrate: with pre-heating, WC dissolution has increased: without pre-heating, cracks were formed.
- No optimum process parameters for high-quality WC-Co clads have been introduced.
- No suitable WC-Co mixture for DED-L processing has been confirmed.
- No suitable processing window to represent the behaviour of WC-Co clads has been confirmed.

b) L-PBF review:

The L-PBF literature review showed that:

- The non-uniform microstructure caused by WC dissolution faced the integrity of WC-Co materials.
- Besides the above, Co evaporation, formations of new ternary carbides, and porosity are other microstructural defects.
- A conflict has raised with respect to energy input: high energy input led to significant cracks and less pores: low energy input reduced cracks but led to increase pores.
- Decreasing WC content in the feedstock to 25 wt.% can lead to produce a single layer without cracks.
- A conflict has raised with respect to Co content in the feedstock: high Co led to increase WC dissolution, but with low matrix pores: low Co led to reduce WC dissolution, but with large matrix pores.
- Cracks can be eliminated by using fine Co particles in a nano size.
- Spherical WC-Co particles can lead to increase the solidification density as compared to irregular morphology.
- Preheating up to 900 °C can lead to produce samples without cracks.
- No optimum process parameters for high-quality WC-Co materials have been obtained.
- No suitable WC-Co mixture for L-PBF processing has been confirmed.

c) Powder preparation review:

The powder preparation literature review showed that:

- WC-Co powders prepared by traditional methods (ball milling, fused and crushing, agglomeration and sintering, and electrodeposition) can present phase changing in the initial constituents.

- The satelliting method can produce applicable composite feedstock for AM resulting in homogenous microstructure without changing the mechanical properties and chemical composition of the initial elements.

d) Gaps in literature

The gaps in literature can be divided into two main parts: gaps in WC-Co laser additive manufacturing and gaps in WC-Co powder preparation methods.

The laser additive manufacturing of WC-Co powders in both DED-L and L-PBF fields showed that a uniform microstructure including uniform distribution of WC particles without cracks and pores has not been achieved. This was due to high dissolution of WC particles during laser processing. The typical employed nano-sized WC particles have a large surface area per unit volume which enhances heat absorption and then dissolution extent. To address this problem, micro-sized WC particles will be investigated which has not been incorporated before with Co powder in any composition. Smaller Co particle size can increase heat absorption and then reduce time of melting resulting in a less melt pool duration and then WC dissolution. Nonetheless, it showed that no optimum process parameters and substrate pre-heating condition for high quality depositions have been obtained. Also, no suitable processing window to represent the relationship between process parameters and deposition behaviour has been confirmed. Moreover, no suitable WC-Co mixture for DED-L and L-PBF processing has been confirmed. Also, the effect of laser spot size on the solidification behaviour has not been reported.

On the other hand, the basic WC-Co powder preparation methods can produce phase changing in the initial elements. To address this, the satelliting powder preparation method can provide a suitable solution which has not been employed before for any WC-Co configuration.

3. Materials and methods

3.1.Introduction

This chapter details the materials, equipment, and experimental works procedures presented in this thesis. WC-Co can be utilized as coatings or bulk parts [85]. To produce coatings, DED-L technique was used. In this process, the deposition performances of blended and satellited WC_M-12 wt.% Co powders were preliminary compared. After that, a multilevel full factorial design of experiments method was undertaken to explore the deposition trend of the satellited powder. The measurements of melt pools geometries and deposition efficiency of the clads are presented.

To produce bulk parts, L-PBF technique was used. In this process, two machines were employed: Realizer SLM-50 and Renishaw AM 125. Smaller powder batch can be used to perform experiments in Realize SLM-50 of ~ 1/10 as compared to that suitable for Renishaw AM 125. Thus, Realize SLM-50 was used to evaluate the solidification behaviour of the satelliting WC_M-12 wt.% Co powder as this feedstock requires manual preparations. On the other hand, Renishaw AM 125 has a laser spot size > 3 times than that of Realize SLM-50. This can enhance the ability of the laser beam to accommodate powder particles and homogenize the temperature within the melt pool. Using smaller particles size improves this effectiveness. In addition, increasing Co content can increase material ductility and reduce cracking propensity. Thus, Renishaw AM 125 was used to investigate the solidification behaviour of plasma densified WC-17 wt.% Co powder which have smaller particle size and higher Co content as compared to that of the satelliting powder.

3.2.DED-L experiments

The DED-L experiments are divided into two stages: single tracks and multitrack coatings. The single tracks experiments show (1) preliminary experiments to examine the deposition behaviour of simply blending WC_M-12 wt.% Co and satelliting WC_M-12 wt.% Co powders and (2) a multi-level full factorial design of experiments for a best deposition powder from (1) to systematically explore the deposition behaviour. In multitrack experiments the effect of overlapping between tracks on the microstructure and then on wear resistance was investigated.

3.2.1. Materials

Two commercially available Spherotene® and Co powders were used to prepare a composite feedstock. Modern WC-Co cutting tools usually contain Co in a range of 4 – 12 wt.% [91]. High Co content can increase material ductility and then reduce cracking susceptibility. Thus, a composition of Spherotene®-Co (88-12) wt.% was selected. The Spherotene® powder has a normal size of (45-125 µm) which was purchased from Technogenia Company, France. It consists of three phases: WC, W_2C, and WC_{1-x}, so it will be denoted as WC_M in this thesis. Co metal powder with average particle size of (1-3 µm) was purchased from ABSCO Limited Company, UK. Ductile mild steel plate with dimensions of 20 × 10 × 6 mm^3 was used as a substrate. This material can diminish the heat conducted at a tribological contact and then enhance the wear resistance of the coating. The substrate surface was grit blasted before cladding process to improve its laser absorptivity.

3.2.1.1.Spherotene® powder analysis

The Spherotene® powder is manufactured by means of a patented technique known as cold crucible electromagnetic levitation. It is specified to have a microhardness of

3000 ± 500 HV [114]. Back scattered electron (BSE) images of a cross section of Spherotene® powder particle is presented in Figure 3.1. It reveals its main metallurgical structure termed, by the manufacturer, as tangled needles. Energy dispersive X-ray spectroscopy analysis (EDXA) showed that the chemical composition of WC_M powder is 94.7 ± 0.1 wt.% W and 5 ± 0.1 wt.% C.

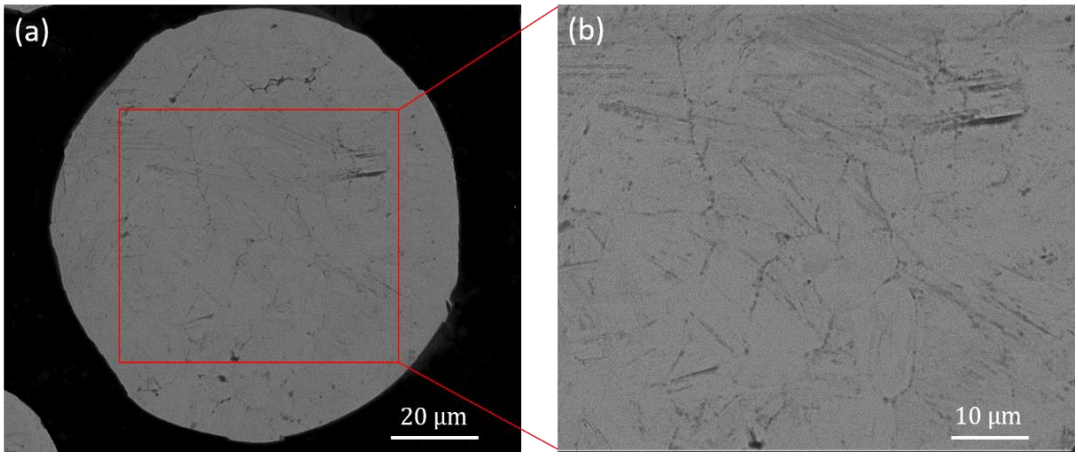

Figure 3.1: BSE images of a cross section of Spherotene® (WC_M) powder particle as supplied by Technogenia, France (a), and a corresponding higher magnification showing the tangled needles shapes (b).

X-ray diffraction (XRD) spectrum of Spherotene® powder is given in Figure 3.2. It shows three phases: WC (hcp), W_2C (hcp), and WC_{1-x} (fcc). Thus, Spherotene® will be adapted as WC_M in this thesis. The W_2C is the major phase due to its highest intensity which is observed at $2\theta = 39.6°$. The peaks identifications at 2θ and the corresponding standard numbers (JCPDS) are summarized in Table 3.1. The raw spectrum containing JCPDS files are given in Appendix D-sections D.1 and D.2.

Table 3.1: 2θ peaks identifications and the corresponding standard numbers of WC, W_2C, and WC_{1-x} phases detected in Spherotene® powder as supplied by the manufacturer.

Phase	2θ / °	JCPDS
WC	31.5, 35.7, 48.4, 64.2, 65.9, 73.2, 77.3, 84.1	00-061-0244
W_2C	34.5, 38, 39.6, 52.3, 61.9, 69.8, 75.1, 76.1, 81.4, 85.3	01-071-6322
WC_{1-x}	36.9, 42.8, 62, 74.2, 78.2	00-020-1316

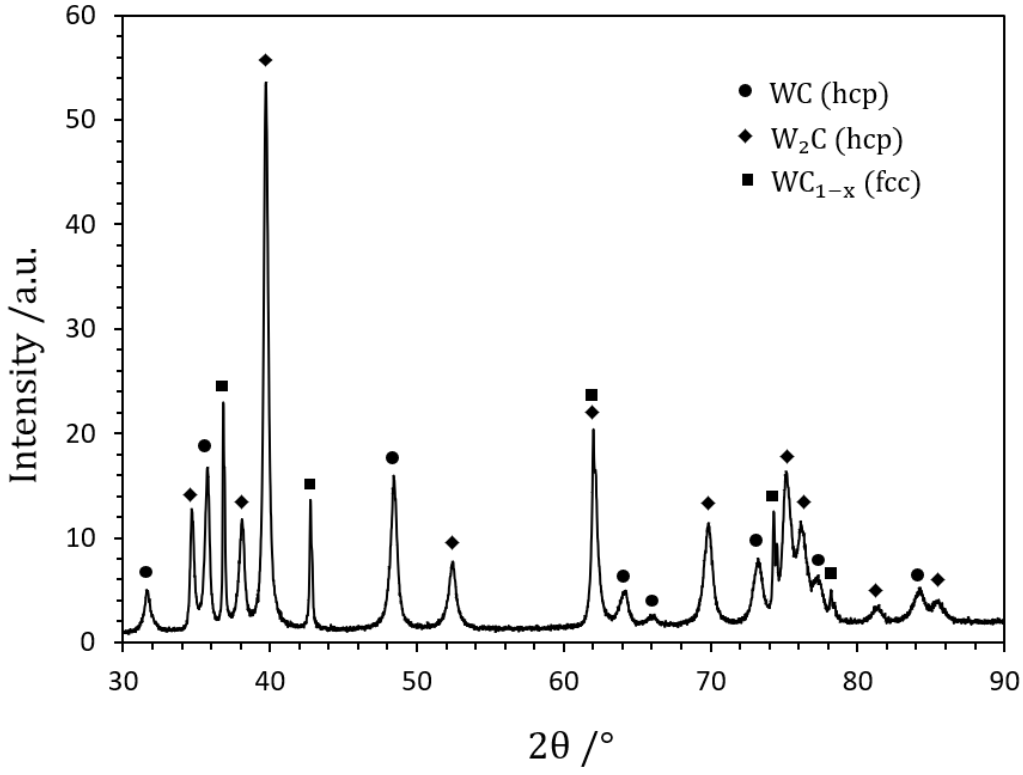

Figure 3.2: XRD investigation of Spherotene® (WC_M) powder as supplied by the manufacturer showing three phases: WC, W_2C, and WC_{1-x}.

3.2.1.2.Composite WC_M-Co powders preparations

The preparations of the WC_M-Co composite powders involve two methods: satelliting method and simply blended method. These will be explained as follow.

3.2.1.2.1. Satelliting WC_M-Co powder preparation

The satelliting powder preparation method can be used to produce composite powders consisting of relatively large particles coated by a layer of small particles [110]. The satelliting process was performed manually by two steps: dry mixing and wet mixing. In dry mixing, the WC_M (large) and Co (small) particles were mixed with certain weight fractions and a total batch of 30 g in a glass beaker. The mixing process lasted 4 – 5 minutes to ensure a homogeneous distribution of WC_M particles. In wet mixing, water-solute polyvinyl alcohol (PVA) was added as a binder in a ratio of 0.02 wt.% from the total batch weight. The water-solute was lab prepared by dissolving a 2.7% of PVA in warm water by volume (3.7 g PVA in 100 g water). This can produce a sufficient bonding between the larger and smaller powder particles. The wet powder batch was then mixed manually for 5 minutes to break down the agglomerates and homogenize the PVA distribution. These steps (dry mixing and wet mixing) were repeated sequentially for several times until the desired amount of composite powder was obtained. Then, the whole wet powder was loaded into a tubular mixer for 30 minutes to ensure a complete mixing step. Later, the powder was distributed onto a steel tray which was covered by aluminium foil and put in the oven for 12 hours for drying where the temperature was set at 50 °C.

3.2.1.2.2. Blending WC_M-Co powder preparation

For comparison purposes, simply blended WC_M-Co feedstock was also prepared by mixing the WC_M and Co powders without adding the PVA binder. This involves two steps: (1) manually dry mixing with certain weight fractions and a total batch of 30 g

in a glass beaker for 4 – 5 minutes to break down any clusters in the initial powders and to homogenize the mixture and then sequentially repeating this step several times until obtaining the desired quantity and (2) loading the whole powder into the tubular mixer for 30 minutes to complete the mixing process and ensure a homogenous distribution of WC_M particles.

3.2.2. Powders size distributions and flowability investigations

Powders size distributions were investigated by Malvern Mastersizer 3000 equipment. This is a laser-based machine. During measurement, the powder particles pass through the laser beam causing light scattering. Then, the scattered light from a field of particles is captured by annular detectors in Mastersizers' optical unit. The powder size is predicted from the light scattering pattern based on the Fraunhofer diffraction model. After that, the raw data is analysed by the Malvern software interfaced with Mastersizer giving particle vol% at different particle sizes.

The flowability behaviour were investigated by using FT4 Powder Rheometer. Schematic representation to the rheology investigation is presented in Figure 3.3. The required energy of the blade to penetrate the powder mass was given at different penetration speeds. Each investigation involves 11 tests. Tests 1-7 are performed at a constant downward penetration speed of 100 mm/s. Tests 8-11 are performed at speeds 100 – 10 mm/s, respectively. For each powder, the total tests were repeated three times and the average values were considered.

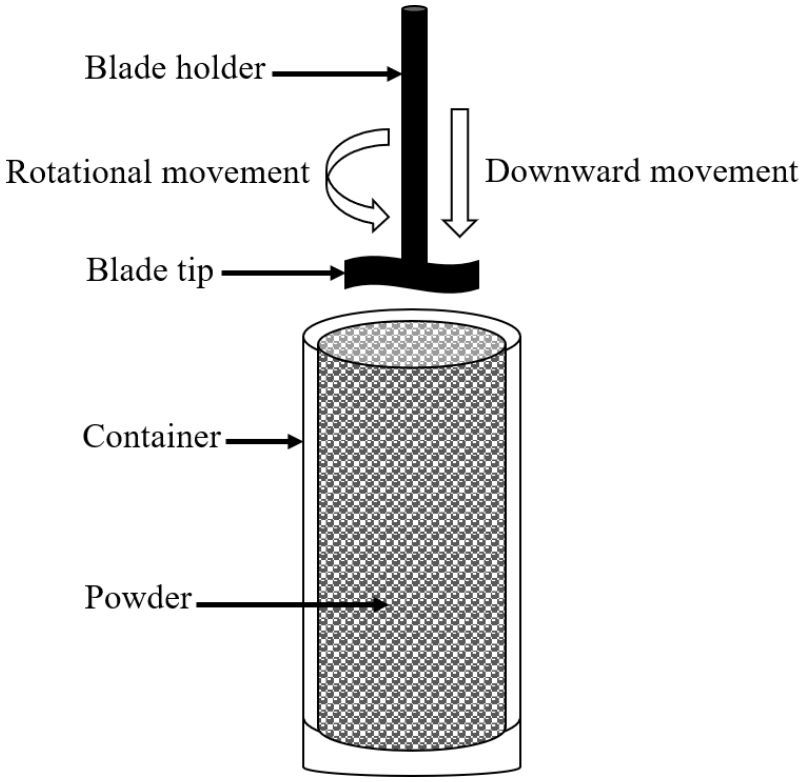

Figure 3.3: Schematic representation of the powder rheology investigation.

3.2.2.1.Characteristics of feedstock materials

This section explores the feedstock characteristics including powder morphology, size distribution analysis, and flowability. This indicates (1) the efficiency of satelliting process to bond the initial constituents, (2) the impact of satelliting on the feedstock flowability, and (3) the potential impact of flowability on the laser-powder interaction behaviour and then material quality. The cross-section analysis and XRD investigation of Spherotene® powder are also presented.

3.2.2.1.1. Feedstock morphology

The morphology of Spherotene® (WC_M), Co, blended, and satellited powders are shown in Figure 3.4. It shows that spherical shape is the main morphology of WC_M particles, and irregular shapes can also be observed (Figure 3.4a). Smaller scale is used to represent the size of Co powder which has irregular tube-like morphology (Figure

3.4b). The Co (dark colour) appears in relatively large agglomerates in blended powder (Figure 3.4c). While the satelliting powder has maintained a uniform mixing where most Co particles coat WC_M surfaces as presented in Figure 3.4d.

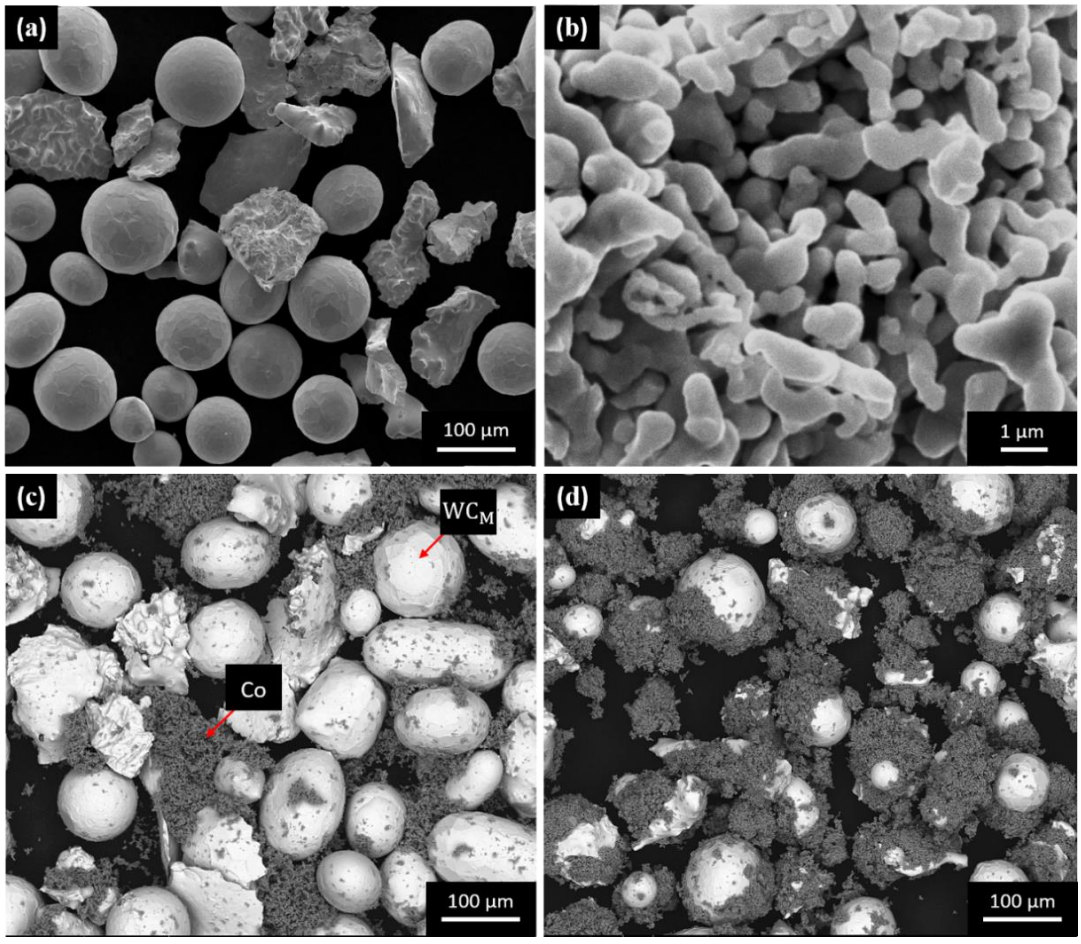

Figure 3.4: SEM/SE images of (a)-Spherotene® (WC_M), and (b)-Co powders, and SEM/BSE images of (c)-blended WC_M-12 wt.% Co, and (d)-satellited WC_M-12 wt.% Co composite powders.

3.2.2.1.2. Particle size distribution

The distributions of powders sizes are given in Figure 3.5. The cumulative particle sizes at D10, D50, and D90 are given in the combined table. It shows that the median size (D50) increases after satelliting as compared to blended powder. The efficiency

of satelliting process can be determined by comparing between the total cumulative volume% of Co in blended and satellited powders. This gives 77% which means that just 23% of Co is still free after satelliting.

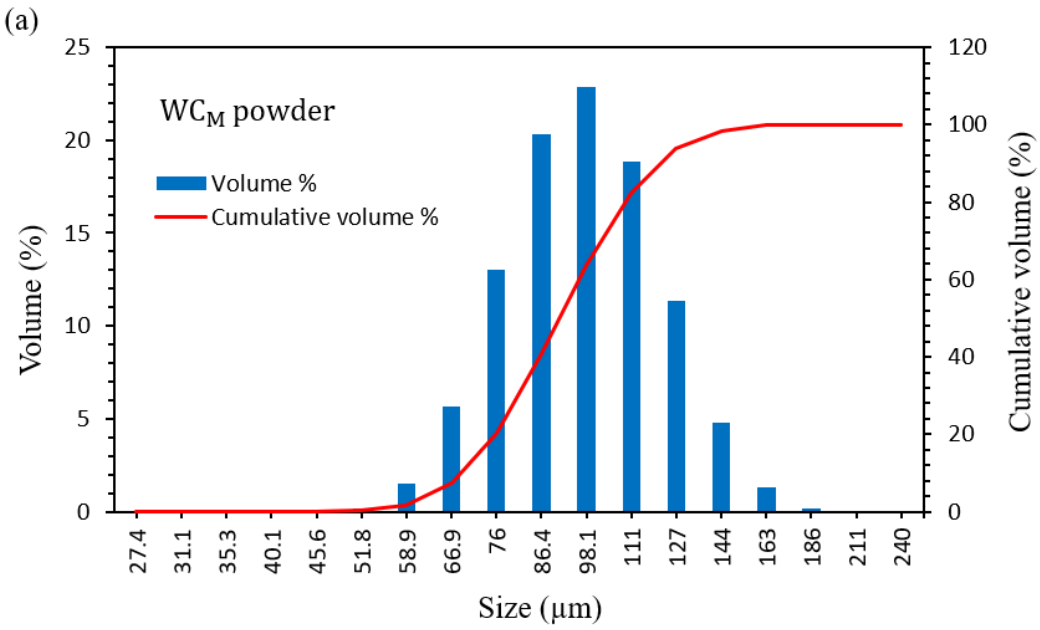

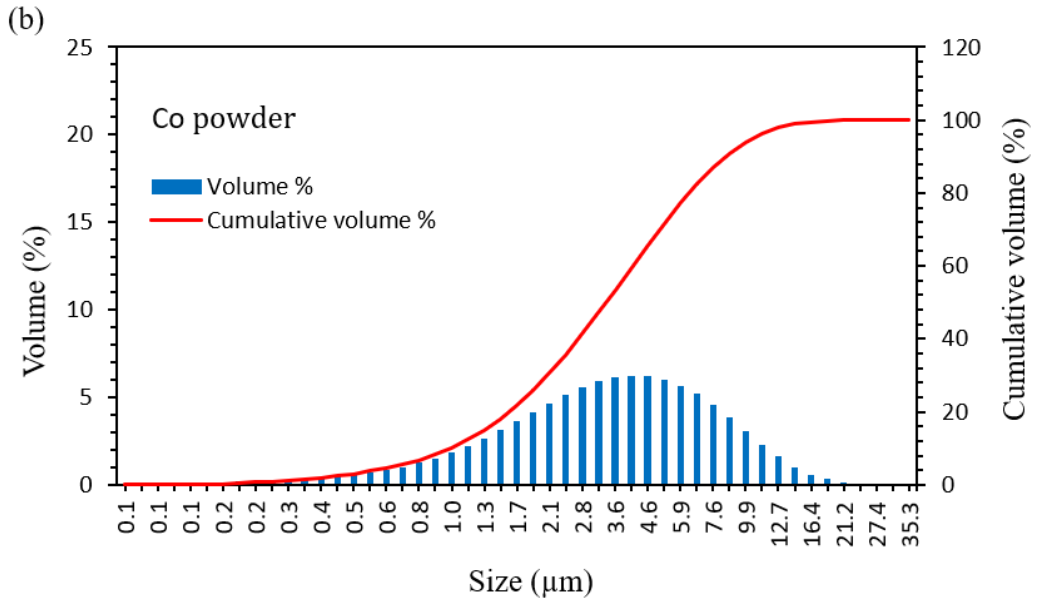

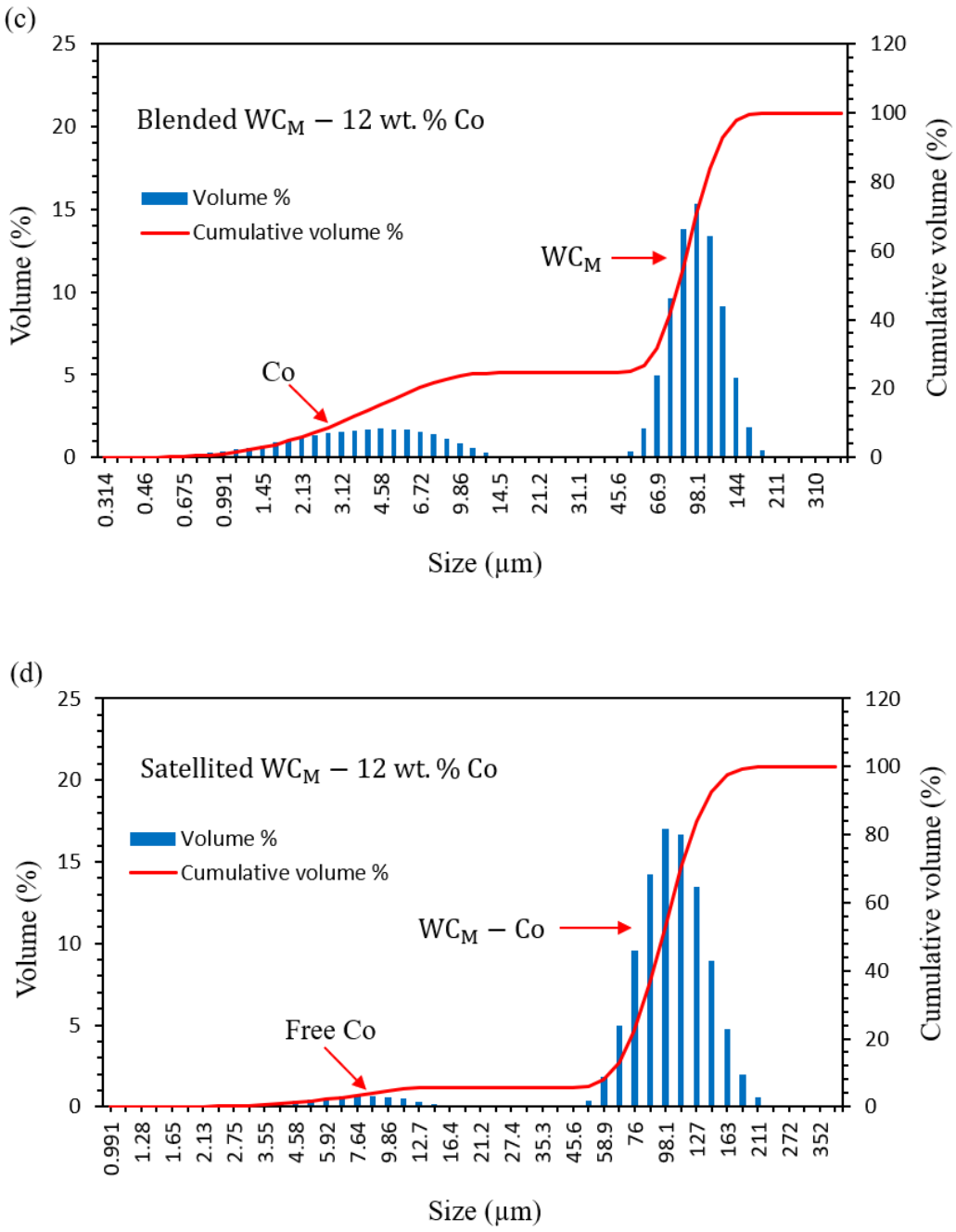

Powder	Size (µm) at D10, D50, and D90		
	D10	**D50**	**D90**
Spherotene® (WC$_M$)	78	103	138
Co	1.1	3.7	9.5
Blended WC$_M$-Co (88-12) wt.%	2.9	89.2	137
Satellited WC$_M$-Co (88-12) wt.%	70.6	109	157

Figure 3.5: Powders size distributions of (a)-WC$_M$, (b)-Co, (c)-blended WC$_M$-Co (88-12) wt.%, and (d)-satellited WC$_M$-Co (88-12) wt.%.

3.2.2.1.3. Flowability analysis

Good powder flowability is an essential characteristic for high quality AM parts. In DED-L, poor flowability can lead to inconsistent delivering of powder to the melt pool generated by the laser beam and then to irregular track morphology containing high and low depositions. In L-PBF, poor flowability can lead to inconsistent powder spreading over the substrate or the previous solidified layer containing high and low thicknesses/amounts of powder.

The flowability characteristics are given in Figure 3.6. This measures the work done (flow energy) by rheometer blade when displacing the powder in a compacting movement. It consists of 11 dynamic tests: tests 1-7 are repeated identically using the same compacting speed of -100 mm/s. The flow energy (F_E) of test 7 is a key flowability parameter which reflects the powder resistance to forced flow. The rheology stability is represented by stability index (SI = test 7/test 1). On the other hand, the sensitivity to blade compacting flow is shown through tests 8-11 where flow speed decreases gradually to -10 mm/s. This illustrates a flow rate index (FRI = test 11/test 8) where FRI =1 reveals a best flowability. The results show no significant variations in tests 1-7 for all powders indicating a good rheology stability. A lower F_E of < 200 mJ is presented in Co powder at a flow speed of -100 mm/s. Decreasing the flow speed to -10 mm/min increases F_E to > 580 mJ which results in a relatively higher FRI. For WC_M powder, F_E increases slightly from 628 ± 11 mJ to 652 ± 5 mJ by decreasing blade flow speed from -100 to -10 mm/s. Higher rheology energies are required to penetrate the composite powders. A maximum F_E of > 2180 mJ is observed in blended powder when flow speed decreases to -10 mm/s. The satelliting gives a better flowability as compared to simply blended mixture. The stability and sensitivity indices are presented in Table 3.2.

Table 3.2: Stability index (SI) and flow rate index (FRI) of Spherotene® (WC_M), Co, blended WC_M-12 wt.% Co, and satellited WC_M-12 wt.% Co powders.

Powder	WC_M	Co	Blended WC_M-12 wt.% Co	Satellited WC_M-12 wt.% Co
SI	0.96	1	1	0.92
FRI	1	3	1.8	1.2

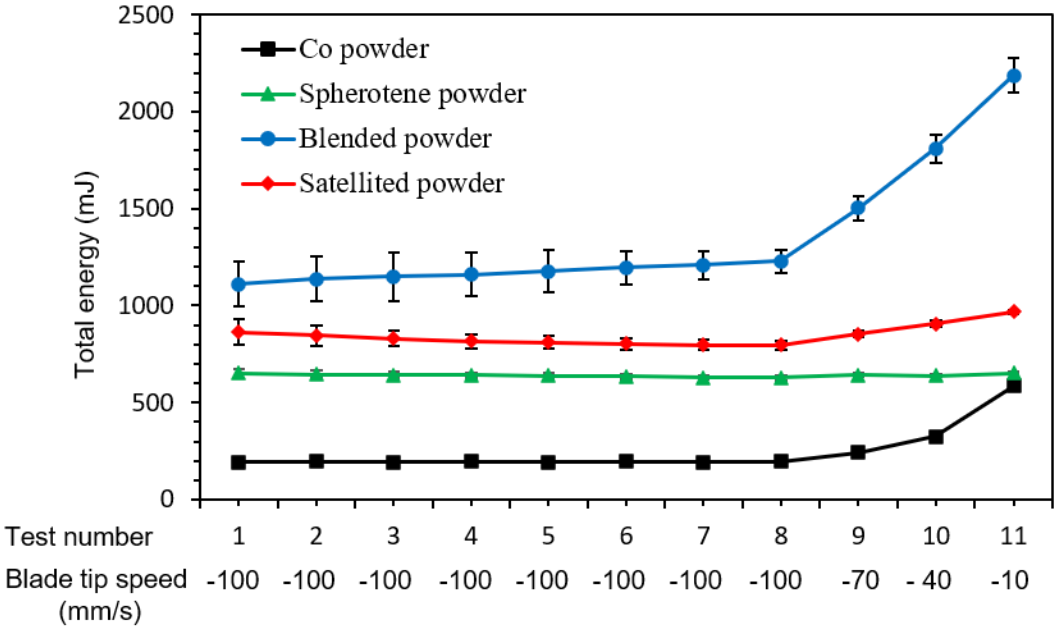

Figure 3.6: Rheology investigations of powders flowabilities of Co, Spherotene®, blended WC_M-12 wt.% Co, and satellited WC_M-12 wt.% Co: tests 1-7 show total processing energy at a constant blade speed of -100 mm/s: tests 8-11 show total processing energy when blade speed decreases from -100 to -10 mm/s: error bars resulted from three repetitions for each test.

3.2.3. Single tracks fabrication using DED-L

Single tracks of 80 mm long were deposited using a 2-kW, Ytterbium-doped, continuous wave, fibre IPG Photonics laser machine with a wavelength of 1.07 µm. The beam-optics system has 125 mm collimating lens, 200 mm focusing lens, and a Precitec YC 50 cladding head. The working distance between the cladding head and substrate surface was 192 mm (in focus) providing 1 mm laser spot size with a top-hat energy profile [39]. This can result in a uniform energy distribution over the spot area. Schematic representation to the machine set up is given in Figure 3.7. The mild steel substrate was fixed on a 4-axis computer numerically controlled (CNC) bed. The substrate motion was in x-y plane while the laser head is kept stationary in z-axis during the cladding process. A powder feeder of Praxair Model 1264 was used to deliver the feedstock through a 2 mm diameter side-fed nozzle into the melt pool via argon carrier gas. The pressure of argon gas inside powder chamber was 10 l/min. This value determines the powder delivering speed and then affects the overall laser-powder interacting time. The angle between powder nozzle and vertical axis of the laser beam was 28°. The vertical distance between the powder nozzle and substrate was 10 mm. The powder feeder was calibrated to obtain a feed rate value (g/min) according to motor revolution speed (rpm) which spins an edge-perforated disk at the basis of the powder chamber. At each disk rotational speed, the delivered powder from the nozzle was collected in a container during 1 minute of feeding and then weighted to calculate a feed rate value. The cladding process was contained in a transparent polythene chamber which was purged by argon gas at a pressure of 30 l/min.

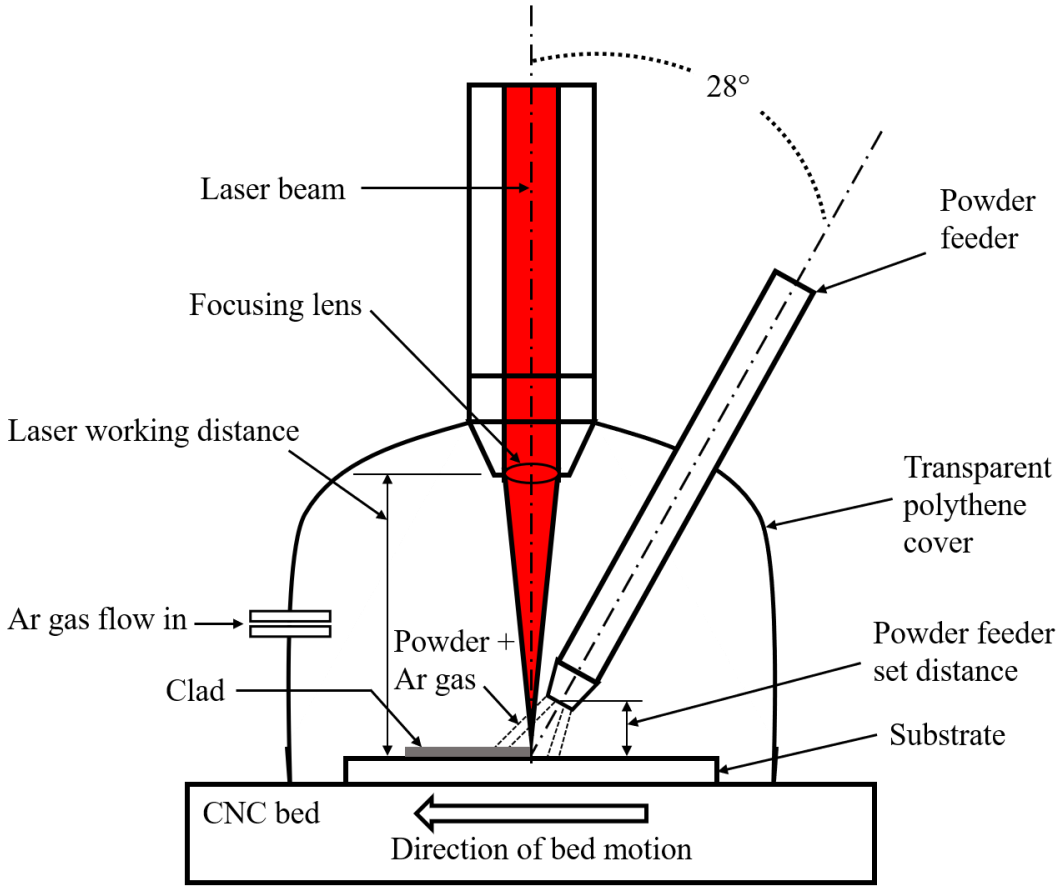

Figure 3.7: Schematic representation of the laser cladding machine set up.

3.2.3.1.Single tracks preliminary experiments

The objectives of the preliminary experiments were to:

1- Deposit a continuous single track using blended WC_M-12 wt.% Co powder.

2- Deposit a continuous single track using satellited WC_M-12 wt.% Co powder.

3- Compare the tracks morphology, melt pools geometries, and microstructural characteristics of the blending and satelliting depositions.

The laser power, scanning speed, and powder feed rate were kept constants throughout the preliminary experiments at 300 W, 240 mm/min, and 4 g/min, respectively. Two tracks were deposited from each feedstock to provide a degree of verification.

3.2.3.2.Full factorial design experiments

The feedstock which gave a better deposition behaviour from the previous section was selected for this stage of experiments. It involves a multilevel full factorial design of experiments method. The objectives of this design of experiments were to explore the impact of process parameters on the following:

1- Microstructural characteristics including porosity.
2- Melt pool geometry including dilution ratio.
3- Deposition efficiency.
4- WC_M dissolution.

The utilized process parameters are given below.

Laser power (W): 200, 350, 500

Scanning speed (mm/min): 180, 240, 360

Powder feed rate (g/min): 4, 6, 10

3.2.4. Metallographic preparations of single clads

The fabricated single tracks were cut perpendicular to laser scanning direction using a SiC cutting disc and then mounted in a conducted resin. The mounted samples underwent grinding using wet SiC papers with grit range of P240 – P1200. Then, the samples were polished using diamond paste to a 6 µm and later to a 1 µm Ra finish. Thereafter, microstructural investigations were conducted. For X-ray diffraction (XRD) investigation, the surface of a single track (parallel to laser scanning direction) was ground to prepare a flat surface without mounting in the risen and then polished. After that, the substrate surfaces extended at the track sides were completely ground to the track edges to remove their potential effects on XRD results.

3.2.5. Metallographic techniques

The morphology of the powders and the microstructures of the polished cross sections were investigated using FEI Quanta600 scanning electron microscopy (SEM) machine equipped with energy dispersive X-ray (EDX). EDX point spot analysis was used to determine the chemical composition of the microstructural features. The accelerating voltage was set at 20 kV. Back scattered electron (BSE) mode was used to differentiate between phases. X-ray diffraction (XRD) D8 advance with DaVinci machine equipped with Cu k(α) radiation source (0.15406 nm wavelength) generated at 40 kV voltage and 40 mA current was used to identify the phases/crystal structures in the fabricated parts. The step size and step time were kept constants at 0.02° and 1s, respectively. After that, the geometrical and microstructural features of the clads were analysed.

3.2.6. Single clads characterization

To study the impact of process parameters, characterization of single clads including microstructure, melt pool geometry, and powder deposition efficiency were carried out. These will be explained sequentially in the following three sections.

3.2.6.1.Microstructure

The microstructural features were defined according to the morphology and the differences in color contrast in SEM/BSE image. The chemical content of each feature was taken as the average of three measurements from three different locations using EDX point spot analysis. These observations were correlated with the crystal structures detected by XRD investigations.

3.2.6.2.Geometrical analysis

The geometrical characteristics of a single clad cross section include clad area above the substrate surface, substrate melted area, clad height, substrate melted depth, width,

and wetting angle as shown schematically in Figure 3.8. SEM/BSE images were processed using an open source software ImageJ 1.46r. This enables measuring the dimensions of melt pool as well as specific microstructure features such as retained WC_M and pores areas. Average values were taken from three cross sections. The ratio of substrate melted area to the total clad area represents the dilution ratio (D_r). This was calculated using Eq.3.1 [56].

$$D_r = \frac{\text{Substrate melted area}}{\text{Clad area} + \text{substrate melted area}} \times 100\% \qquad (3.1)$$

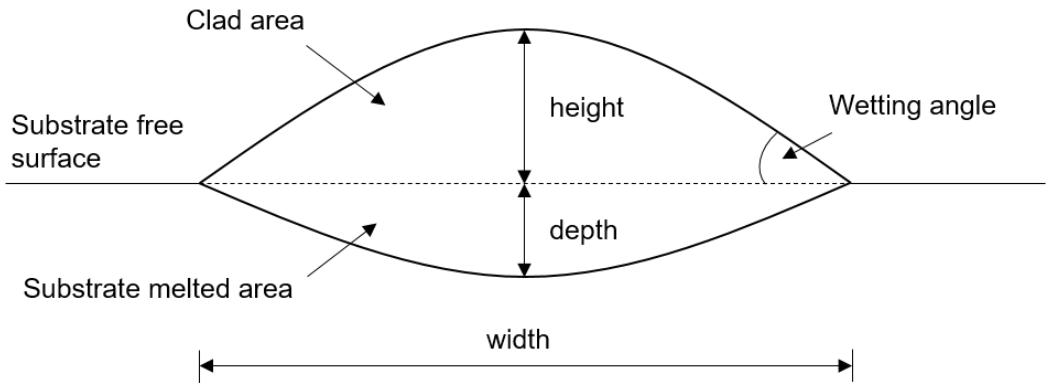

Figure 3.8: Schematic representation of the geometrical characteristics of a single clad.

3.2.6.3.Powder deposition efficiency

The powder deposition efficiency was determined by using a weighing method. It has the following assumptions:

- The powder flow is consistent throughout the deposition process.
- The melt pool consistently accommodates the impinging powder (bouncing of relatively large particles is neglected).

The step-by-step calculation is presented below.

(1) Calculating the substrate density from the volume and mass of a cubic sample which was 7.6×10^{-3} g/mm³.

(2) Calculating the total mass of clad and substrate ($M_{clad+substrate}$). Then, measuring the involved substrate volume to calculate the substrate mass ($M_{substrate}$) by considering its density (step 1).

(3) The mass of the deposited clad (M_{clad}) = $M_{clad+substrate} - M_{substrate}$.

(4) Calculating the powder delivered mass (M_{powder}) by considering the PFR and feeding time.

(5) The powder deposition efficiency (D_E) was determined by Eq.3.2.

$$D_E = (M_{clad}/M_{powder}) \times 100\% \quad (3.2)$$

3.2.7. Fabrications of multitrack coatings

To study the impact of overlapping on the microstructure, multitrack coatings were produced from 8 tracks. The process parameters and overlapping ratio are given in Table 3.3. The selected sets of parameters represent a relatively high (Sample 1) and low (Sample 2) energy densities.

Table 3.3: Process parameters used to produce multitrack coatings.

Coatings	Process parameters			
	Laser power (W)	Scanning speed (mm/min)	Powder feed rate (g/min)	Overlapping ratio (%)
Sample 1	500	180	10	50
Sample 2	500	360	10	50

3.2.7.1.Metallographic preparations of multitrack coatings

The coatings were cut perpendicular to the laser scanning direction (Figure 3.9a) using a SiC cutting disc. Then, the samples preparations were carried out in two directions: perpendicular and parallel to the laser scanning direction. The perpendicular sides (Figure 3.9b) were used to study the cross-sectional characteristics. The parallel sides (Figure 3.9c) were used to study the surface features and mechanical properties. The mechanical investigations include microhardness and wear. The microhardness and perpendicular sides samples were mounted in a conducted resin and then ground and polished. The wear samples were ground and polished without mounting to investigate the coating thickness after polishing. In addition, a substrate area of 25 × 25 mm² was ground and polished. In all cases, the grinding was performed using wet SiC papers with grit range of P240 – P1200. And the polishing was performed using diamond paste of 6 µm and finally 1 µm surface finish.

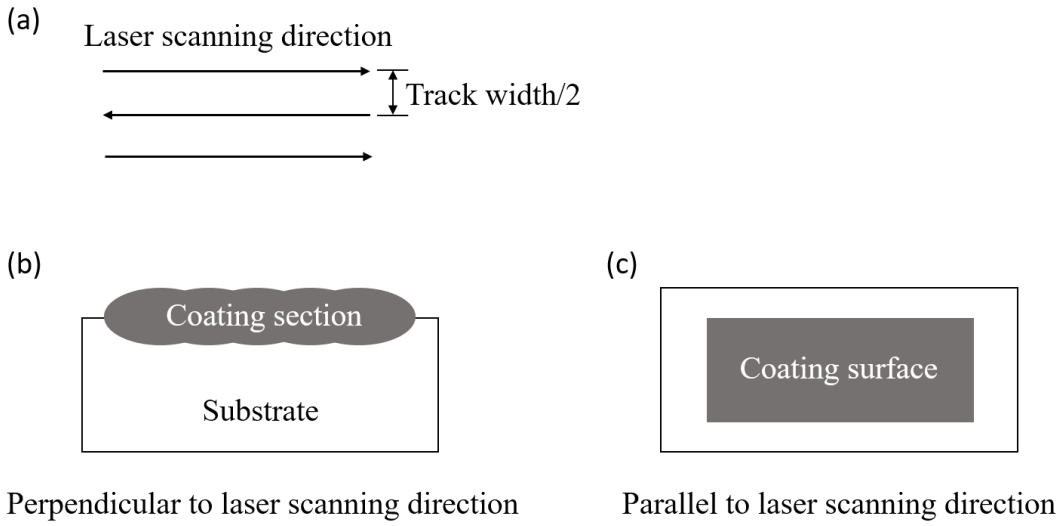

Figure 3.9: Schematic representations of metallographic preparations of multitrack coatings showing (a) laser scanning direction, (b) coating cross section sample, and (c) coating surface sample.

3.2.7.2.Characterizations of multitrack coatings

The surfaces properties of multitrack coatings were investigated using the optical microscope Nikon Eclipse LV100ND. This was also used to measure the coating thickness from the difference of vertical scale readings between the coating surface and the substrate surface. The coating thickness of Sample 1 and Sample 2 (Table 3.3) after polishing was about 200 µm. The cross sections were investigated using FEI Quanta600 scanning electron microscopy (SEM). Open source software ImageJ 1.46r was used to process the SEM/BSE images to measure the porosity and height of each coating section.

3.2.7.3.Mechanical testing

To examine the performance of the multitrack coatings, mechanical testing including microhardness and dry sliding wear was performed. These will be explained as follow.

3.2.7.3.1. Microhardness testing

The microhardness testing was carried out on the polished surfaces of the coatings and the substrate using Buehler Microhardness machine (Buehler 1600 – 6400, USA) equipped with a diamond indenter and a maximum load of 1000 gf. This was targeting the coating matrices (WC_M-free) to determine the contribution of WC_M addition and WC_M dissolution on matrix properties. The average of 12 Vickers microhardness measurements was taken to provide the mean value. The load and dwell time were 300 gf and 15 s, respectively. The microhardness test samples were also investigated using SEM/SE mode to study the indents properties.

3.2.7.3.2. Reciprocating wear testing

Ball-on-flat reciprocating dry sliding wear test were performed on the polished coatings surfaces and the mild steel substrate using Tribometer TRB^3 machine. A

schematic representation to the machine set up is given in Figure 3.10. The test was repeated three times on each sample. Silicon nitride Si_3N_4 ceramic ball (~ 1700 HV hardness [115]) of 6 mm diameter was used as a counter body which was fixed in a stationary holder. The load was applied vertically downward on the sample surface through the ball holder. The ball was changed after each test to avoid the potential effect of already worn surface on the next test. The tests were carried out under a maximum allowable load of 15 N using 5 mm linear displacement amplitude, 20 mm/s sliding speed, and 30 m sliding distance. This provides 3000 cycles of working where each cycle represents one completed forward and backward movement of the ball along the 5 mm contact length. The coefficient of friction was continuously recorded by the computer connected to the tribometer. The resulted contact surfaces were evaluated using SEM/SE investigations.

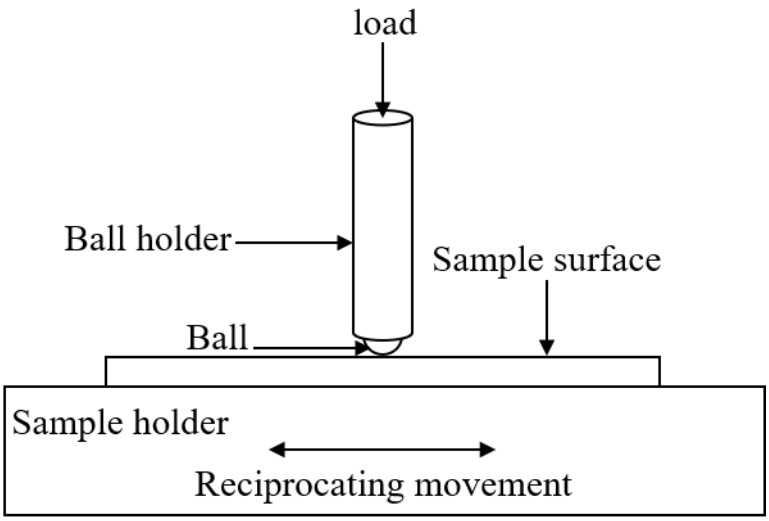

Figure 3.10: Schematic representation of reciprocating dry sliding wear in the Tribometer TRB^3 machine used in wear tests.

3.1.L-PBF experiments

L-PBF technique was used to produce bulk WC-Co materials. In this process, two machines were employed: Realizer SLM-50 and Renishaw AM 125. Smaller powder batch of ~ 200 ml can be used to perform the experiments in Realize SLM-50 as compared to ~ 2000 ml suitable for Renishaw AM 125. For economic usage of powder, Realize SLM-50 was used to evaluate the solidification behaviour of the satelliting WC_M-12 wt.% Co powder as this requires manual preparations. On the other hand, Renishaw AM 125 has a laser spot size of 75 µm which is > 3 times larger than that of Realize SLM-50. This can enhance the ability of the larger laser spot to accommodate powder particles and homogenize the temperature within the melt pool. Using small powder particles increases this effectiveness. Moreover, increasing Co content can enhance material ductility and reduce cracking propensity. Thus, Renishaw AM 125 was used to examine the solidification behaviour of plasma densified WC-17 wt.% Co powder which has smaller particle size and higher Co content as compared to that of the satelliting powder.

The L-PBF experiments involve three successive steps as follow.

1- Calculating the thermo-physical properties of the composite powders used in this study to estimate the corresponding melt pools sizes.
2- Estimating the melt pool size using the Rosenthal equation to find out the likely values of laser power and scanning speed that can be used to generate a suitable melt pool according to the thermo-physical properties of a given powder. To effectively melt the powder, the estimated melt pool width is taken to be more than the maximum powder particle size.
3- Then, the experiments were performed in two stages: (1) examining the validity of the process parameters used to predict the melt pool size of a given powder

and (2) systematically expanding the process parameters to explore the solidification behaviour.

The above steps are detailed sequentially in the coming three sections.

3.1.1. Thermo-physical properties of the composite powders

The volume ratio, thermal conductivity, material density, specific heat capacity, and thermal diffusivity of the satellited WC_M-12 wt.% Co and plasma densified WC-17 wt.% Co composite powders are calculated in the following manner.

1- **Volume fraction:** The volume fractions of WC and Co in the feedstock is calculated as explained below:

- Considering 100 g of the feedstock: The weight ratio of the WC and Co gives their individual weights (i.e. in satellited WC_M-Co (88-12 wt.%), the WC_M and Co weights are WC_{mass} =88 g and Co_{mass} =12 g, respectively, and in plasma densified WC-Co (83-17 wt.%), the WC and Co weights are 83 g and 17 g, respectively.

- Calculating the volume: The volumes of WC (WC_{vol}) and Co (Co_{vol}) in the feedstock are calculated from the ratio of mass/density; $WC_{vol} = WC_{mass}/\rho_{WC}$, and $Co_{vol} = Co_{mass}/\rho_{Co}$, where ρ_{WC} and ρ_{Co} are the materials densities of the WC and Co, respectively.

- The total volume: The total volume of the feedstock (V_{total}) = $WC_{vol} + Co_{vol}$.

- Volume fraction: The volume fraction of the WC (V_{WC}) = WC_{vol}/V_{total}, and the volume fraction of Co (V_{Co}) = Co_{vol}/V_{total}.

2- **Thermal conductivity:** The effective thermal conductivity (λ_e) is calculated by Eq.3.3 [116].

$$\lambda_e = \lambda_{Co} \frac{(1+ V_{WC})\,\lambda_{WC}+(1- V_{WC})\,\lambda_{Co}}{(1- V_{WC})\,\lambda_{WC}+(1+ V_{WC})\,\lambda_{Co}} \quad (3.3)$$

Where λ_{Co} = thermal conductivity of Co, λ_{WC} = thermal conductivity of WC, and V_{WC} = volume fraction of WC.

3- **Material density:** The effective material density (ρ_e) is calculated by Eq.3.4 [116].

$$\rho_e = \rho_{WC}\, V_{WC} + \rho_{Co}\, V_{Co} \quad (3.4)$$

4- **Specific heat capacity:** The effective specific heat capacity (C_e) is calculated by Eq.3.5 [116]:

$$C_e = \frac{\rho_{WC}}{\rho_e} C_{WC}\, V_{WC} + \frac{\rho_{Co}}{\rho_e} C_{Co}\, V_{Co} \quad (3.5)$$

Where C_{WC} and C_{Co} are the specific heat capacities of the WC and Co, respectively.

5- **Thermal diffusivity:** The effective thermal diffusivity (α_e) is calculated from the following equation [78].

$$\lambda_e = \alpha_e\, C_e\, \rho_e \quad (3.6)$$

6- **Laser absorption coefficient:** The effective laser absorption coefficient (η_e) is estimated by considering the volume ratio and laser absorptivity of each of WC and Co constituents in the feedstock as shown in Eq.3.7.

$$\eta_e = \eta_{WC}\, V_{WC} + \eta_{Co}\, V_{Co} \quad (3.7)$$

Where η_{WC} and η_{Co} are the laser absorption coefficients of WC and Co, respectively.

The thermo-physical properties of the WC and Co powders are given in Table 3.4.

Table 3.4: Thermo-physical properties of the initial WC and Co powders [71, 83].

Property and unit	Powder	
	WC	Co
Thermal conductivity (W/m/K)	84	100
Material density (kg/m³)	15800	8900
Specific heat capacity (J/g/K)	0.05	0.42
Laser absorption coefficient	0.82	0.58
Melting point (°C)	2687	1495

The estimated thermo-physical properties of the satellited WC_M-12 wt.% Co and plasma densified WC-17 wt.% Co composite powders are given in Table 3.5.

Table 3.5: Estimated thermo-physical properties of the satellited WC_M-12 wt.% Co and plasma densified WC-17 wt.% Co composite powders.

Property and unit	Powder	
	Satellited WC_M-12 Co	Plasma densified WC-17 Co
WC volume ratio	0.8	0.73
Co volume ratio	0.2	0.27
Thermal conductivity (W/m/K)	87	88
Material density (Kg/m³)	14420	13937
Specific heat capacity (J/g/K)	0.095	0.114
Thermal diffusivity $\times 10^{-5}$ (m²/s)	6	5
Laser absorption coefficient	0.77	0.75

3.1.2. Estimation of melt pool size

The melt pool sizes for the satelliting WC_M-12 wt.% Co and plasma densified WC-17 wt.% Co composite powders were estimated by using Rosenthal equation as given in Eq.3.8 [117]. The depth of the melt pool has been considered as a half of its width.

$$T_m - T_o = \frac{\eta_e P}{2\pi\lambda_e r} \exp\left[-\frac{v(\xi+r)}{2\alpha_e}\right] \quad (3.8)$$

Where T_m = melting point of the powder in K (Co melting point was considered here), T_o = initial powder temperature in K, η_e = effective laser absorption coefficient of the powder, P = laser power in W, λ_e = effective thermal conductivity of the powder in $Wm^{-1}K^{-1}$, v = laser scanning speed in m/s, ξ = melt pool dimension in the direction of the laser scanning in m, $r = \sqrt{x^2 + y^2 + z^2}$ is the radius of melt pool from the centre of the laser spot in m, and α_e = effective thermal diffusivity of the powder in m^2s^{-1}. A schematic representation to melt pool shape is shown in Figure 3.11.

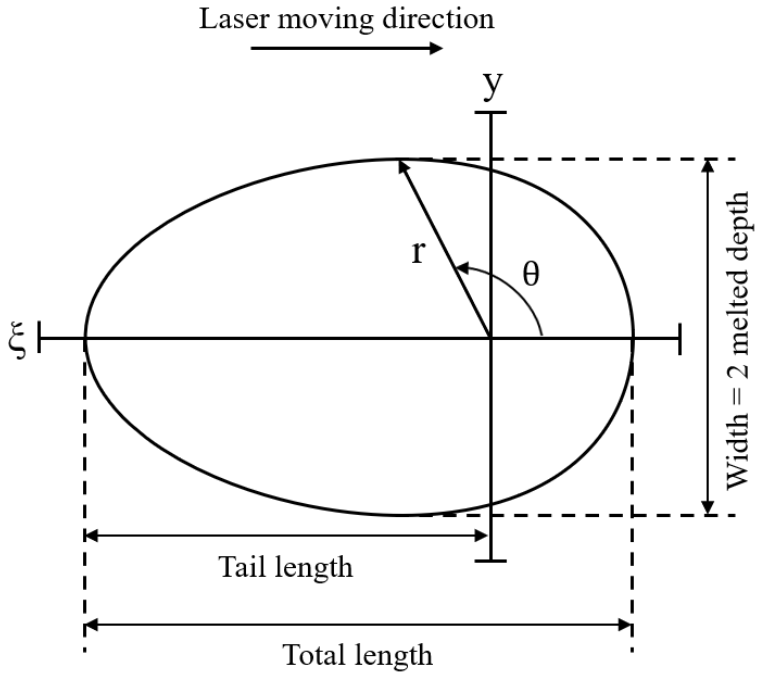

Figure 3.11: Schematic representation of the theoretical melt pool dimensions (plan view) in L-PBF according to Rosenthal equation. The laser beam is centred at the intersection of the ξ and y axes [117].

The Rosenthal equation is based upon the following assumptions:

1- The thermo-physical properties of the material are independent of temperature.
2- Speed and rate of heat are constant.
3- Convection and radiation heats are absent.
4- The melt pool is in a conduction melting mode (no keyholing).
5- Point heat source is considered (no effect of laser spot size).

The Rosenthal model comes with the following limitations:

1- The thermal properties of the materials can vary with temperature: The thermal conductivity and specific heat capacity increase with temperature while density decreases [118].
2- The continuous inert gas flowing while melting in progress can affect the heat absorbed and then melt pool size.
3- The melt pool shape can transition from conduction melting mode to keyhole melting mode by increasing the heat input.
4- The laser beam is not a point heat source: Increasing the laser spot size reduces the energy density even with a constant value of laser power.

To find out r as a function of θ, the Rosenthal equation was solved using MATLAB software. A simplification to the Rosenthal equation and a MATLAB code are given in Appendix E – section E.1. The r values were calculated in a θ range of 0 – 360 °. Then, the corresponding x and y dimensions of the melt pool at each combination of r and θ values were calculated as follow: $x = r \cos \theta$, and $y = r \sin \theta$. After that, x values were plotted against y values to represent the melt pool profile. The process parameters used to predict the melt pool sizes for the satellited WC_M-12 wt.% Co and plasma densified WC-17 wt.% Co powders are given in Table 3.6.

Table 3.6: Process parameters used to calculate the melt pool sizes of the satellited WC_M-12 wt.% Co and plasma densified WC-17 wt.% Co powders in L-PBF using Rosenthal equation.

Powder	Process parameters	
	Laser power (W)	Scanning speed (m/s)
Satellited WC_M-12 wt.% Co	100	0.14
Plasma densified WC-17 wt.% Co	120	0.6

3.1.3. L-PBF processing

The L-PBF processing was carried out in two different machines: Realizer SLM-50 using satelliting WC_M-12 wt.% Co powder and Renishaw 125 AM using plasma densified WC-17 wt.% Co powder. The reasons behined each machine and the employed powder are explained in the coming sections.

3.1.3.1.L-PBF processing using Realizer SLM-50

Realizer SLM-50 requires a small amount of powder to perform the experiments. This represents ~ 1/10 ratio as compared to that amount required for Renishaw 125 AM. Thus, Realizer SLM-50 provides economic usage of powder which saves resources and time of preparation especially for manually prepared composite powders.

3.1.3.1.1. Materials

Satelliting WC_M-12 wt.% Co powder was used as a feedstock. The powder preparation was described in section 3.2.1.2.1. The melting point of steel (1435 °C) is comparable to that of Co (1495 °C) which is to be melted [83]. Thus, 304 stainless steel plate of 2 mm thickness was used as a substrate.

3.1.3.1.2. Single tracks fabrications

A Realizer GmbH SLM-50, Germany, machine equipped with a continuous 100 W yttrium fibre laser (YLM-100-AC) was used to melt a single layer of satellited feedstock into tracks of 5 mm long. The substrate was sand blasted prior to powder spreading to remove oxidations and other types of contaminations. The layer thickness was determined by referencing the substrate to the level of the machine platform. Then the substrate was lowered by 150 µm with respect to the machine platform. After that, the powder was spread on the substrate using the automatic re-coating system of the machine. Before the melting experiments, the laser was focused to a spot size of 22 µm (nominal spot size of the laser at the focal point) at a full measured power of 100 W. The process parameters used to perform these single-track experiments are listed in Table 3.7. The nominal scanning speed value was calculated from the ratio of point distance/exposure time. And the point distance was fixed at 10 µm. For each process parameter set, three tracks were produced and characterized. A schematic representation to the machine set up is shown in Figure 3.12.

Table 3.7: Process parameters used to produce single tracks from satellited WC_M-12 wt.% Co powder in L-PBF using Realizer SLM-50.

L-PBF parameter	**Values (units)/direction**			
Measured powder layer thickness	150 (µm)			
Oxygen level	< 0.5%			
Substrate pre-heating temperature	200 (°C)			
Scanning strategy	Uni-directional			
Measured laser power	100 (W)			
Exposure time	70 (µs)	50 (µs)	30 (µs)	20 (µs)
Nominal laser scanning speed	0.14 (m/s)	0.2 (m/s)	0.33 (m/s)	0.5 (m/s)

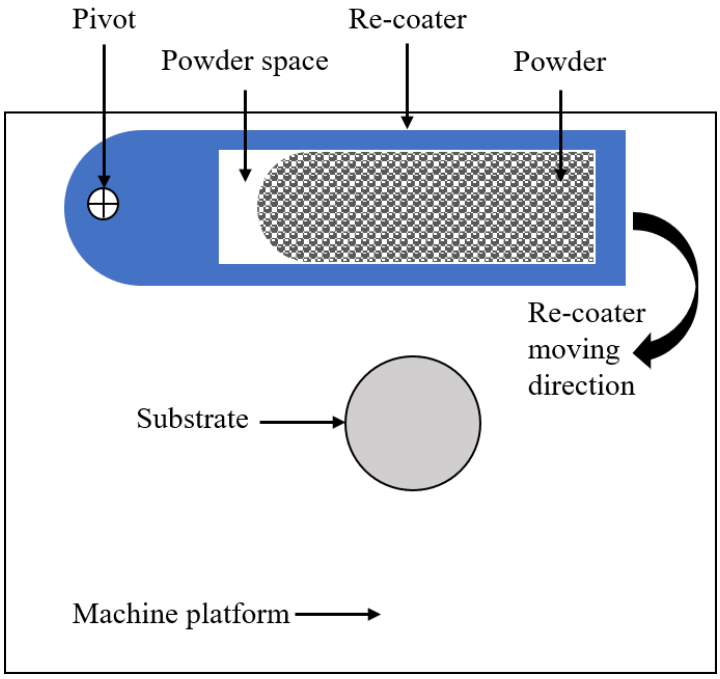

Figure 3.12: Schematic representation of the Realizer SLM-50 machine set up.

3.1.3.1.3. Characterization of single tracks

The morphological measurements of the single tracks produced were taken at the middle segments to investigate the melting and solidification that occurs during the steady state regime of laser. The width and height of these tracks were measured by an optical microscope (OM), Nikon Eclipse LV100ND. Care was taken to measure the width consistently at the track bottom/substrate boundary. The track height was calculated from the difference in vertical scale readings between the substrate and the top of the track. The average track width and height were calculated from six measurements. The melt pools at the ends of tracks were defined by using scanning electron microscopy (SEM). It is noteworthy that the laser will decrease its acceleration of speed towards the end of the track to come to stop or a turn. However, in the present study it is assumed that the melt pools at the end of tracks are still representatives of the melt pool during steady state melting - at least in the first order of approximation. The length and width of the melt pool were calculated by fitting an

ellipse around the solidification line of the last laser point exposure. And the width was extracted from the minor axis considering the boundary between the solidified material and substrate.

For cross sectional investigations, selected single tracks were cut perpendicular to the laser scanning direction using a SiC cutting disc and then mounted in conducting resin followed by the normal grinding/polishing procedure. The melted depth between the free surface of the substrate and the bottom of the molten pool as well as the length and width of melt pool morphology at the end of track were measured from three representative images at each set of process parameters by using the open source software ImageJ 1.46r. For morphological analyses, a Quanta600 (SEM) equipped with energy dispersive X-ray analysis (EDX) was used with 20 kV as an accelerating voltage. To differentiate WC_M particles sintered to the track to melt pool instabilities such as balling, backscattered (BSE) imaging was undertaken.

3.1.3.1.4. Fabrications of layered components

The fabrications of layered components involve three stages. Firstly, the substrate was referenced to the machine platform and a powder layer thickness of 150 µm was deposited manually using the re-coater to spread the powder. A square single layer in the dimensions of 5×5 mm² was fabricated in the x-y plane. The process parameters are given in Table 3.8. A schematic representation to layers formation is given in Figure 3.13. The thickness of solidified single layer was measured from 6 readings by using an optical microscope (OM) of Nikon Eclipse LV100ND from the difference of vertical scale readings between the layer surface and the substrate surface. In the second stage, the surface of the single solidified layer was referenced to the machine platform. Then, the substrate was lowered by 150 µm. After that, another 150 µm powder thickness was added on the surface of the first solidified layer. Then, the laser

melts this powder layer to form the two layers component. The average height of these two combined layers was measured as before. In the third stage, the surface of the two combined layers was referenced to the machine platform. Then, the substrate was lowered by 150 µm. After that, a third 150 µm powder layer was added on the surface of the two solidified layers. Finally, the laser melts this third powder layer to form the three layers component.

Table 3.8: Process parameters used to produce layered components (single layers and multilayers) from satelliting WC_M-12 wt.% Co powder using Realizer SLM-50.

PBF parameter	Values (units)/direction
Measured laser spot size	22 (µm)
Oxygen level	< 0.5%
Substrate pre-heating temperature	200 (°C)
Scanning strategy	Uni-directional
Scanning speed	0.14 (m/s)
Hatch distance	120 (µm)
Laser power	100, 90, 80 (W)

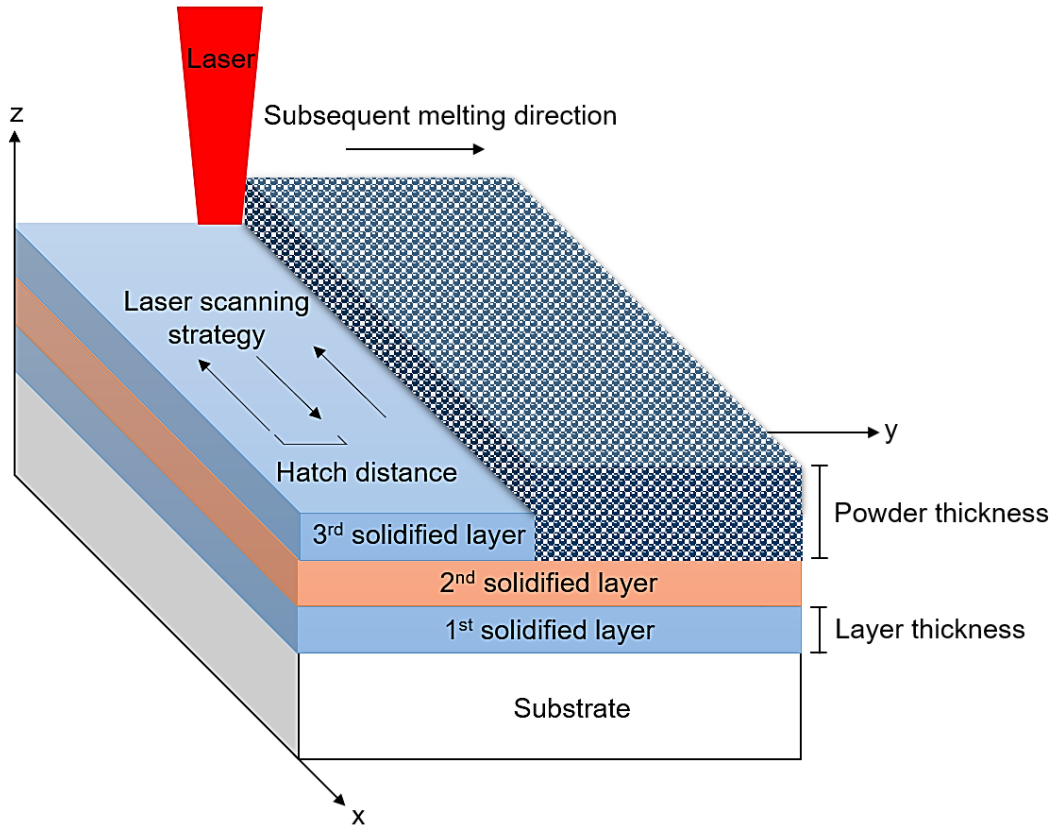

Figure 3.13: Schematic representation of layers fabrications in L-PBF.

3.1.3.1.5. Characterisation of layered components

For surface morphological analyses, SEM investigations were undertaken. To differentiate WC_M particles sintered to the layer surface to melt pool instabilities such as balling, BSE mode was undertaken. For cross sectional investigations, the layered components were cut perpendicular to the laser scanning direction using a SiC cutting disc and then mounted in conducting resin followed by the normal grinding/polishing procedure. The microstructures of cross sections were investigated using SEM/BSE mode. This also includes the bonding between adjacent tracks in a single layer and between sequential layers.

3.1.3.2.L-PBF processing using Renishaw AM 125

Renishaw AM 125 L-PBF machine equipped with maximum laser power and spot size of 200 W and 75 µm, respectively, was used. The spot size is more than 3 times than that in Realizer SLM-50. This can increase the ability of the larger laser spot to accommodate the powder particles and homogenize the temperature within a powder layer. Thus, tracks of uniform morphology and then surfaces of less irregularities are expected. The experiments are divided into two parts: walls fabrication to investigate the behaviour of single track morphology in a multi-layer component and then cubic samples fabrications in a process window of laser power and scanning speed to study the impact of energy density on the evolution of surface morphology.

3.1.3.2.1. Materials

Plasma densified WC-17 wt.% Co composite powder was used. The powder has a normal size of 15 – 45 µm which was purchased from Praxair Surface Technologies company, USA. The particle size is smaller than that of the satelliting WC_M-12 wt.% Co powder. A smaller particle size can (1) enhance laser beam effectiveness to accommodate the powder particles and then homogenize the temperature within a given powder layer and (2) allow using a lower layer thickness which can lead to increase the bulk density. Thus, high density samples are expected. The standard machine substrate is steel. This was sand blasted prior the experiments to remove any oxidations or contaminations.

3.1.3.2.2. WC-17 wt.% Co powder characterization

The morphology and size distribution of plasma densified WC-17 wt.% Co powder were investigated by Quanta600 (SEM) and Malvern Mastersizer 3000, respectively. The powder phases were investigated by XRD D8 advance with DaVinci.

3.1.3.2.3. Morphology and size distribution of WC-17 wt.% Co powder

SEM investigations and particle size distribution of plasma densified WC-17 wt.% Co powder are presented in Figure 3.14. It shows that spherical shape is the main morphology of powder particles (Figure 3.14a). The high magnification reveals voids within a particle surface and WC agglomerates (Figure 3.14b). Particles size distribution is given in Figure 3.14c. The median particle size is 38.7 µm.

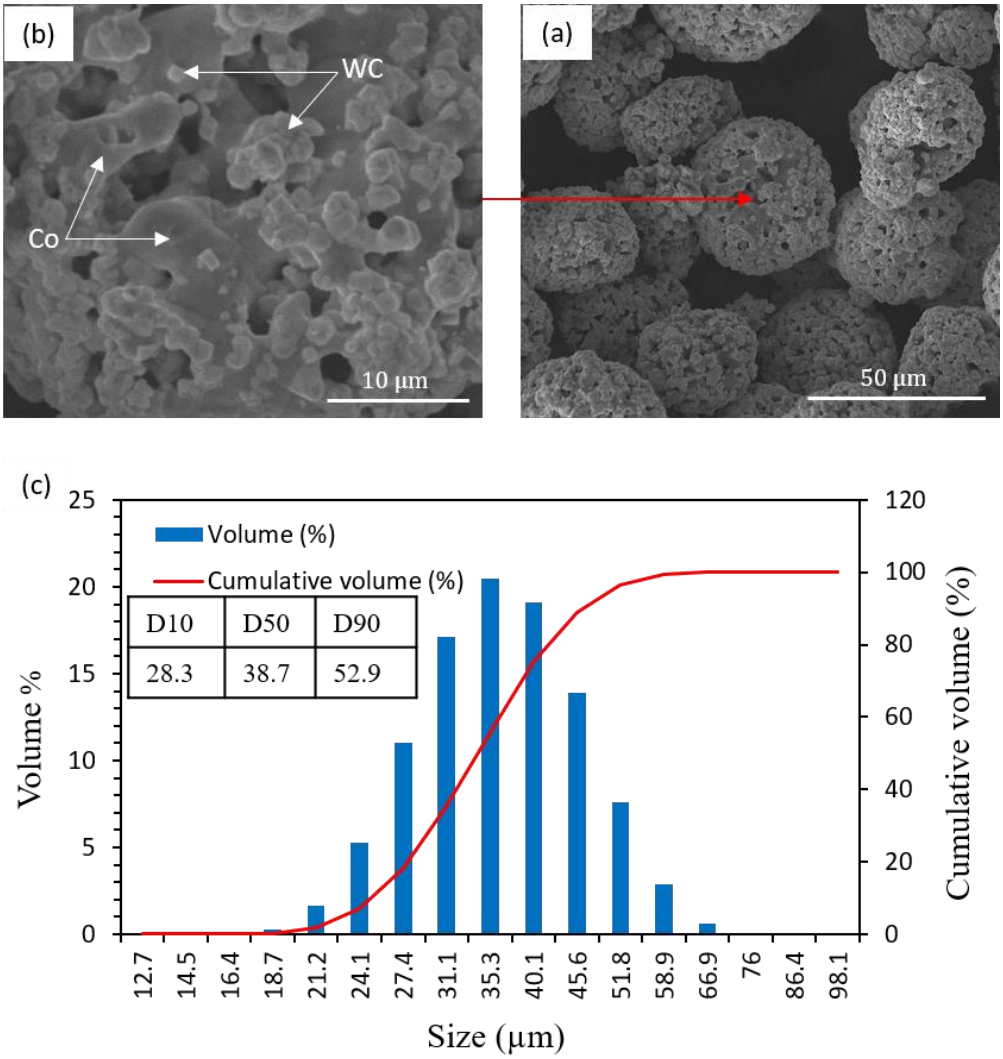

Figure 3.14: Plasma densified WC-17 wt.% Co powder: SEM/SE investigations of morphology (a, b) and size distribution analysis (c).

3.1.3.2.4. Single walls fabrication

To examine the ability of producing continuous multilayer tracks without cracks and pores, single walls of 10 mm length were fabricated from multi tracks overlapped vertically layer by layer. The walls height above the substrate surface was 10 mm. The process parameters are given in Table 3.9.

Table 3.9: Process parameters used to fabricate single walls from plasma densified WC-17 wt.% Co powder using Renishaw AM 125.

Process parameter	Values/unit/ direction
Laser power	120 W
Scanning speed	600 mm/s
Powder layer thickness	30 µm
Substrate pre-heating temperature	175 °C
Oxygen level	< 900 ppm

3.1.3.2.5. Fabrication of cubic samples

To systematically study the impact of energy density on the surface morphology, cubic samples in a size of 10 × 10 × 10 mm^3 were fabricated in a process window. This has constant intervals of laser power and scanning speed increments. The cubic samples were modelled by using MITT Auto Fab software then the models were uploaded to the machine. The machine chamber is purged by argon gas. The substrate set up is shown in Figure 3.15. The powder is uploaded in the cartridge. This has a bottom gate which allows the powder to fall on the machine platform by the gravity effect. The re-coater spreads the fallen powder on the substrate surface. The overflow powder is collected in a downward container through sets of holes in the machine platform. The process parameters are given in Table 3.10.

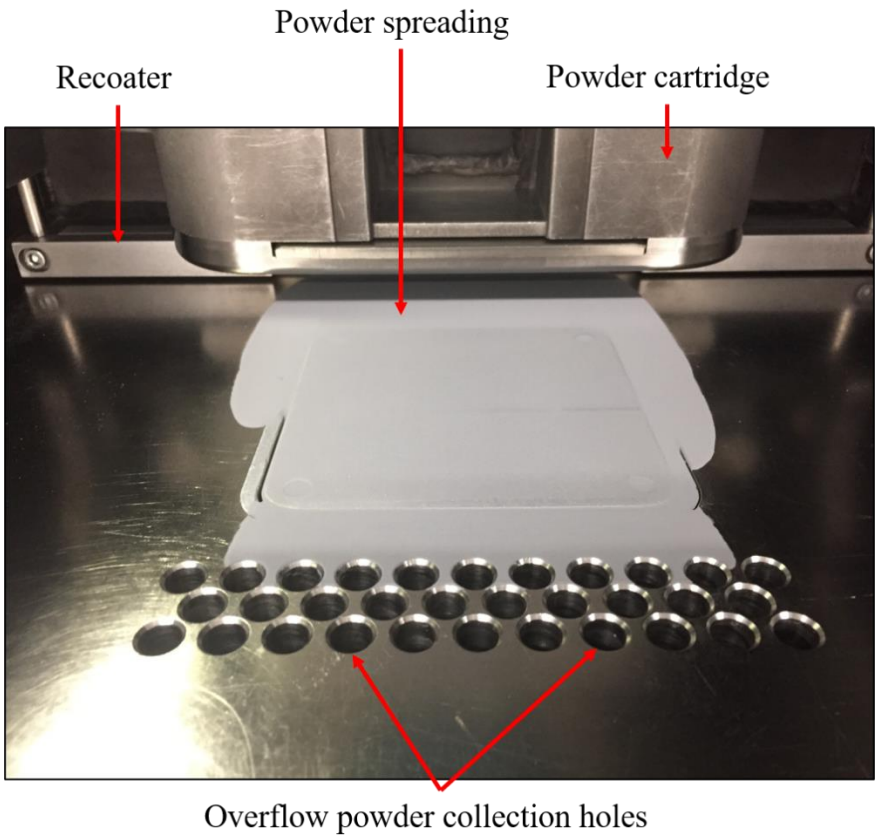

Figure 3.15: Renishaw AM 125 substrate set up showing spreading of the first layer of plasma densified WC-17 wt.% Co powder.

Table 3.10: Process parameters used to fabricate cubic samples from plasma densified WC-17 wt.% Co powder using Renishaw AM 125.

Process parameter	**Values/unit/ direction**
Laser power	100 – 160 W
Scanning speed	500 – 900 mm/s
Powder layer thickness	30 µm
Hatch distance	70 µm
Laser scanning strategy	Uni-directional
Substrate pre-heating temperature	175 °C
Oxygen level	< 900 ppm

3.1.3.2.6. Characterizations of cubic samples

The morphology of as-laser-scanned surfaces were investigated by Quanta600 (SEM). For microstructural analysis, a sample was cross sectioned using a SiC disc and the section was mounted in a conducting resin followed by the normal grinding/polishing procedure. Then, SEM/BSE mode and EDX investigations were undertaken. XRD investigation was also carried out using D8 advance with DaVinci.

4. Direct laser deposition of satellited WC_M-12 wt.% Co clads

4.1. Introduction

This chapter includes four main sections. The first section shows preliminary experiments which start with blended powder and later the satellited powder to compare the deposition behaviours. In the second section, a multilevel full factorial design of experiments is reported using the satellited powder. This examines the deposition properties of the clads from almost none to relatively higher deposition rates. The deposition efficiency, percentage of dissolved WC_M volume, porosity ratios, and microstructures of representative clads are presented. In the third section, potential processing maps are investigated by comparing two hypotheses: linear energy density versus powder feed rate, and effective energy density versus powder deposition density. This can provide valuable relationship between process parameters and the desired deposition characteristics. In the last section, the microstructure, microhardness, and wear resistance of multitrack coatings are reported.

4.2. Initial deposition experiments

To examine the deposition behaviours of simply blended Spherotene® (WC_M) and Co powders and satellited WC_M-12 wt.% Co mixtures, experiments were carried out with both these feedstocks. The results are presented in this section.

4.2.1. Results

4.2.1.1. Trial with blended powder

A single track deposited from blended powder is given in Figure 4.1. The laser power (P), scanning speed (V), and powder feed rate (PFR) are 300 W, 240 mm/min, and 4

g/min, respectively. It shows inconsistent deposition: portions of low and others of relatively higher deposition. The high deposition regions represent 22% of the total track length of 80 mm. It is probable that this inconsistent feeding is due to the small particles of Co, (1-3 µm), easily agglomerating together within the blended powder mass, resulting in unstable powder flow [119, 120].

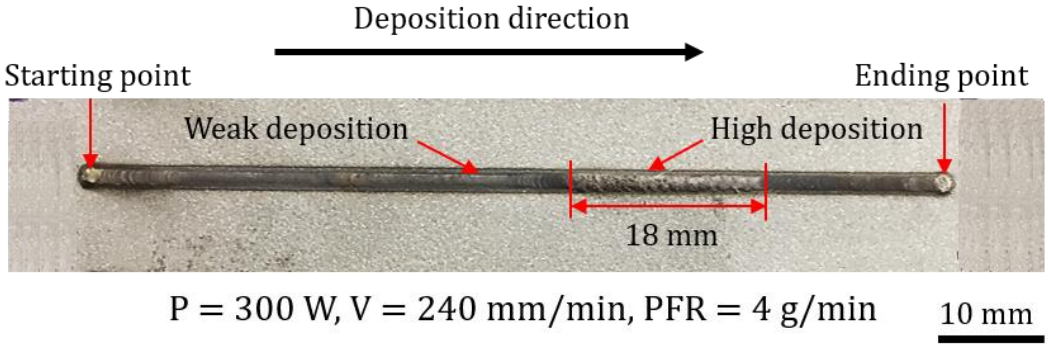

Figure 4.1: Macrophotograph of a non-uniform single track deposited at laser power, scanning speed, and powder feed rate of 300 W, 240 mm/min, and 4 g/min, respectively, using the blended WC_M-12 wt.% Co composite powder.

BSE investigations of two representative cross sections are shown in Figure 4.2. It demonstrates two behaviours: a relatively low cross-sectional area of clad where visually good bonding with the substrate, Figure 4.2a, and a high clad area with a reduced melting of the substrate and a large pore feature (Figure 4.2b). A clad region with only a few micropores is observed at a higher magnification (Figure 4.2c) and the dendritic structure appears non-faceted suggesting a solidification of an iron-rich melt with little dissolution of the WC_M. The high magnification image of Figure 4.2b reveals a lack of fusion with the substrate, relatively larger pores, continuous crack

through WC_M-matrix, and a carbide phase with a faceted dendritic structure derived from partial dissolution of WC_M particles.

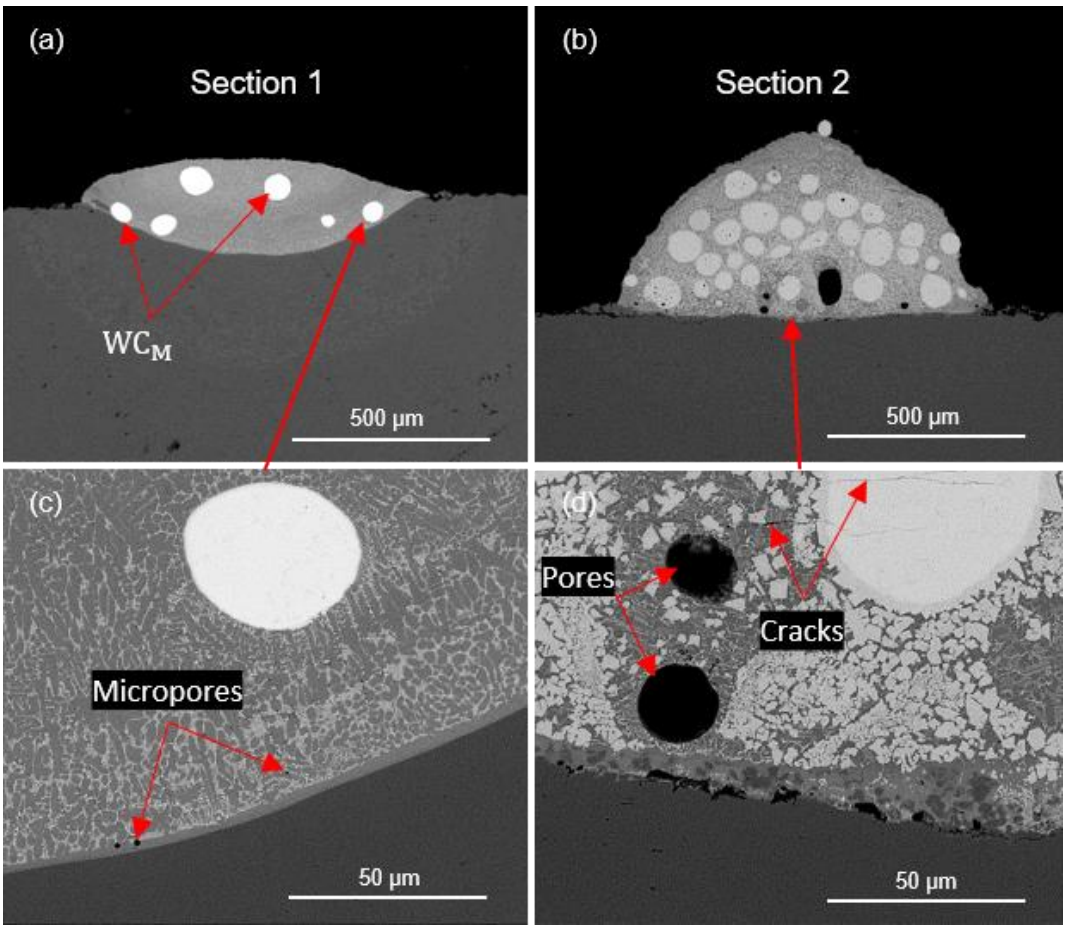

Figure 4.2: SEM/BSE images of two cross sections showing low deposition (a) and high deposition (b) with corresponding higher magnifications (c) and (d), respectively, of a single track laser cladding produced from blended WC_M-12 wt.% Co composite powder at laser power, scanning speed, and powder feed rate of 300 W, 240 mm/min, and 4 g/min, respectively.

The geometrical characteristics are given in Table 4.1. It shows that the mean clad area above the substrate surface is 8 times higher than that of the substrate melted area. However, relatively higher uncertainties are also observed due to the significant variability in the powder feeding. The deposition stability can be indicated from

dilution which represents the percentage ratio of substrate melted area to the total clad area. Its uncertainty limits give a wide range of variation. Despite this high fluctuation, it shows that this powder mixture has a little tendency for porosity formation as the porosity ratio of measured cross sections is < 2% at a maximum limit. The mean size of matrix pores is 27 ± 8 µm. It is possible that the entrapped gas in such a relatively large melt pool did not have sufficient time to escape before solidification [45].

It was found to be difficult to obtain uniform powder deposition with the blended powder and for this reason work was not undertaken with this feedstock material.

Table 4.1: Geometrical characteristics of blended WC_M-12 wt.% Co single track laser cladding produced at laser power, scanning speed, and powder feed rate of 300 W, 240 mm/min, and 4 g/min, respectively.

Mean clad area above substrate (mm^2)	Mean substrate melted area (mm^2)	Mean dilution %	Mean pore size (µm)	Mean porosity %
0.24 ± 0.08	0.03 ± 0.02	19 ± 16	27 ± 8	1.2 ± 0.6

4.2.1.2. Trial with satellited powder

The macrophotograph of a representative single laser clad track is presented in Figure 4.3. It shows a continuous and apparently uniform (no variations in track width) deposition when the values of P, V, and PFR were 300 W, 240 mm/min, and 4 g/min, respectively. In addition, the clad is consistent as there is no variation in track morphology can be observed between the starting and ending points along the

deposition path. This indicates the stability of powder feeding process for the process parameters employed.

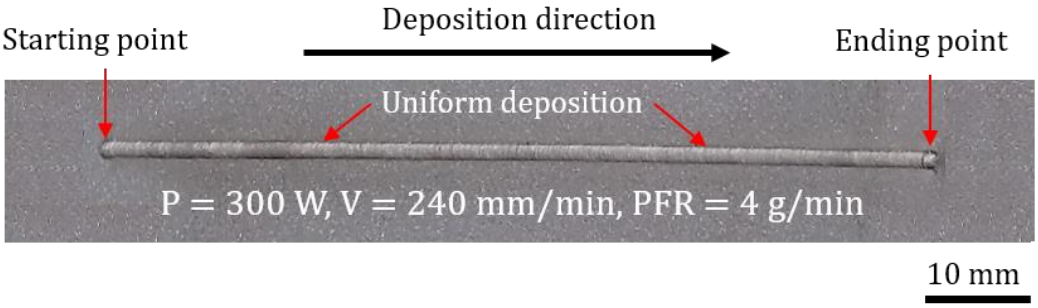

Figure 4.3: Macrophotograph of a uniform single track deposited at laser power, scanning speed, and powder feed rate of 300 W, 240 mm/min, and 4 g/min, respectively, using the satellited WC_M-12 wt.% Co composite powder.

BSE images of two representative cross sections from a single track are presented in Figure 4.4. The low magnifications images show comparable depositions with a uniform distribution of WC_M particles throughout clad areas (Figure 4.4a, b). The corresponding higher magnifications (Figure 4.4c, d) illustrate good bonding with the substrate and little evidence of porosity in the clad. Moreover, the faceted dendritic structures are also noticeable, probably the solidification of a faceted carbide phase.

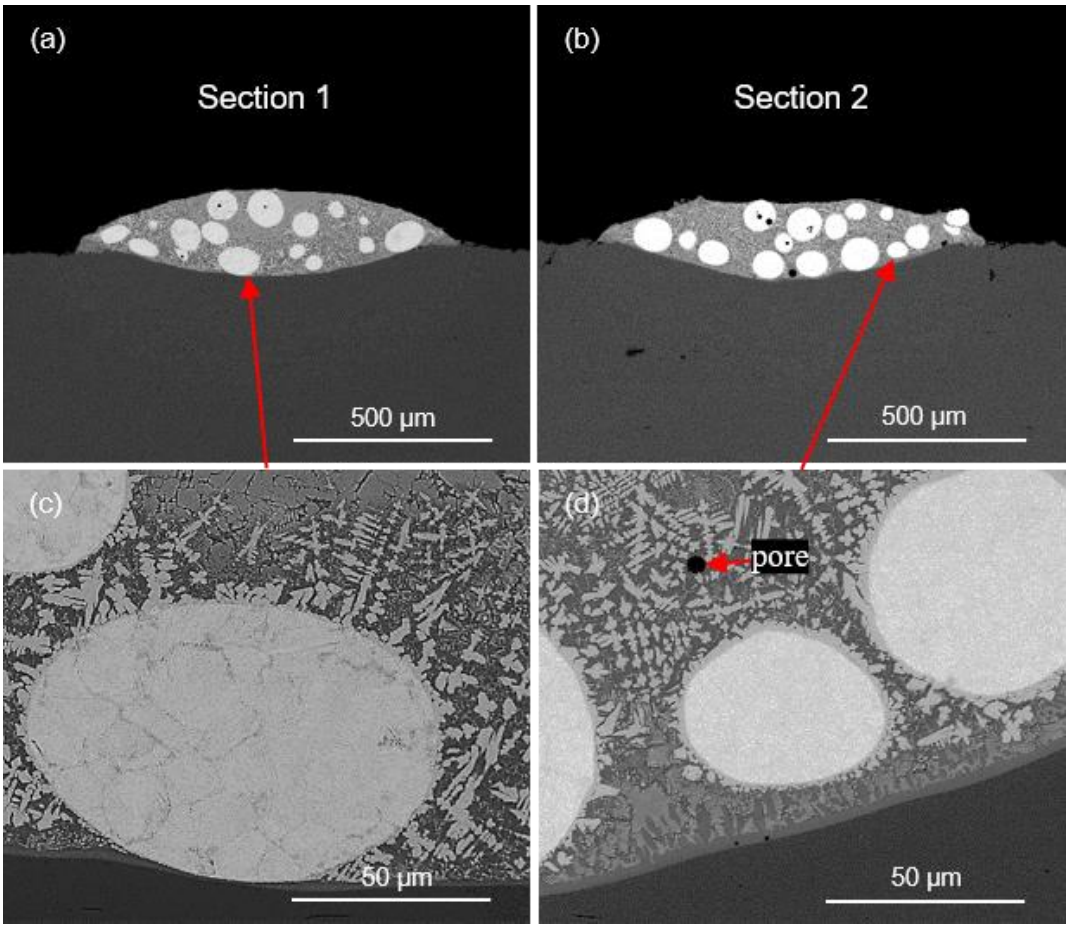

Figure 4.4: SEM/BSE images of two cross sections showing uniform depositions (a) and (b) with corresponding higher magnifications (c) and (d), respectively, of a single track laser cladding produced from satellited WC_M-12 wt.% Co composite powder at laser power, scanning speed, and powder feed rate of 300 W, 240 mm/min, and 4 g/min, respectively.

Measurements of macro and microstructural features are given in Table 4.2. The results from three cross sections reveal low uncertainties indicating a stable deposition. The mean pore size is 10 ± 4 µm. The pore volume percentage is much lower than that of blended clad giving a material density of 99.9%.

Table 4.2: Geometrical characteristics of satellited WC_M-12 wt.% Co single track laser cladding produced at laser power, scanning speed, and powder feed rate of 300 W, 240 mm/min, and 4 g/min, respectively.

Mean clad area above substrate (mm^2)	Mean substrate melted area (mm^2)	Mean dilution %	Mean pore size (µm)	Mean porosity %
0.1 ± 0.01	0.04 ± 0.003	31 ± 3.4	10 ± 4	0.1 ± 0.1

The satelliting process has effectively enhanced the powder flowability resulting in a consistent deposition. Thus, the satellited powder will be used in the next stage of experiments.

4.2.2. Discussion

4.2.2.1. Blended and satellited depositions

High quality clad can be defined as a low porosity, uniform and continuous, containing homogenous microstructure with strong metallurgical bonding with the substrate, and a low dilution [41]. The blending powder has led to inconsistent deposition containing lack of fusion with the substrate and relatively large pores. In comparison, a uniform deposition containing homogenous microstructure and low porosity with good visual bonding with the substrate was observed by using the satelliting powder.

Park et al. [121] reported that the powder containing smaller particles has higher viscosity due to higher inter-particle contact area. This results in higher inter-particle friction and then poor powder flowability [122]. Due to Van der Waals forces, smaller particles can also agglomerate easily together [119]. These reasons can lead to inconsistent powder flow which leads in turn to irregular deposition. Schematic

representations to the blended and satellited depositions are illustrated in Figure 4.5. It illustrates Co clusters in the blended feedstock giving flow in pulses form (Figure 4.5a). While satelliting can maintain a uniform Co distribution in the feedstock and then give a consistent flow leading to a uniform deposition (Figure 4.5b). This finding provides a simple powder preparation method for high quality clads. Considering the relatively small Co particles decorating WC_M, it can also indicate the impact of the feedstock design on the powder melting.

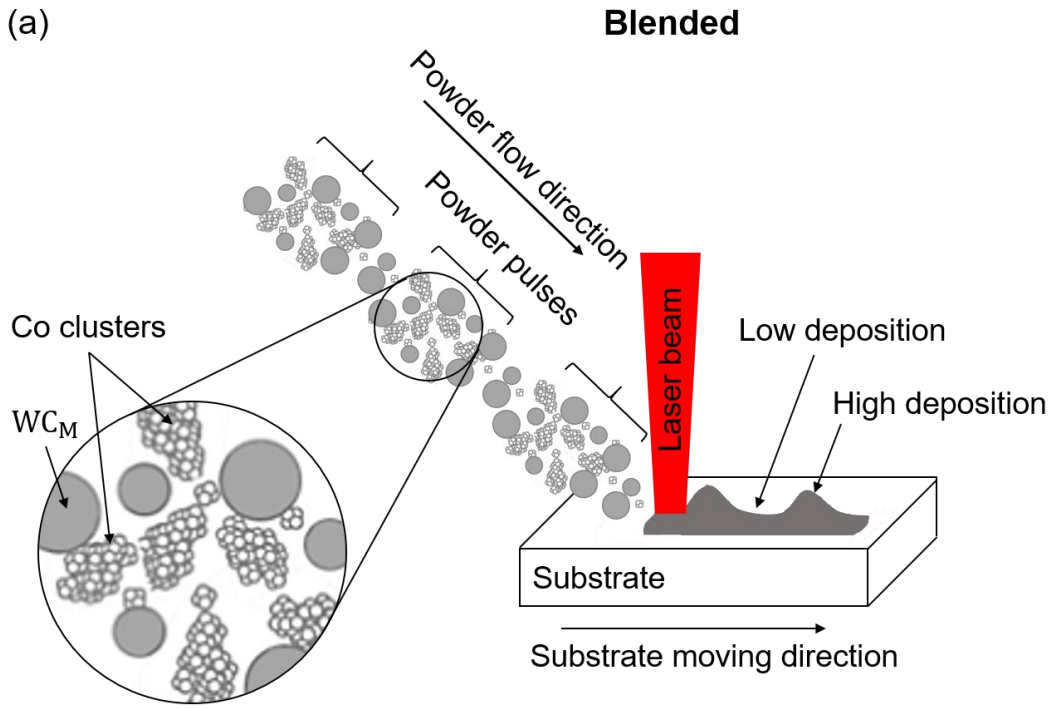

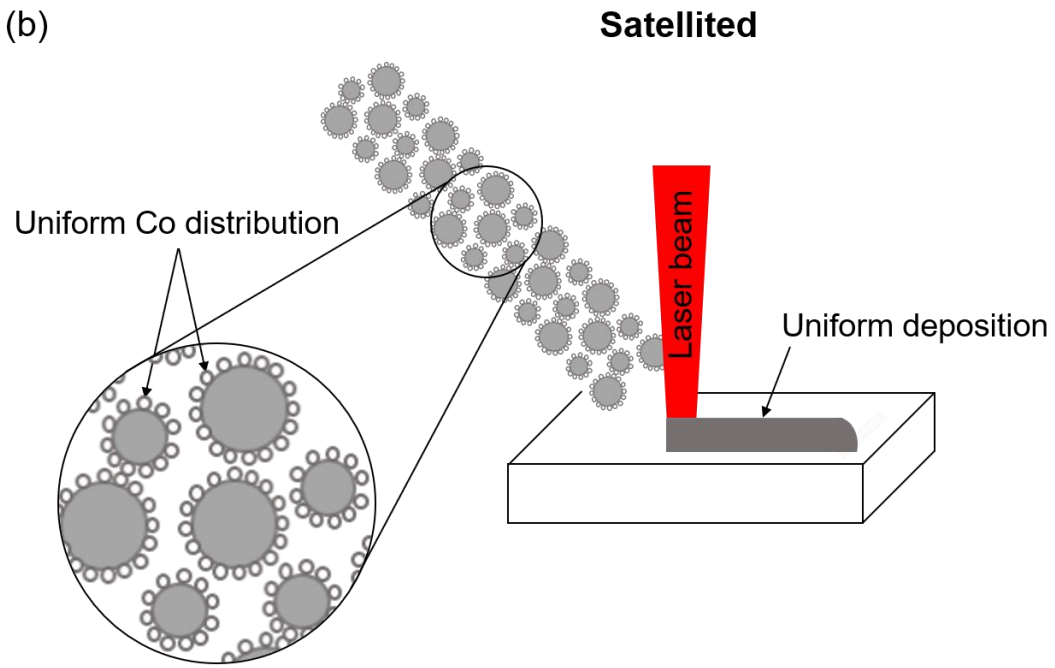

Figure 4.5: Schematic representations of two cladding mechanisms using blended (a) and satellited (b) WC_M-12 wt.% Co powders.

4.2.2.2. In-laser-flight powder temperature

The powder particles are heated when they pass through the laser before reaching to substrate. The amount of heat absorbed depends on energy density, thermo-physical properties of particle material, and particle velocity. The energy density is calculated from the ratio of laser power to laser spot area ($P/\pi r^2$). The particle velocity (v_p) can be estimated from the velocity of the carrier gas as given in Eq. 5.1 [123]. The potential effect of gravity on the particle velocity is neglected.

$$v_p = \frac{F_g}{4\pi\, r_o\, L_h} \qquad (5.1)$$

where F_g is the flow rate of the carrier gas (mm^3/s), r_o is the outlet radius of the powder nozzle (mm), and L_h is the horizontal distance from nozzle outlet to the laser beam centre (mm). The values of F_g, r_o, and L_h used in this study were 10 l/min (166667 mm^3/s), 1 mm, and 5.3 mm, respectively. The later was calculated according to the law

of triangles using the measured vertical distance of nozzle outlet from the substrate surface (L_v=10 mm) and nozzle inclined angle with the horizontal (62°) as explained schematically in Figure 4.6. This also shows a representation of particle-laser flighting distance.

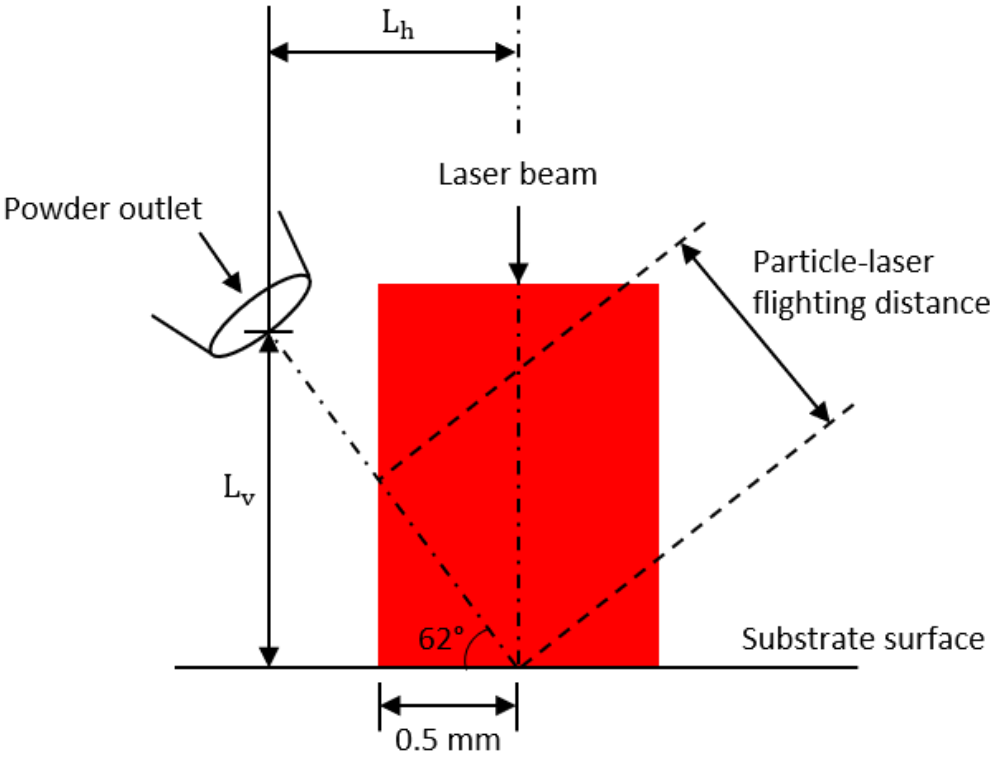

Figure 4.6: Schematic representation of the particle-laser flighting distance and powder nozzle set up.

The temperature of a powder particle (T_p) can be calculated using the following heat balance equation [46]:

$$q\,\alpha_p \pi\, r_p^2 \frac{\Delta l}{v_p} = \frac{4}{3}\pi\, r_p^3\, \rho_p\, c_p^p\, (T_p - T_o) \qquad (5.2)$$

This equation can be simplified as:

$$T_p = \frac{3}{4} \frac{q\,\alpha_p\,\Delta l}{r_p\,\rho_p\,v_p c_p^p} + T_o \quad (K) \qquad (5.3)$$

This model comes with the following assumptions:

- The attenuation of laser power density by powder flow is not considered.
- The reflection of laser from particles surfaces is neglected.
- The particle-laser flighting distance is taken as a constant.
- The effect of particle size distribution on particle velocity is not considered (median particle size is taken).
- The effect of particle velocity on convection heat capacity is not considered.

The definitions and values of the variables in Eq.5.3 are given in Table 4.3.

Table 4.3: Properties used to calculate the temperature rise of powder particles while interacting with the laser beam before reaching to the substrate.

Symbol	Definition	Values		Unit
		WC_M	**Co**	
q	Laser power density	64, 111, 159		W/mm^2
α_p	Laser absorption coefficient	0.82 [83]	0.58 [83]	---
Δl	Particle-laser flighting distance	1		mm
r_p	Particle radius	0.05	0.002	mm
ρ_p	Particle density	0.158 [83]	0.089 [83]	g/mm^3
v_p	Particle velocity	2500		mm/s
c_p^p	Specific heat capacity	0.05 [71]	0.42 [71]	J/g/K
T_o	Initial powder temperature	293		K

The estimated temperatures are presented in Figure 4.7. It shows that Co temperature is higher than that of WC_M. It has been showed that smaller particle size absorbs more energy while interacting with the laser beam [48]. The maximum Co temperature is about 660 K indicating that Co is not melted until reaching to melt pool. Considering the weak depositions and shallow melt pools at a laser powder of 200 W (Figure 4.9a), it can be suggested that the model used provides plausible estimations of temperatures. Increasing the incident energy density and/or decreasing the particle velocity can lead to particle melting [46]. However, the laser radiation can cause recoil pressure due to metal evaporation, especially at a low powder feed rate, which accelerates the particles [124]. Moreover, increasing the powder feed rate increases particles concentration in the powder stream and then energy attenuation [125]. High energy attenuation results in low powder catchment efficiency due to low heat irradiates the substrate [47, 49]. Consequently, the interaction between laser beam and powder alters the temperature of powder particles and the energy density reaching the melt pool and then deposition characteristics.

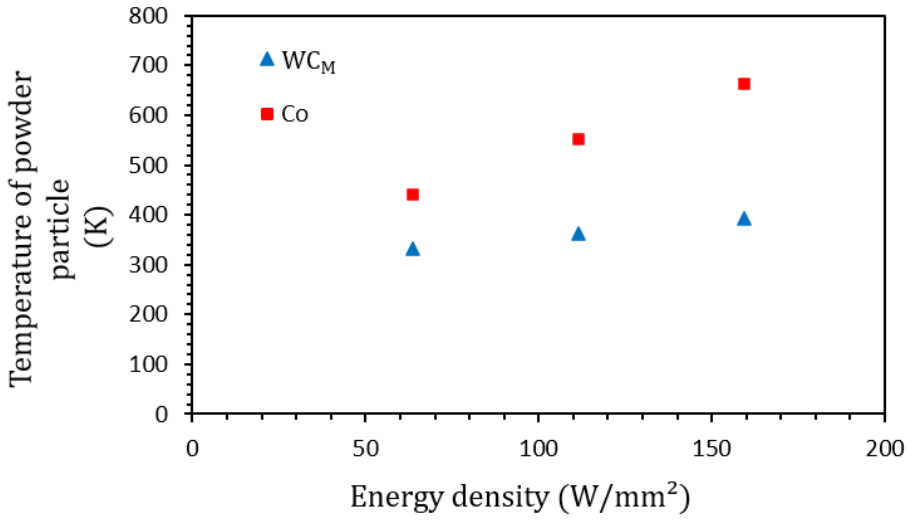

Figure 4.7: Temperature evolution as a function of energy density (laser power to laser spot area ($P/\pi r^2$)) of WC_M and Co particles before reaching to the substrate surface.

4.2.2.3. Evolution of melt pool

The evolution of melt pool geometry is a correlation between two main parameters; effective energy density (E), which represents the delivered energy by the laser beam as shown in Eq.5.4, and powder deposition density (PDD), which illustrates the amount of delivered powder to melt pool as defined in Eq.5.5 [62].

$$E = \frac{P}{VD_L} \qquad [J/mm^2] \qquad (5.4)$$

$$PDD = \frac{PFR}{VD_L}\frac{D_L^2}{D_p^2} \qquad [g/mm^2] \qquad (5.5)$$

where P is the laser power (W), V is the speed of the work plane (mm/s), D_L is the laser spot size (mm), PFR is the powder feed rate (g/min), D_L and D_p are the laser spot and powder nozzle diameters, respectively, where both are in (mm). According to the above equations, increasing V can reduce both the delivered energy and the amount of powder to the melt pool which resulted in a reduction of the deposited material. Increasing the delivered powder for a given energy density leads to a less excessive energy to melt the substrate. On the other hand, increasing the laser power while other parameters remain unchanged leads to enlarge the melt pool and then to increase the amount of melted powder [126]. Schematic representations to the deposition mechanism are illustrated in Figure 4.8. The laser head and powder nozzle are fixed during the cladding process while the CNC bed allows moving the substrate in x-y plane (Figure 4.8a). The powder impinging zone on the substrate covers the laser melting zone (Figure 4.8b). The ratio of melting area to powder delivering area is 22%. This represents a maximum ratio as powder can diverge after passing the nozzle neck [127]. Figure 4.8c shows that a part of the laser beam is shielded by powder particles. Another part is absorbed by the bouncing particles out of the melt pool. Also, a part is reflected from particles surfaces. From the total energy, only a fraction irradiates the

substrate. It heats a thin layer on the substrate to form the melt pool. Subsequently, powder is injected into laser melting zone. To start deposition, the delivered energy should be enough to melt the underlaying substrate and incoming powder [128]. The interaction of powder flux with liquid pool determines the deposition efficiency [129]. The fluid flow in the melt pool is explained in Figure 4.8d. Due to temperature difference between the centre and edge of the laser beam, a thermal gradient is formed in the melt pool resulting in surface tension gradient. This induces a thermocapillary-driven flow from low surface tension (hot) to high surface tension (cold) which has termed as Marangoni convection flow [54]. Meanwhile, the laser-powder delivery system propagates along laser scanning path according to a given scanning speed resulting in a new melt pool. Simultaneously, previous melt pool starts solidification through a steepest thermal gradient and the clad is formed [52]. A good metallurgical bonding between the clad and the substrate is essential for high quality coating [63].

(a)

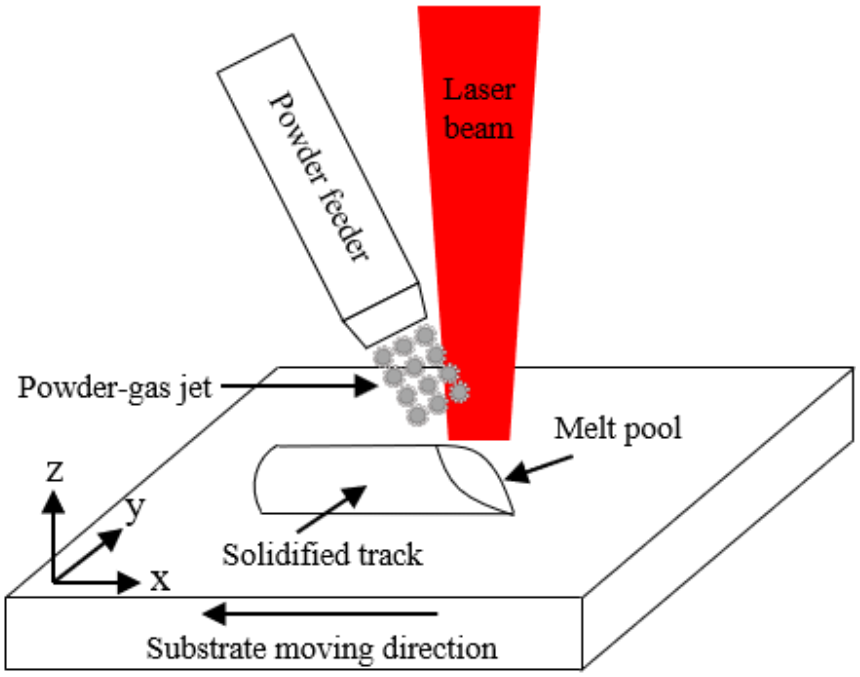
Laser beam
Powder feeder
Powder-gas jet
Melt pool
z
y
x
Solidified track
Substrate moving direction

(b)

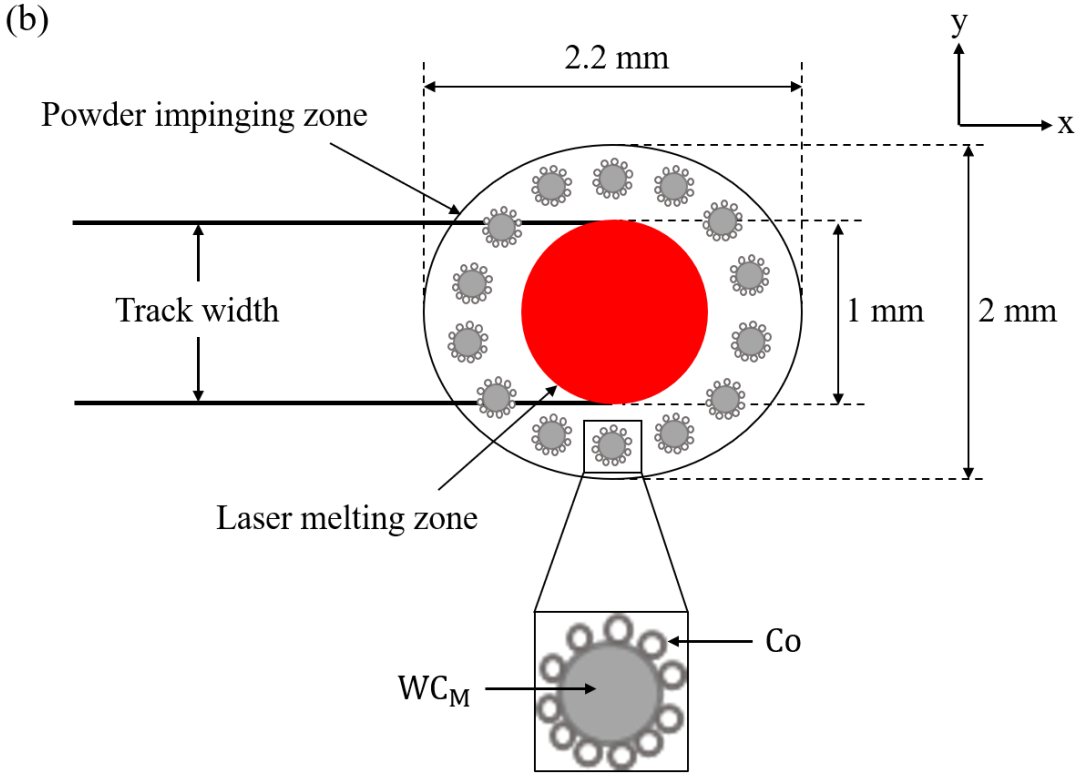
y
x
2.2 mm
Powder impinging zone
Track width
1 mm
2 mm
Laser melting zone
Co
WC$_M$

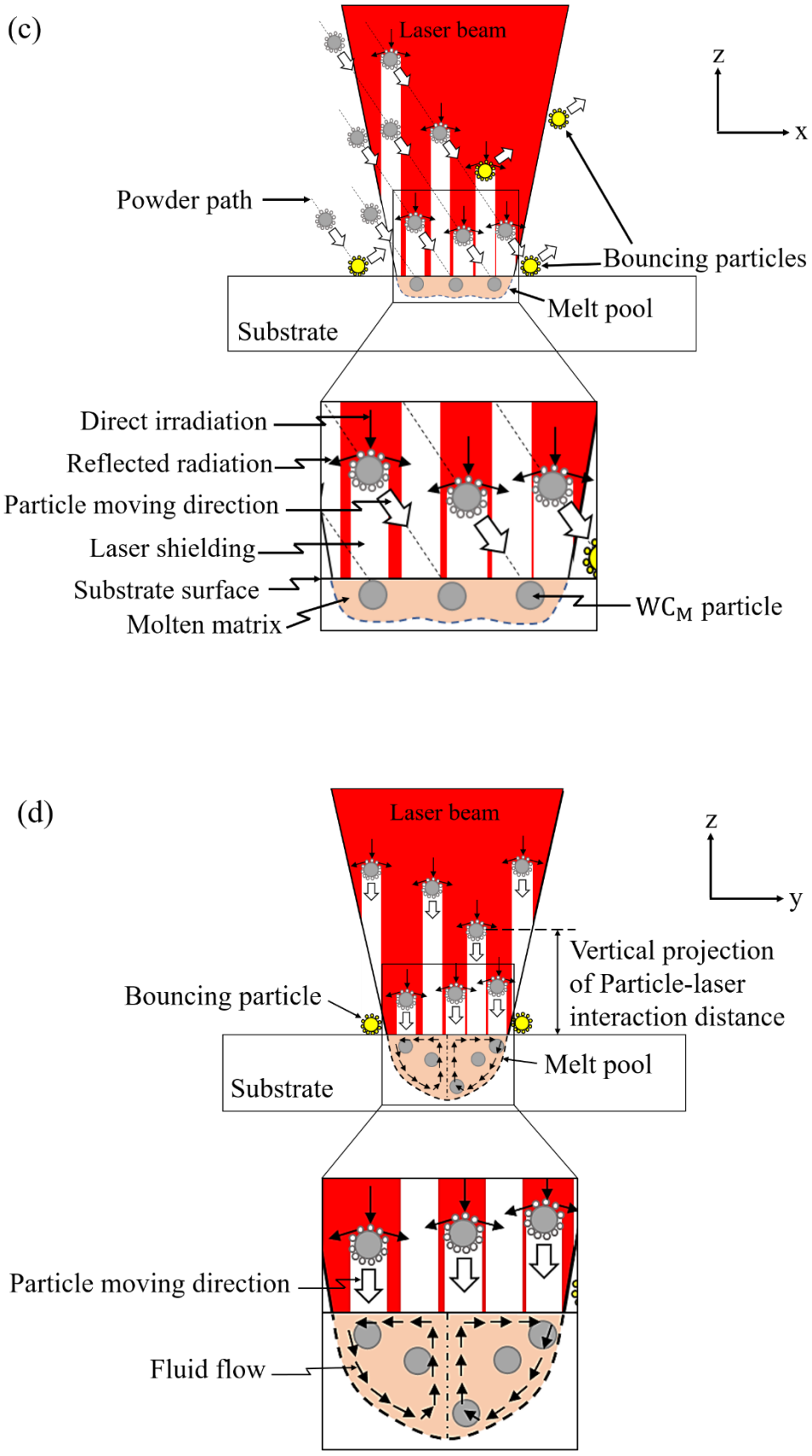

Figure 4.8: Schematic representation of DED-L deposition mechanism: (a) 3D overview, (b) x-y plane, (c) x-z plane, and (d) y-z plane.

4.3. Full factorial design experiments

To explore the deposition trends due to process parameters variations, a multilevel full factorial design of 27 experiments was undertaken. It investigated the cladding behaviour using ranges of P, V, and PFR of (200 – 500 W), (180 – 360 mm/min), and (4 – 10 g/min), respectively. The responses observed include cross-sectional observations, geometrical properties, deposition efficiency, dissolution ratio of WC_M, and microstructural characteristics. The overall measurements are given in Appendix A.

4.3.1. Results

4.3.1.1. Cross-sectional observations

Figure 4.9a shows three levels of V, and PFR for P=200 W, and Figure 4.9b and c are for P=350 W and 500 W, respectively. A very low deposition efficiency is observed for all the experiments performed at P of 200 W (Figure 4.9a). A sign of WC_M particle is observed at V and PFR of 180 mm/min and 4 g/min, respectively. No sign of WC_M particles can be seen by increasing V from 180 – 240 mm/min with a relatively lower PFR of 4 g/min. A further increasing of V to 360 mm/min results in almost no deposition. The energy density (P/V) is insufficient for substrate melting and hence bonding of powder to the substrate [23]. Increasing PFR to 6 g/min reveals a comparable behaviour. A relatively higher deposition rate is recognised at V and PFR of 180 mm/min and 10 g/min, respectively. Furthermore, the presence of WC_M particles (in light contrast) in the metal matrix (dark contrast) can easily be detected. By keeping the PFR at 10 g/min, a sign of pore which is comparable in size to the presented WC_M particles is noticed at V of 240 mm/min. This can be entrapped gas porosity or a WC_M particle pulled out during cutting/grinding preparations. Moreover, the deposition rate decreases significantly by a further increasing of V to 360 mm/min

due to decreasing both the energy density and the amount of delivered powder to melt pool.

In comparison, the substrate melt pool interfaces become clear when P increases to 350 W (Figure 4.9b). This gives relatively higher penetration depths into the substrate and visually good bonding characteristics. At 180 mm/min V, increasing PFR results in decreasing of the substrate melted depth and increasing of solidified clad above the substrate. However, comparable clads are observed at 240 mm/min with respect to the increasing of PFR. This can be due to insufficient energy density to accommodate the increasing amount of powder. The decreasing of clad area at V of 360 mm/min by increasing PFR confirms this trend. On the other hand, the melt pool size has decreased clearly by increasing V for all PFR values. The WC_M particles (in light colour) are uniformly dispersed in the melted areas. In addition, signs of entrapped gas pores can also be observed.

By moving to 500 W (Figure 4.9c), the melt pools shapes become wider and penetrated deeper into the substrate. The clad area is proportional to PFR as more powder involves with the laser beam, and inversely to V values as explained before. Some WC_M particles sink down into the bottom of the melt pool. In addition, signs of gas pores can be recognized.

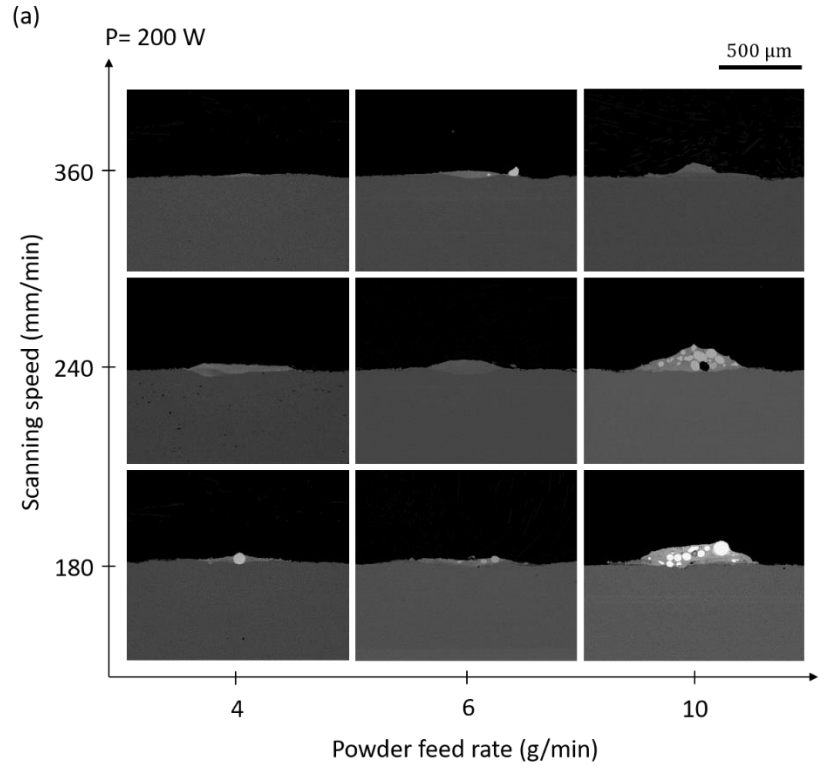
(a)
P= 200 W
500 µm
360
240
180
Scanning speed (mm/min)
4
6
10
Powder feed rate (g/min)

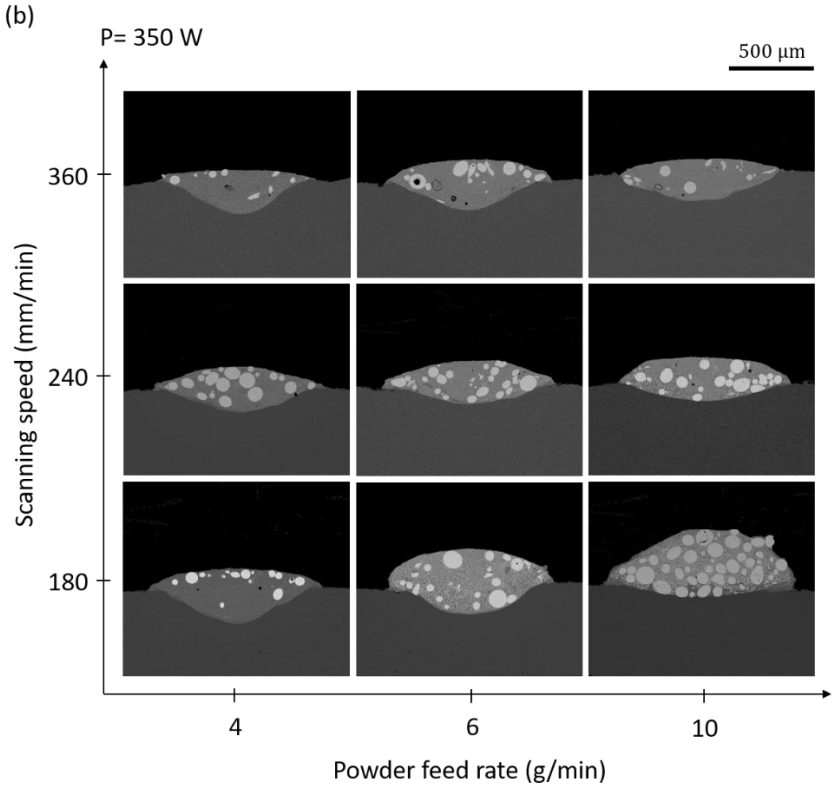
(b)
P= 350 W
500 µm
360
240
180
Scanning speed (mm/min)
4
6
10
Powder feed rate (g/min)

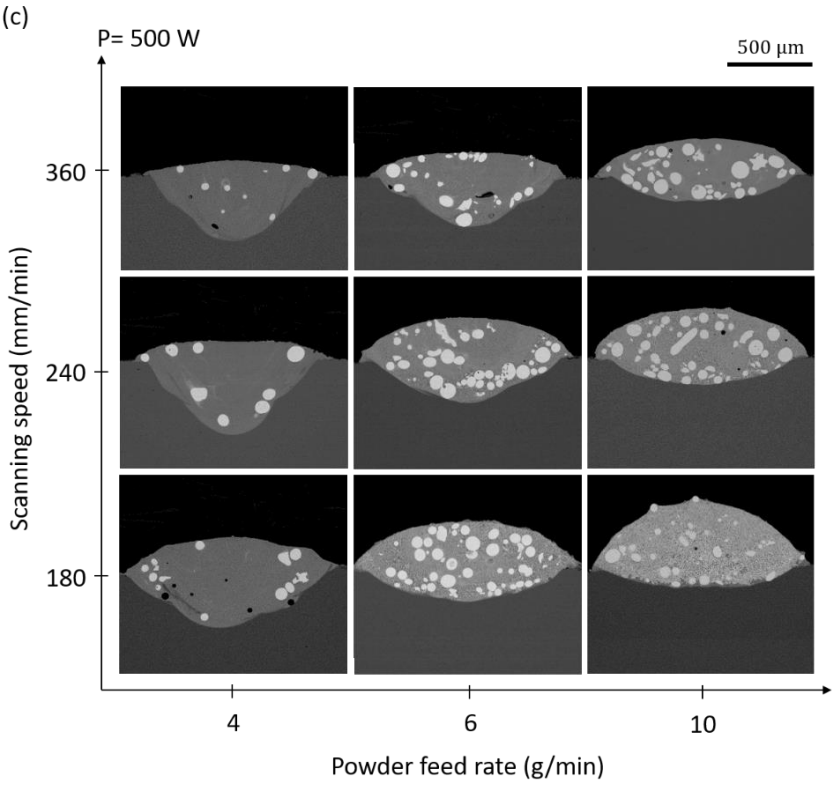

Figure 4.9: SEM/BSE images of single track cross-sections produced at scanning speed and powder feed rate ranges of (180 – 360 mm/min) and (4 – 10 g/min), respectively, where three values of laser power are employed; 200 W (a), 350 W (b), and 500 W (c).

4.3.1.2. Geometrical characteristics

This section discusses the evolution of clad area above the substrate free surface, the substrate melted area, and the resulted dilution ratio.

4.3.1.2.1. Clad area above the substrate free surface

Bar charts of clad area above the substrate (A_c) are presented in Figure 4.10. The smaller scale is used to represent the variations at the lowest laser power of 200 W (Figure 4.10a). It shows that A_c increases with PFR and decreases with V. It increases from 0.017 ± 0.01 mm² to 0.071 ± 0.0003 mm² when PFR increases from 4 – 10 g/min at 180 mm/min due to increased mass per unit length of powder delivered to the substrate. By increasing V from 180 – 360 mm/min, the clad area decreases gradually

for all PFRs due to decreasing the energy density and decreasing mass per unit length incident on the substrate.

Overall an increase can be observed by increasing P to 350 W (Figure 4.10b). It shows that at 180 mm/min, A_c increases from 0.108 ± 0.005 mm² to 0.318 ± 0.007 mm² when PFR increases from 4 g/min to 10 g/min. However, no similar trend can be observed at the other scanning speeds. At 240 mm/min, comparable results are obtained by increasing PFR from 6 g/min to 10 g/min, which can also be noticed at 360 mm/min. For a given laser power, the amount of delivered energy by the laser beam at a relatively higher V cannot accommodate all the delivered powder to the melt pool which results in a decreasing in deposition rate.

The trends become clearer by increasing P to 500 W (Figure 4.10c). It shows that A_c is proportional to PFR. A maximum deposited area of 0.406 ± 0.011 mm² is obtained at V and PFR of 180 mm/min and 10 g/min, respectively. On the other hand, a gradual decreasing in A_c is noticed with respect to the increase of V as explained before.

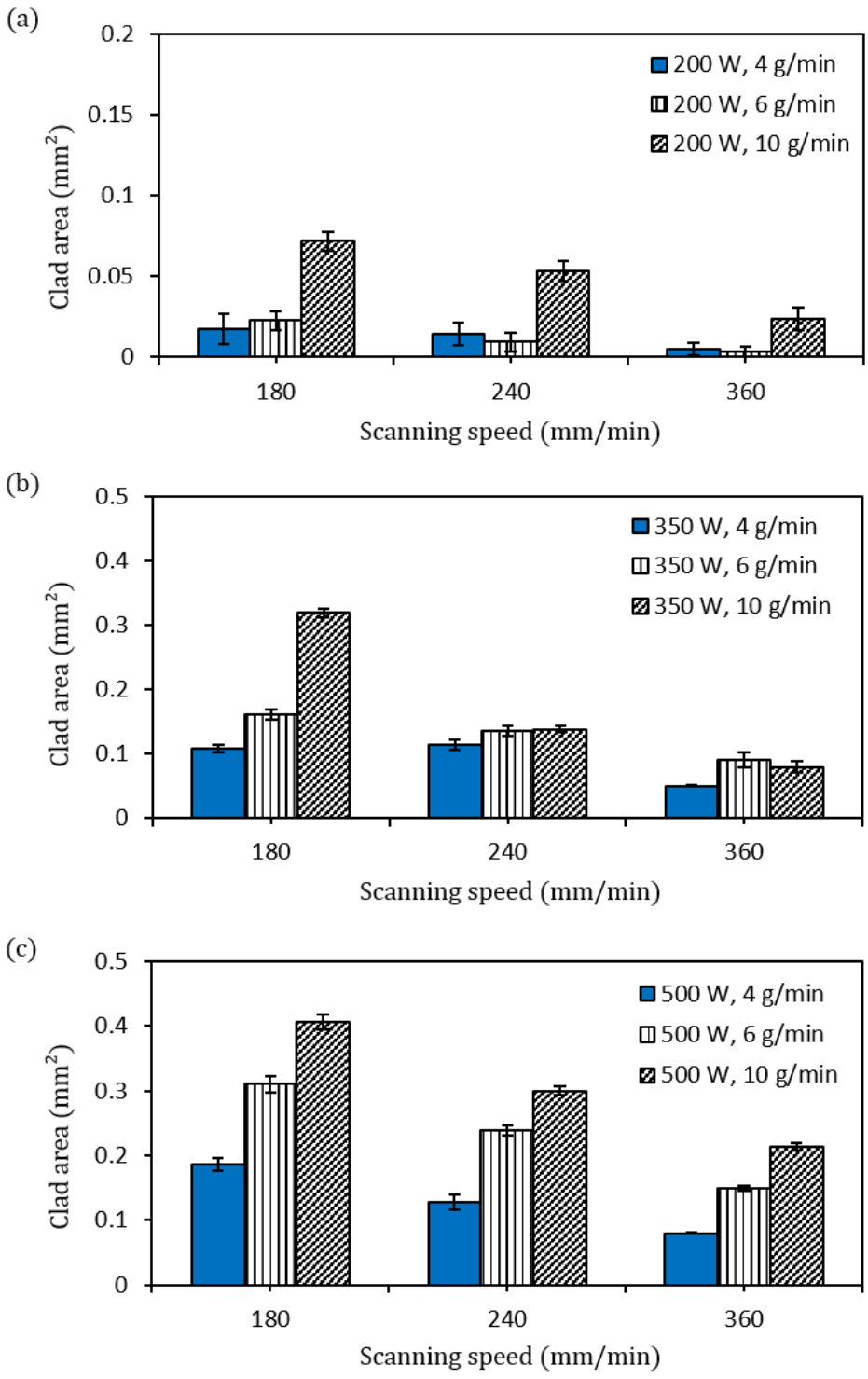

Figure 4.10: Clad areas above the substrate-free surface (A_c) at scanning speed and powder feed rate ranges of (180 – 360 mm/min) and (4 – 10 g/min), respectively, where three values of laser power are employed; 200 W (a), 350 W (b), and 500 W (c).

4.3.1.2.2. The substrate melted area

The measurements of substrate melted area (A_s) are shown in Figure 4.11. Smaller scale reading is used at a laser power of 200 W (Figure 4.11a). The resulted A_s can be correlated with the corresponding A_c as presented before in Figure 4.10a. It was noticed that when V is kept at 180 mm/min, increasing the PFR from 4 – 10 g/min produces an increase in A_c. While the corresponding A_s decreases from 0.007 ± 0.001 mm² to 0.001 ± 0.001 mm² as illustrated in Figure 4.11a. However, no trend can be observed by increasing V from 180 – 360 mm/min at PFR of 6 g/min and 10 g/min. Overall increasing in A_s is observed when P increases to 350 W (Figure 4.11b). At 4 g/min, A_s increases after initial decreasing when V increases from 180 – 360 mm/min. Similar trend can be observed at 6 g/min. While at 10 g/min, A_s increases gradually. The effect of increasing P to 500 W is presented in Figure 4.11c. The substrate melted area reaches to a maximum value of 0.27 ± 0.006 mm² at V and PFR of 240 mm/min and 4 g/min, respectively. For all Vs, increasing of PFR from 4 – 10 g/min decreases A_s significantly. However, no clear trend is observed with respect to the increasing of V.

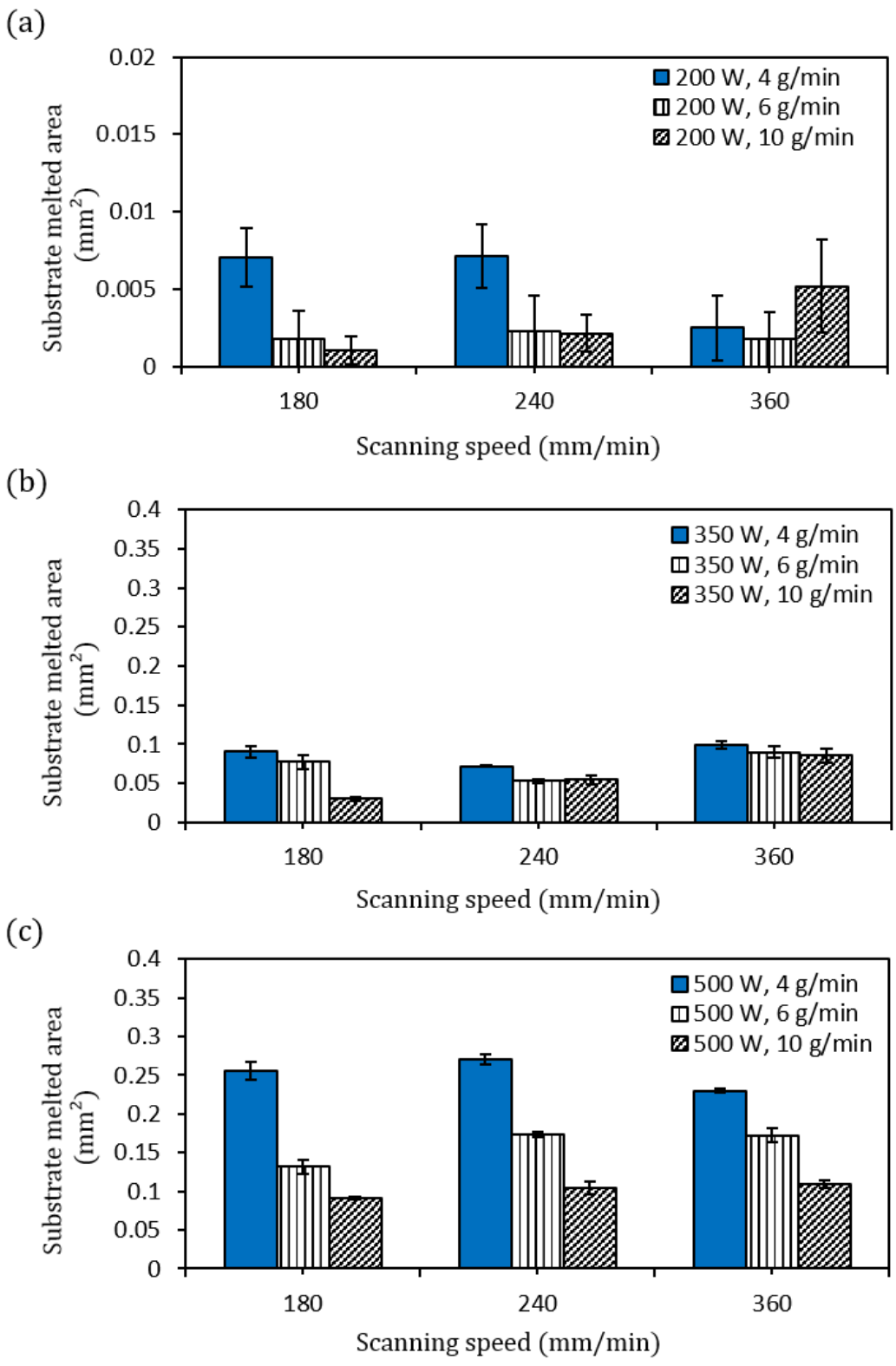

Figure 4.11: Substrate melted areas at scanning speed and powder feed rate ranges of (180 – 360 mm/min) and (4 – 10 g/min), respectively, where three values of laser power are employed; 200 W (a), 350 W (b), and 500 W (c).

4.3.1.2.3. The dilution ratio

The dilution ratio (D_r) is given in Figure 4.12. This parameter represents the ratio of the substrate melted area to the total melted area (substrate melted area + clad area above the substrate) which indicates the degree of mixing between the deposited material and the substrate material. It shows lower values at 200 W (Figure 4.12a). The D_r reaches to 33.1 ± 5.4% at V and PFR of 180 mm/min and 4 g/min, respectively. Increasing PFR to 10 g/min decreases D_r to 1.4 ± 1.1% which reflects a weak bonding with the substrate. However, no trend can be observed at other scanning speeds.

The effect of V can be noticed by increasing P to 350 W (Figure 4.12b). At 4 g/min, D_r increases from 45.3 ± 3.3% to 66.8 ± 0.6% by increasing V from 180 – 360 mm/min after initial decreasing. A similar behaviour is observed by keeping PFR at 6 g/min. While at 10 g/min, D_r increases gradually. Increasing PFR from 4 – 10 g/min at V of 180 mm/min decreases D_r due to more absorbed energy by the delivered powder. This is also seen at V of 240 mm/min and 360 mm/min when PFR increases initially from 4 – 6 g/min. However, a further increasing of PFR to 10 g/min results in comparable results to that obtained at 6 g/min. Increasing P to 500 W is given in Figure 4.12c. It shows that D_r is proportional to V and inversely proportional to PFR. A maximum D_r of 74.1 ± 0.6% is obtained at PFR and V of 4 g/min and 360 mm/min, respectively.

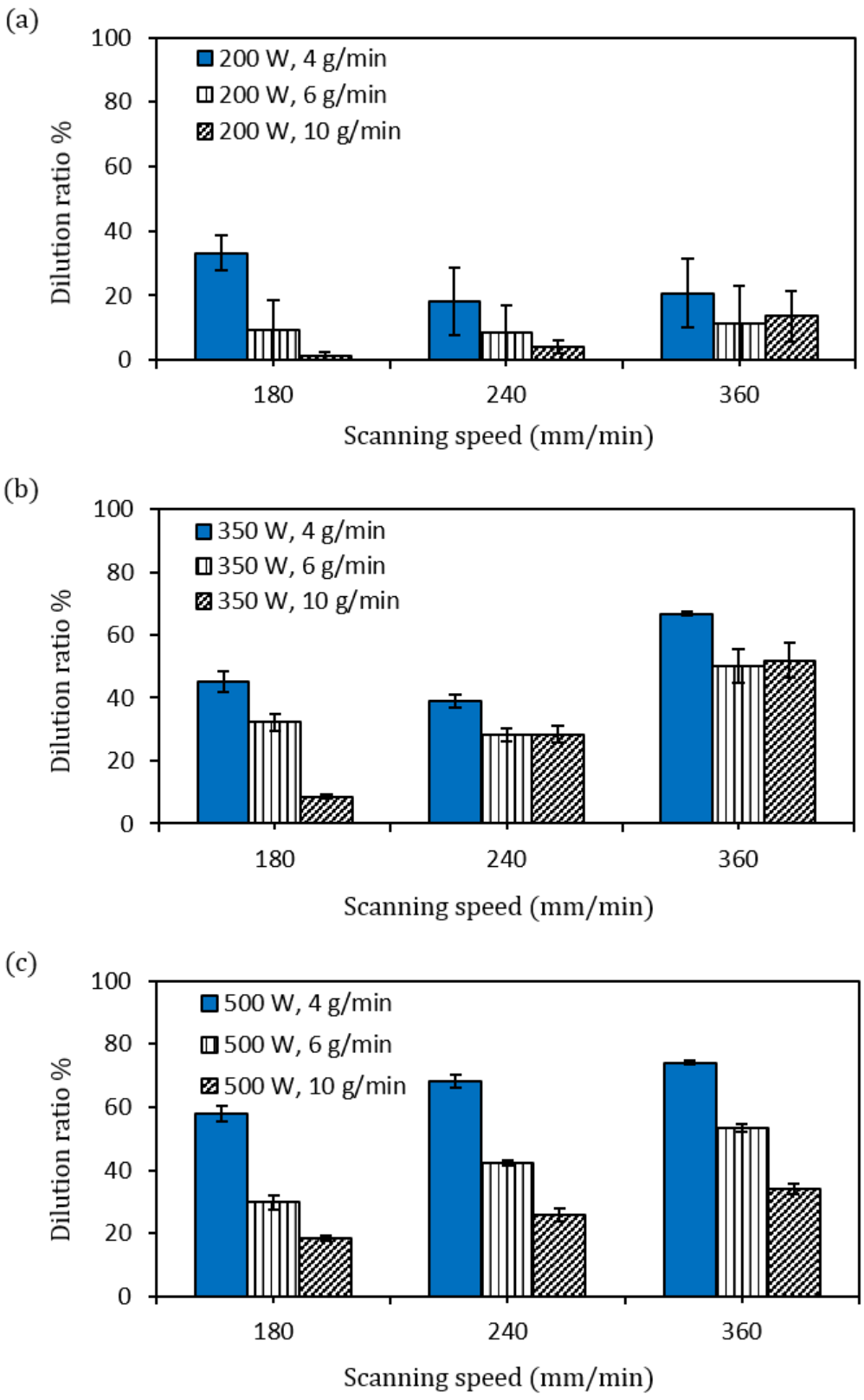

Figure 4.12: Dilution ratios at scanning speed and powder feed rate ranges of (180 – 360 mm/min) and (4 – 10 g/min), respectively, where three laser power are employed; 200 W (a), 350 W (b), and 500 W (c).

4.3.1.3. The porosity

The porosity volume measurements are shown in Figure 4.13. Despite a lower laser power, it reveals that the porosity is < 2.5% for all sets of process parameters performed at 200 W (Figure 4.13a). However, no trend can be observed with respect to the increase of V or PFR. The effect of increasing P to 350 W is presented in Figure 4.13b. It shows that the porosity is still < 0.8% for all values of V and PFR. By keeping V at 180 mm/min, increasing PFR from 4 – 10 g/min has led to decrease the porosity ratio. Similar trend can be observed by keeping PFR at 4 g/min and increasing V from 180 – 360 mm/min. However, at V of 360 mm/min, the increase of PFR from 4 – 10 g/min produces a slight increase in porosity from 0.04 ± 0.03% to 0.33 ± 0.06%. A similar trend can also be noticed at PFR of 10 g/min when V increases from 180 – 360 mm/min. Increasing P to 500 W is illustrated in Figure 4.13c. It shows that increasing P results in comparable results where the maximum porosity limit is < 2%. A slight increase in porosity to 0.7 ± 0.1 is observed at V and PFR of 180 mm/min and 4 g/min, respectively, as compared to same parameters at 350 W. Increasing the energy input can increase the substrate melted depth then the entrapped gas in melt pool.

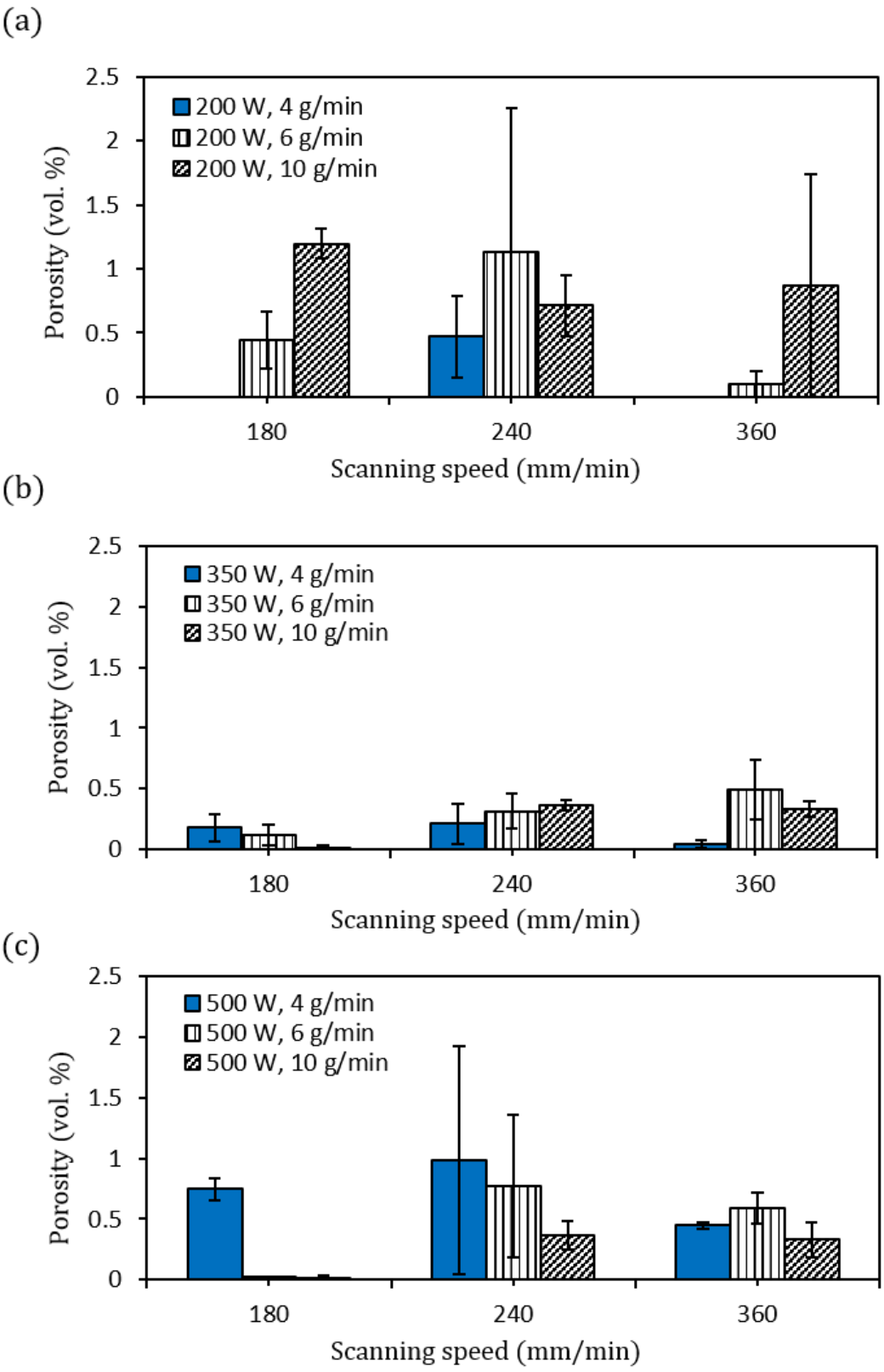

Figure 4.13: Porosity volume% at scanning speed and powder feed rate ranges of (180 – 360 mm/min) and (4 – 10 g/min), respectively, where three laser powers are investigated; 200 W (a), 350 W (b), and 500 W (c).

4.3.1.4. The deposition efficiency

The deposition efficiency (D_E) measurements are presented in Figure 4.14. At a relatively lower P of 200 W (Figure 4.14a), no clear trend can be observed. The D_E reaches to a maximum limit of 6.6 ± 0.4% at V and PFR of 180 mm/min and 4 g/min, respectively. Low applied P results in insufficient energy to melt the delivered powder. Increasing P to 350 W is given in Figure 4.14b. It shows that D_E reaches to 60.4 ± 0.7% at V and PFR of 180 mm/min and 4 g/min, respectively. Then it starts to decrease gradually to 37.1 ± 1.3% by increasing PFR to 10 g/min. This can also be observed at 240 mm/min and 360 mm/min. For all PFRs, increasing V from 180 – 360 mm/min decreases D_E. Increasing V reduces the energy density and then the ability to melt the delivered powder. However, comparable results are observed at PFR of 10 g/min by increasing V from 240 – 360 mm/min. Increasing P to 500 W enhances the overall values of D_E as illustrated in Figure 4.14c. It shows that D_E is inversely proportional to V and PFR. A maximum D_E of 71.2 ± 1.4% is observed at V and PFR of 180 mm/min and 4 g/min, respectively.

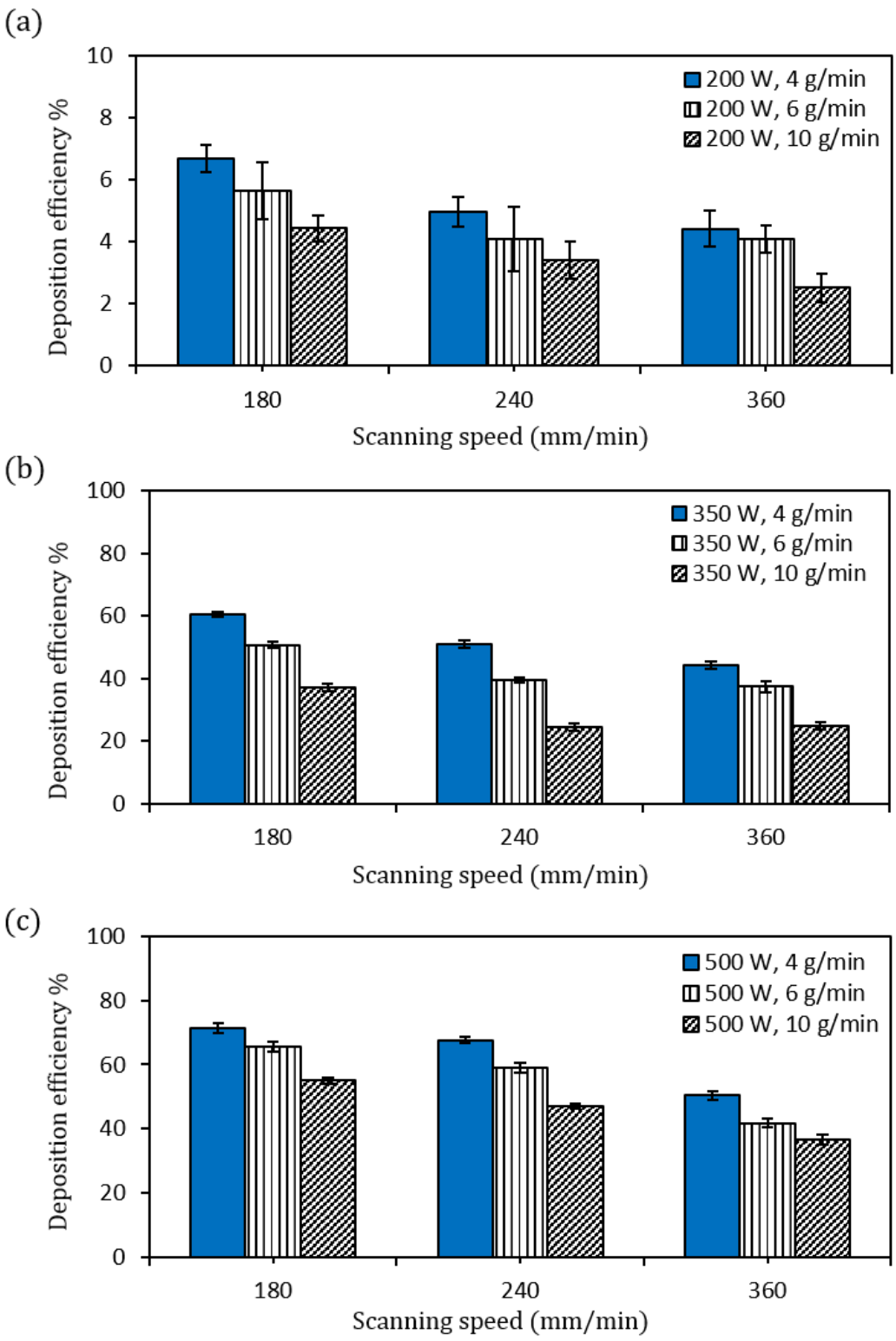

Figure 4.14: Deposition efficiency at scanning speed and powder feed rate ranges of (180 – 360 mm/min) and (4 – 10 g/min), respectively, where three laser powers are investigated; 200 W (a), 350 W (b), and 500 W (c).

4.3.1.5. WC_M dissolution ratio

The dissolution ratio (V_{dis}) of WC_M volume is shown in Figure 4.15. It represents the ratio of the dissolved WC_M volume fraction in the clad to the original WC_M volume fraction in the feedstock. The details are given in Appendix C. Small melt pools caused by P of 200 W (Figure 4.9a) resulted in no/weak capturing of WC_M particles. Thus, V_{dis} at P of 200 W has been excluded from the analysis.

V_{dis} at P of 350 is given in Figure 4.15a. It shows that V_{dis} reaches to 60.8 ± 10.3% at V and PFR of 180 mm/min and 4 g/min, respectively. Comparable results can be observed by keeping V at 180 mm/min and increasing PFR values. Similar behaviour is observed at 360 mm/min. By keeping PFR at 4 g/min, increasing V to 240 mm/min leads to decrease V_{dis} to 38.1 ± 4.5%. Further increasing of V to 360 mm/min causes an increasing of V_{dis} to 69.4 ± 2.7%. Increasing V can reduce both the energy density and delivered powder to melt pool. And at some point, the reduction in the amount of powder can be more than that of energy density. Thus, increasing in dissolving extent is expected due to increasing in the absorbed energy. However, no clear trend can be observed at the other values of V or PFR.

By increasing P to 500 W, V_{dis} values have increased as illustrated in Figure 4.15b. It shows by keeping PFR at 4 g/min, V_{dis} reaches to 77.5 ± 5% at V of 180 mm/min. V_{dis} increases to 87.8 ± 2.1% after initial decreasing by increasing V to 360 mm/min. Similar behaviour can be observed at PFR of 6 g/min by increasing V from 180 – 360 mm/min. At PFR of 10 g/min, increasing V causes a gradual decreasing in V_{dis} to reach 53.3 ± 0.8% at V of 360 mm/min. Similar behaviour can also be observed by keeping V at 360 mm/min when PFR increases from 4 – 10 g/min.

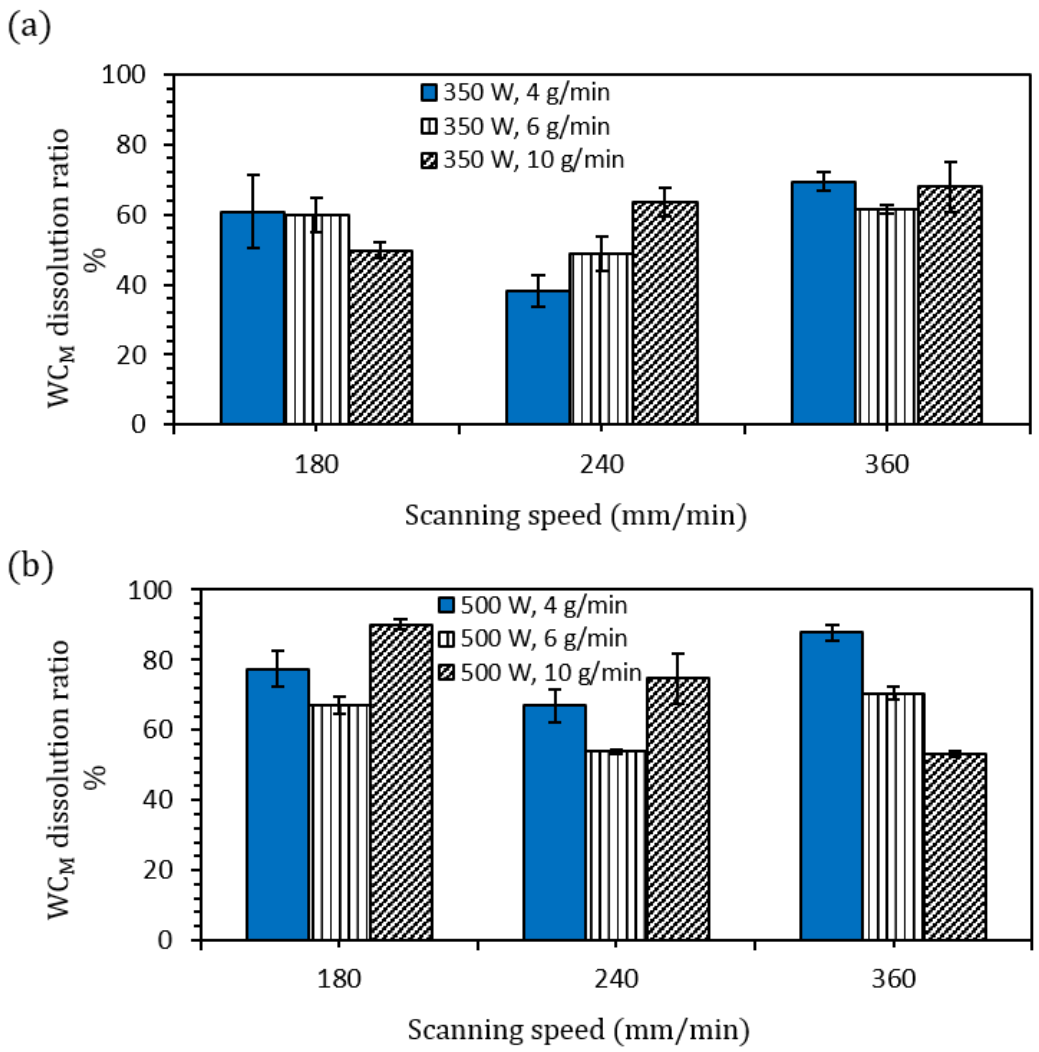

Figure 4.15: Dissolution ratios, V_{dis}, of WC_M at scanning speed and powder feed rate ranges of (180 – 360 mm/min) and (4 – 10 g/min), respectively, considering two laser power values; 350 W (a), and 500 W (b).

4.3.2. Discussion

4.3.2.1. Effect of scanning speed on melt pool

4.3.2.1.1. Substrate melted area

Increasing V can reduce both the delivered energy from the laser beam and the delivered powder from the nozzle feeder per unit length of the track [64]. This new correlation results in a new laser-powder-substrate interaction. It can lead to decrease the substrate melted area. In case when the substrate melted area has increased, it

indicates that the reduction in the amount of captured powder by the melt pool was higher than that of the delivered energy. Thus, more energy irradiates the substrate and then a relatively higher melted area is expected. These findings are consistent with the cladding behaviour of AISI 316L stainless steel powder on low alloyed steel where no clear trend was observed [63].

4.3.2.1.2. Dilution ratio

The increasing of dilution with the increase of V is consistent with other investigations [130, 131]. Pekkarinen et al. [130] urges that when excessive heat applied, the melt pool becomes larger which creates thicker and better shielding against the laser light. This assumption led to a conclusion that increasing the scanning speed makes the melt pool thinner and the laser is more able to melt the substrate then increasing the dilution. Liu et al. [131] explained that increasing the scanning speed decreases the laser-substrate interaction time. And at some point, the variation of interaction time will not affect the amount of melted substrate significantly as that of clad deposition above the substrate which leads to increase the dilution. However, both explanations above have not discussed the effect of scanning speed on the delivered powder to melt pool.

4.4. Microstructural characterisation

This section compares the microstructures produced at two scanning speeds; 180 mm/min (represents high energy density) and 360 mm/min (represents relatively low energy density) where the laser power and powder feed rate are kept constant at 500 W and 10 g/min, respectively.

4.4.1. Results

4.4.1.1. Microstructure at 180 mm/min

Figure 4.16 show the BSE/SEM images of a cross section. At a lower magnification (Figure 4.16a), a good bonding with the substrate, no visual pores, and a distribution of WC_M particles (in light colour) throughout the clad can be observed. Higher magnification image of region b shows that WC_M particles are surrounded by angular faceted particles (light contrast) embedded in a dark contrast matrix as given in Figure 4.16b. In addition, it can be seen that faceted plate and needle shapes are formed at the boundary of WC_M particles as shown in Figure 4.16c. This results in apparently five different level of contrast in the deposited material as illustrated in Figure 4.16d; the original WC_M material (1), faceted feature (2), lighter contrast region (3), at the core of the grey contrast region (4), and a dark region (5).

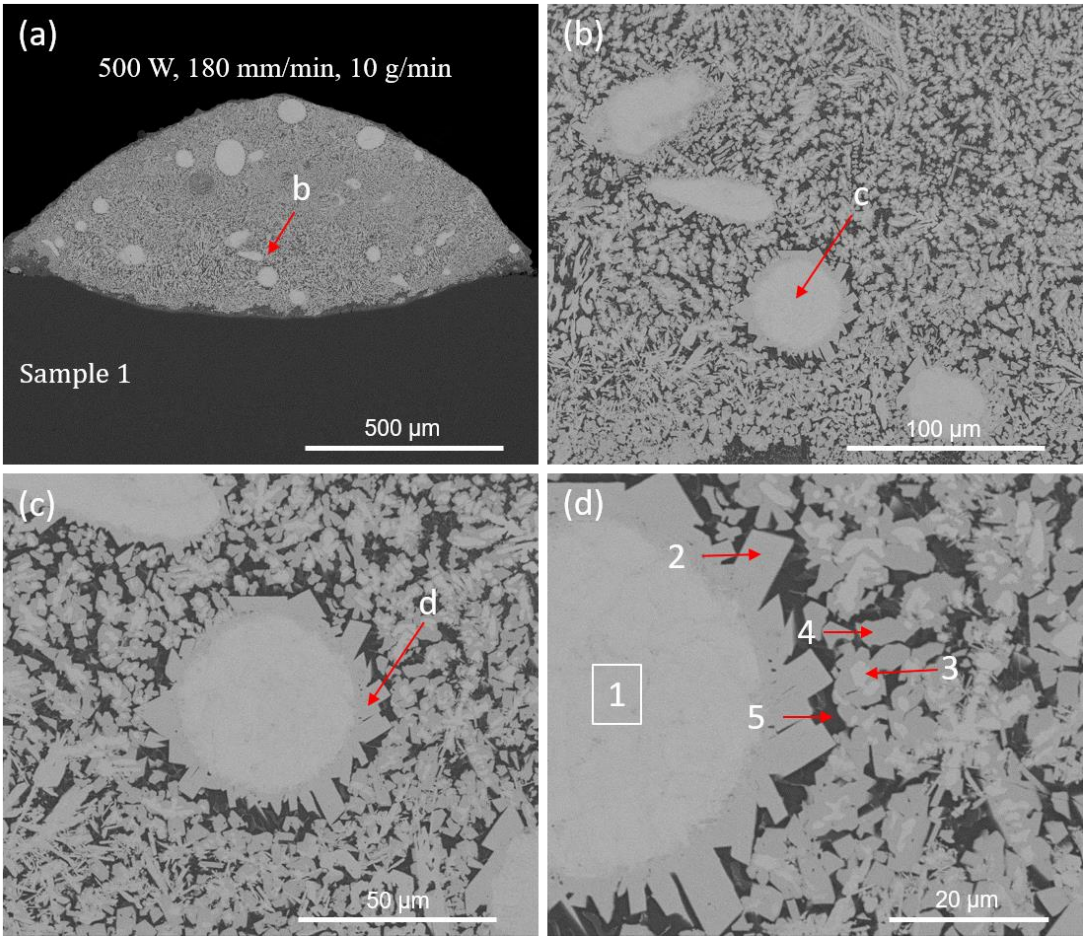

Figure 4.16: SEM/BSE investigation of a cross section produced at laser power, scanning speed, and powder feed rate of 500 W, 180 mm/min, and 10 g/min, respectively (a), with corresponding higher magnifications (b), (c), and (d) of three different positions b, c, and d, respectively.

EDX mapping is presented in Figure 4.17 for elements of atomic number greater than 6 (i.e. mapping of C is excluded). To explore the effect of the mild steel substrate on the microstructure, Fe element is also analysed. As expected, it shows that the original multiphase WC_M particle contains W and no detectable Co or Fe (feature 1). The microstructural feature 2 is also seen to be W-rich with no detectable Co or Fe. The dark contrast feature 5 contains Co and Fe, and no sign of W appears. The microstructural features 3 and 4 appear to be also W-rich but with possibly traces of Co and Fe.

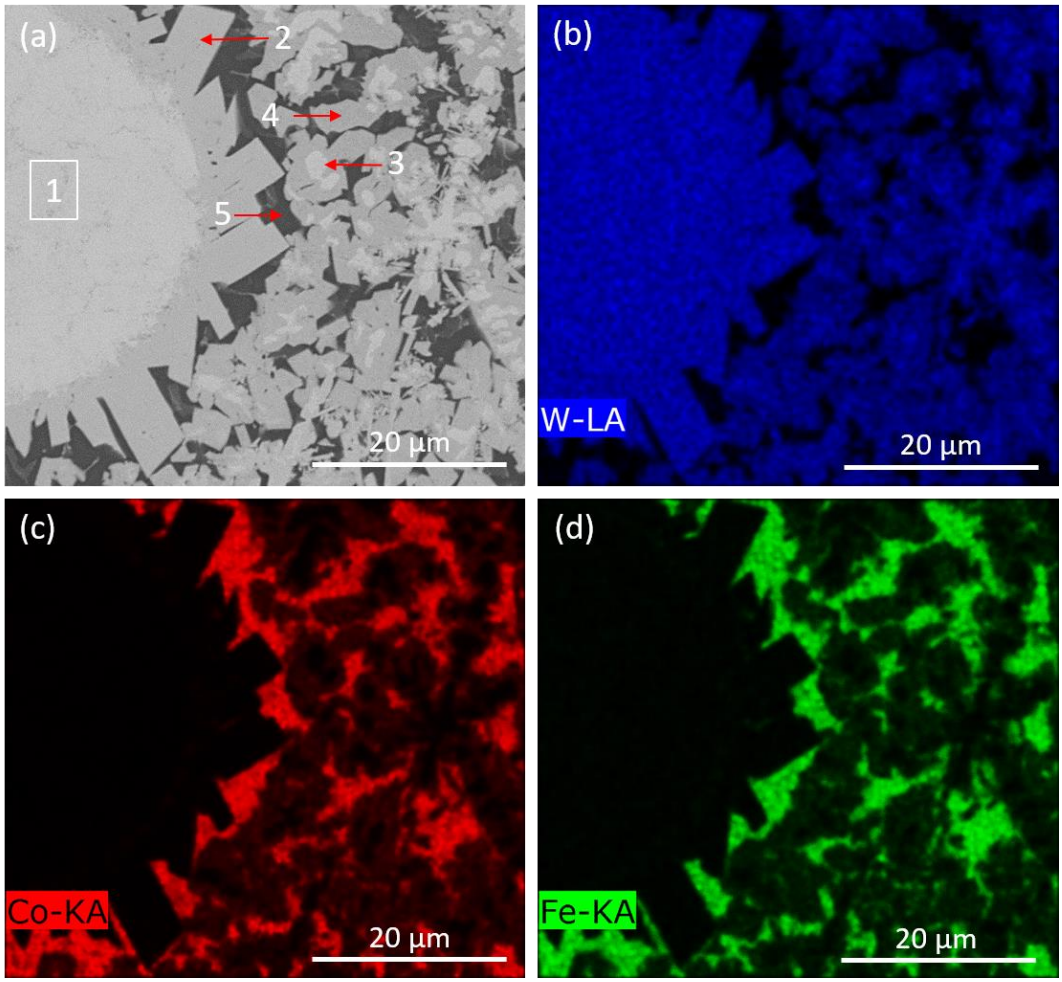

Figure 4.17: SEM/EDX mapping of a cross section produced at laser power, scanning speed, and powder feed rate of 500 W, 180 mm/min, and 10 g/min, respectively, showing BSE image (a), and the distributions of W (b), Co (c), and Fe (d).

The compositions of the features 1 – 5 determined by EDX spot analysis are given in Table 4.4 where in this case C has been included in the analysis. Light elements generate weak X-ray signals to be detected, thus, C can be difficult to measure reliably. In addition, EDX cannot resolve the composition of features less than 2 – 3 µm, so the compositions of features 3 and 4 are unreliable. It shows that the W content is highest in feature 1 and decreases gradually by moving to feature 5. A comparable C content is observed in features 1 – 3, while it decreases slightly in feature 5. No sign of Co or Fe appears in features 1 and 2. This gives that the faceted shapes are formed from W

and C elements. By moving from feature 3 to feature 5, the Co and Fe contents reveal an opposite trend to W.

Table 4.4: The chemical contents of W, C, Co, and Fe in features 1 – 5 presented in Figure 4.17a.

Element	Feature and content (wt.%)				
	1	2	3	4	5
W	94.5 ± 0.2	93.2 ± 0.3	90.9 ± 0.5	69.9 ± 0.8	10.2 ± 0.5
C	5.1 ± 0.1	5.4 ± 0.2	5.1 ± 0.2	3.8 ± 0.1	3 ± 0.2
Co	0	0	2.1 ± 0.2	18 ± 0.7	55.4 ± 0.2
Fe	0	0	1.7 ± 0.2	8.1 ± 0.1	31.2 ± 0.5

4.4.1.2. Microstructure at 360 mm/min

The BSE observations of a laser clad cross section produced at P, V, and PFR of 500 W, 360 mm/min, and 10 g/min, respectively, are presented in Figure 4.18. A low magnification (Figure 4.18a) shows a dense clad, good visual bonding with the substrate, and uniform distribution of WC_M particles (in light contrast). The higher magnification of zone b reveals dendritic structure around the edges of WC_M particles and signs of small circular pores as shown in Figure 4.18b.

More details appear in Figure 4.18c. It shows that the WC_M material consists of more than one level of BSE contrast which corresponds with the original observations before laser processing. Four main features can be observed: original WC_M in light contrast at low magnification (1), dendritic morphology (2), cellular clusters (3), and dark contrast intercellular region (4). The higher magnification for the position d, as shown in Figure 4.18d, shows a uniform distribution of cellular clusters in the clad matrix.

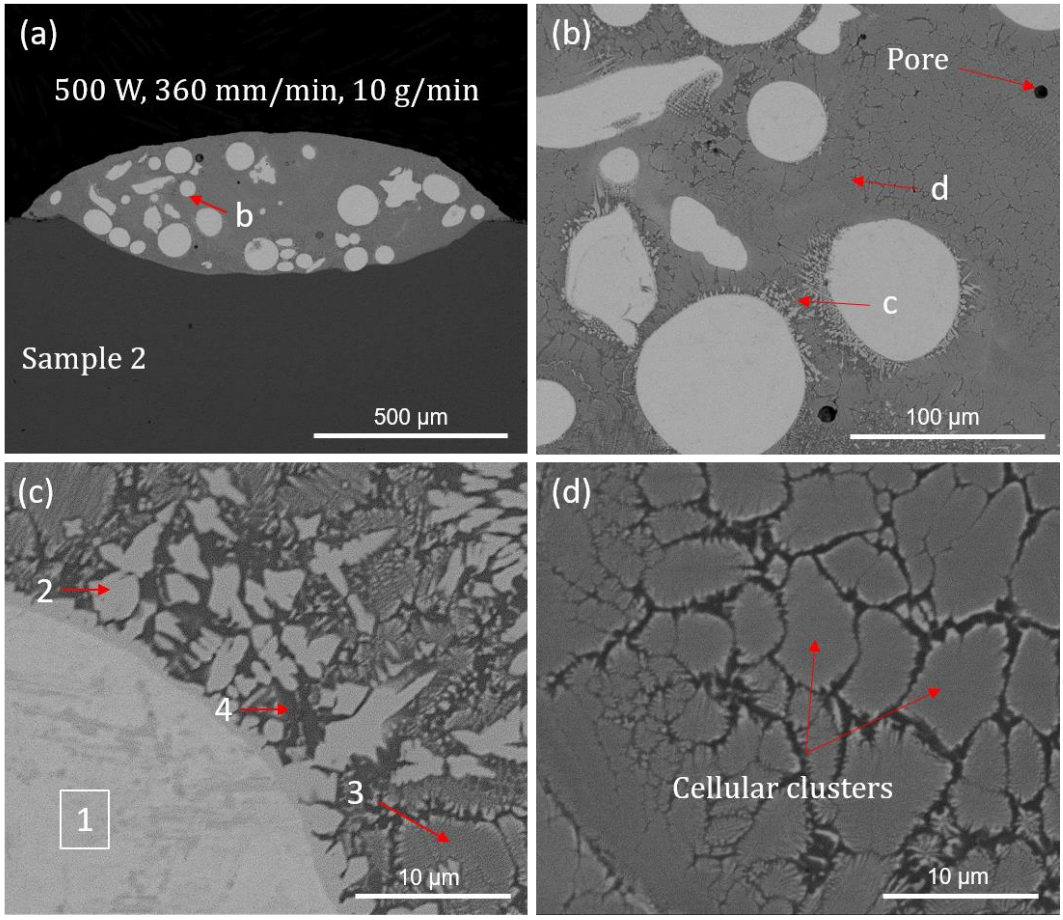

Figure 4.18: SEM/BSE investigation of a cross section produced at laser power, scanning speed, and powder feed rate of 500 W, 360 mm/min, and 10 g/min, respectively (a), with corresponding higher magnifications (b), (c), and (d) of three different positions b, c, and d, respectively.

EDX mapping is presented in Figure 4.19. It shows that W is the main element in the WC_M (feature 1) and no detectable Co or Fe as given in Figure 4.19a-d. The dendritic structure (feature 2) contains W and possibly small amounts of Co and Fe. EDX mapping of cellular region (feature 3) is given in Figure 4.19e-h and shows the presence of W, Co, and Fe. The dark contrast intercellular region (feature 4) reveals lower W and higher contents of Co and Fe.

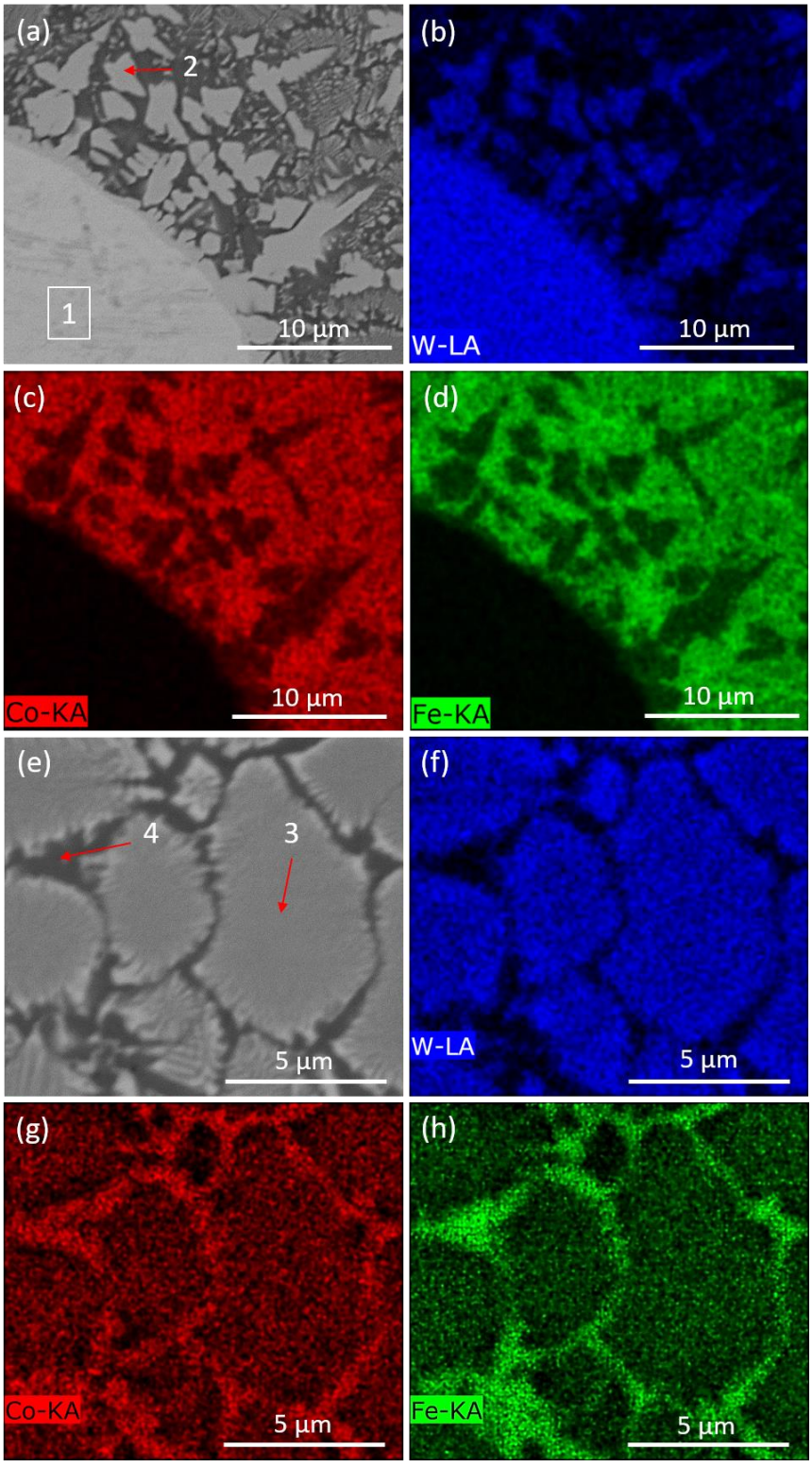

Figure 4.19: SEM/BSE image of dendritic structure (a), and corresponding EDX mapping for W (b), Co (c), and Fe (d), and BSE image of cellular clusters (e) and corresponding EDX mapping for W (f), Co (g), and Fe (h) of a cross section produced at laser power, scanning speed, and powder feed rate of 500 W, 360 mm/min, and 10 g/min, respectively.

C, as a light element, is difficult to be detected in EDX due to a weak X-ray signal. Also, small intercellular features (4) can make the EDX value is affected by beam spreading onto neighbouring regions so it may not represent a true value. The compositions of the features 1 – 4 are given in Table 4.5. It shows that feature 1 has a highest W. The W decreases gradually by moving from dendritic (2) to dark region (4). The C decreases slightly by moving from feature 1 to feature 4. Except for feature 1, Fe is higher in all other features as compared to Co.

Table 4.5: The chemical contents of W, C, Co, and Fe in features 1 – 4 presented in Figure 4.19a, e.

Element	Feature and content (wt.%)			
	1	2	3	4
W	95	71.2 ± 0.1	39 ± 0.2	17 ± 0.9
C	4.8	3.8 ± 0.1	3.2	2.7
Co	0	11.8 ± 0.1	26.7	35.5 ± 0.2
Fe	0	13.1 ± 0.1	30.9 ± 0.2	44.5 ± 1.1

XRD spectra for the above two clads (Sample1 and Sample2) in addition to original feedstock constituents and the substrate are given in Figure 4.20. As explained before, the Co powder is composed of hcp and fcc phases (Figure 4.20a). The WC_M powder consists of three phases; W_2C (hcp), WC (hcp), and WC_{1-x} (fcc) (Figure 4.20b). And the substrate consists of Fe (bcc) (Figure 4.20c).

In Sample 1 (Figure 4.20d), the main phases identified are W_2C (hcp), WC (hcp), and Co_3W_3C. Also, two solid solutions; γ (bcc) and γ (fcc) are seen which are comparable to Fe (bcc) and Co (fcc), respectively. These γ phases are formed due to interaction

between Fe and Co. The ternary carbide Co_3W_3C can relate to dendritic feature (4) in Figure 4.17a.

In Sample 2 (Figure 4.20e), the main phases identified are W_2C (hcp), WC (hcp), WC_{1-x}, and Co_3W_3C. The solid solutions, γ (bcc) and γ (fcc), can also be observed. The intensities of WC peaks appear higher in Sample 1 than Sample 2. The correlations between XRD phases and microstructural features are given in Table 4.6. The ICDD files and XRD patterns are given in Appendix D – sections D.1 and D.2, respectively.

Table 4.6: Correlations between XRD phases of Sample 1 (Figure 4.20d) and Sample 2 (Figure 4.20e) and the microstructural features presented in Figure 4.17a and Figure 4.19a, e, respectively.

Sample	XRD spectrum		Corresponding image	
	Figure	Phase	Figure	Feature
Sample 1	Figure 4.20d	W_2C + WC + WC_{1-x}	Figure 4.17a	1
	Figure 4.20d	WC	Figure 4.17a	2
	Figure 4.20d	W_2C	Figure 4.17a	3
	Figure 4.20d	Co_3W_3C	Figure 4.17a	4
	Figure 4.20d	γ (bcc) + γ (fcc)	Figure 4.17a	5
Sample 2	Figure 4.20e	W_2C + WC + WC_{1-x}	Figure 4.19a	1
	Figure 4.20e	Co_3W_3C	Figure 4.19a	2
	Figure 4.20e	γ (bcc) + γ (fcc)	Figure 4.19e	4

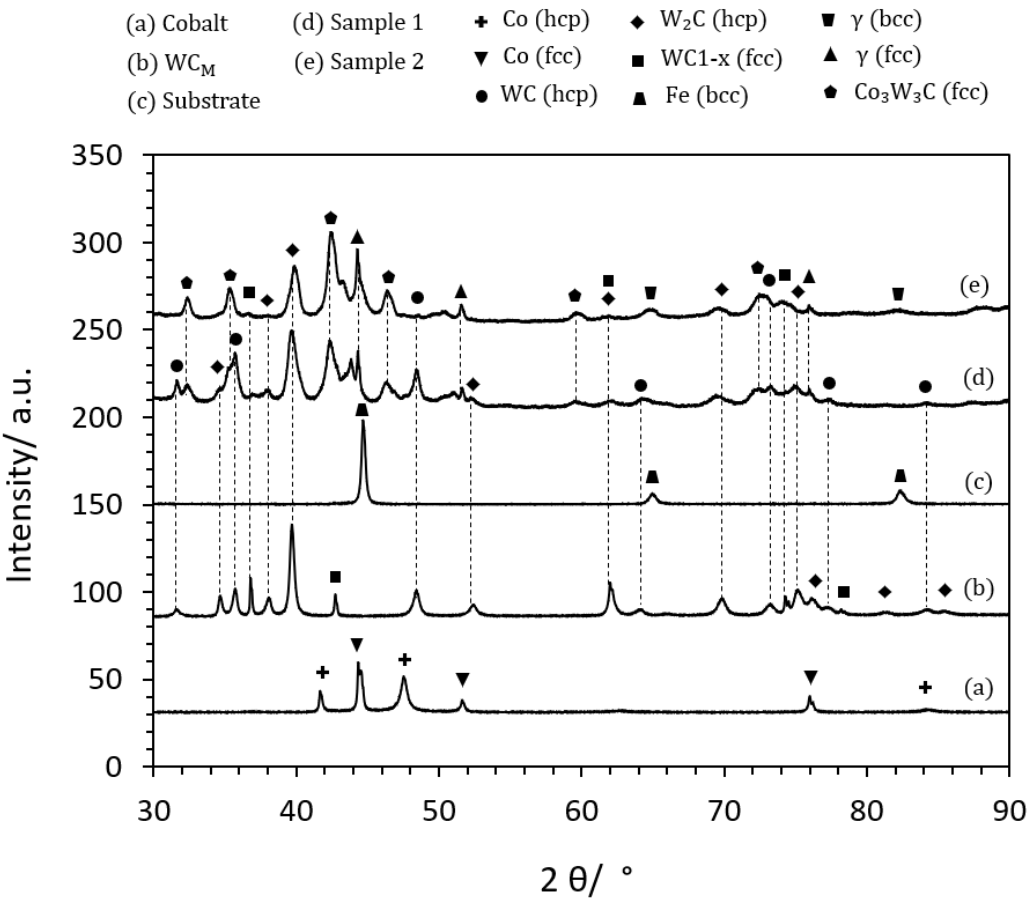

Figure 4.20: XRD patterns of Co powder (a), WC_M powder (b), mild steel substrate (c), Sample 1 (P= 500 W, V= 180 mm/min, PFR= 10 g/min) (d), and Sample 2 (P= 500 W, V= 360 mm/min, PFR= 10 g/min) (e).

4.4.2. Discussion

4.4.2.1. WC_M dissolution

The quality of WC reinforced clads is directly affected by the degree of WC dissolution. Wu et al. [132] reported that WC is apt to dissolve in laser-generated melt pool due to a low enthalpy formation of 38.5 kJ/mol. This can be compared to 92.9 kJ/mol for TiC as an example [133]. The dissolution extent depends on temperature and duration of the melt pool [134]. It resulted in a ternary carbide phase Co_3W_3C which can reduce the material ductility [135]. However, a high concentration and uniform dispersion of this hard phase can enhance the wear resistance [132]. In

addition, a limited dissolution of WC_M edges can produce a strong metallurgical bonding between the WC_M particles and the matrix [136]. This can enhance the pulling out resistance of WC_M particles during a tribological contact. The dissolution of WC belongs to the effects of two main concepts: process parameters including pre-heating and feedstock properties.

The effects of energy input and pre-heating condition are explained as follow. It has been shown that increasing the energy input (laser power/scanning speed) and pre-heating temperature can lead to increase the dissolution of WC particles [69, 86]. And according to Abioye et al. [137], increasing the energy input leads to increase (1) the amount of carbide particles captured in the clad due to increasing the melt pool size and then deposition efficiency and (2) the carbide dissolution. This is consistent with the current observations (Figure 4.14-deposition efficiency and Figure 4.15-WC_M dissolution ratio).

The evolution of microstructure can also be explained according to energy input. When powder enters in the melt pool, WC_M surface will absorb heat from surrounded molten matrix. This absorption results in dissolution of the WC_M surface into W and C atoms. Due to Marangoni convection flow, the diffusion of these elements in the molten matrix can lead to produce the dendritic W-rich morphology as a result of W-C-Co interaction (Figure 4.17a – features 3 and 4) [138]. Excessive WC_M dissolution can increase the viscosity of W and C atoms around the retained WC_M particles where the Marangoni driving force has a less ability to diffuse these dissolved elements into the matrix away from the retained WC_M. This allows the dissolved W and C atoms to re-precipitate again as a WC phase on the retained WC_M resulting in evolution of WC faceted morphology (Figure 4.16d – feature 2). As a physical observation, the amount of these features (dendritic and faceted) around the boundaries of the retained WC_M

particles can indicate the degree of WC_M dissolution. A higher number density of these features was observed in the clad deposited at the scanning speed of 180 mm/min (Sample 1-Figure 4.16) as compared to the scanning speed of 360 mm/min (Sample 2-Figure 4.18). This confirms the previous analysis (Figure 4.15c) giving that there was more WC_M dissolution at higher energy input.

Nonetheless, the energy input can be correlated with XRD results. Miao et al. [139] showed that increasing the energy input to 1900 W promoted excessive WC grain growth to ~ 20 times larger than that in the original powder. Thus, a higher intensity of WC peaks in the XRD pattern has been observed as compared to that detected at lower energy inputs of ≤ 1500 W. This confirms XRD results where higher intensities of WC peaks were observed in the microstructure containing faceted WC morphology (Figure 4.20d corresponded to Figure 4.16) as compared to XRD pattern of the another microstructure where no such morphology was observed (Figure 4.20e corresponded to Figure 4.18). Farayibi et al. [140] showed that the WC_{1-x} phase in the carbide powder was not detected in XRD pattern after cladding with Ti-based powder while the other original W_2C and WC phases still appeared. Also, W phase has been detected. In comparison, all the three phases (W_2C, WC, and WC_{1-x}) in the carbide powder used in this study were detected in XRD patterns of the clads (Figure 4.20d, e) and no W was observed.

On the other hand, the effect of feedstock properties on WC dissolution includes four aspects: powder shape, powder size, constitutive volume fraction, and matrix material. These are explained as follow.

Firstly, it has been shown that spherical WC particles reduced the carbide dissolution by ~ 7% as compared to irregular WC particles [87]. Spherical morphology minimizes

the contact area with the molten pool and then reduces the absorbed heat. Secondly, using finer carbide particles (10 – 45 µm particle size) can absorb more energy during laser processing due to a larger surface area per unit volume which resulted in a higher WC dissolution as compared to 45 – 125 µm particle size [88]. Thirdly, increasing the matrix content increases the duration of the melt pool and then WC dissolution due to more heat absorption [132]. Finally, the effect of matrix material has been studied by Zhou et al. [141]. It revealed that the edges of irregular WC particles (10 – 40 µm particle size) were dissolved in Ni-based matrix (40 – 90 µm particle size). When Fe-based powder (same particle size as Ni-based) has been used as a matrix, most of the WC particles were dissolved almost completely. This was due to a higher melting point of Fe-based (1362 °C) as compared to Ni-based (1027 °C) which required a higher energy input to melt the powder. Fine Co powder (1 – 3 µm particle size) used in this study can enhance laser absorptivity [142], then reduce the time of melting and, as a result, the dissolution of WC_M particles. This can be proved as follow. Despite a higher melting point of Co (1495 °C) as compared to that of Fe-based powder, no completely dissolution of WC_M particles was observed especially at the highest energy input with the lowest amount of powder feed rate (Figure 4.9c). However, coarser WC_M powder (45 – 125 µm) was employed. This indicates the impact of the constitutive feedstock properties on the WC_M dissolution.

4.5. Processing map

To better understanding the influence of process parameters on cladding deposition, several cladding trials were performed. The details of the parameters used are given in Appendix B. The results obtained are plotted in two different ways: firstly, linear energy density (L_E) versus powder feed rate (PFR), and secondly, effective energy density (E) versus powder deposition density (PDD). L_E represents the ratio of laser

power to scanning speed. E determines the delivered energy by the laser beam per unit area, and PDD represents the delivered powder per unit area.

4.5.1. Results

4.5.1.1. First approach: Linear energy density versus powder feed rate

Figure 4.21 shows a processing map obtained from linear energy density (L_E) versus powder feed rate (PFR) [60]. Three main regions can be observed; weak deposition (zone I), including high quality (zone II), and relatively high dilution (zone III). The weak depositions were produced at a laser powder of 200 W regradless the values of scanning speed and powder feed rate. The high quality representation indicates clads of uniform deposition, low porosity (< 1%), no cracks, good visual bonding with the substrate, and with a dilution ratio of < 40%. The dilution ratio is > 40% in the high dilution category. Moreover, the cracking is another material response.

The map shows that some different sets of process parameters are shared same positions inside the map because they have a same L_E ratio and PFR. For instance, two depositions A and B from zone III are compared. The material A obtained at P, V and PFR of 600 W, 240 mm/min, and 4 g/min, respectively. This gives L_E of 150 J/mm where a relatively higher melted depth can be seen. On the other hand, a deposition B produced at P, V, and PFR of 450 W, 180 mm/min, and 4 g/min, respectively, has also L_E of 150 J/mm. However, its melted depth and total melted area are clearly less than that of deposition A.

Another trend of results is observed from other two depositions from zone II; C produced at P = 400 W, V = 240 mm/min, and PFR = 10 g/min, and D produced at P = 300 W, V = 180 mm/min, and PFR = 10 g/min. Despite they have the same L_E ratio of 100 J/mm, they show different deposition behaviours.

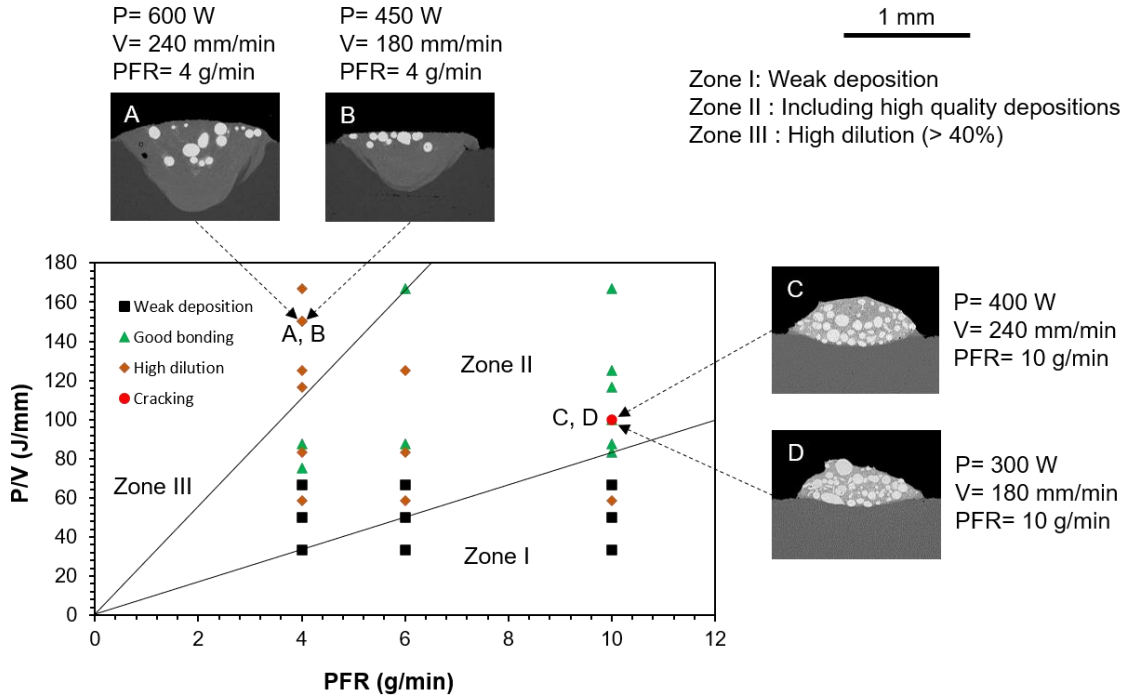

Figure 4.21: Process map produced by linear energy density (P/V) versus powder feed rate (PFR), including SEM/BSE images of four clads cross sections (A-D), showing three main behaviours: weak deposition (zone I), including high quality depositions (zone II), and high dilution (zone III).

The geometrical measurements of the above four depositions (A – D) are given in Figure 4.22. It shows that at PFR of 4 g/min, the clad area above substrate decreases from 0.18 ± 0.016 mm² to 0.11 ± 0.01 mm² by decreasing V from 240 mm/min (A) to 180 mm/min (B) as presented in Figure 4.22a. Subsequently, the substrate melted area decreases from 0.4 ± 0.01 mm² to 0.21 ± 0.003 mm². This indicates that both the delivered energy and delivered powder have decreased significantly considering a relatively lower PFR of 4 g/min. Similar trend of results can be observed at PFR of 10 g/min by decreasing V from 240 mm/min (C) to 180 mm/min (D).

The dilution ratios are illustrated in Figure 4.22b. It shows comparable results of ~70% in materials A and B. Decreasing V from 240 mm/min (C) to 180 mm/min (D) and

keeping PFR at 10 g/min decreases the dilution ratio from 20.4 ± 1% to 14 ± 0.7%. More delivered powder decreases the laser beam ability for a given scanning speed to accommodate all delivered powder. This results in decreasing the deposition rate and diminishing the heat transferred to the substrate.

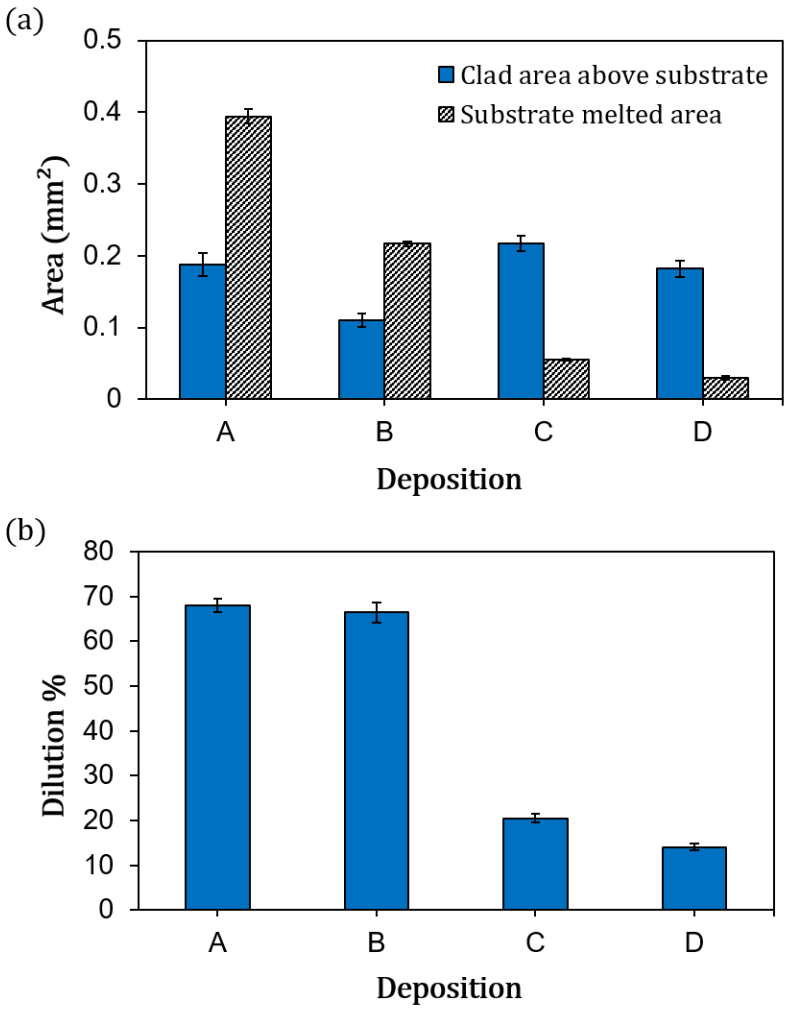

Figure 4.22: (a) clad area and substrate melted area, and (b) the corresponding dilution ratios. The process parameters and corresponding depositions are given in table below.

Deposition	Laser power (W)	Scanning speed (mm/min)	Powder feed rate (g/min)
A	**600**	**240**	**4**
B	**450**	**180**	**4**
C	**400**	**240**	**10**
D	**300**	**180**	**10**

4.5.1.2. Second approach: Effective energy density versus powder deposition density

A process map obtained by effective energy density (E) versus powder deposition density (PDD) is shown in Figure 4.23 [62]. E and PDD represent the delivered energy per unit area and the delivered powder per unit area, respectively. It gives a different distribution of experiments as compared to Figure 4.21. The same clads presented in previous processing window (A-D) are repeated here. It shows that A and B have a same E of 150 J/mm². And despite of a constant PFR of 4 g/min, decreasing V from 240 mm/min (A) to 180 mm/min (B) has led to increase PDD from 0.0041 g/mm² to 0.0055 g/mm². This can illustrate the reduction in substrate melted area of clad B due to more powder involving with the laser beam as explained before. On the other hand, clads C and D have also a same E of 100 J/mm². However, it also shows that PDD increases from 0.0104 g/mm² (C) to 0.0139 g/mm² (D) by decreasing V from 240 mm/min to 180 mm/min and keeping PFR at 10 g/min.

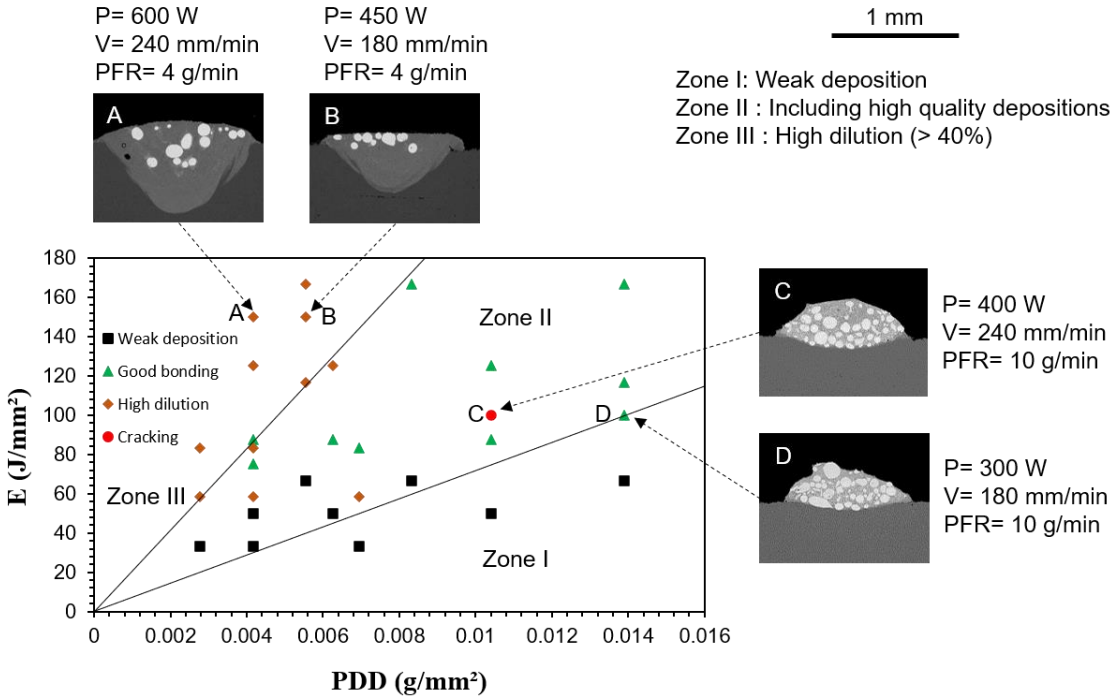

Figure 4.23: Processing map produced by effective energy density (E) versus powder deposition density (PDD), including SEM/BSE images of four clads cross sections (A-D), showing three main behaviours: weak deposition (zone I), including high quality depositions (zone II), and high dilution (zone III).

4.5.2. Discussion

4.5.2.1. Processing map

The process map provides a prior knowledge about the likely ranges of process parameters which can produce high-quality clads. This saves time and resources during the initial experiments [57]. However, controlling of DED-L processing is complicated due to the potential effect of one variable on the effective laser-powder residence time. It is well known that the variation of scanning speed affects the laser dwelling time and then the amount of heat input to the melt pool [143]. And according to Dass et al. [60], the amount of powder transferred to laser spot area is determined by the values of powder feed rate. However, the current results revealed that this parameter alone cannot catch the laser-powder physics in the melt pool. Goodarzi et al. [63] results

showed that despite the linear energy (laser power/scanning speed) has been kept at 300 J/mm through a scanning speed range of (400 – 800) mm/min, the total melted area and corresponding substrate melted area have changed significantly. It is plausable to suggeste that scanning speed affects also the amount of delivered powder to melt pool. As a result, the hypothesis of linear energy input versus powder feed rate cannot describe the actual laser-powder interaction (Figure 4.21). Bax et al. [61] reported the behaviour of Inconel 718 single clads using laser power versus powder feed rate values at two scanning speeds: 500 mm/min and 1000 mm/min. This strategy of multi-processing window cannot provide a clear vision to the applicable working zone considering a full range of process parameters. In comparison, the E-PDD representation (Figure 4.23) provided a logic vision to the relationship between process parameters and deposition characteristics.

4.6. Multitrack coatings

4.6.1. Results

The analyses of multitrack coatings involve three aspects: macrographic morphology, microstructure, and mechanical properties. The details are as follow.

4.6.1.1. Morphology

The macrographic topography of multitrack coatings are presented in Figure 4.24. It shows two coatings referred to as Sample 1 and Sample 2. Sample 1 produced at P, V, and PFR of 500 W, 180 mm/min, and 10 g/min, respectively, has a nearly flat surface without visible cracks or open pores (Figure 4.24a). Sample 2 produced at P, V, and PFR of 500 W, 360 mm/min, and 10 g/min, respectively, (Figure 4.24b) has similar characteristics as in Sample 1. Each coating consists of 8 tracks overlapped horizontally in an overlapping ratio of 50% from the corresponding track width.

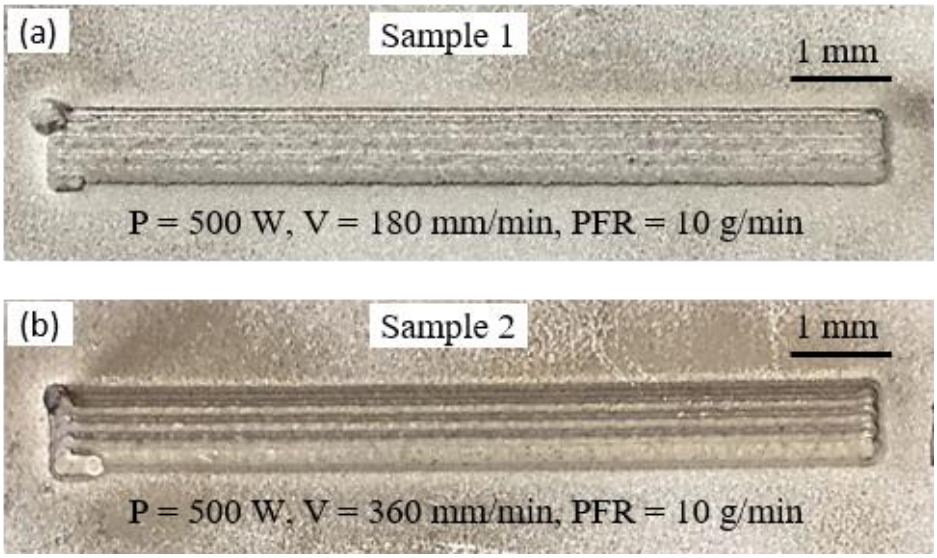

Figure 4.24: Macrophotographs of uniform coatings topographies produced at scanning speeds of (a) 180 mm/min and (b) 360 mm/min, where the laser power and powder feed rate are kept at 500 W and 10 g/min, respectively.

4.6.1.2. Microstructure

Optical microscopic investigations of the as-polished surfaces of multitrack coatings are given in Figure 4.25. It shows that coating produced at a lower scanning speed of 180 mm/min (Sample 1) demonstrates a relatively high number of cracks dispersed randomly on the solidified surface (Figure 4.25a). Also, it shows a high number density of pores with a maximum pore size of 360 µm. In comparison, less cracking tendency, and a smaller number of pores with a maximum pore size of 200 µm can be observed on the coating surface produced at a higher scanning speed of 360 mm/min (Sample 2) as presented in Figure 4.25b.

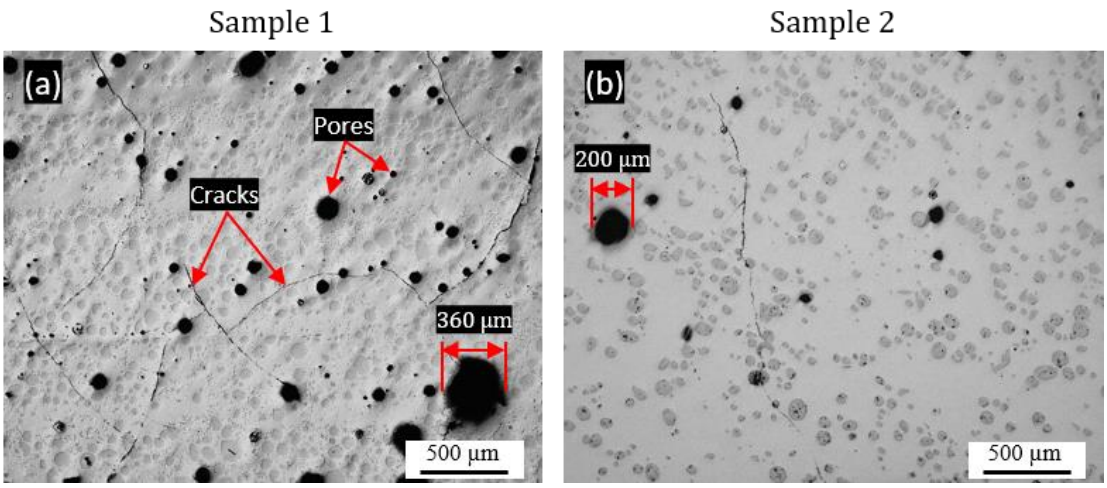

Figure 4.25: Cracks and pores observed in optical microscopic images of the as-polished surfaces of multitrack coatings produced at scanning speeds of (a) 180 mm/min and (b) 360 mm/min, where the laser power and powder feed rate are kept at 500 W and 10 g/min, respectively.

BSE images of the coatings cross sections are presented in Figure 4.26. The cross section of Sample 1 (Figure 4.26a) can be characterised by (1) a good bonding with the substrate, (2) no lack of fusion or inter-run pores between adjacent melt pools, and (3) uniform distribution of WC_M particles in light colour contrast. However, cracks initiated from the top layer surface towards the substrate can also be observed in the overlapping zone. Similar features are observed in the cross section of Sample 2 with a smaller coating height above the substrate as shown in Figure 4.26b.

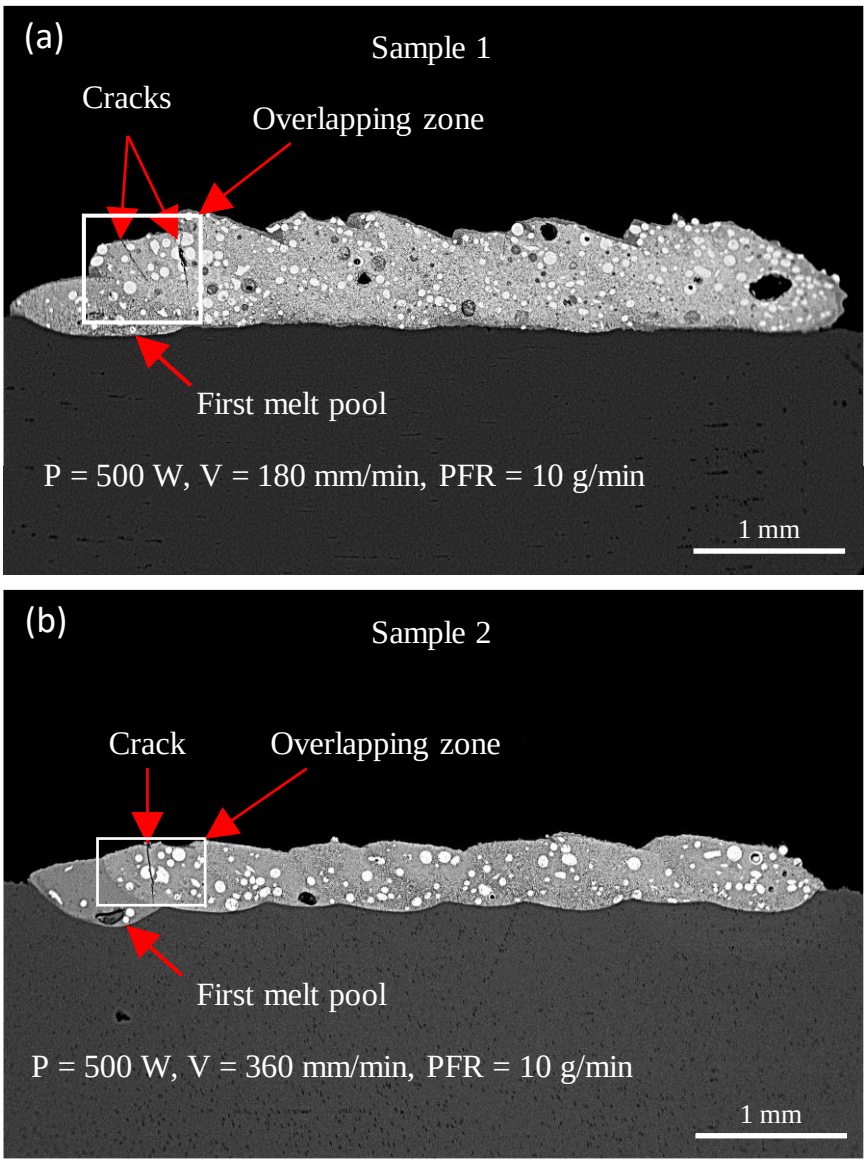

Figure 4.26: SEM/BSE images of cross sections of multitrack coatings produced at scanning speeds of (a) 180 mm/min and (b) 360 mm/min, where the laser power and powder feed rate are kept at 500 W and 10 g/min, respectively.

The measurements of height, porosity, and average pore size are given in Table 4.7. The height of Sample 1 is thicker by about 30% than the corresponding single track (445 µm). This represents 2.4 times of Sample 2 thickness which in turn is thicker by 17% than the corresponding single track (224 µm). The relatively low uncertainties of the heights of the two coatings confirm the uniformity of the fabricated surfaces. The

porosity ratio and average pore size of Sample 1 are about 2.5 times and 1.5 times that values of Sample 2, respectively.

Table 4.7: Height, porosity, and pore size measurements of coatings produced at scanning speeds of 180 mm/min (Sample 1) and 360 mm/min (Sample 2), where the laser power and powder feed rate are kept at 500 W and 10 g/min, respectively.

Measurement	Sample 1	Sample 2
Height (µm)	650 ± 35	270 ± 20
Porosity %	2.5 ± 0.7	1 ± 0.1
Pore size (µm)	142 ± 106	90 ± 64

4.6.1.3. Mechanical properties

The mechanical properties include microhardness and reciprocating dry sliding wear. These are explained as follow.

4.6.1.3.1. Microhardness

The microhardness measurements of the coatings' matrices and the substrate are given in Figure 4.27. It shows that the matrix microhardness of the Sample 1 is 1120 ± 30 $HV_{300\ gf}$. This represents 1.8 times and 4.8 times that values of the Sample 2 and the substrate, respectively.

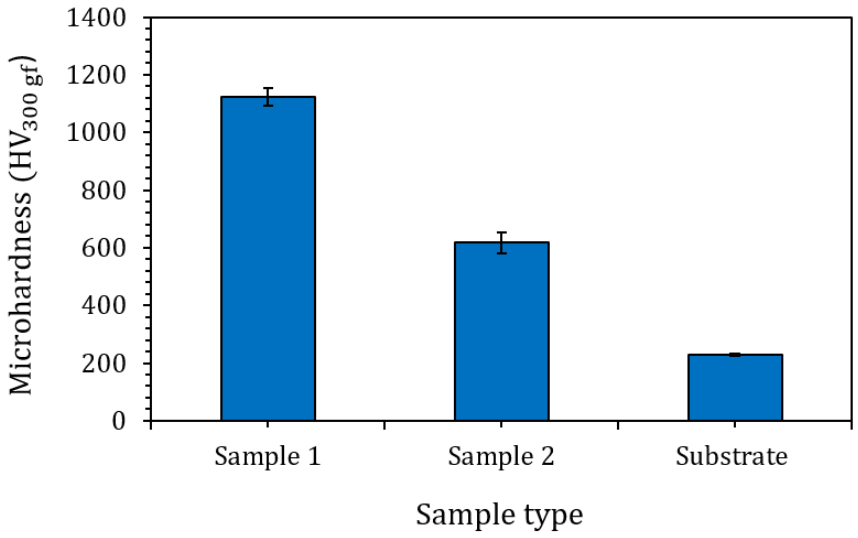

Figure 4.27: Microhardness measurements of the substrate and coatings matrices produced at scanning speeds of 180 mm/min (Sample 1) and 360 mm/min (Sample 2), where the laser power and powder feed rate are kept at 500 W and 10 g/min, respectively.

Figure 4.28 shows the morphology of microhardness indents at 300 gf and 1000 gf loads targeting WC_M-free areas of Sample 1 (Figure 4.28 a and b) and Sample 2 (Figure 4.28 c and d), respectively. No cracks can be observed on the samples surfaces at the indents' edges. The ratio of indents widths of Sample 1/Sample 2 at 300 gf and 1000 gf loads are 0.75 and 0.73, respectively.

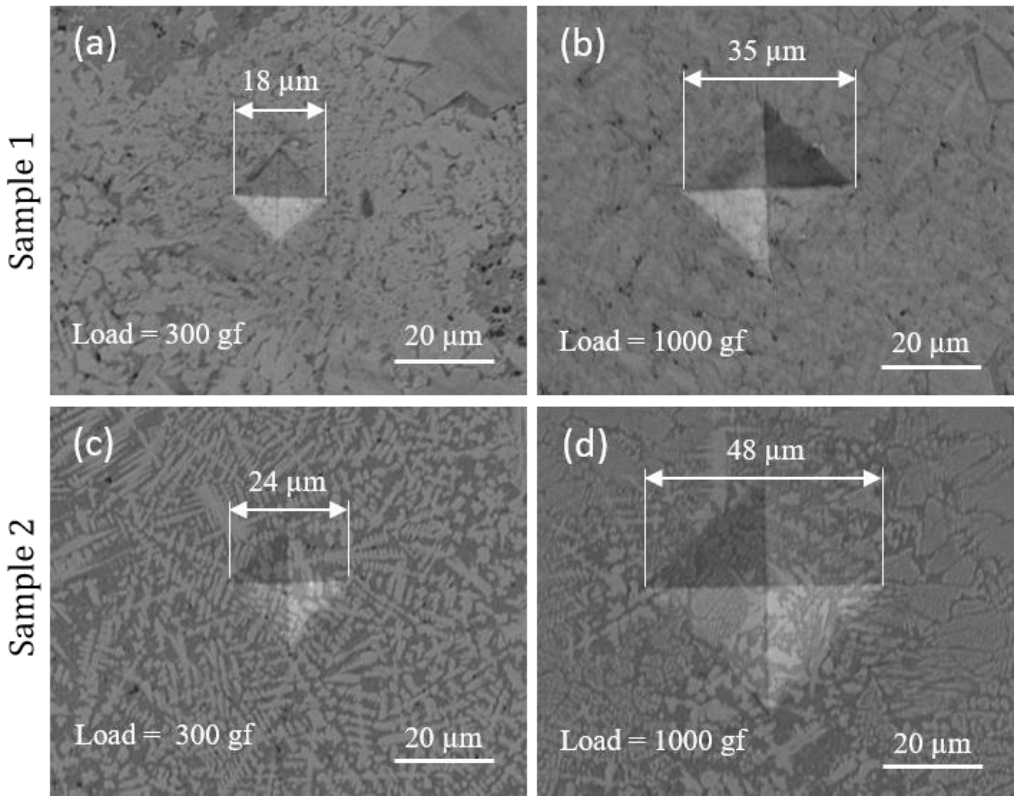

Figure 4.28: SEM/SE images of the microhardness indents in the coatings' matrices at 300 gf (left column) and 1000 gf (right column): (a and b) produced at a scanning speed of 180 mm/min: (c and d) produced at a scanning speed of 360 mm/min: the laser power and powder feed rate are kept at 500 W and 10 g/min, respectively.

4.6.1.3.2. Coefficient of friction and wear resistance

The variations of the coefficient of friction (COF) during the wear tests are presented in Figure 4.29. It shows stable COFs of all tests at the end period of the sliding distance of 25 – 30 m. The Sample 1 presents lower maximum (0.5) and average stable (0.36) COFs as compared to that of the Sample 2 (0.77 and 0.72) and the substrate (0.91 and 0.82), respectively.

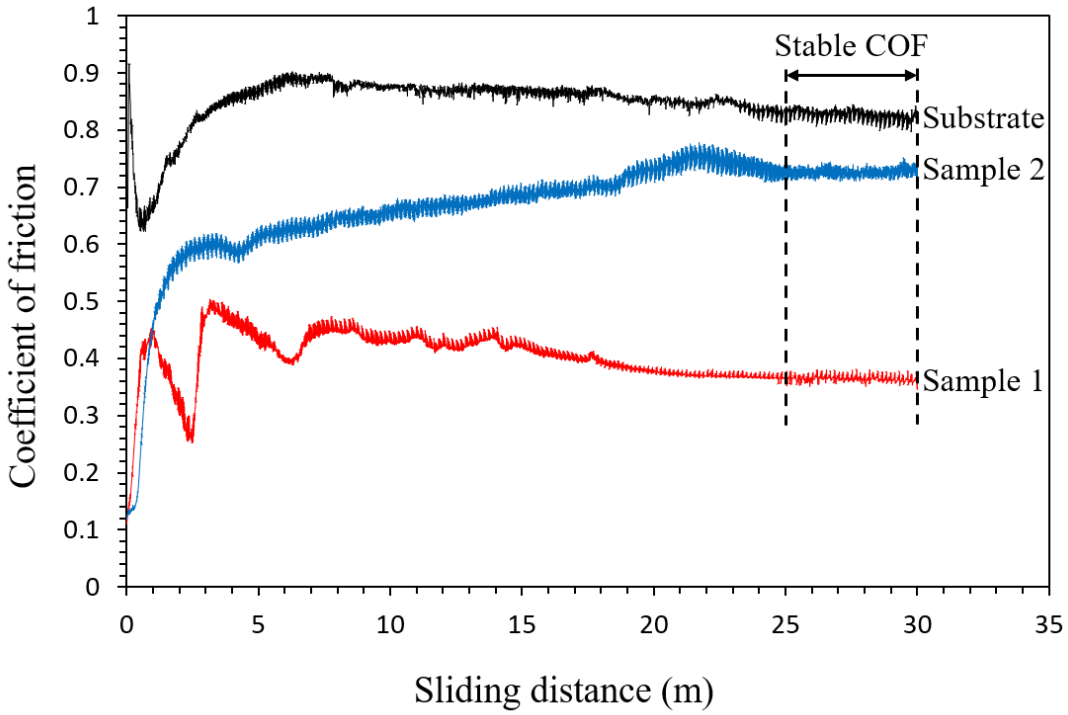

Figure 4.29: Variations of coefficient of friction as a function of sliding distance during the wear tests of the mild steel substrate, Sample 1 (multitrack coating produced at laser power, scanning speed, and powder feed rate of 500 W, 180 mm/min, and 10 g/min, respectively), and Sample 2 (multitrack coating produced at laser power, scanning speed, and powder feed rate of 500 W, 360 mm/min, and 10 g/min, respectively).

The morphologies of dry sliding contacts are presented in Figure 4.30. It shows no removal surface from Sample 1 (Figure 4.30a, b) although a maximum load of 15 N has been applied in the tribometer for 3000 cycles of working where each cycle represents one completed forward and backward movement of the counter ball on the contact length. In Sample 2, the removed surface is difficult to be recognized at the low magnification (Figure 4.30c). A removed thin film of 400 µm width can be observed at the high magnification (Figure 4.30d). No pull out of the WC_M particles or cracks can be seen. In comparison, the width of the substrate contact surface (Figure 4.30e) is more than 1.8 times that of Sample 2. Moreover, grooves in the direction of the tribometer movement are noticed at the high magnification (Figure 4.30f).

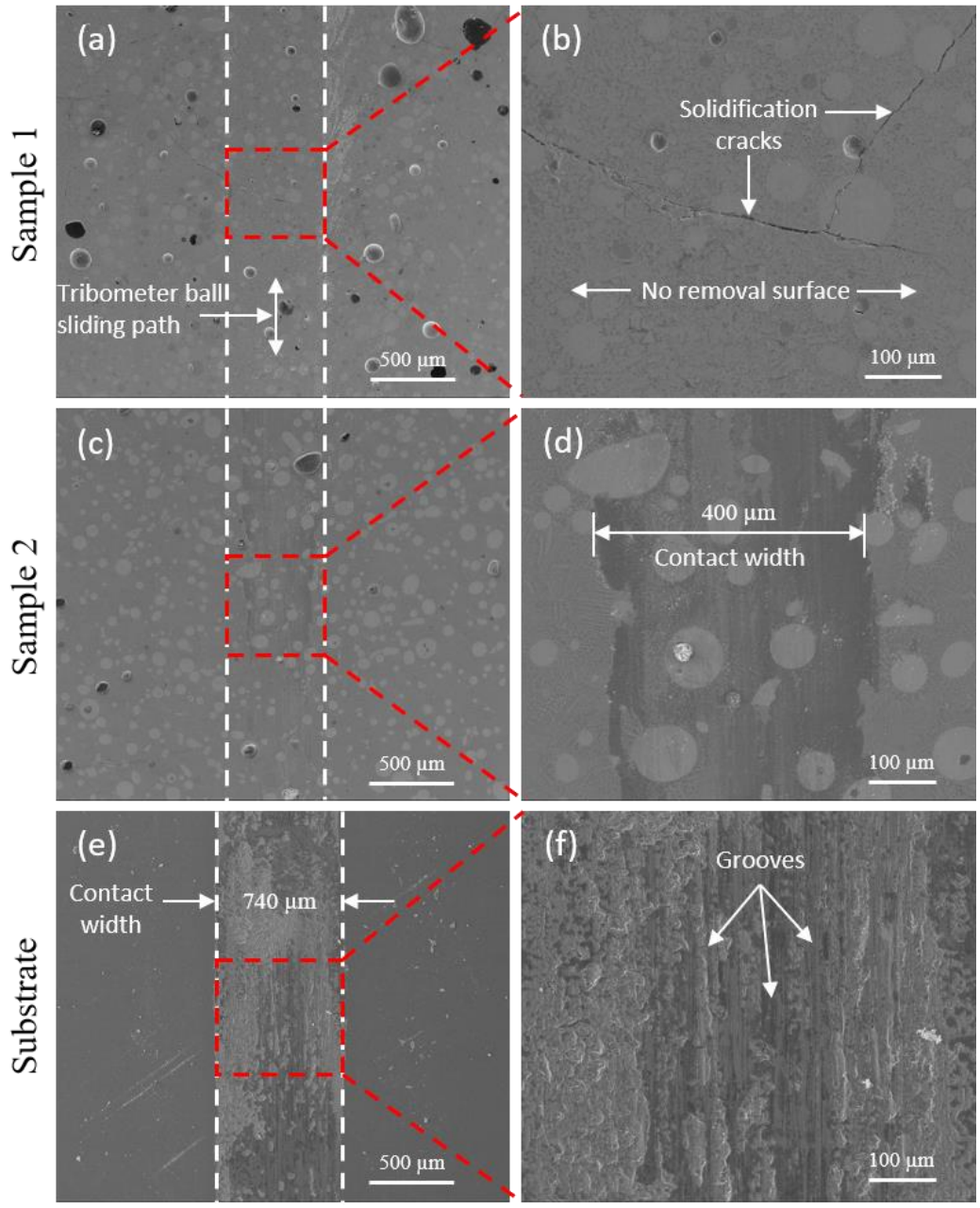

Figure 4.30: SEM/SE images of dry sliding contact surfaces resulted from the wear tests: (a, b) multitrack coating produced at laser power, scanning speed, and powder feed rate of 500 W, 180 mm/min, and 10 g/min, respectively: (c, d) multitrack coating produced at laser power, scanning speed, and powder feed rate of 500 W, 360 mm/min, and 10 g/min, respectively: (e, f) mild steel substrate.

4.6.2. Discussion

4.6.2.1. Porosity

The effect of energy input on porosity has not been fully understood. Balla et al. [85] observed that increasing energy input from 350 W to 450 W has led to decrease the porosity range from (2-3)% to (1-2)% when a cast and crushed WC-12 Co powder of 45-75 µm particle size has been used. While Erfanmanesh et al. [58] showed different behaviour; it appeared that by keeping the scanning speed and powder feed rate at 4 mm/s and 100 mg/s, respectively, the increase of laser power from 150 W to 300 W has led to increase the porosity ratio from 0.4% to 11.81% when agglomerated WC-12 Co powder in a size range of 15-45 µm has been used to deposit single clads. However, no clear trend can be observed with respect to the other variations of process parameters. The effect of laser working distance on material density has been studied by Xiong et al. [79] using a nanocrystalline WC-10 Co powder in a size range of 45-90 µm. It showed comparable densities of 97% and 96% by increasing the working distance above the focal plane from 2 mm to 4 mm, respectively.

It has been reported that the porosity is independent of process parameters and instead it is mostly dependent on feedstock [144]. Considering a maximum porosity of < 2% (Figure 4.13c), it can be indicated that the satellited feedstock can produce high quality clads of negligible porosity. The residual porosity can be attributed to gas entrapped due to insufficient time to completely escape from the melt pool [45]. Ng et al. [70] showed that the gas bubbles in the melt pool are driven by Marangoni flow which was in order of 5 times higher than the flotation effect. This can contribute to the pores distribution and increase gas retention. In the overlapped tracks (Figure 4.25), the dynamic of the melt pool caused by Marangoni flow can be higher in a further order of magnitude due to a more heat absorbed by powder particles. On the other hand,

coalescence between adjacent gas pores can also occur during laser processing. Besides a typical high cooling rate of DED-L processing (> 10^3 °C/s) [45], these reasons can explain the increase of overall porosity and average pore size in the multitrack coatings as compared to the corresponding single tracks. The higher porosity observed in the coating produced at the higher energy input caused by a lower scanning speed of 180 mm/min as compared to that produced at 360 mm/min (Table 4.7) confirms the effect of melt pool dynamic on pores formation.

4.6.2.2. Cracking of multitrack coatings

The cracks in DED-L clads can be classified into two types: solidification cracks and liquation cracks [66]. The solidification cracks occur within the melt pool due to thermal stresses caused by thermal expansion/shrinkage movement of the material during heating/cooling cycle. The liquation cracks occur in the heat affected zone (HAZ) away from the melt pool where the material is heated to a lower than its overall liquidus temperature. Due to melting of some low melting point compounds, liquid films can form in HAZ around specific grain boundaries which act as crack initiation sites when the induced thermal stresses are large enough. In the multitrack coatings (Figure 4.26), the cracks were observed within melt pools (overlapped regions), thus, it can be suggested that those were solidification cracks.

Moreover, it is well known that a part of laser energy is absorbed by the blown powder and the rest melts the substrate to form the melt pool. In the overlapping zone between melt pools, the heat conducted to the substrate will be diminished as this part is covered by a portion from the previous solidified melt pool. Thus, this part of the clad will be subjected to a higher energy and repeating of melting which result in higher thermal stresses than that in direct contact to the substrate. This can explain the initiation of cracks in the overlapping regions especially between the initial tracks more than the

tracks deposited later due to a faster cooling rate (less preheating effect) as observed in Figure 4.26. Wang et al. [27] reported that post-heat treatment or hot isostatic pressing can improve material ductility. On the other hand, Huang et al. [36] showed that crack-free WC-based coatings cannot be produced by laser cladding without preheating the substrate to 300 °C, however, the retained WC volume has decreased as compared to non-preheated samples. This has been attributed to the reduction in cooling rate at preheating condition which diminishes the induced thermal stresses [89]. Another research showed that a feedstock containing more than 80 vol.% WC particles is not recommended for high-quality clads due to cracking propensity [132]. Reducing WC content can improve material ductility and then reduce cracks. However, low carbide content can also lead to reduce the wear resistance. These three strategies (post-heating, pre-heating, and lower WC content) can be studied to confirm their impacts on the microstructure and then mechanical properties.

4.6.2.3. Mechanical performance

The mechanical performance of the depositions largely depends on the microstructural characteristics. The high degree of dendritic morphology observed due to high WC_M dissolution at the high energy input (Sample 1-Figure 4.16) can explain the highest matrix microhardness obtained (Figure 4.27) as compared to that of the relatively low WC_M dissolution at the low energy input (Sample 2-Figure 4.18). This resulted in a lower coefficient of friction on the harder coating (Figure 4.29) due to improving of the loading capacity [115] which in turn led to no degradation during the wear tests indicating excellent wear resistance (Figure 4.30b). Moreover, considering no dislocation/pulling out of the WC_M particles, it indicates a good metallurgical bonding between the WC_M particles and the matrix. Nonetheless, the coating presented excellent fracture toughness as there were no cracks extensions observed around the

edges of the microhardness indents (Figure 4.28a, b). However, this hard coating can also abrade the counterpart. Thus, introducing a harder counterpart instead of the Si_3N_4 ceramic ball can be more proper for tribological testing of this material. In comparison, a relatively low WC_M dissolution in Sample 2 has led to a relatively low matrix microhardness and then to a high COF resulting in removing of a thin surface film (Figure 4.30d). However, no fragmentation or pulling out of WC_M particles was observed on the worn surface which has a smooth morphology. This is superior to another research observation where some cracks appeared on the WC particles even though they still combined with the Ni matrix after the reciprocating wear test [132]. It has been reported that shear removing of thin platelets from the WC grains can occur during the wear tests giving a smooth WC surface morphology [145]. Thus, the wear mechanism in Sample 2 can be micro-cutting and shear removing of the matrix as well as portions from the WC_M particles.

On the other hand, the higher COF and severe wear mechanism observed on the substrate were due to a lower surface microhardness as compared to Sample 1 and Sample 2. Hard asperities can be formed on the ceramic ball surface due to transferring of some of the counterpart material by a micro-welding and fracturing process [146]. Sliding against those hard morphologies can produce grooves on the substrate as presented in Figure 4.30f which indicates severe abrasive wear mechanism.

As a result, high mechanical performance can be obtained by improving the matrix microhardness through producing a microstructure containing a dense and uniform distribution of fine and hard inclusions.

4.7. Summary

The DED-L results can be divided into four main parts: processing of the blended and satellited WC_M-12 wt.% Co composite powders, microstructural characteristics, processing map, and mechanical properties. The outcomes are summarized below.

A- Processing of the blended and satellited WC_M -12 wt.% Co composite powders

- Non-uniform morphology containing high and low depositions was observed in the blended WC_M-12 wt.% Co single clad.
- It appeared that satelliting method is a flexible approach to prepare a suitable feedstock for DED-L processing to produce a continuous and uniform clad morphology.
- The multilevel full factorial design of experiment method showed a significant impact of laser power, scanning speed and powder feed rate on the clad geometrical and microstructural characteristics.
- The deposition efficiency of the feedstock is proportional to laser power.
- Based on a simple heat balance model, it showed that Co powder cannot be melted while transferring in the laser field before reaching to the substrate surface considering the maximum employed energy density.
- Uniform multitrack coatings without outside cracks or lack of fusion between tracks were produced from the satellited WC_M-12 wt.% Co feedstock.

B- Microstructural characteristics

- The average porosity ratio in the blended clad was 12 times that observed in the satellited deposition.
- A lack of fusion was observed between the blended clad and the substrate.

- The satellited single clads demonstrated good bonding with the substrate, no cracks, almost full density matrix, and uniform distribution of the WC_M particles inside the cladding area.
- The formation of new ternary carbide Co_3W_3C due to WC_M dissolution in the metal matrix was confirmed by the XRD investigations.
- EDX investigations showed that the iron from the substrate has interacted with the molten Co from the feedstock to form the Co-Fe metal matrix.
- The dissolution of WC_M particles during cladding process was proportional to laser power.
- Recrystallization of WC faceted morphology due to WC_M dissolution was confirmed by the SEM/BSE, EDX, and XRD investigations at a specific set of laser power, scanning speed, and powder feed rate.
- Cracks were observed in the multitrack coatings in the overlapping regions between melt pools.
- Cracks, pore size, and porosity ratio initiated in the multitrack coating were proportional to energy density.

C- Processing map

- A suitable processing map was identified by comparing between two approaches: linear energy density versus powder feed rate and effective energy density versus powder deposition density.
- Three main responses were recognized inside each processing map: weak deposition, high quality materials, and high dilution.
- The results showed that the hypothesis of linear energy density versus powder feed rate cannot describe the actual laser-powder physics in the melt pool.

- Coherent correlations between the process parameters and melt pools were obtained from compromising between effective energy density and powder deposition density.
- It appeared that the scanning speed can play a vital role in determination not just the delivered energy by the laser beam, but also the amount of delivered powder to melt pool.

D- Mechanical properties

- The WC_M dissolution increased the matrix microhardness.
- The microhardness indents showed no cracks around their boundaries even though a maximum allowable load was applied indicating a good fracture toughness.
- The microhardness of the multitrack coatings reached to 4.8 times that of the mild steel substrate.
- The coefficient of friction was inversely proportional to the microhardness.
- Although cracks, excellent wear resistance was observed on the multitrack coating produced at a high energy density where no evidence of surface removing was observed.
- A removing of a thin surface film after 3000 cycles of reciprocating dry sliding wear using a maximum allowable load was observed on the multitrack coating produced at a relatively low energy density.
- No cracking, dislocation, or pulling out of the WC_M particles were observed on the contact surfaces of the multitrack coatings after the wear tests.
- Severe abrasive wear mechanism including grooves was observed on the worn surface of the mild steel substrate.

5. L-PBF of two different WC-Co powders preparations: satelliting and plasma densifying

5.1. Introduction

This chapter involves two main parts: L-PBF of satelliting WC_M-12 wt.% Co powder and L-PBF of plasma densified WC-17 wt.% Co powder.

The satellited powder is investigated by using the Realizer SLM-50. Smaller powder batch of ~1/10 can be used to perform the experiments as compared to that required for Renishaw AM 125. This provides economic usage of powder and reduces the preparation time of the manually prepared satellited powder. Prior the experiments, the melt pool size is estimated using the Rosenthal model to predict the likely values of laser power and scanning speed that can be used to generate a suitable melt pool for a given powder. To effectively melt the powder, the estimated melt pool width exceeds the maximum powder particle size. The experimental results are presented in three sections: single tracks processability, single layer, and multilayer components. The evolution of single tracks shows the effect of laser scanning speed on tracks morphology, geometrical characteristics, evolution of melt pools, cross-sectional observations, and the transition of keyhole to conduction melting mode. In single layer and multilayer fabrications, the effect of laser power on surface morphology and cross section is studied.

The plasma densified powder is used to produce walls and cubic samples by Renishaw AM 125. The powder has a smaller particle size distribution and higher Co content as compared to that of the satellited powder. Smaller particle size enhances laser beam effectiveness to accommodate powder particles which can result in a smoother surface morphology. Also, it can lead to homogenisation of the temperature within the melt

pool and thereby reduce cracking tendency. Higher Co content can also lead to reduce cracks by increasing material ductility. The Renishaw AM 125 has a laser spot size of 3.4 times that of the Realizer SLM-50. Besides a smaller powder particle size, this can also enhance the effectiveness of the laser beam to accommodate powder particles and homogenize the temperature within the melt pool. The laser power and scanning speed values are preliminary estimated using the Rosenthal model as explained above. The applicabilty of these prediced process parameters to produce a contiuous multitrack wall without pores or cracks is examined. Then, the results detail the effects of laser power (P) and scanning speed (V) on as-built cubic samples in a process window. This implies macrographic properties and SEM investigations to as-laser-scanned surfaces. The microstrucure is also investigated. This includes optical microscopic, XRD, BSE, EDX mapping, and chemical compositions analyses.

5.2. Results

5.2.1. Laser-powder bed fusion of satelliting WC_M-12 wt.% Co powder using Realizer SLM-50

5.2.1.1. Theoretical melt pool size

Although Rosenthal model has limitations that come from its assumptions, it can indicate the likely values of laser power and scanning speed that can be used to produce a suitable melt pool size for a given powder. This reduces the number of experiments by indicating a suitable starting set of process parameters.

Figure 5.1 shows the theoretical melt pool size obtained from Rosenthal model at laser power and scanning speed of 100 W and 0.14 m/s, respectively, using the estimated thermo-physical properties of satellited WC_M-12 wt.% Co powder as explained before in section 3.1.1 – chapter 3. However, the effect of powder particle size or powder layer thickness is not considered in the Rosenthal model. The MATLAB solution code

is given in Appendix E – section E.2. The melt pool length and width are 194 µm and 190 µm, respectively, resulting in a nearly circular shape with small elongation in ξ axis. The estimated width is more than 1.5 times that of the maximum WC_M particle size (125 µm) as provided by the manufacturer. This indicates the ability of the melt pool, within the current process parameters, to accommodate the powder particles. Considering a half of the width, it gives a melted depth of 95 µm.

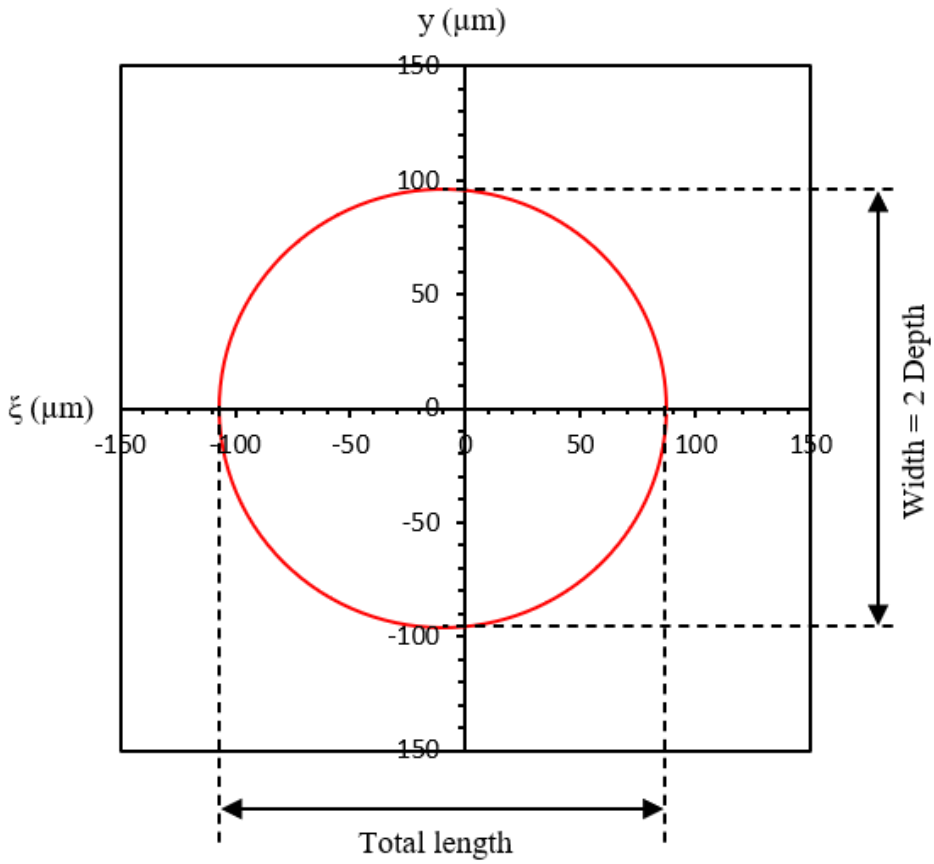

Figure 5.1: Theoretical melt pool dimensions of satellited WC_M-12 wt.% Co composite powder using Rosenthal equation at laser power and scanning speed of 100 W and 0.14 m/s, respectively.

5.2.1.2. Single tracks

The processability of single tracks is performed at a maximum laser power of 100 W to enhance powder melting. The scanning speed has increased gradually from 0.14 m/s to 0.5 m/s.

5.2.1.2.1. Evolution of the track morphology as a function of laser scanning speed

Figure 5.2 shows the morphology of four tracks which differ vastly with an increase in laser scanning speed. At a lower scanning speed of 0.14 m/s (Figure 5.2a), a continuous track with no visible cracks and relatively uniform surface morphology can be observed. Images at higher magnification (Figure 5.2b) indicate two more aspects; WC_M particles appear on the top surface of the track and relatively fine particles are also observed on the substrate near the track sides. With an increase of the scanning speed to the value of 0.2 m/s, the track surface morphology becomes more irregular (Figure 5.2c). Cracks can clearly be observed on the outside track surface at a higher magnification (Figure 5.2d). Balling is significant at a scanning speed of 0.33 m/s: this leads to numerous discontinuities where the solidified material is accumulated is some places and diminished at the others (Figure 5.2e). Moreover, non-melted powder clearly appears at higher magnification (Figure 5.2f). An increase in the scanning speed to the 0.5 m/s, has led to extensive discontinuities and balling, as shown in Figure 5.2g. In addition, the higher magnification image shows that the formation of fine particles along the track sides and cracks become predominant as presented in Figure 5.2h.

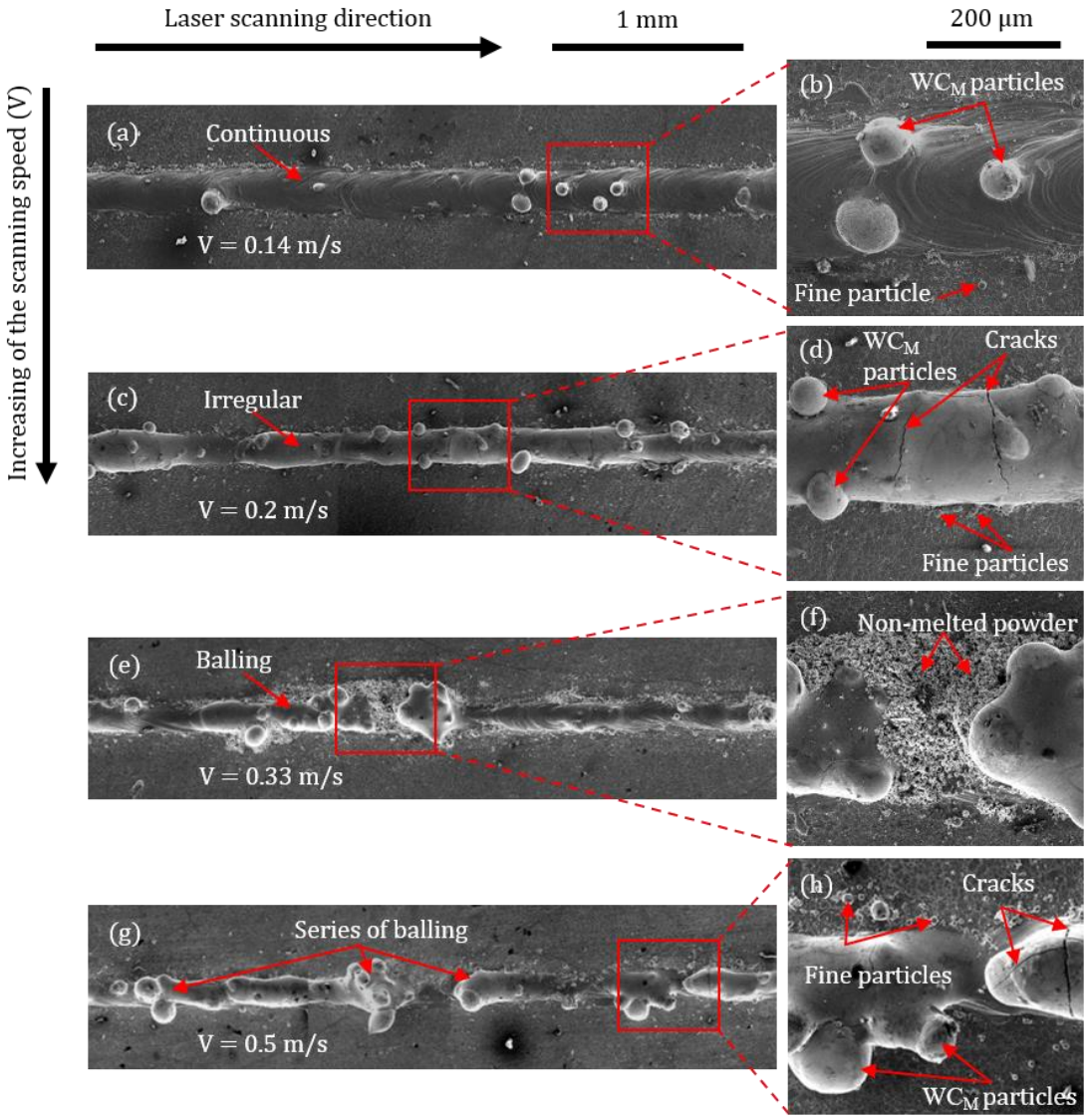

Figure 5.2: Consolidation behaviours of satellited WC_M-12 wt.% Co single tracks produced at scanning speeds of 0.14 m/s (a), 0.2 m/s (c), 0.33 m/s (e), and 0.5 m/s (g), with corresponding higher magnifications track images in (b), (d), (f), and (h), respectively.

5.2.1.2.2. Track width, height, and melt pool length measurements

Figure 5.3 shows the variation of track width and height as a function of laser scanning speed. It is observed that the track reached a maximum width of 225 ± 10 µm at a scanning speed of 0.14 m/s. The track width decreases to a minimum of 112 ± 20 µm when the laser scanning speed is increased to 0.5 m/s. It was observed that the track width decreases consistently when the scanning speed increases although precise

measurements are challenging due to the irregular morphology of the tracks. On the other hand, the track height does not follow a regular trend-within the explored parameter space. It increases from 40 ± 5 µm to 86 ± 16 µm when the scanning speed increases from 0.14 m/s to 0.2 m/s. While further increase of the scanning speed to 0.5 m/s leads to a decrease in track height to 47 ± 24 µm where highest uncertainty value can be observed indicating track morphology irregularities.

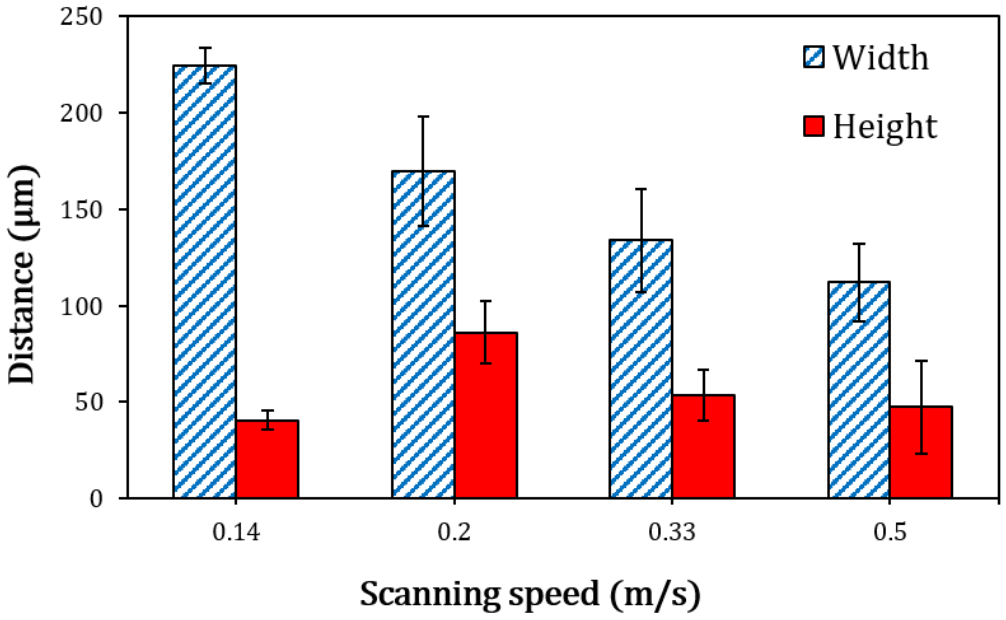

Figure 5.3: Variation in track widths and heights of satellited WC_M-12 wt.% Co with respect to the laser scanning speed. Noting track height does not vary significantly with the parameters evaluated here.

The effect of laser scanning speed on the evolution of melt pool shapes at the ends of the solidified tracks is presented in Figure 5.4a. The results confirm the previous trend, where the reduction in melt pool width can be observed as the scanning speed increases. It shows that the ratio of melt pool length (L), which represents the major axis of first elliptical edge appeared on the surface far from the melt pool centre, to its width (D) increases from 1.9 ± 0.3 to 2.6 ± 0.3 as the scanning speed increases from

0.14 m/s to 0.5 m/s. The melt pool width decreases from 210 ± 47 µm to 122 ± 14 µm when the scanning speed increases from 0.14 m/s to 0.5 m/s as shown in Figure 5.4b. No significant variations between the melt pool width and the measured track width are observed confirming that the method of investigation produces accurate estimates of the melt pool produced during the steady state laser melting. No noticeable variations in melt pool length are observed as a function of laser scanning speed. On the other hand, significant difference is observed between the sizes of experimental and predicted melt pools due to the assumptions of the model used.

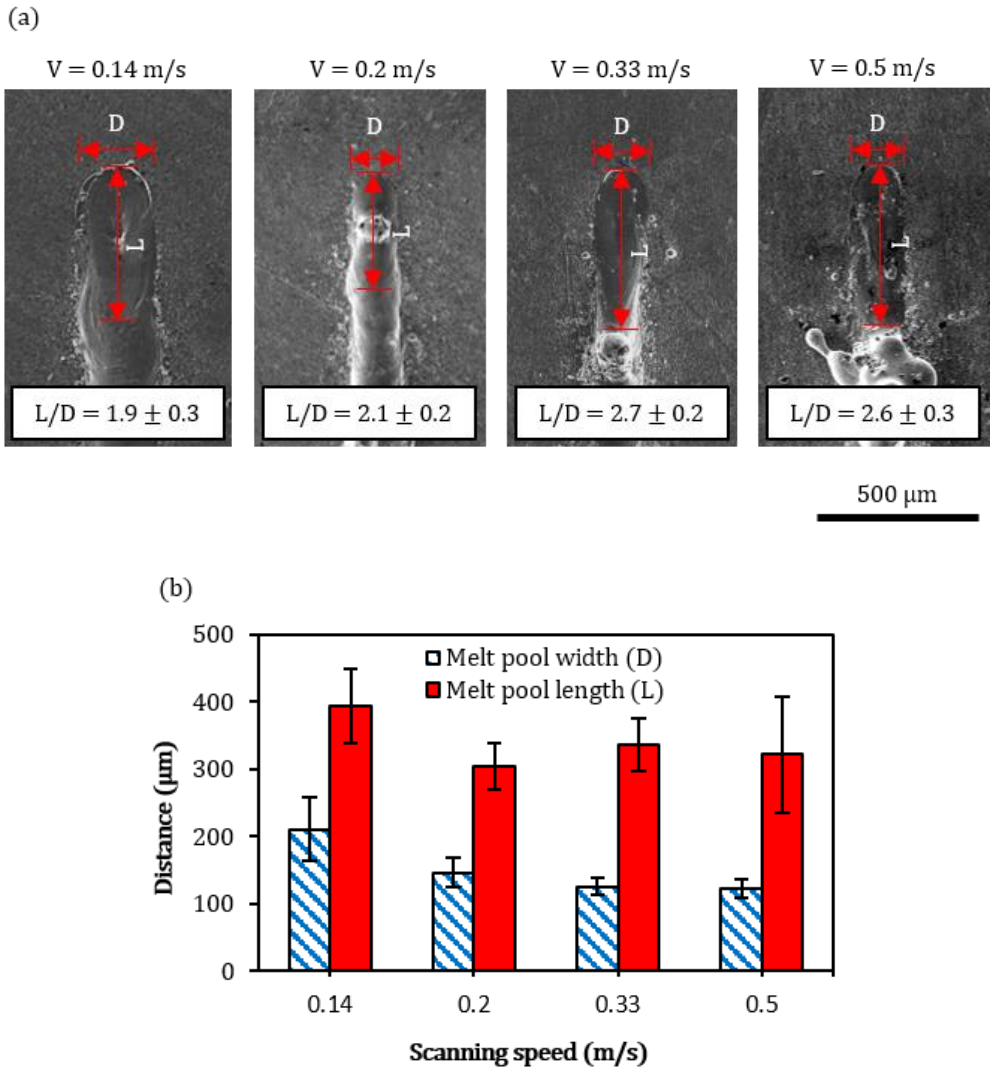

Figure 5.4: (a) Top view images of representative satellited WC_M-12 wt.% Co melt pool shapes at the end of the solidified tracks, and (b) bar chart showing the measurements of the corresponding melt pool widths and lengths.

5.2.1.2.3. Cross-sections and melted depth characteristics

The cross-sectional investigations of the tracks are presented in Figure 5.5. BSE imaging (Figure 5.5a-d) reveals that WC_M particles are present inside the metal matrix, although partial dissolution may have taken place. Keyhole porosity is occasionally observed as shown in Figure 5.5a. The limits of the melt pools are defined from the Co element EDX maps (Figure 5.5e-h). The melt pool geometry becomes shallow and narrow as the laser scanning speed is increased. A progression of a crack from the outer solidified surface for a specific distance inside a WC_M particle through its centre appears at a scanning speed of 0.2 m/s (Figure 5.5b). For relatively low applied energies (corresponding to relatively higher scanning speeds), it can be observed there is a reduction of the dissolution of the WC_M particles with only traces of W appearing in the melt pool at scanning speeds of 0.2 m/s and 0.5 m/s as shown in Figure 5.5j, and l, respectively.

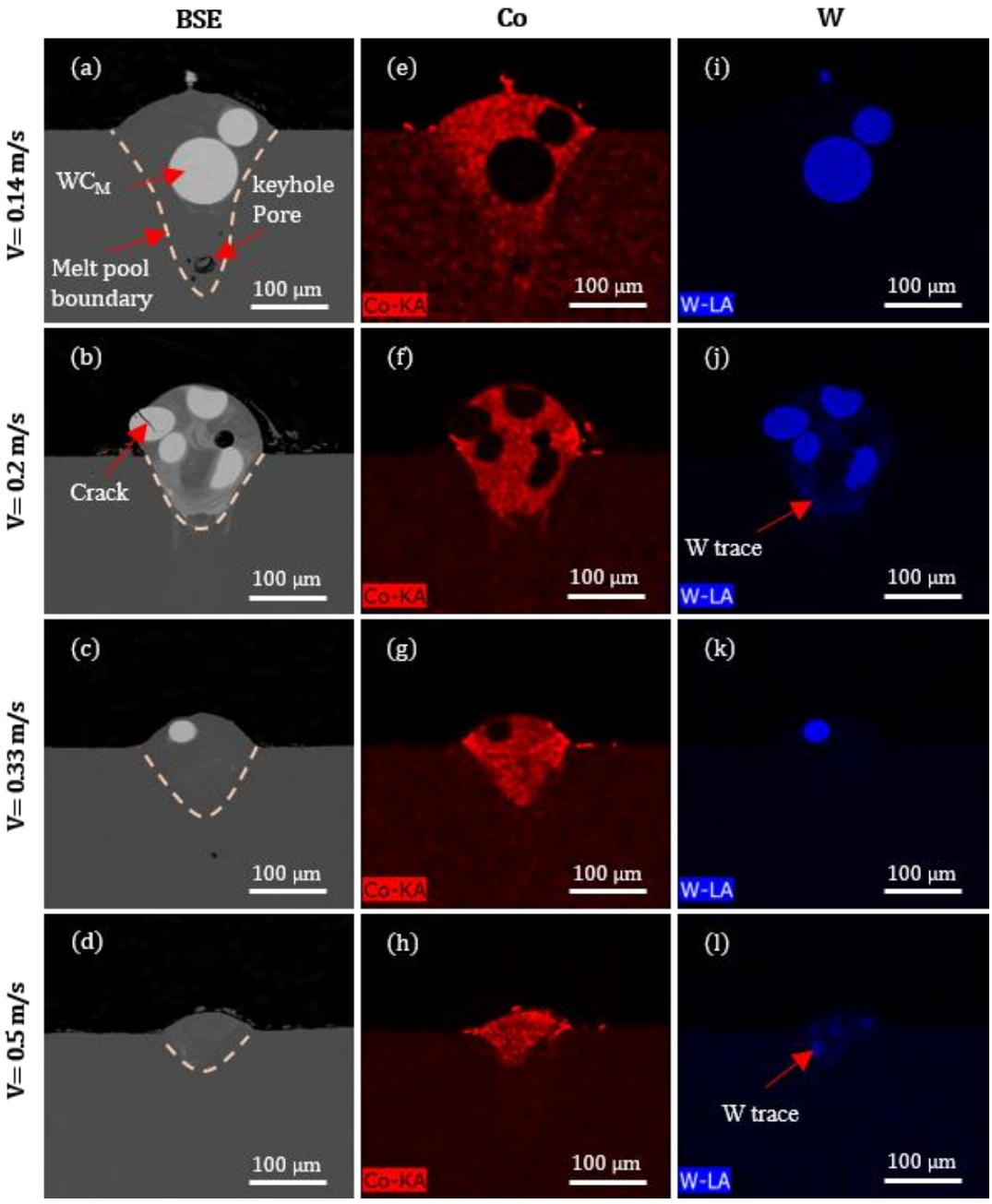

Figure 5.5: BSE images and EDX composition maps obtained from cross-sections of satellited WC_M-12 wt.% Co melt tracks for different laser scanning speeds. (a) – (d) BSE images for scanning speeds of 0.14, 0.2, 0.33, and 0.5 m/s, respectively. (e) – (h) EDX maps for Co at scanning speeds of 0.14, 0.2, 0.33, and 0.5 m/s, respectively. (i) – (h) EDX maps for W at scanning speeds of 0.14, 0.2, 0.33, and 0.5 m/s, respectively.

The variation of melt pool depth as a function of scanning speed value is illustrated in Figure 5.6. This shows that the increase of the scanning speed from 0.14 m/s to 0.5

m/s leads to a decrease of the melted depth from 245 ± 10 to 48 ± 20 µm. Moreover, it can be observed that the measured uncertainties are proportional to the increase of scanning speed. The morphological irregularities observed for scanning speed > 0.14 m/s are also reflected in the substantial variations of the measured melt pool depth along the tracks.

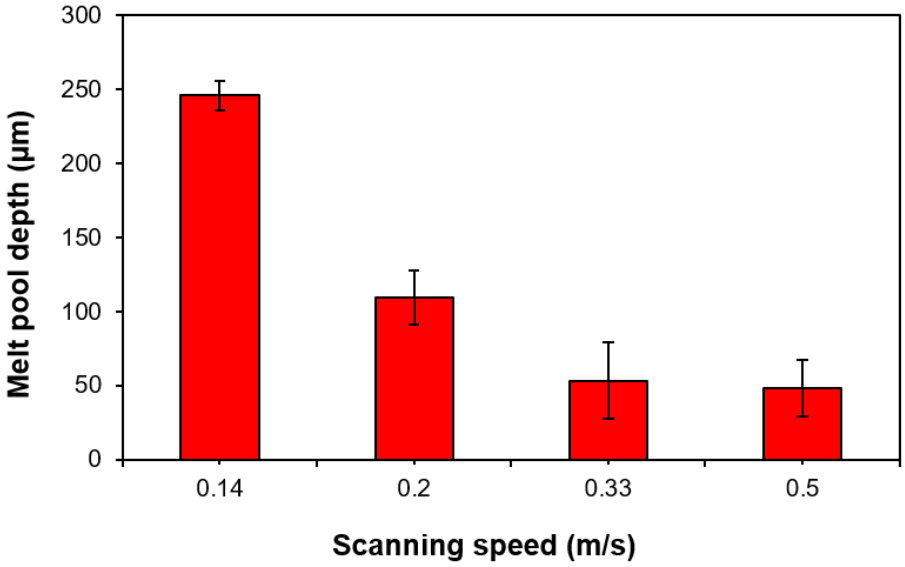

Figure 5.6: Bar chart showing the effect of laser scanning speed on melt pool depth of satellited WC_M-12 wt.% Co single tracks.

5.2.1.3. Single-layer components

Based on single tracks observations, the laser scanning speed which leads to continuous track without cracks is 0.14 m/s. The powder layer thickness is kept at 150 µm. The hatch distance between laser scans is taken as 120 µm. This gives an overlapping ratio of < 50% between adjacent melt pools. Three laser power values are employed: 100 W, 90 W, and 80 W.

5.2.1.3.1. Surface morphology

SEM topography of a single layer produced at 100 W is given in Figure 5.7. It shows a relatively smooth surface without balling, cracks, or gaps between adjacent tracks. Alternating laser directions are observed due to using the meander scanning strategy. The chevron pattern can be recognized in each single track within the consolidated layer. Spatter can also be observed. The layer thickness upon solidification is 48 ± 10 µm.

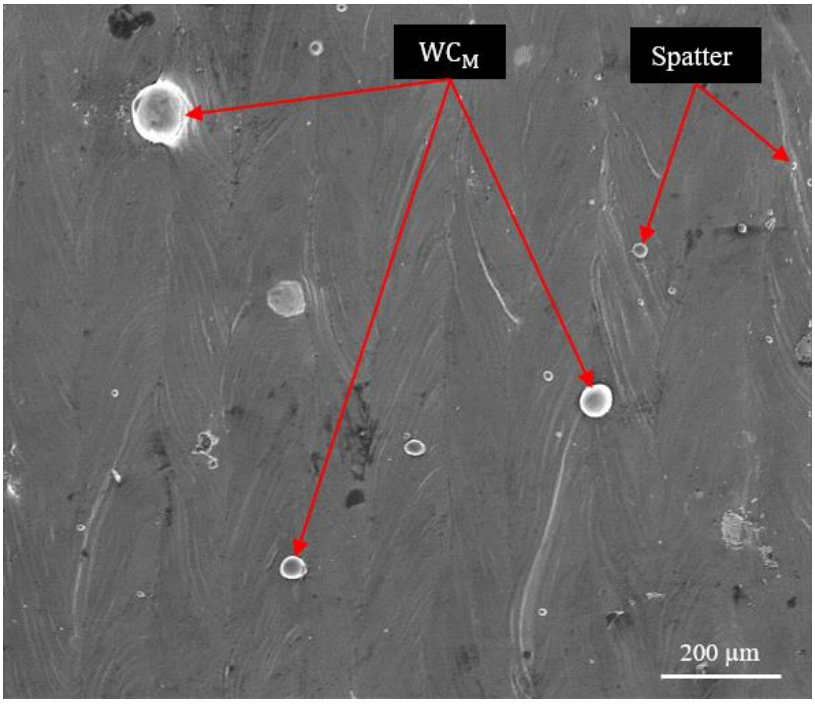

Figure 5.7: SEM/SE topography of satellited WC_M-12 wt.% Co single-layer component produced at a laser power of 100 W. The scanning speed, powder layer thickness, and hatch distance were kept at 0.14 m/s, 150 µm, and 120 µm, respectively.

The effect of reducing laser power to 90 W is given in Figure 5.8. It shows increasing spatter content and non-melted Co particles as compared to a single layer produced at 100 W. Sintered WC_M particles are noticed. No gaps between adjacent laser scans can

be seen. A sign of balling including crack is observed on the top surface. The measured layer thickness is 40 ± 15 µm.

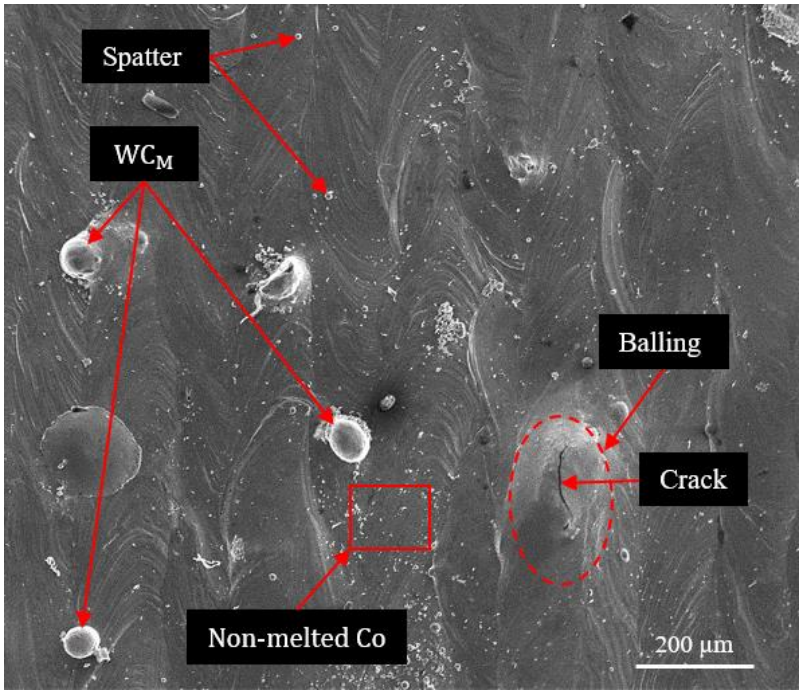

Figure 5.8: SEM/SE topography of satellited WC_M-12 wt.% Co single-layer component produced at a laser power of 90 W. The scanning speed, powder layer thickness, and hatch distance were kept at 0.14 m/s, 150 µm, and 120 µm, respectively.

A single-layer surface morphology produced at 80 W laser power is given in Figure 5.9. The laser scanned patterns in the steady state can be recognized. It shows no lack of fusion between neighboring tracks. However, the balling becomes dominant as compared to single-layer morphology at 90 W and 100 W. It has extended to about 480 µm on the surface. Nonetheless, the amount of non-melted Co powder on the solidified surface is highest as compared to single-layer components at 90 W and 100 W. The steady state layer thickness where no balling is 43 ± 11 µm.

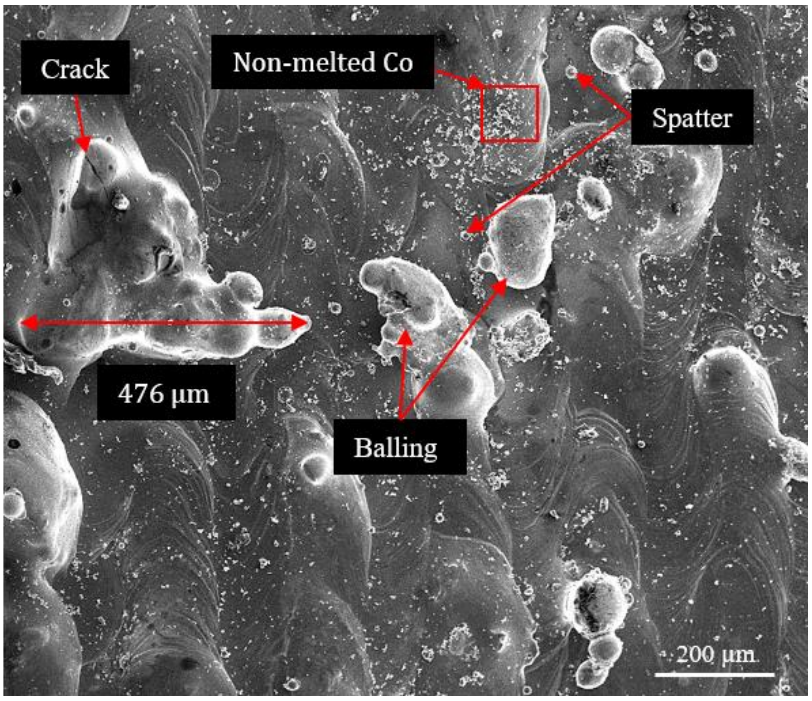

Figure 5.9: SEM/SE topography of satellited WC_M-12 wt.% Co single-layer component produced at a laser power of 80 W. The scanning speed, powder layer thickness, and hatch distance were kept at 0.14 m/s, 150 µm, and 120 µm, respectively.

5.2.1.3.2. Cross sections

BSE investigation of a single-layer cross section fabricated at 100 W laser power is shown in Figure 5.10. It shows full density with no signs of cracks or matrix pores as appeared in the low magnification (Figure 5.10a). The overlapping between adjacent melt pools is illustrated in the high magnification (Figure 5.10b). It shows a good metallurgical bonding where no lack of fusion or gaps between neighboring melt pools or between melt pools and the substrate. The WC_M particles have retained their original spherical morphology. The substrate melted depth is 203 ± 38 µm.

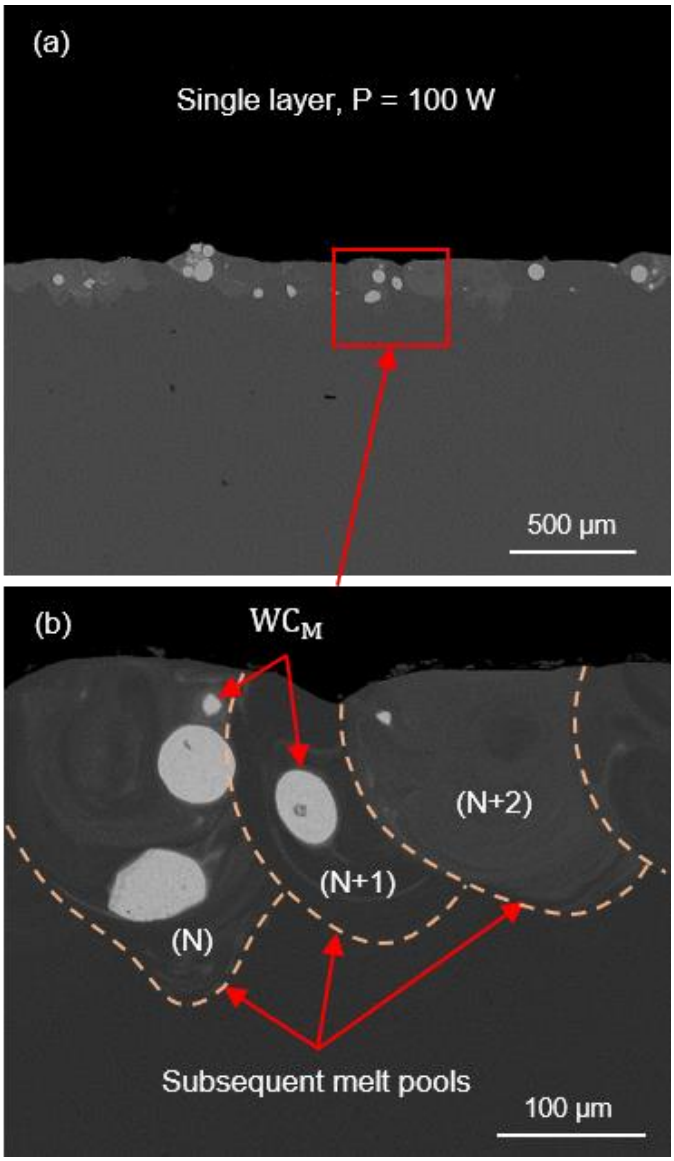

Figure 5.10: SEM/BSE images of a cross section of satellited WC_M-12 wt.% Co single-layer component produced at a laser power of 100 W. The scanning speed, powder layer thickness, and hatch distance were kept at 0.14 m/s, 150 µm, and 120 µm, respectively.

The cross section of single-layer component produced at 90 W laser power is given in Figure 5.11. Despite a decrease in laser powder to 90 W, some keyhole pores can be observed in the low magnification (Figure 5.11a). The substrate melted depth is 200 ± 35 µm which is comparable to that of a single layer at 100 W. The higher magnification (Figure 5.11b) shows a full density matrix with good metallurgical bonding between melt pools.

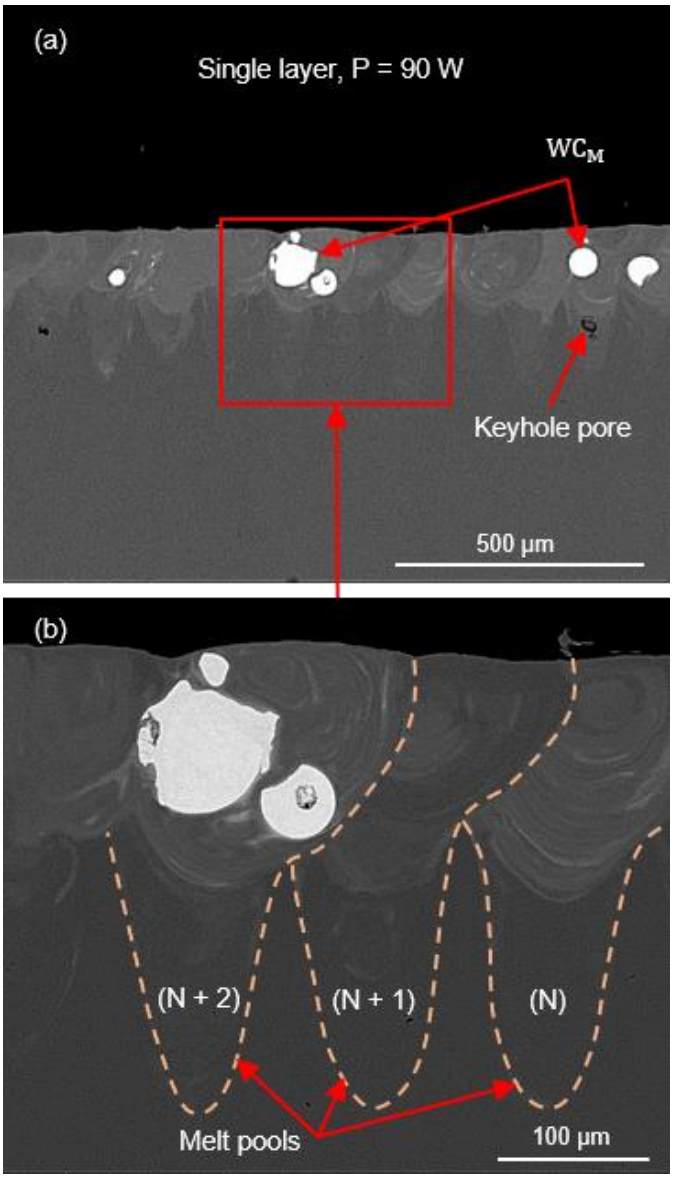

Figure 5.11: SEM/BSE images of a cross section of satellited WC_M-12 wt.% Co single-layer component produced at a laser power of 90 W. The scanning speed, powder layer thickness, and hatch distance were kept at 0.14 m/s, 150 µm, and 120 µm, respectively.

The single layer above revealed a keyhole melting mode defined when the melt pool depth is larger than its half width. The keyhole melting mode is a result of excessive energy input which can lead to high cracking propensity when multilayer components are to be fabricated. Thus, a further step by reducing the laser power to 80 W was also examined.

A single-layer cross section produced at 80 W laser power is given in Figure 5.12. The low magnification shows a good metallurgical bonding between adjacent melt pools as presented in Figure 5.12a. No lack of fusion between the deposited layer and the substrate can be detected. However, cracking can be observed. The substrate melted depth is 90 ± 32 μm which is lower than that of single layers produced at 90 W and 100 W. The high magnification reveals a difference in microstructures between balling above substrate surface and the lower part of melt (Figure 5.12b). It shows new formed feature A resulted from partial dissolving of WC_M particles (feature B). No such distinctive morphology can be noticed in the parts of melt pools conducted-to-substrate (feature C).

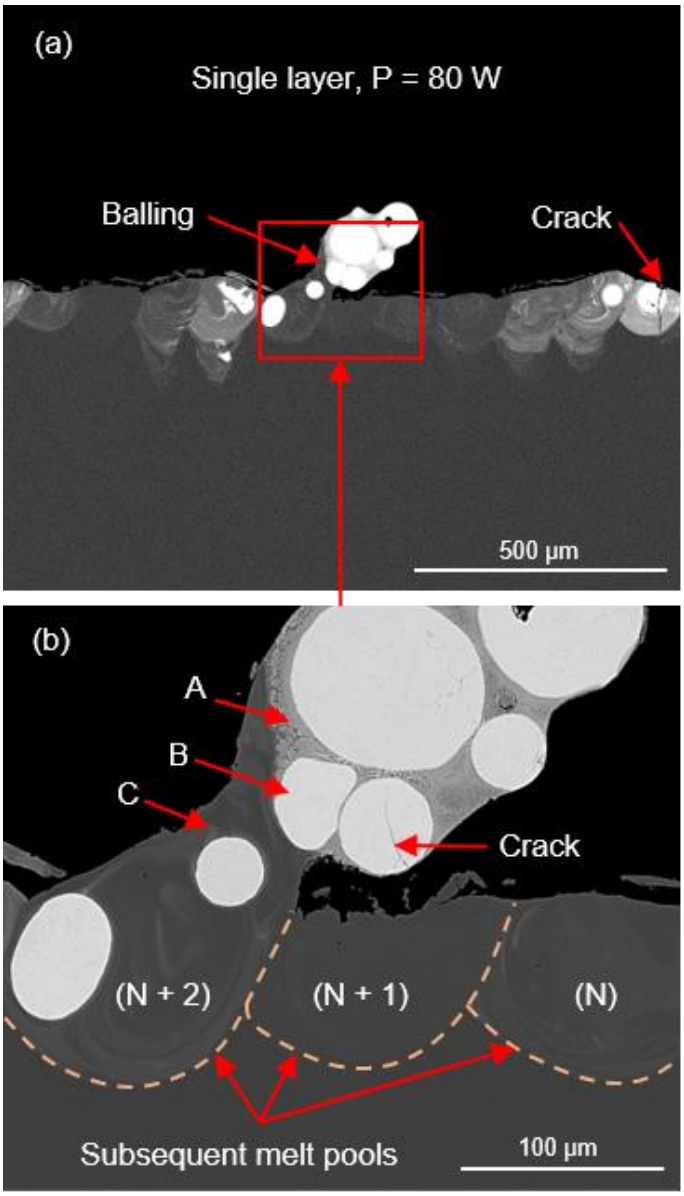

Figure 5.12: SEM/BSE images of a cross section of satellited WC_M-12 wt.% Co single-layer component produced at a laser power of 80 W. The scanning speed, powder layer thickness, and hatch distance were kept at 0.14 m/s, 150 µm, and 120 µm, respectively.

5.2.1.4. Two-layer components

5.2.1.4.1. Surface morphology

The surface morphology of two-layer component fabricated at 100 W laser power is shown in Figure 5.13. It reveals no signs of cracks or gaps between adjacent laser scans. A sintered WC_M particle can be observed. Non-melted Co particles are sintered

on the surface. The layer thickness is 100 ± 10 µm. The surface irregularity has increased by decreasing the laser power to 90 W (Figure 5.14). Balling can also be observed. The layer thickness is 94 ± 12 µm. Although the single-layer produced at 80 W laser power revealed balling formation (Figure 5.9), it is useful to study how this deterioration can affect the solidification behaviour of the next layer. The results show that balling has extended to form like a bridge on the second solidified surface at a further decreasing the laser power to 80 W (Figure 5.15). The maximum balling dimension has reached to 840 µm. However, the total layer thickness is 95 ± 18 µm representing the steady state solidification where no balling.

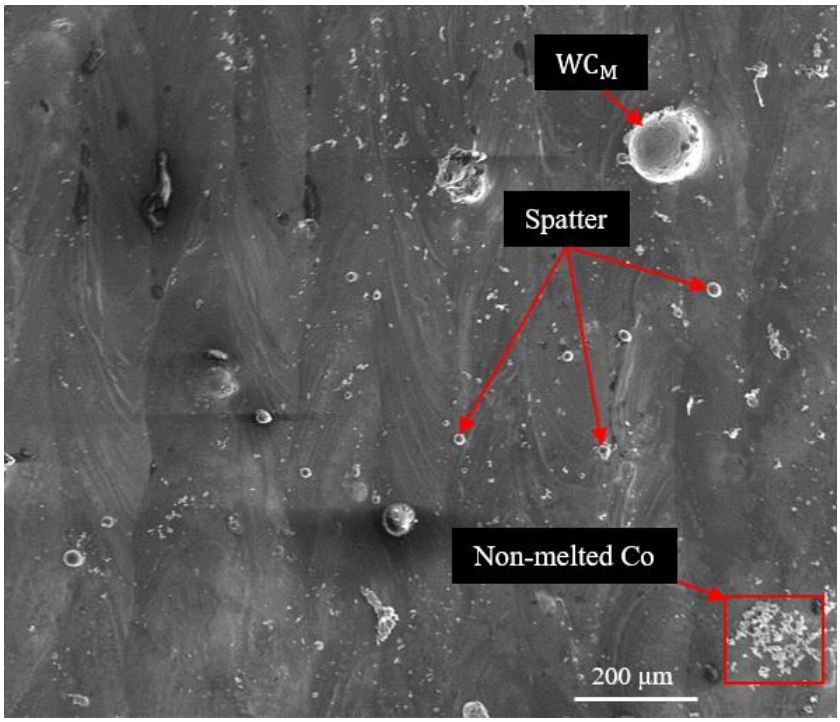

Figure 5.13: SEM/SE topography of satellited WC_M-12 wt.% Co two-layer component produced at laser power, scanning speed, powder layer thickness, and hatch distance of 100 W, 0.14 m/s, 150 µm, and 120 µm, respectively.

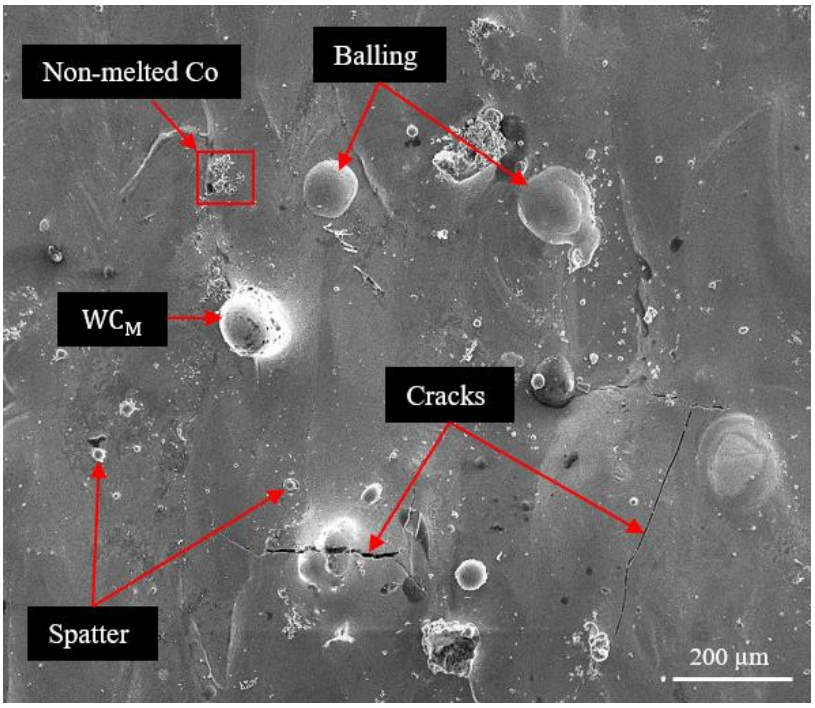

Figure 5.14: SEM/SE topography of satellited WC_M-12 wt.% Co two-layer component produced at laser power, scanning speed, powder layer thickness, and hatch distance of 90 W, 0.14 m/s, 150 µm, and 120 µm, respectively.

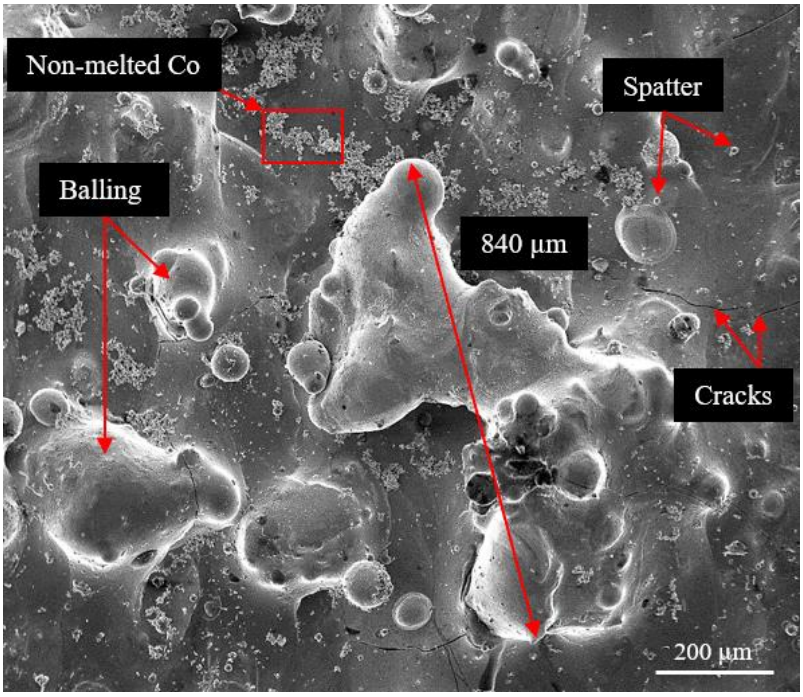

Figure 5.15: SEM/SE topography of satellited WC_M-12 wt.% Co two-layer component produced at laser power, scanning speed, powder layer thickness, and hatch distance of 80 W, 0.14 m/s, 150 µm, and 120 µm, respectively.

5.2.1.4.2. Cross sections

BSE investigation of a cross section of two-layer component produced at 100 W laser power is given in Figure 5.16. The low magnification shows dense solidification with no matrix pores or lack of fusion (Figure 5.16a). However, occasional keyhole pores and cracks are noticeable. A higher magnification shows that cracks are initiated in the areas where molten material overlaps and propagated downward through WC_M particles towards the bottom of the melt pools (Figure 5.16b).

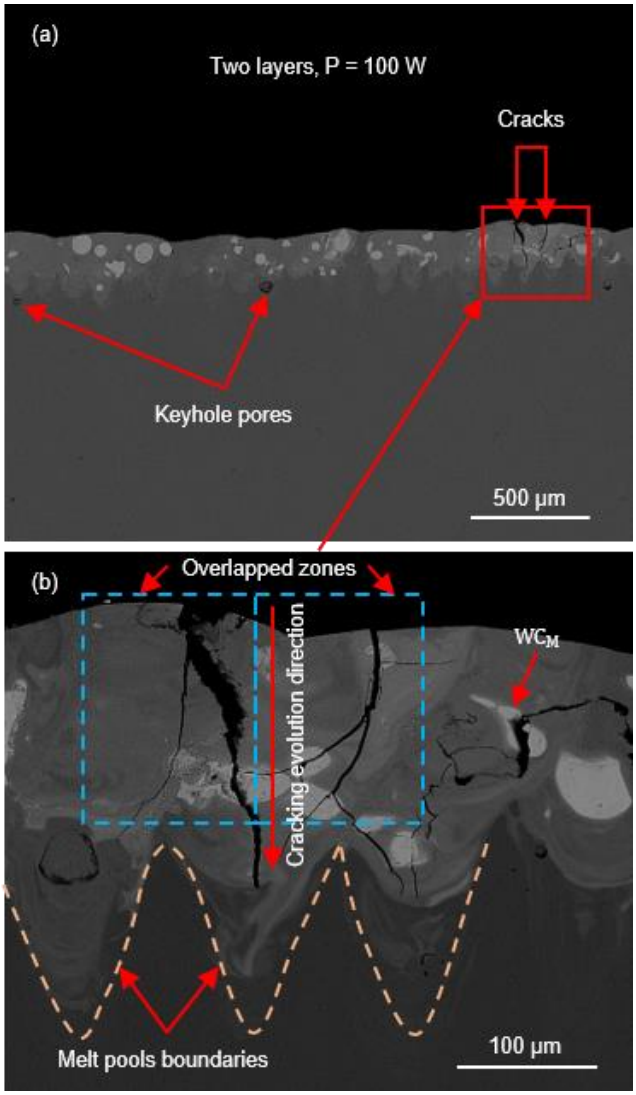

Figure 5.16: SEM/BSE images of a cross section of satellited WC_M-12 wt.% Co two-layer component produced at laser power, scanning speed, powder layer thickness, and hatch distance of 100 W, 0.14 m/s, 150 µm, and 120 µm, respectively.

BSE investigation of a cross section of two-layer component produced at 90 W laser power is given in Figure 5.17. It shows a full density material with a sign of crack (Figure 5.17a). The high magnification reveals good metallurgical bonding between melt pools within a layer and between the two layers as shown in Figure 5.17b. The melt pools in the 2nd layer are shallower as compared to 1st layer depositions. However, the current energy density can also produce cracking.

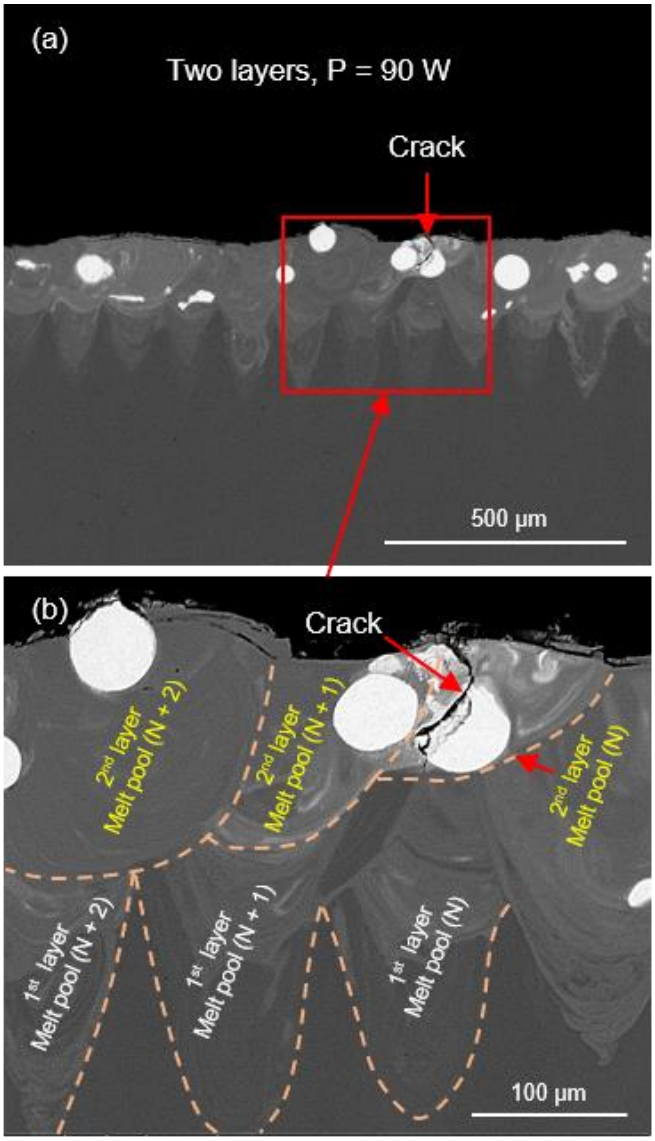

Figure 5.17: SEM/BSE images of a cross section of satellited WC_M-12 wt.% Co two-layer component produced at laser power, scanning speed, powder layer thickness, and hatch distance of 90 W, 0.14 m/s, 150 µm, and 120 µm, respectively.

BSE investigation of a cross section of two-layer component produced at 80 W laser power is given in Figure 5.18. The low magnification (Figure 5.18a) shows a full density with good metallurgical bonding between melt pools and no lack of fusion with the substrate. However, an uneven top surface including peaks and troughs is observed. The higher magnification demonstrates cracks through WC_M particles (Figure 5.18b).

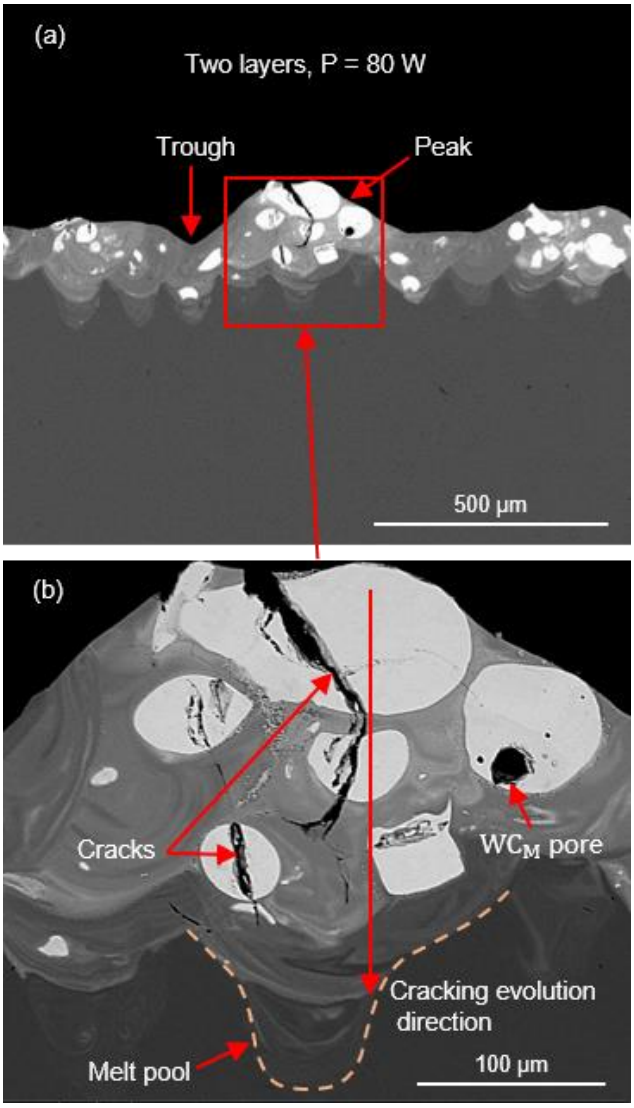

Figure 5.18: SEM/BSE images of a cross section of satellited WC_M-12 wt.% Co two-layer component produced at laser power, scanning speed, powder layer thickness, and hatch distance of 80 W, 0.14 m/s, 150 µm, and 120 µm, respectively.

5.2.1.5. Three-layer components

5.2.1.5.1. Surface morphology

The surface morphology of a three-layer component fabricated at 100 W laser power is given in Figure 5.19. The layer thickness is 157 ± 12 µm. It shows random dispersed cracks on the solidified surface. The effect of reducing the laser power to 90 W is presented in Figure 5.20. The cracks intensity is not reduced. Moreover, a relatively large balling size of 900 µm is formed. The steady state layer thickness is 144 ± 28 µm. The three-layer component fabricated at 80 W laser power is also analyzed (Figure 5.21) to systematically study the evolution of surface morphology. Besides cracks, it shows excessive balling extension which forms cave-like shape including a relatively large pore inside. The maximum balling dimension has reached to 1120 µm. Such irregularity complicates measuring of a representative layer thickness.

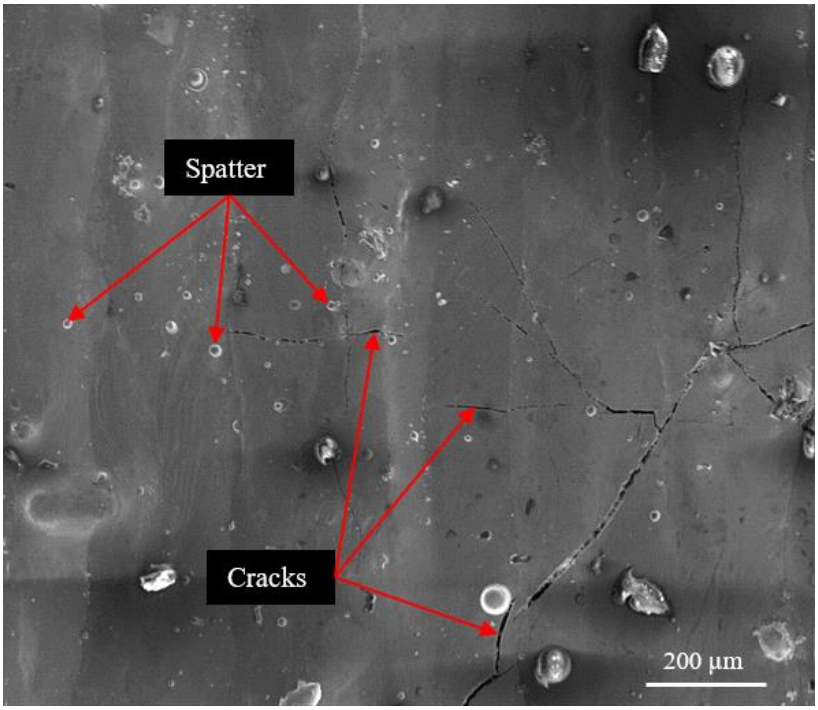

Figure 5.19: SEM/SE topography of satellited WC_M-12 wt.% Co three-layer component produced at a laser power of 100 W. The scanning speed, powder layer thickness, and hatch distance were kept at 0.14 m/s, 150 µm, and 120 µm, respectively.

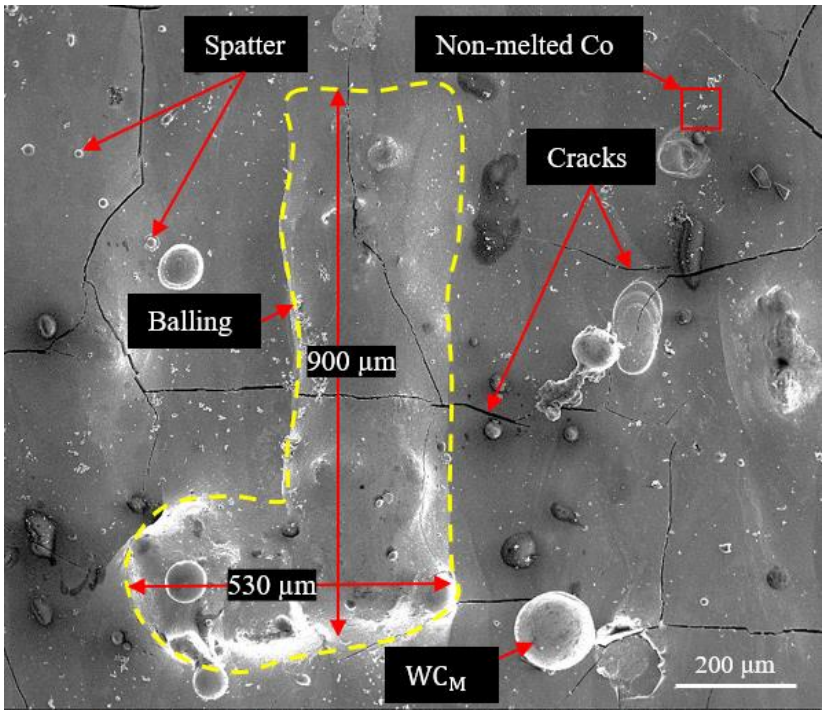

Figure 5.20: SEM/SE topography of satellited WC_M-12 wt.% Co three-layer component produced at a laser power of 90 W. The scanning speed, powder layer thickness, and hatch distance were kept at 0.14 m/s, 150 µm, and 120 µm, respectively.

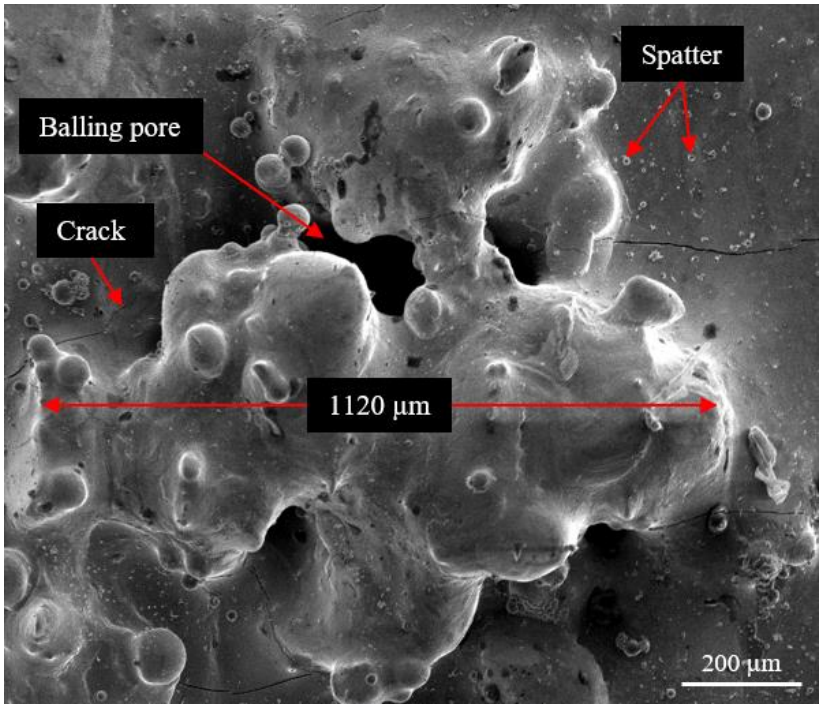

Figure 5.21: SEM/SE topography of satellited WC_M-12 wt.% Co three-layer component produced at a laser power of 80 W. The scanning speed, powder layer thickness, and hatch distance were kept at 0.14 m/s, 150 µm, and 120 µm, respectively.

5.2.1.5.2. Cross sections

Figure 5.22 presents a cross section of three-layer component produced at 100 W laser power. The low magnification shows a highly cracking intensity (Figure 5.22a). The cracking evolution starts from upper surface towards substrate as presented in the high magnification (Figure 5.22b). The cracks are in overlapping zone. Interestingly, it starts from a position where a WC_M particle is located and propagates though it into matrix toward the direction of the laser beam. The matrix also contains cracks which are not extended from the layer surface; even though, they keep the same downward evolution direction.

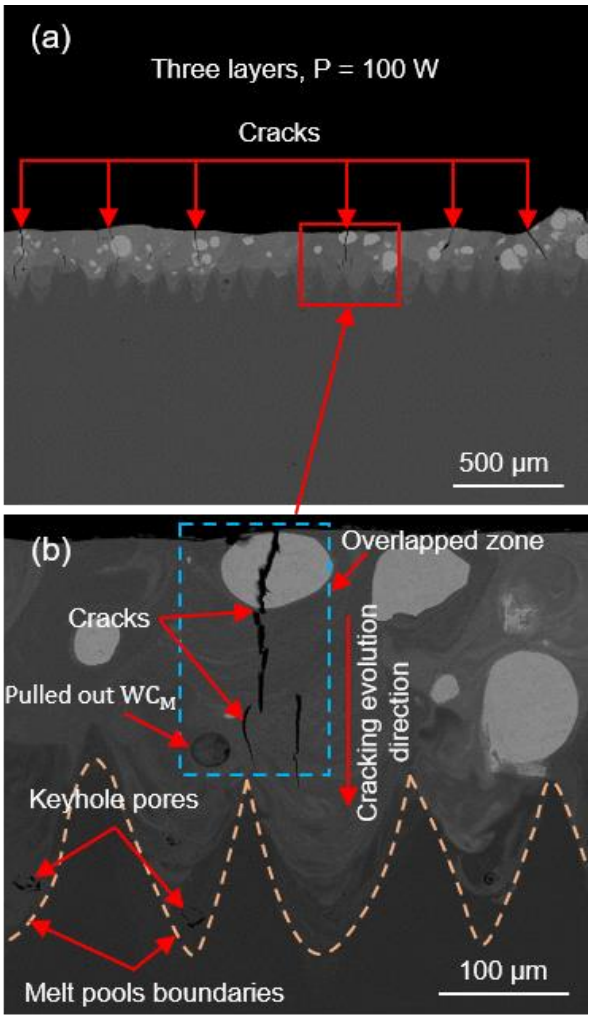

Figure 5.22: SEM/BSE images of a cross section of satellited WC_M-12 wt.% Co three-layer component produced at a laser power of 100 W. The scanning speed, powder layer thickness, and hatch distance were kept at 0.14 m/s, 150 µm, and 120 µm, respectively.

The cross section of a three-layer component produced at 90 W laser power is shown in Figure 5.23. It confirms the existing of keyhole pores as shown in the low magnification (Figure 5.23a). The WC_M particles in light colour contrast are distributed uniformly. Despite a high density, it reveals that the current energy density is enough to produce cracks. The high magnification reveals that cracks are generated in the overlapping zones between adjacent melt pools as presented in Figure 5.23b. The cracking evolution direction is always from the top surface towards the bottom of the melt pools.

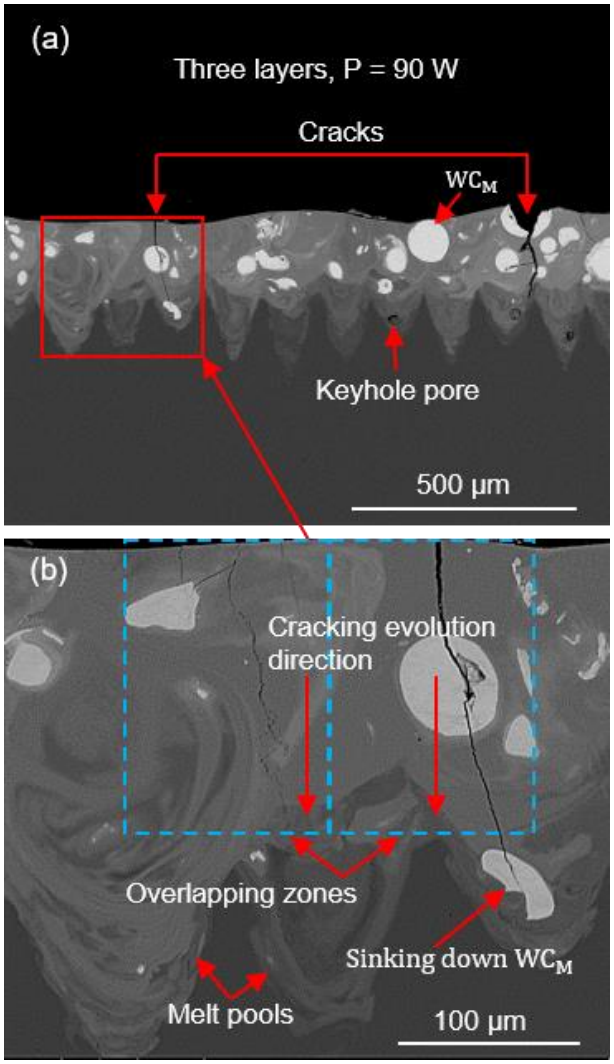

Figure 5.23: SEM/BSE images of a cross section of satellited WC_M-12 wt.% Co three-layer component produced at a laser power of 90 W. The scanning speed, powder layer thickness, and hatch distance were kept at 0.14 m/s, 150 µm, and 120 µm, respectively.

The cross section of a three-layer component produced at 80 W laser power is given in Figure 5.24. The low magnification (Figure 5.24a) shows a high fluctuation in layer thickness. The maximum difference exceeds 300 µm. Signs of pores and cracks are also observed. The higher magnification (Figure 5.24b) reveals two zones; upper zone showing a light colour contrast (feature 1) resulted from partial dissolution of spherical WC_M particles (feature 2) and lower zone where no such morphology can be observed. The matrix (dark contrast-feature 3) can be observed in both zones. The microstructure shows no lack of fusion with the substrate. However, cracks are dispersed randomly.

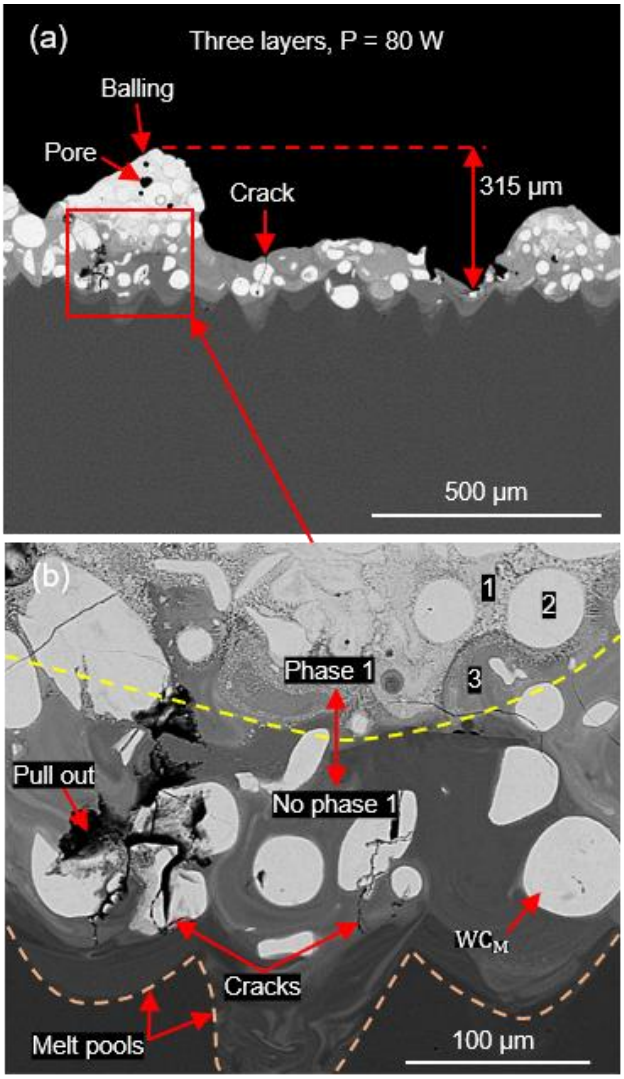

Figure 5.24: SEM/BSE images of a cross section of satellited WC_M-12 wt.% Co three-layer component produced at a laser power of 80 W. The scanning speed, powder layer thickness, and hatch distance were kept at 0.14 m/s, 150 µm, and 120 µm, respectively.

As a result, the satellited multilayer components reveal a clear cracking tendency. Increasing material ductility by increasing Co content can mitigate this problem. In addition, employing a feedstock of a smaller particle size allows using a lower layer thickness. This can increase the effectiveness of the laser beam to melt the powder and homogenize the temperature within a given layer and then reduce cracking. Moreover, the temperature homogeneity within the melt pool can be enhanced to a further degree of magnitude by using a L-PBF machine of larger laser spot size such as Renishaw AM 125. The potential impact of these aspects on the solidification behaviour of multilayer parts will be explained in the next section.

5.2.2. Laser-powder bed fusion of plasma densified WC-17 wt.% Co powder using Renishaw AM 125

To reduce cracking propensity, plasma densified WC-17 wt.% Co powder was used which has a higher Co content (to enhance material ductility) and smaller particle size as compared to those of the satellited powder. On the other hand, Renishaw AM 125 was employed which has a laser spot size of 3.4 times that of the Realizer SLM-50. Moreover, the powder layer thickness was 1/5th that used in the satellited experiments. The above aspects can enhance the effectiveness of the laser beam to melt the powder and homogenize the temperature within the given powder layer which can reduce possibly residual stresses and then cracks. The examining starts with defining a theoretical melt pool size that can effectively accommodate the powder particles considering their maximum size. This provides a set of laser power and scanning speed that can be used as a starting point in the experiments. Then, the values of laser power and scanning speed are expanded systematically in a process window to show the solidification behaviour.

5.2.2.1. Theoretical melt pool size

The theoretical melt pool size of plasma densified WC-17 wt.% Co powder using Rosenthal equation is presented in Figure 5.25. The laser power and scanning speed are 120 W and 0.6 m/s, respectively. The MATLAB solution code is given in Appendix E – section E.3. The melt pool length and width are 183 µm and 164 µm, respectively. The estimated width is more than 3.6 times that of the maximum powder particle size (45 µm) as provided by the manufacturer. This indicates the effectiveness of the melt pool, within the current process parameters, to accommodate the powder particles. Considering a half of the width, it gives a melted depth of 82 µm.

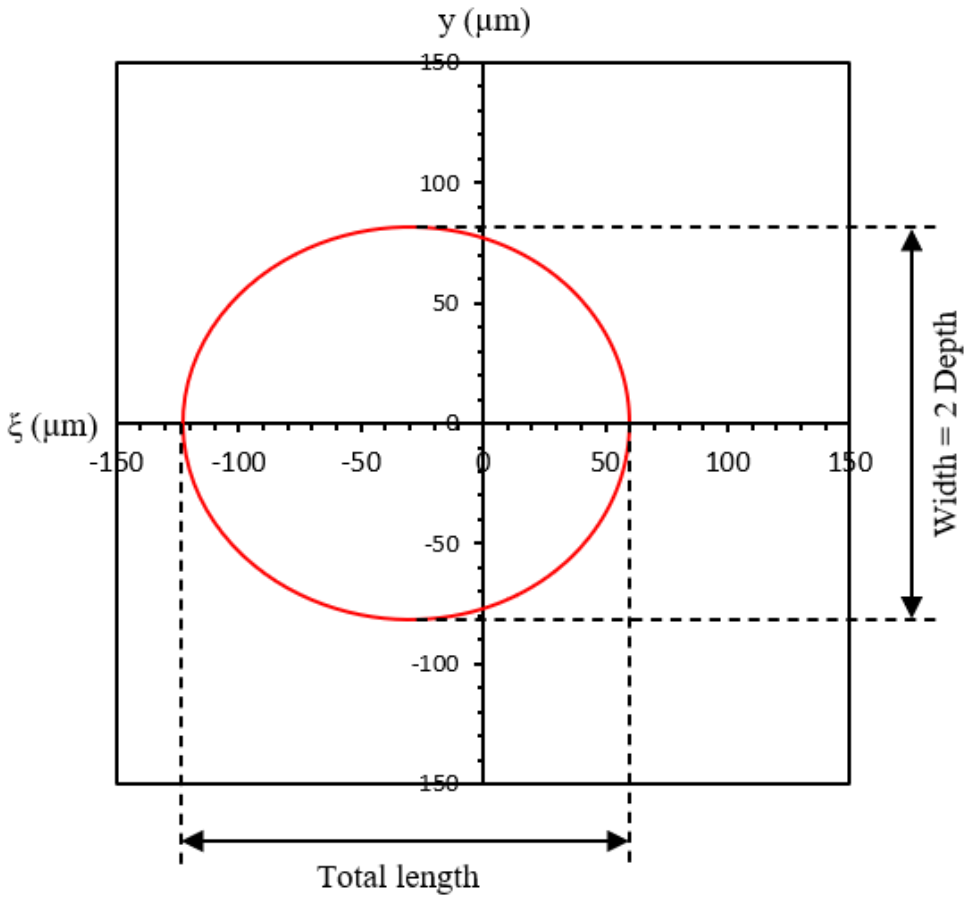

Figure 5.25: Theoretical melt pool dimensions of plasma densified WC-17 wt.% Co powder using Rosenthal equation at laser power and scanning speed of 120 W and 0.6 m/s, respectively.

5.2.2.2. Wall topography

Continuous walls with a relatively uniform width can be fabricated at laser power and scanning speed of 120 W and 0.6 m/s, respectively, as presented in Figure 5.26a. The wall width is 252 ± 8 µm. However, it has irregular surface morphology (Figure 5.26b). The higher magnification (Figure 5.26c) reveals sintered powder particles on surface and along wall edges. Pores can also be observed on wall surface.

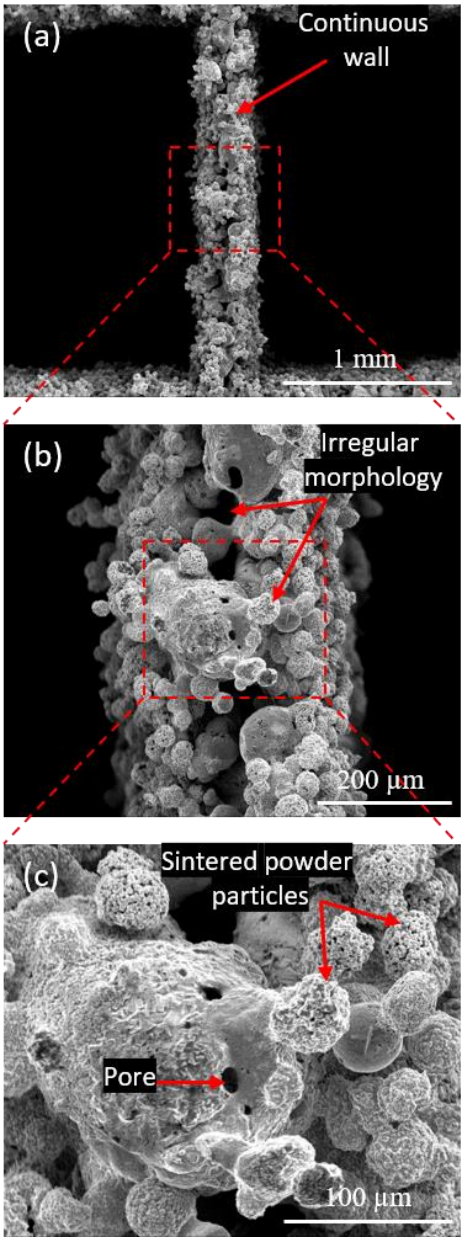

Figure 5.26: SEM/SE topography of a continuous wall fabricated by L-PBF using plasma densified WC-17 wt.% Co powder at laser power and scanning speed of 120 W and 0.6 m/s, respectively.

5.2.2.3. Process window to produce cubic samples

5.2.2.3.1. As-built samples

The effects of laser power and scanning speed on morphology of as-built cubic samples are given in Figure 5.27. The side dimension is 10 mm. The bottom sides are presented. Uniform cubic sample without distortion or delamination is produced at lower P and V of 100 W and 500 mm/s, respectively, (Figure 5.27a). Increasing P to 120 W results in a distortion in bottom of the sample (Figure 5.27b). This can also be observed at 140 W and 160 W-although V has increased to 600 mm/s (Figure 5.27c, d). Uniform sample without bottom deformation is obtained at P and V of 120 W and 600 mm/s, respectively, (Figure 5.27e). Similar morphology is observed at relatively lower energy inputs (Figure 5.27f-i). Bottom deformation can also be compensated by using stronger supports.

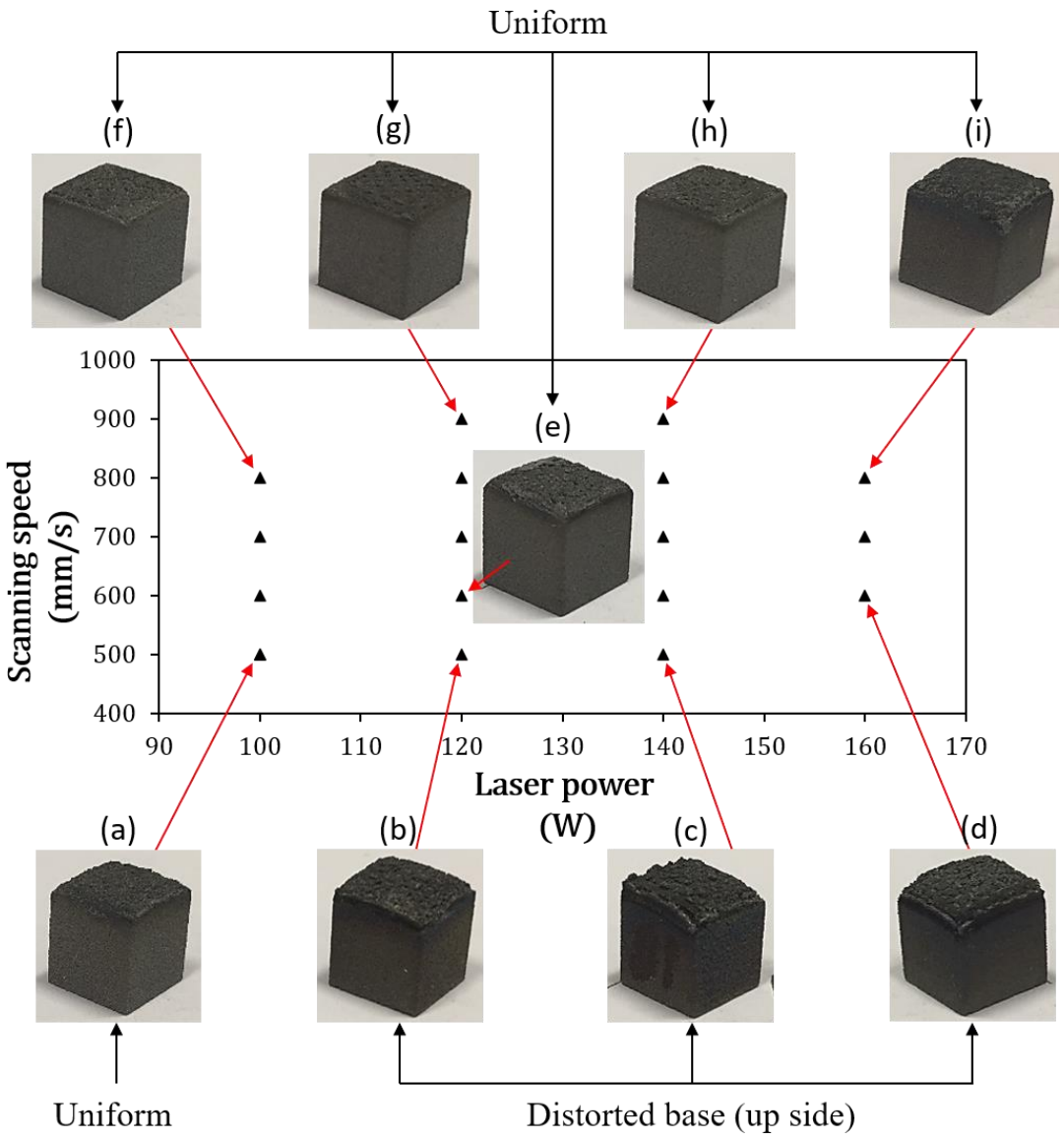

Figure 5.27: Process window and morphology of as-built cubic samples produced at laser power and scanning speed ranges of (100 – 160 W) and (500 – 900 mm/s), respectively, from plasma densified WC-17 wt.% Co powder.

5.2.2.3.2. Surface morphology

The low magnifications of as-laser-scanned surfaces are presented in Figure 5.28. It shows irregular topography and open pores within the surface at lower P and V of 100 W and 500 mm/s, respectively, (Figure 5.28a). Increasing P decreases the irregularities gradually giving a relatively smoother and less open pores morphology at 120 W and

140 W (Figure 5.28b, c). Despite of a relatively higher P of 160 W, increasing V to 600 mm/s increases surface irregularity (Figure 5.28d). The open pores and irregularities increase significantly by increasing V to ≥ 800 mm/s where comparable morphologies can be observed when P = 100 – 140 W (Figure 5.28e-g). In comparison, a slight enhance can be observed by increasing P to 160 W (Figure 5.28h).

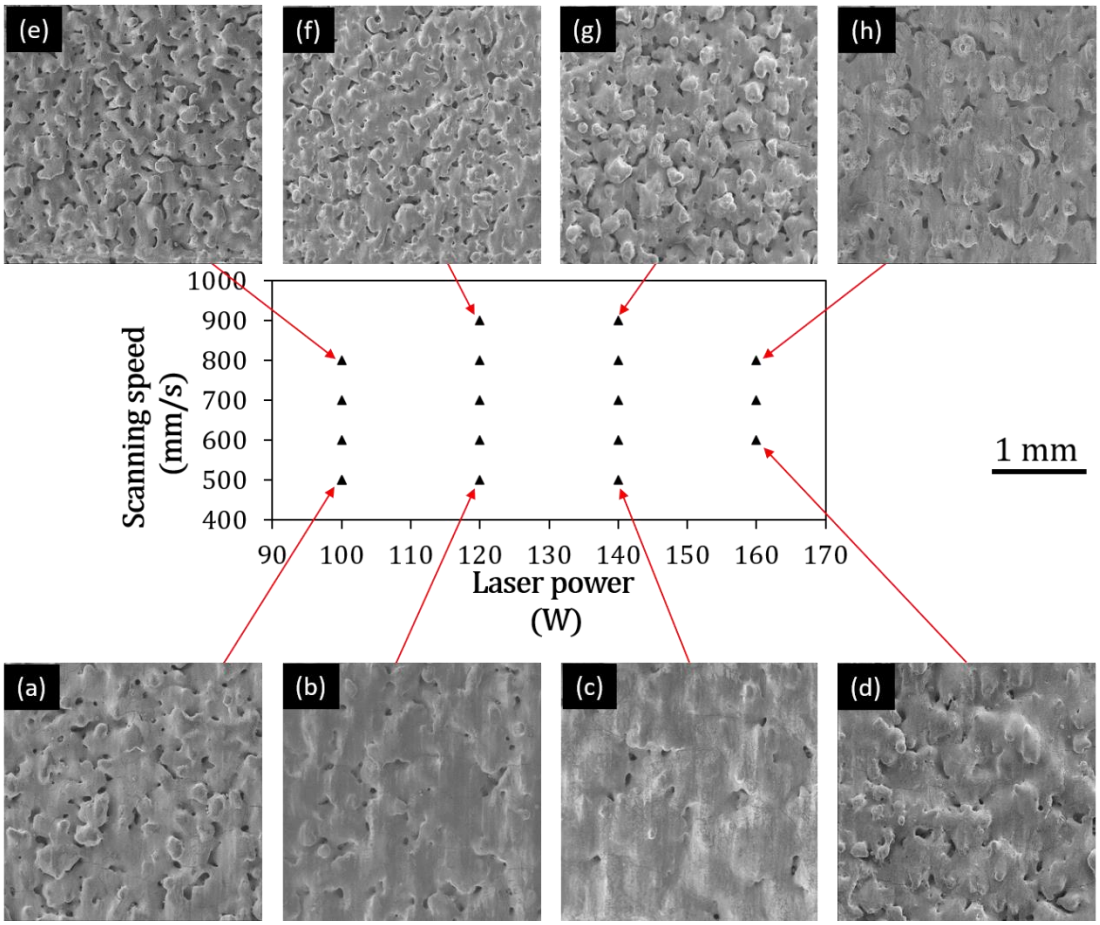

Figure 5.28: Process window and low magnifications SEM topography of the as-built cubic samples produced at laser power and scanning speed ranges of (100 – 160 W) and (500 – 900 mm/s), respectively, from plasma densified WC-17 wt.% Co powder.

High magnifications of surface morphology at P and V ranges of (120 – 140 W) and (500 – 800 mm/s), respectively, are presented in Figure 5.29. It shows that all samples

contain microcracks which are dispersed randomly on the solidified surfaces. The pores are irregular and become dominant at low energy densities represented by a low P (for all Vs) and high V of 800 mm/s (regardless P values). Non melted powder particles can be observed within these pores. Comparable results are noticed at P of 120 W and 140 W when V increases from 500 – 700 mm/s.

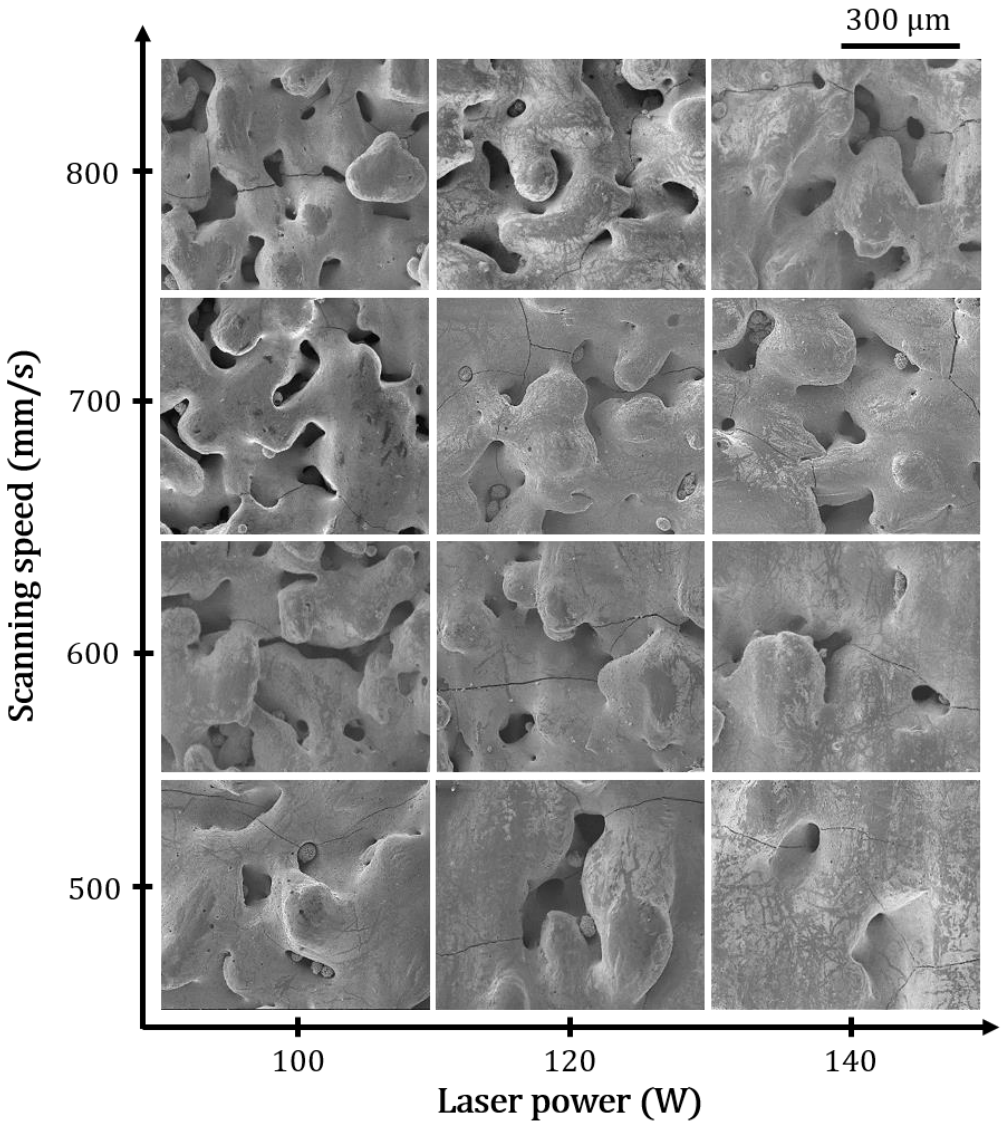

Figure 5.29: Cracks observed in high magnifications SEM topography of cubic samples produced at laser power and scanning speed ranges of (100 – 140 W) and (500 – 800 mm/s), respectively, from plasma densified WC-17 wt.% Co powder.

5.2.2.3.3. Microstructure

Optical microscopic investigation of a cross section produced at P and V of 120 W and 600 mm/s, respectively, is presented in Figure 5.30. It shows three main features: macro-pores, micro-pores, and cracks. The size of individual macro-pore can exceed 400 µm. The micro-pores are densely dispersed all over the section area. The resulted material density is < 90%. The cracks propagate continuously to > 1420 µm in a random way.

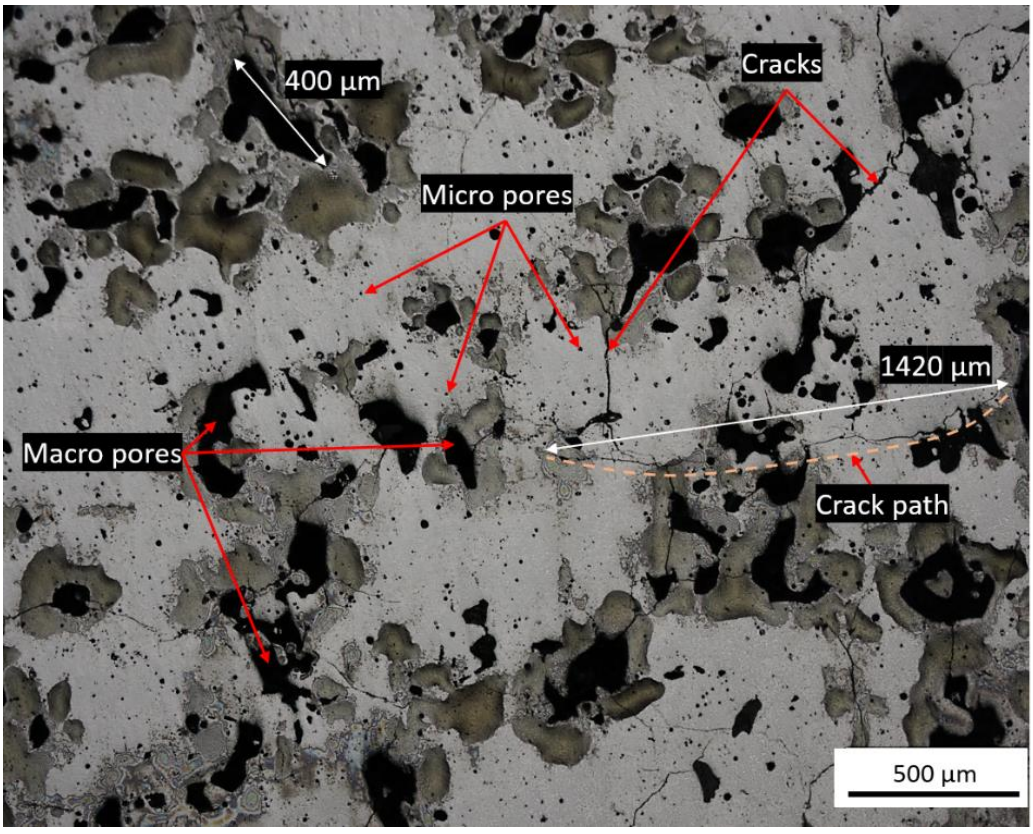

Figure 5.30: Optical microscopic investigation of a cross section of cubic sample produced at laser power and scanning speed of 120 W and 600 mm/s, respectively, from plasma densified WC-17 wt.% Co powder.

XRD spectra of the powder and L-PBF sample are presented in Figure 5.31. Two phases appear in the powder; WC (hcp) and Co (fcc) (Figure 5.31a). It shows a high concentration of WC (hcp) which can be inferred from intensity of the highest peaks. The L-PBF sample reveals no residual free Co (fcc) (Figure 5.31b). It shows new phases formed; W_2C (hcp) and Co_6W_6C (fcc). The intensity of W_2C (hcp) is higher than that of WC (hcp). The ICDD files and XRD patterns are given in Appendix D – sections D.3 and D.4, respectively.

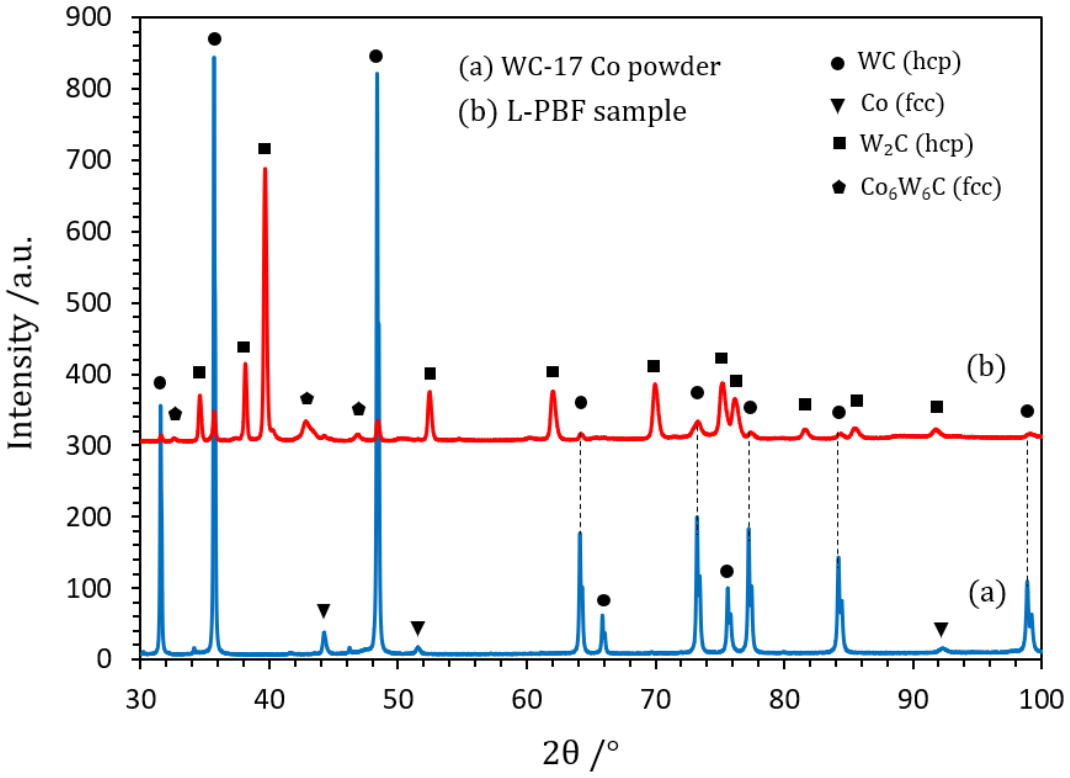

Figure 5.31: XRD spectra of (a) plasma densified WC-17 wt.% Co powder, and (b) cubic sample produced at laser power and scanning speed of 120 W and 600 mm/s, respectively.

BSE investigations are given in Figure 5.32a, b. It shows a uniform distribution of grains where no segregations can be observed in the low magnification (Figure 5.32a). The high magnification (Figure 5.32b) reveals three main features; 1 which represents irregular blocks and triangular prism shapes containing pores, 2 which also contains

white spots (as shown in the right top BSE image), and 3 in the dark contrast zone. The blocks and prism shapes are in micron and sub-micron sizes. The dark zone also includes a cellular structure in light contrast.

EDX mapping for elements of atomic number greater than 6 (i.e. mapping of C is excluded) is presented in Figure 5.32c, d. It reveals that feature 1 is richer in W followed by feature 2 and there is a weak concentration in feature 3 as shown in Figure 5.32c. While Co has a higher concentration in feature 3 followed by feature 2 and there is no Co apparent in feature 1 (Figure 5.32d).

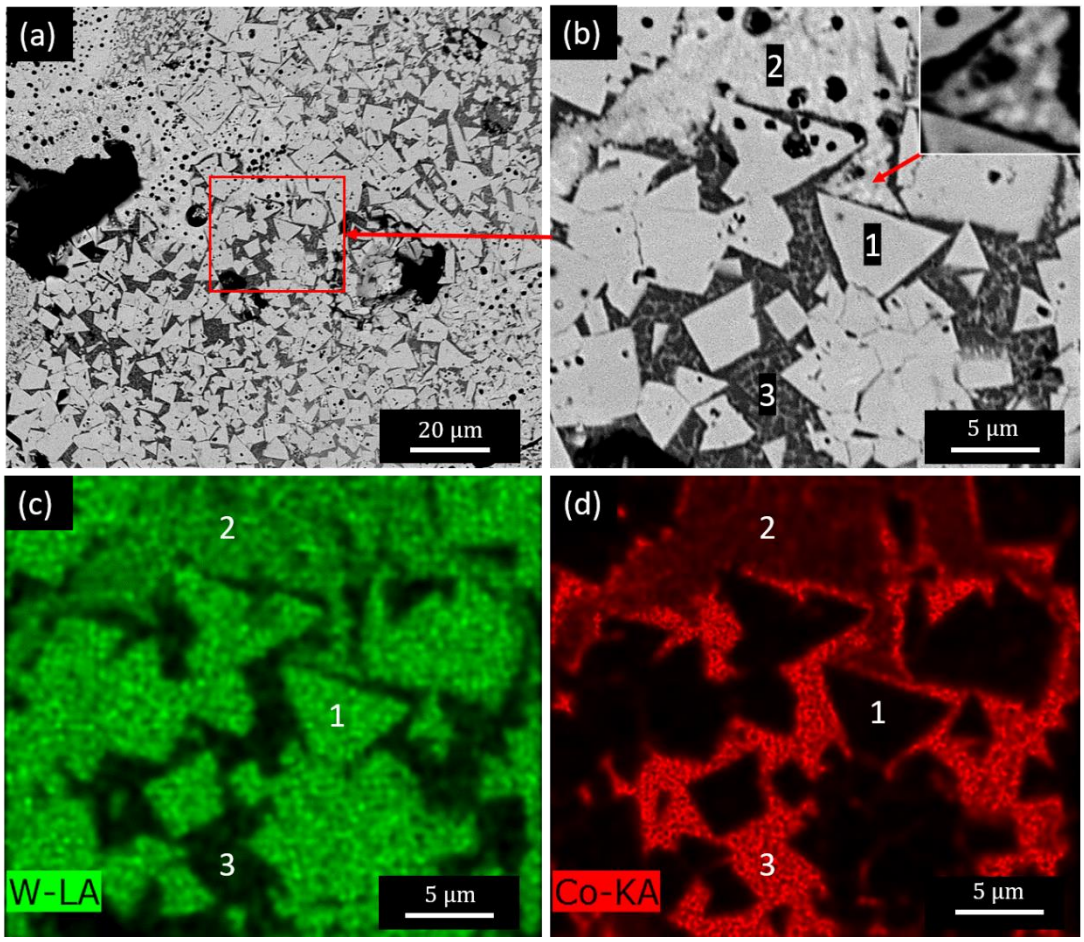

Figure 5.32: BSE investigation of a cross section of WC-17 wt.% Co cubic sample produced at laser power and scanning speed of 120 W and 600 mm/s, respectively (a), with higher magnification (b), and EDX mapping for W (c) and Co (d).

The compositions of the features 1 – 3 determined by EDX spot analysis are given in Table 5.1 where in this case C has been included in the analysis. Weak X-ray signals emitted from the light elements make them difficult to measure reliably. In addition, EDX cannot resolve the composition of features less than 2 – 3 μm, so X-ray signals emitted from surrounded features can also be detected. However, the results can represent the composition trend. It shows that feature 1 is richer in W and C with a lower Co content as compared to the other features. This indicates that feature 1 is the WC phase.

Table 5.1: EDX chemical compositions of the microstructural features in Figure 5.32b showing the trend of content of W (↓), C (↓), and Co (↑) elements by gradual transferring from feature 1 to feature 3.

Element	Feature and content (wt.%)		
	1	2	3
W	92.9 ± 0.2	78.7 ± 1.6	35.2 ± 2.9
C	4.6 ± 0.4	3.4 ± 0.2	2.7 ± 0.1
Co	2.4 ± 0.1	17.8 ± 1.7	62.1 ± 3

5.3. Discussion

In this chapter, two powders were used in two different L-PBF machines; satelliting WC_M-12 wt.% Co powder processed in Realizer SLM-50, and plasma densified WC-17 wt.% Co powder processed in Renishaw AM 125. Uniform single tracks and single layers without cracks were produced from the satellited powder and uniform cubic samples without distortions were produced from the plasma densified powder. However, all multilayer components produced from both powders revealed cracking tendency.

The discussion includes three main sections. Firstly, the effect of energy density on the solidification behaviour of the satellited and plasma densified components is analysed. The second section shows the mechanisms of cracking formation in L-PBF parts. The reliability of using the Rosenthal model to predict the melt pool size in L-PBF field is explained in the third section. Nonetheless, the potential effect of WC-Co mixture design on the solidification behaviour is also discussed.

5.3.1. Evolution of the satellited WC_M-12 wt.% Co track morphologies as a function of laser scanning speed

The objective was to produce a uniform track morphology free from cracking and porosity. This presented several challenges due to the large particle size distribution of the feedstock. In the first place, the physical size of the individual particles affected significantly the material melting during laser processing. It is well known that when the laser scans over the applied powder bed, energy is absorbed by the surface of individual particles [147]. This leads to an increase of the temperature of particle surface before heat can penetrate to the centre of powder. By taking into consideration the thermal conductivity and melting point of WC_M (84 W/m/K and 2687 °C), Co (100 W/m/K and 1495 °C), and steel (68 W/m/K and 1435 °C), respectively [83], the location of the Co fine particles (which decorate WC_M), and the difference in physical size, it is likely that Co powder and the surface of steel substrate started to melt first to form the molten pool. Molten Co then reacted with larger WC_M particles as demonstrated by the partial undesirable dissolution of WC_M observed in the tracks for lower scanning speeds (Figure 5.5j, l).

The large particle size distribution of the satellited feedstock imposed the necessity to use an unconventional layer thickness of 150 µm (most of the L-PBF equipment is typically using a layer thickness of 30 – 50 µm). This, combined with the low thermal

conductivity of the feedstock, required a relatively long laser dwelling time to accommodate and homogenize the temperature of Co within a given layer thickness. Longer dwell time enables laser to penetrate deeper resulting in keyhole melting mode where the depth of melt pool is larger than its half width. A common way to describe the combined effect of process parameters on the material densification during L-PBF processing is expressed by the volumetric energy density (VED) as given in Eq.6.1 [148]:

$$VED = P/vdt \qquad [J/mm^3] \qquad (6.1)$$

where P is the laser power (W), v, d, and t are the laser scanning speed (mm/s), laser beam diameter (mm), and applied layer thickness (mm), respectively. In this study the applied VED ranged between 60 and 215 J/mm^3 – figures comparable or higher to the processing of other structural alloys in the same L-PBF platform. However, the energy density of additively manufactured WC-Co has been often calculated using the hatch distance (distance between two adjacent tracks) instead of laser beam diameter in the above equation [90, 91].

A schematic representation of the effect of scanning speed on the evolution of melt pool geometry from current results is shown in Figure 5.33. Within the range of experimental parameters investigated, it was noted that the width and the depth of the tracks varies significantly with the laser scanning speed (widest tracks and highest penetration depths are observed for lowest laser scanning speeds). While no definite trends can be evinced regarding the track height.

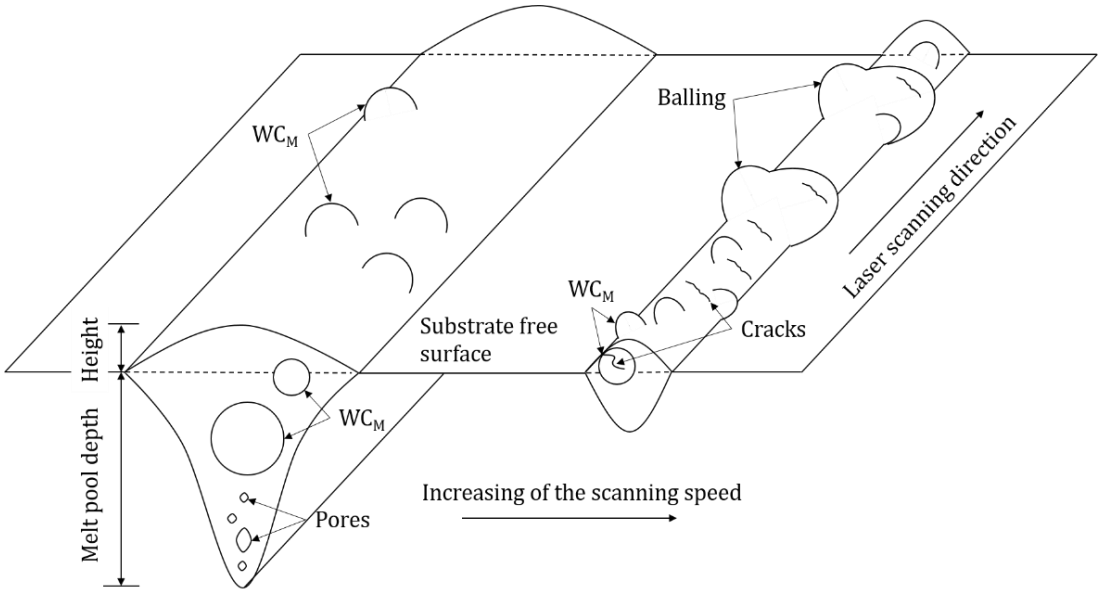

Figure 5.33: Schematic representation of the effect of scanning speed on the solidification of satellited WC_M-12 wt.% Co single tracks.

Particular attention was dedicated to the analysis of the material accumulation along the track sides – in the present investigation in the form of balling and sintered particles – as this can impose severe barriers to the fabrication of successful components in 3D. Except for the tracks produced at a laser scanning speed of 0.14 m/s, extensive balling was observed along the track edges. Balling results as a consequence of capillary instability of the melt pool [148]. According to Rayleigh-Plateau criteria, balling can be modelled as a cylindrical volume of liquid, with a length (l) and a diameter (d), on the substrate. The instability condition of such a free cylinder is satisfied when its harmonic disturbances have wavelengths comparable to l, or $l/d > \pi$. Under this condition, the cylinder minimizes its surface energy by breaking into droplets. As observed in Figure 5.4, the increase of laser scanning speed produced higher values of the L/D elongation ratio and therefore supported the break-up of the melt pool into large spherical deposits.

Sintered WC_M particles were also occasionally found outside the tracks' surfaces. From a practical point of view, sintered WC_M particles have the same deleterious influence associated to balling as they limit the spreading of powders in successive layers and might encourage melt pool break-up during deposition of continuous tracks. The analysis of the tracks suggested that less substrate interactions due to increasing the scanning speed values leads, at least qualitatively, to higher sensitivity to cracking (Figure 5.2d, h). An increase in the laser scanning speed might lead to higher cooling rates and temperature gradients resulting in high residual thermal stresses [149].

Finally, it is noteworthy that the track height for the most uniform track morphology produced at a scanning speed of 0.14 m/s was 40 $\pm$ 5 µm, as shown in Figure 5.3, which gives a ratio of ~0.27 with respect to the applied layer thickness of 150 µm. This indicates a low packing density of the feedstock, as compared to a ratio up to 0.8 for 316L stainless steel powder [148]. It implies that the next spreading powder layer will be increased by 73% above the nominal layer thickness, thus, indicating an actual layer thickness of 260 µm. This can lead to different solidification behaviour where the delivered energy is less effective to melt the powder and homogenize the temperature within such layer thickness. As a result, balling and discontinuities in the formed tracks are expected which can reduce the bulk density when a multi-layered component is to be fabricated.

5.3.2. Melting regimes of satellited WC_M-12 wt.% Co single tracks

The substrate penetration depth depends strongly on the laser scanning speed as shown in Figure 5.6. It is useful to classify the melting behaviour observed in the tracks according to two melting regimes defined in the literature: conduction mode melting, for which the penetration depth (D_m) is approximately equal to half of melt pool width W_p (e.g. $D_m/0.5W_m \leq 1$), and keyhole mode melting for which $D_m/0.5W_m > 1$ [150].

As shown in Figure 5.34, for high values of VED (> 150 J/mm³) keyhole mode melting is observed. Interestingly, this is a suitable condition to produce continuous tracks.

This research has revealed several challenges related to the laser melting of the satelliting feedstock exhibiting a large particle size distribution. Firstly, to melt a relatively thick powder bed, long laser exposures are required. In the present investigation, continuous tracks are only formed by reaching a key-hole mode melting regime, where porosity and melt pool dynamics are however difficult to predict and control. A possible solution to minimize key-holing might be that of using a laser of higher power and larger spot size to directly increase the melt pool width. Secondly, during the laser exposure, regardless of the parameters used, given the marked particle size difference, the fine Co particles are likely to melt first with only partial dissolution of WC_M. Although the preservation of WC_M might be beneficial from a microstructural point of view, large WC_M are impractical for successful spreading of subsequent layers of the powders and homogenous melting. It is noteworthy the positive effect of a ductile substrate, that form a ductile matrix resistant to crack formation for most of the processing conditions explored in this investigation.

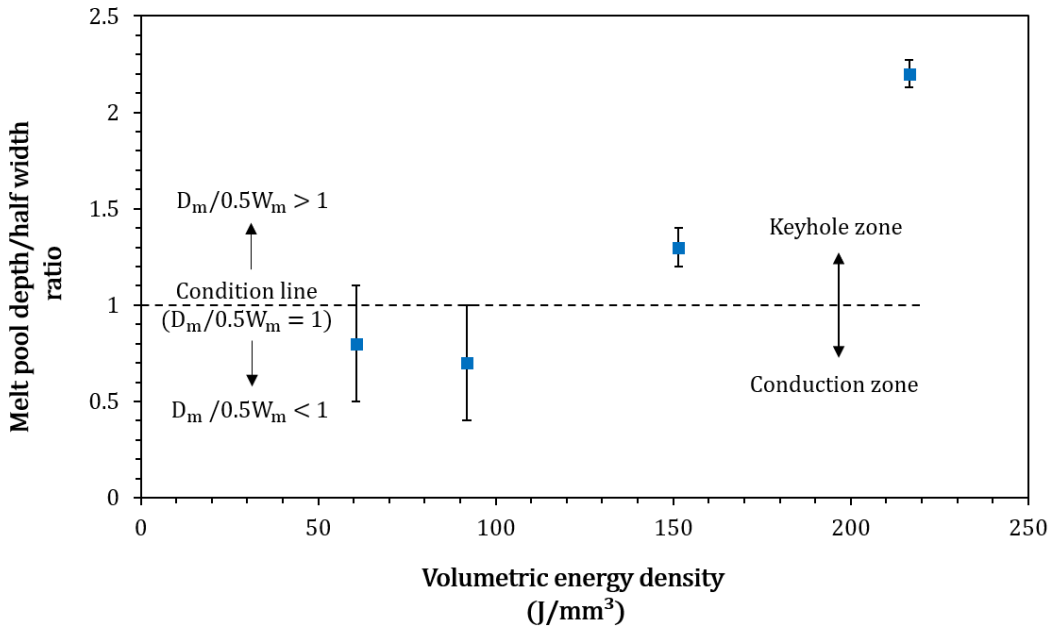

Figure 5.34: The ratio of melted depth/half of track width of satellited WC_M-12 wt.% Co single tracks as a function of volumetric energy density. The variation in measurements is consistent with instability during the consolidation process.

5.3.3. Satellited WC_M-12 wt.% Co layers morphology

A smooth surface morphology is essential for high density bulk material [151]. It can indicate a uniform spreading of powder over the substrate before laser melting which reflects applicable powder flowability. Poor flowability leads to high porosity in the fabricated parts [152]. It has been reported that at a moderate laser power, the laser irradiation is mostly absorbed by the upper part of the melt pool and the lower part is melted by heat conducted [153]. The heat input should be sufficient to homogenize the temperature within a deposited powder layer in a given period of time [154]. Due to inadequate laser energy, the amount of liquid Co might be not sufficient to wet all the involved WC_M particles when the laser power was <100 W (Figure 5.8 and Figure 5.9) [155].

The low energy input encourages capillary instability in the melt pool and then balling formation [156]. Wei et al. [153] showed that decreasing the laser power led to reduce

the width of melt pool then to increase its length-to-width ratio resulting in the track is prone to split into small drops to reduce surface energy. Moreover, a low energy density leads to a high temperature gradient then a surface tension gradient between the centre (low) and the edge (high) of melt pool resulting in molten metal flows from low surface tension to high surface tension [157]. However, it has been pointed out that a transition in surface tension gradient can occur at a certain temperature [138]. This generates inward surface flow from periphery to centre of the molten pool. The inward flow causes the liquid to accumulate near the laser beam centre. After solidification, relatively large balls can be formed along the laser scanning path. This can explain the relatively large extension of balling on the solidified surface (Figure 5.21).

It is plausible to suggest that the increase of surface irregularity with increasing the number of solidified layers is a result of cumulative surface deteriorations due to improper powder deposition on the previous solidified layer combined with instability of melt flow. It has been stated that the surface quality strongly correlates with such critical metrics as density and hardness [158]. Thus, monitoring the surface morphology can provide a significant flexibility to adjust energy input and evaluate the feedstock applicability based on responses of one metric alone. This can establish a reliable strategy to produce high quality parts in L-PBF by in-situ monitoring the surface morphology while building is in progress.

5.3.4. Spatter formation mechanism

A high energy input leads to metal evaporation which results in vapor cavities in the melt pools due to rapid solidification [159]. The evaporation produces recoil pressure back to melt pool. This represents a driving force for spatter [160]. A high recoil pressure causes removal of molten material by melt expulsion. According to

Gunenthiram et al. [161], most of the spatter is generated at the interface between front of the melt pool and powder bed. The tiny powder particles near melt pool are entrained by gas plume velocity. Interestingly, the recent study showed that spatters are widely generated in balling regime caused by low energy density. This can be confirmed by the current results (Figure 5.15). It can lead to voids in the fabricated parts and then to a low material density [162].

5.3.5. The impact of energy density on WC-17 wt.% Co cubic samples

The volumetric energy density (E_v) is calculated as in Eq.6.2 [90]:

$$E_v = P/vht \qquad [J/mm^3] \qquad (6.2)$$

where P is the laser power (W), v, h, and t are the laser scanning speed (mm/s), hatch distance (mm), and powder layer thickness (mm), respectively. The applied E_v was in the range of (60 – 133 J/mm³). The sensitivity of surface morphology to E_v has been confirmed [163]. At a low E_v, the flowability of molten Co might not be sufficient to fill all cavities and pores between powder particles. This can lead to open pores due to track discontinuity [164]. While a high E_v can enhance track morphology which results in a uniform overlapping with neighbouring tracks. However, a high energy density encourages thermal cracks (Figure 5.27b-d) [165]. Uhlmann et al. [90] used E_v range of (154-1852 J/mm³) to fabricate cubic samples from WC-17 Co powder. Schwanekamp et al. [91] used a comparable E_v range of ~ (150-1650 J/mm³) to produce bulk materials from WC-12 Co powder. The cracks and pores were presented in all samples in the above studies. In addition, a conflict has raised between cracks and pores: a high E_v increases cracks while a low E_v increases pores.

5.3.6. Cracking susceptibility

The cracking in L-PBF manufactured parts can be classified into three kinds [99]; solidification cracking, liquation cracking, and delamination. Solidification cracking is caused by thermal stresses in the melt pool due to thermal expansion followed by shrinkage during heating/cooling cycle. The liquation cracking is formed in the heat affected zone (HAZ) away from the melt pool. In HAZ, the temperature is lower than the liquidus temperature of the alloy, however, it causes melting of certain grain-boundary resulting in liquid films. During cooling down, the solidification shrinkage causes a tensile force in HAZ. Under this condition, the liquid film around the grain-boundary phases may act as cracking sites. The susceptibility of alloys to liquation cracking can be increased when there is (1) wide HAZ (large difference between solidus and liquidus temperatures), (2) large solidification shrinkage (large melt pool), and (3) large thermal contraction (high coefficient of thermal expansion). The delamination cracking is caused by high residual stresses at the interfaces between layers leading to separation of two consecutive layers.

It has been shown that WC particles can start dissolving in molten Co at 1200 °C and a rapid grain growth occurs at a temperature range of 1300 – 1350 °C [166]. Partial melting of WC particles leads to carbon deficiency due to precipitation of C as graphite as follow: $2WC \leftrightarrow W_2C + C$ [83]. Besides W_2C, this dissolving can produce ternary carbides such as Co_6W_6C as shown in the XRD results of the plasma densified WC-17 Co sample (Figure 5.31) [167]. Feature 2 in Figure 5.32b can represent this brittle phase combined with W_2C (lighter tiny spots) which can cause material cracking [95]. However, the satelliting results (Figure 5.16, Figure 5.17, Figure 5.18, Figure 5.22, and Figure 5.23) showed no such distinctive morphology in the matrix or around the edges of WC_M particles. Thus, it can be suggested that those surface cracks were

solidification cracks caused by thermal stresses. While the bases distortions of plasma densified cubic samples at relatively high energy inputs (Figure 5.27b-d) can be as a result of delamination cracking in the early built layers.

The origin of residual stresses belongs to three physical factors [99, 168, 169] (1) temperature gradient mechanism (TGM) due to localized heating and cooling by the travelling heat source, (2) cool-down mechanism (CDM) which describes the thermal expansion and contraction of the material due to such heating and cooling, and (3) strain compatibility (uneven distribution of plastic strains) of the material constituents especially under cyclic plastic flow. Cracks are initiated when these stresses exceed the ultimate tensile strength of the material [170].

The TGM can be used to describe the induced stress of a single melted track, whereas CDM describes the solidification behaviour of entirely melted powder layer. A schematic representation to TGM is given in Figure 5.35. It starts when the laser heats up the feedstock rapidly and the heated material tends to expand. This expansion is restrained by the surrounded lower temperature material resulting in a compressive stress. When laser is removed, cooling starts, and the previously heated zone begins to shrink which is restrained by the plastic strain formed during heating stage. As a result, tensile residual stress is formed in the heated zone which is balanced by a surrounded compressive stress zone.

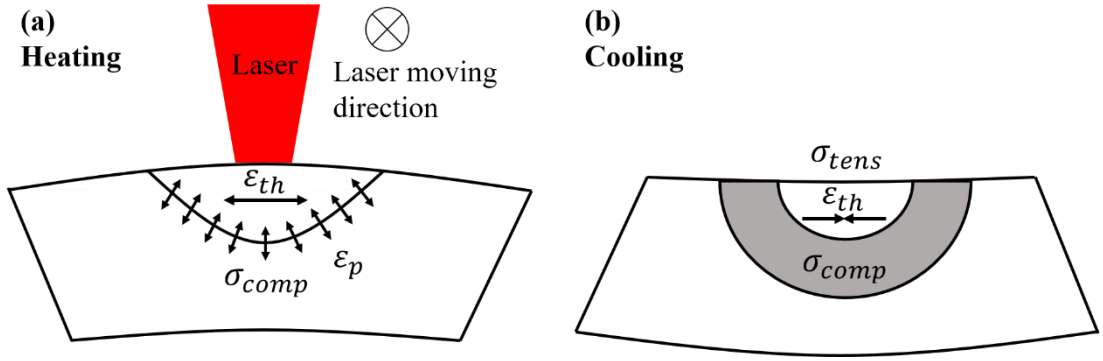

Figure 5.35: Thermal gradient mechanism of a single melted track inducing residual stress based on [168] (a) heating, and (b) cooling: Plastic ε_p and thermal ε_{th} elongations, tensile σ_{tens} and compressive σ_{comp} stresses.

In CDM, the melted top layer has a relatively higher temperature than the lower layer. After cooling, the upper layer contracts to a greater extent as compared to colder down layer. Due to metallurgical connection between layers, this contraction is inhibited. As a result, tensile stresses are formed in the top layer and compressive stresses in the underlying layer as shown schematically in Figure 5.36. This can explain the downward evolution of cracks from the top surface in the direction of laser beam (Figure 5.16, Figure 5.22, and Figure 5.23). High residual stress caused by high energy input can cause wrapping and cracking and then distortion of the fabricated part (Figure 5.27b, c, d) [171, 172].

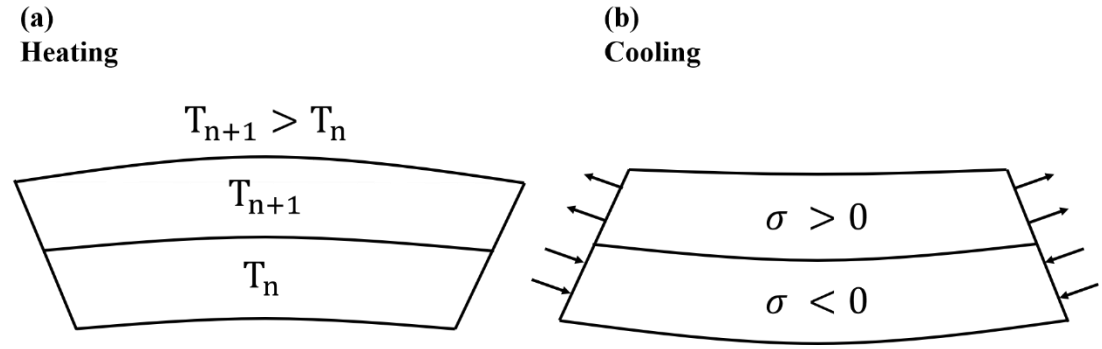

Figure 5.36: Cool-down mechanism of a melted powder layer inducing residual stress based on [169] (a) heating, and (b) cooling: Temperature of the previous solidified layer (T_n), temperature of new layer (T_{n+1}), and induced stress (σ).

The extent to which a material will deform or deflect at a given heat input and geometry can be indicated from the thermal stability concept. This is quantified by the ratio of λ/α_{th} [173]; where λ is the thermal conductivity and α_{th} is the coefficient of thermal expansion. It assumes that 'good thermal stability' refers to a minimum deflection which is illustrated by a maximum λ/α_{th} ratio. The thermal properties of WC and Co and the corresponding thermal stability ratios are given in Table 5.2. It shows that WC has a λ/α_{th} ratio of more than 2.7 times that of Co. This indicates that the expansion/shrinkage cycles of Co can contribute more to the induced residual stresses. However, the laser absorptivity of WC is higher than that of Co. Moreover, the brittleness nature of WC may cause cracking even with smaller deflections.

Table 5.2: Thermal properties of WC and Co materials [83] and corresponding thermal stability ratios.

Element	**WC**	**Co**
Thermal conductivity (λ) W/m/K	84	100
Thermal expansion coefficient (α_{th}) m/m/K	4.3	14
Thermal stability ratio (λ/α_{th}) W/m	19.5	7.1
Laser absorption coefficient	0.82	0.58

Increasing the number of deposited layers increases the expansion/shrinkage cycles in the re-melted regions resulting in high cumulative residual stresses [174]. This can explain the initiation of cracks in the overlapped zones of the layered components (Figure 5.16, Figure 5.22, and Figure 5.23).

Regarding the L-PBF processing, two strategies have been tried to reduce the thermal gradient and then residual stresses: multi moderate laser scanning and high preheating temperature. Schwanekamp et al. [91] showed that using multiple laser scanning with

a moderate energy density can reduce cracks. However, re-scanning strategy can also generate residual stresses in the fabricated samples [100]. On the other hand, Fries et al. [101] showed that crack-free WC-17 Co tools can be produced by preheating up to 900 °C. However, the presence of fusible Co (melting point = 1495 °C) can cause partial powder sintering during powder spreading which can completely interrupt the manufacturing process [93]. Thus, more research needs to be done to confirm the applicability of the recent strategy.

5.3.7. Theoretical track width

The Rosenthal equation allows prediction of track width (which is taken as the same of melt pool width) during welding process for a moving heat source [175]. It was observed that the steady state width of the most uniform satellited track produced at V of 0.14 m/s (Figure 5.3) was slightly larger than the corresponding melt pool width at the end of the track (Figure 5.4). In addition, the steady state measurements resulted in a less uncertainty limit which indicates a relatively more stability of solidification. Thus, it will be more reliable to compare the predicted tracks widths with the steady state measurements.

This comparison shows underestimation of tracks widths by 15% and 35% for the satellited WC_M-12 wt.% Co (Figure 5.2a) and plasma densified WC-17 wt.% Co (Figure 5.26) tracks, respectively, for the given process parameters. The Rosenthal model assumes that melted depth is equal to half of the melt pool width [117], therefore, providing a conduction melting mode [150]. He et al. [176] reported that this model often fails to provide accurate prediction for keyhole melt pool dimension, where the melted depth is higher than half of melt pool width. In this mode, the power density is sufficient to cause metal evaporation. This leads to vapor cavity which enhances laser absorption then enables the laser beam to melt a deeper distance than

that in conduction mode [150]. Thus, it can be suggested that Rosenthal model underestimates the laser absorptivity when keyhole melting mode is underlying. To prove this, the melt width is re-estimated for the satellited feedstock at laser power and scanning speed of 100 W and 0.5 m/s, respectively, where conduction melting mode was defined (Figure 5.5d). The new melt pool is given in Figure 5.37. It has a width of 154 µm which indicates a melted depth of 77 µm. This now overestimates the track width by 27%. The assumptions of the Rosenthal model can be a source of error. It neglects the temperature dependent material properties and the effects of convection and radiation heat losses. The values of thermal conductivity and specific heat capacity increase with temperature while material density decreases [118]. High prediction accuracy can be achieved if the values used are at elevated temperature [175]. Promoppatum et al. [177] showed increasing of overestimating trend and the sensitivity to laser absorptivity of Rosenthal model by increasing the heat input as compared to a finite element model. This was because the latter has included the radiative losses from the surface which intern increased with heat input. The overestimating trend of Rosenthal model has been observed also by Hekmatjou et al. [178]. To enhance accuracy of this model, heat density (the effect of laser spot size), powder bed density (the effect of particle size), and powder layer thickness are also to be considered.

As a result, the Rosenthal model can help as a preliminary step prior the experiments to imagine the likely values of laser power and scanning speed which can be used to generate a suitable melt pool for a given powder. However, the reliability of this model in L-PBF has not been proved.

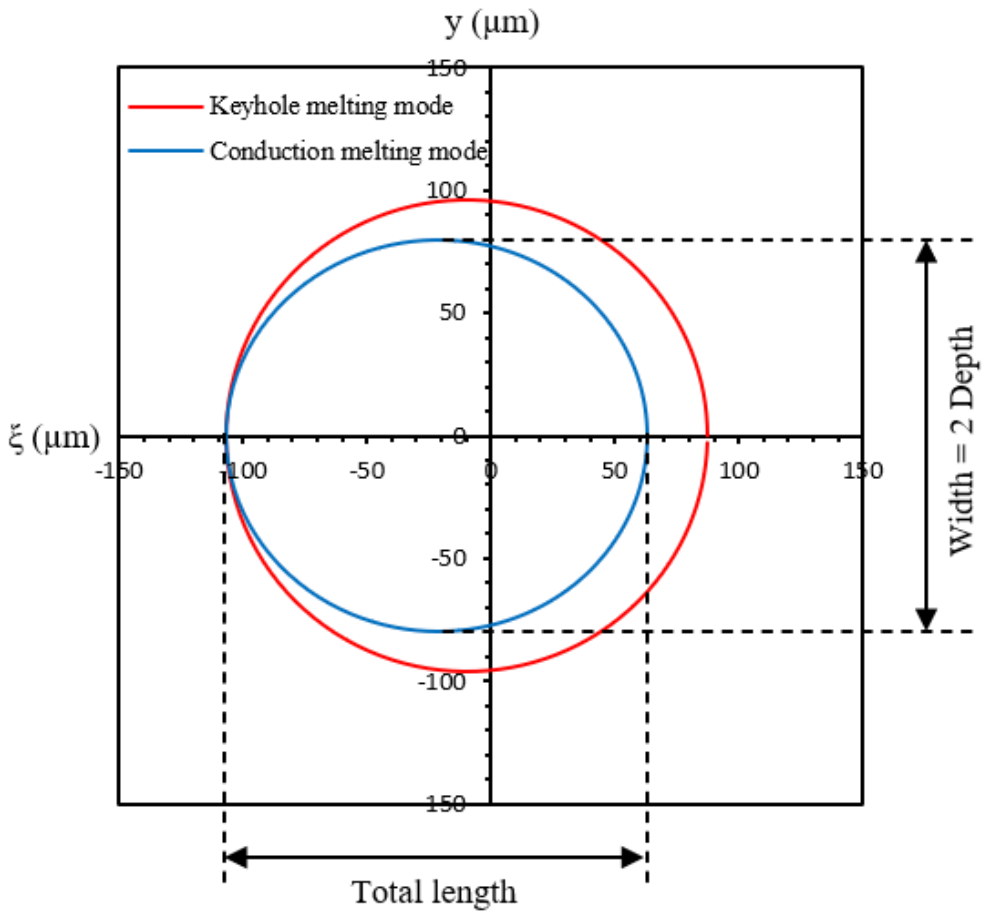

Figure 5.37: Theoretical melt pool dimensions of satellited WC_M-12 wt.% Co powder using Rosenthal equation at a laser power of 100 W considering two values of scanning speed: 0.14 m/s (keyhole melting mode) and 0.5 m/s (conduction melting mode).

5.3.8. WC-Co mixture design

In addition to laser power and scanning speed, the energy density is also affected by powder layer thickness which determines how much powder will be melted in a single laser scanning [179]. The feedstock mixture containing large particles requires a high powder thickness to accommodate all particles. On the other hand, the density of a powder layer is basically determined by the particle size distribution. The combination of fine and coarse particles increases powder packing density [180]. This is a crucial characteristic which determines how particles can efficiently arrange themselves in a

maximum particle-to-particle contact containing minimum voids within a granular network [181]. A high packing density reduces powder shrinkage during laser melting then next layer compensation resulting in a consistent melting/solidification. It has been reported that smaller WC-Co particles can lead to produce parts of less porosity and less cracking propensity due to a better laser absorptivity as compared to larger powder particles [91, 98]. A high laser absorptivity can lead to a high homogenization temperature within the powder bed [182]. However, the multilayer parts produced from both powders employed in this study, satellited (median particle size =109 µm) and plasma densified (median particle size =38.7 µm), revealed a high cracking tendency.

Regarding the feedstock properties, three strategies can be suggested to mitigate WC-Co cracking in L-PBF. Firstly, decreasing WC_M size allows applying a lower layer thickness which can increase the effectiveness of the laser beam to melt the powder and homogenize the temperature within powder bed. In other words, there should be a compatibility between the powder size distribution and laser spot size. Moreover, a better wettability can be achieved within liquid Co by using smaller WC_M size which can lead to a smoother surface morphology. Secondly, decreasing WC content in the feedstock can enhance material ductility and then reduce cracks [95]. However, low WC content can also lead to a low wear resistance. Finally, using a nano-sized Co powder, which has a lower melting point as compared to that of micron powder, allows applying a lower energy density to melt Co which can reduce both the induced thermal stresses and WC dissolution [97]. However, the nano particles can reduce powder flowability by increasing powder cohesion [119]. Thus, more research is required to explore at which extent of size and content can the nano Co powder be implemented to obtain applicable WC-Co mixture for L-PBF.

5.4. Summary

The results of this chapter were divided into two parts: satellited WC_M-12 wt.% Co and plasma densified WC-17 wt.% Co powders. The summaries are given below.

5.4.1. Satellited WC_M-12 wt.% Co powder

In this study for the first time, the satelliting method was used to prepare a WC_M -12 wt.% Co composite powder for L-PBF. The study can be divided into two parts: single tracks processability and the fabrication of single layers and multilayers components.

A- Single tracks processability

The results showed that the satellited feedstock is highly sensitive to laser scanning speed and only a small processing window was capable to produce continuous tracks. It was found that:

- For VED > 200 J/mm³, continuous tracks of WC_M -12 wt.% Co can be formed; the tracks present minimal cracking and porosity but large WC_M particles are found to be sintered to sides of the tracks.
- For VED < 200 J/mm³, as the energy is decreased, tracks become discontinuous with evidence of balling and powder bed denudation.
- A clear transition between conduction to keyhole-mode melting with respect to the values of volumetric energy density was observed and correlated to the melt pool characteristics.
- The low packing density of the feedstock produced a significant shrinkage during melting.
- The Rosenthal model can be used as a preliminary step before the experiments to imagine the melt pool size. However, the reliability of this model has not been proved.

B- Layered components morphology

The results revealed that laser power has a significant impact on the evolution of surface morphology of the layered components. It showed that:

- A relatively smooth single layer surface with a good bonding to the substrate and no cracks or gaps between adjacent laser scans was obtained at 100 W.
- Increasing the number of solidified layers has led to increase cracking susceptibility.
- Reducing the laser power to 90 W resulted in balling formation and surface irregularity.
- Massive balling was observed at a lower laser power of 80 W where balling size was proportional to the number of solidified layers.

5.4.2. Plasma densified WC-17 wt.% Co powder

In this chapter, plasma densified WC-17 wt.% Co powder was also used to produce cubic samples by L-PBF. A process window was defined through ranges of laser powder and scanning speed. It was found that:

- Using a relatively high E_v of ≥ 114 J/mm³ resulted in a thermal distortion in the bottom of the samples.
- Uniform samples without distortions were produced at E_v of < 114 J/mm³.
- All samples topography revealed open pores which increased by decreasing E_v.
- All samples contained microcracks on their as-built topography regardless the process parameters.
- The formations of W_2C and Co_6W_6C carbides after laser processing were confirmed by XRD results.

6. Conclusions and recommendations for future work

6.1.Introduction

This chapter is divided into two parts: conclusions and recommendations for future work. The conclusions include the DED-L and L-PBF results. The recommendations propose studies that can be expanded from this research for future work. These are given in the following sections.

6.2.Conclusions

6.2.1. DED-L conclusions

In this study for the first time, the satelliting method was used to incorporate WC_M powder with Co powder to produce a composite feedstock. It showed that:

- The satelliting method was a flexible approach to prepare a suitable feedstock for DED-L processing.
- High quality single clads were fabricated. They revealed uniform depositions, good bonding to the substrate, no cracks, almost full density matrices, and a uniform distribution of the WC_M particles inside the cladding area.
- The deposition efficiency and the WC_M dissolution were proportional to energy density.
- The microstructure revealed recrystallization of WC faceted morphology from the original WC_M particles at a high energy density.
- Ternary carbide Co_3W_3C phase was formed in a dendritic morphology due to WC_M dissolution in the metal matrix.
- Appropriate process window to represent the relationship between process parameters and the deposition behaviour was determined from the values of effective energy density versus powder deposition density.

- The scanning speed has a vital role in determination not just the delivered energy by the laser beam, but also the amount of delivered powder to melt pool.
- Uniform multitrack coatings without outside cracks or lack of fusion between tracks were produced.
- The microstructure of multitrack coatings maintained a uniform distribution of WC_M particles.
- Cracks, pore size, and porosity ratio in multitrack coatings were proportional to energy density.
- The dissolution of WC_M particles enhanced matrices microhardness and led to excellent wear resistant coatings.
- The mechanical tests revealed excellent metallurgical bonding between WC_M particles and the matrices with a good indication of fracture toughness.

6.2.2. L-PBF conclusions

In this section, the conclusions of L-PBF processing of satellited WC_M -12 wt.% Co and plasma densified WC-17 wt.% Co powders are presented.

A) L-PBF conclusions of satellited WC_M -12 wt.% Co

- Continuous tracks were formed; the tracks presented no cracks and negligible porosity.
- Conduction to keyhole-mode melting regimes of single tracks were defined according to the values of volumetric energy density.
- The powder presented a low packing density giving a significant shrinkage during melting.
- A relatively smooth single layer surface with a good metallurgical bonding to the substrate and no cracks or gaps between adjacent laser scans was fabricated.

- Multilayer components of almost full density matrices and relatively smooth surface morphology were produced at a high energy density.
- Increasing the number of solidified layers led to increase material cracking susceptibility.
- The balling size increased massively when a multilayer component was fabricated at a relatively low energy density.

B) L-PBF conclusions of plasma densified WC-17 wt.% Co

- A continuous multitrack wall can be fabricated.
- Uniform cubic samples without distortion or outside cracks were fabricated within a suitable process window of laser power and scanning speed.
- The samples surfaces revealed open pores and micro cracks regardless the process parameters.

6.3.Recommendations for future work

Although this research work has covered wide ranges of process parameters using different types of powders in both DED-L and L-PBF techniques, there is still more to be done regarding process conditions and feedstock properties. The recommendations for future work are divided into two fields: DED-L and L-PBF.

6.3.1. DED-L recommendations

The results showed successful depositions of satellited WC_M- 12 wt.% Co single tracks. However, cracks appeared in the multitrack coatings. To eliminate cracks, the specific proposals are:

- Pre-heating the substrate: This can also affect the evolution of melt pool geometry, WC_M dissolution, and then the microstructure.

- Increasing the Co content to increase material ductility and then reduce cracking propensity.

6.3.2. L-PBF recommendations

A high cracking sensitivity has appeared in L-PBF multilayer parts regardless the process parameters and feedstock composition. The following suggestions can be implemented to reduce cracking susceptibility:

- Preheating the substrate to a high temperature to reduce the thermal stresses.
- Using a multi laser scanning strategy with a moderate energy density instead of a single laser scanning strategy with a high energy density to reduce the thermal stresses.
- Increasing the Co content to enhance material ductility.

Appendices

Appendix A

A.1: The overall results of the full factorial design experiments (section 4.3 in chapter 4) are given in the following tables.

Table A.1: Process parameters of full factorial design experiments (section 4.3 in chapter 4) and the resulted clad area and substrate melted area.

Test No.	Laser Power (W)	Scanning speed (mm/min)	Powder feed rate (g/min)	Clad area (mm^2)	Substrate melted area (mm^2)
1	200	180	4	0.017 ± 0.01	0.007 ± 0.001
2	200	240	4	0.014 ± 0.007	0.005 ± 0.003
3	200	360	4	0.005 ± 0.004	0.002 ± 0.002
4	200	180	6	0.022 ± 0.005	0.001 ± 0.001
5	200	240	6	0.009 ± 0.006	0.002 ± 0.002
6	200	360	6	0.003 ± 0.003	0.001 ± 0.001
7	200	180	10	0.071 ± 0.0003	0.001 ± 0.0008
8	200	240	10	0.053 ± 0.006	0.002 ± 0.001
9	200	360	10	0.023 ± 0.006	0.005 ± 0.003
10	350	180	4	0.108 ± 0.005	0.09 ± 0.007
11	350	240	4	0.113 ± 0.007	0.072 ± 0.001
12	350	360	4	0.049 ± 0.001	0.099 ± 0.005
13	350	180	6	0.161 ± 0.008	0.077 ± 0.009
14	350	240	6	0.135 ± 0.008	0.052 ± 0.002
15	350	360	6	0.09 ± 0.011	0.089 ± 0.007
16	350	180	10	0.318 ± 0.007	0.03 ± 0.002
17	350	240	10	0.137 ± 0.005	0.054 ± 0.005
18	350	360	10	0.078 ± 0.008	0.085 ± 0.009
19	500	180	4	0.185 ± 0.01	0.255 ± 0.011
20	500	240	4	0.127 ± 0.012	0.27 ± 0.006
21	500	360	4	0.08 ± 0.001	0.229 ± 0.002
22	500	180	6	0.31 ± 0.012	0.131 ± 0.008
23	500	240	6	0.238 ± 0.008	0.173 ± 0.003
24	500	360	6	0.149 ± 0.004	0.172 ± 0.008
25	500	180	10	0.406 ± 0.011	0.091 ± 0.001
26	500	240	10	0.3 ± 0.007	0.104 ± 0.007
27	500	360	10	0.213 ± 0.006	0.109 ± 0.005

Table A.2: Process parameters of full factorial design experiments (section 4.3 in chapter 4) and the resulted dilution and porosity ratios.

Test No.	Laser Power (W)	Scanning speed (mm/min)	Powder feed rate (g/min)	Dilution %	Porosity %
1	200	180	4	33.1 ± 5.4	0
2	200	240	4	18.1 ± 10.4	0.4 ± 0.3
3	200	360	4	20.7 ± 10.5	0
4	200	180	6	9.3 ± 9.3	0.4 ± 0.2
5	200	240	6	8.3 ± 8.3	1.1 ± 1.1
6	200	360	6	11.4 ± 11.4	0.1 ± 0.1
7	200	180	10	1.4 ± 1.1	1.2 ± 0.1
8	200	240	10	4 ± 2	0.7 ± 0.2
9	200	360	10	13.5 ± 7.7	0.8 ± 0.8
10	350	180	4	45.3 ± 3.3	0.1 ± 0.1
11	350	240	4	38.9 ± 1.9	0.2 ± 0.1
12	350	360	4	66.8 ± 0.6	0.04 ± 0.03
13	350	180	6	32.2 ± 2.7	0.1 ± 0.08
14	350	240	6	28.2 ± 2	0.3 ± 0.1
15	350	360	6	49.9 ± 5.3	0.4 ± 0.2
16	350	180	10	8.6 ± 0.5	0.01 ± 0.01
17	350	240	10	28.4 ± 2.8	0.35 ± 0.04
18	350	360	10	51.8 ± 5.6	0.33 ± 0.06
19	500	180	4	57.8 ± 2.3	0.7 ± 0.1
20	500	240	4	68 ± 2.1	0.9 ± 0.9
21	500	360	4	74.1 ± 0.6	0.44 ± 0.02
22	500	180	6	29.8 ± 2.2	0.02 ± 0.005
23	500	240	6	42.1 ± 0.7	0.7 ± 0.5
24	500	360	6	53.5 ± 1.3	0.6 ± 0.1
25	500	180	10	18.4 ± 0.6	0.01 ± 0.01
26	500	240	10	25.8 ± 1.8	0.3 ± 0.1
27	500	360	10	33.9 ± 1.6	0.3 ± 0.1

Table A.3: Process parameters of full factorial design experiments (section 4.3 in chapter 4) and the resulted melt pool dimensions.

Test No.	Laser Power (W)	Scanning speed (mm/min)	Powder feed rate (g/min)	Track width (µm)	Track height (µm)	Track depth (µm)	Wetting angle (°)
1	200	180	4	600 ± 93	36 ± 6	26 ± 5	24 ± 6
2	200	240	4	500 ± 252	28 ± 7	26 ± 6	20 ± 3
3	200	360	4	225 ± 118	16 ± 9	10 ± 7	7 ± 2
4	200	180	6	452 ± 40	55 ± 20	8 ± 8	17 ± 2
5	200	240	6	244 ± 134	42 ± 21	10 ± 10	15 ± 6
6	200	360	6	124 ± 124	8 ± 8	8 ± 8	3 ± 2
7	200	180	10	758 ± 47	139 ± 16	7 ± 7	32 ± 3
8	200	240	10	608 ± 63	145 ± 10	9 ± 5	40 ± 9
9	200	360	10	424 ± 71	85 ± 6	14 ± 7	29 ± 5
10	350	180	4	1054 ± 4	136 ± 8	185 ± 11	44 ± 3
11	350	240	4	1068 ± 5	152 ± 6	129 ± 6	31 ± 3
12	350	360	4	962 ± 6	70 ± 4	192 ± 2	20 ± 2
13	350	180	6	1043 ± 16	201 ± 16	147 ± 15	72 ± 11
14	350	240	6	1049 ± 9	169 ± 8	95 ± 5	63 ± 2
15	350	360	6	1016 ± 11	119 ± 14	169 ± 4	44 ± 4
16	350	180	10	1135 ± 6	395 ± 22	58 ± 4	59 ± 2
17	350	240	10	1035 ± 3	168 ± 7	96 ± 7	57 ± 4
18	350	360	10	987 ± 21	110 ± 16	150 ± 7	34 ± 2
19	500	180	4	1276 ± 17	200 ± 12	357 ± 21	38 ± 6
20	500	240	4	1220 ± 39	134 ± 16	429 ± 11	38 ± 8
21	500	360	4	1122 ± 28	93 ± 3	363 ± 10	43 ± 3
22	500	180	6	1364 ± 22	308 ± 13	157 ± 17	62 ± 8
23	500	240	6	1275 ± 8	253 ± 7	257 ± 8	50 ± 2
24	500	360	6	1189 ± 2	160 ± 4	261 ± 18	49 ± 5
25	500	180	10	1342 ± 14	445 ± 10	111 ± 2	48 ± 2
26	500	240	10	1302 ± 10	305 ± 11	128 ± 15	59 ± 2
27	500	360	10	1244 ± 19	224 ± 4	140 ± 5	51 ± 4

Table A.4: Process parameters of full factorial design experiments (section 4.3 in chapter 4) and the resulted WC_M retained area, WC_M dissolution ratio, and deposition efficiency.

Test No.	Laser Power (W)	Scanning speed (mm/min)	Powder feed rate (g/min)	Retained WC_M area (mm^2)	WC_M dissolution ratio %	Deposition efficiency %
1	200	180	4	0.0055 ± 0.0038	---	6.6 ± 0.4
2	200	240	4	0.0004 ± 0.0004	---	4.9 ± 0.4
3	200	360	4	0.0006 ± 0.0006	---	4.4 ± 0.5
4	200	180	6	0.0027 ± 0.0008	---	5.6 ± 0.9
5	200	240	6	0.0009 ± 0.0009	---	4 ± 1
6	200	360	6	0.0008 ± 0.0008	---	4.1 ± 0.4
7	200	180	10	0.0198 ± 0.0018	---	4.4 ± 0.4
8	200	240	10	0.0145 ± 0.0023	---	3.4 ± 0.6
9	200	360	10	0.0084 ± 0.0041	---	2.5 ± 0.4
10	350	180	4	0.0341 ± 0.009	60.8 ± 10.3	60.5 ± 0.7
11	350	240	4	0.0557 ± 0.0021	38.1 ± 4.5	50.9 ± 1.1
12	350	360	4	0.0121 ± 0.0013	69.4 ± 2.7	44.2 ± 1.3
13	350	180	6	0.051 ± 0.0034	59.8 ± 4.7	50.7 ± 1
14	350	240	6	0.0558 ± 0.008	48.8 ± 4.9	39.5 ± 0.8
15	350	360	6	0.0275 ± 0.0026	61.5 ± 1.3	37.3 ± 1.8
16	350	180	10	0.1283 ± 0.0054	49.6 ± 2.2	37.1 ± 1.3
17	350	240	10	0.0398 ± 0.003	63.5 ± 4	24.6 ± 1.2
18	350	360	10	0.0197 ± 0.004	67.8 ± 7.1	25.1 ± 1.2
19	500	180	4	0.0342 ± 0.0093	77.5 ± 5	71.2 ± 1.4
20	500	240	4	0.0327 ± 0.0018	67 ± 4.6	67.6 ± 1
21	500	360	4	0.0078 ± 0.0013	87.8 ± 2.1	50.4 ± 1.4
22	500	180	6	0.0815 ± 0.0062	67.1 ± 2.6	65.5 ± 1.4
23	500	240	6	0.0882 ± 0.0026	53.8 ± 0.6	58.9 ± 1.5
24	500	360	6	0.0352 ± 0.0021	70.5 ± 1.8	41.7 ± 1.4
25	500	180	10	0.0318 ± 0.0034	90.1 ± 1.3	55 ± 1
26	500	240	10	0.0599 ± 0.0162	74.6 ± 7.3	47 ± 1
27	500	360	10	0.0798 ± 0.0038	53.3 ± 0.8	36.6 ± 1.6

Appendix B

B.1: The process parameters and the resulted clads qualities which were represented in the process map in section 4.5 – chapter 4 are given in the following two tables. Table B.1 (in three parts) shows the process parameters and clad qualities of the full factorial design experiments. Table B.2 presents specific sets of process parameters and corresponding clads qualities. In general, four clads categories are recognised; (1) weak deposition at a laser power of 200 W regardless the values of scanning speed and powder feed rate, (2) high-quality clads including good bonding with the substrate, no cracks, low porosity (< 1%), and a dilution ratio of < 40%, (3) high dilution ratio of > 40%, and (4) cracking.

Table B.1: Process parameters and clads qualities of the full factorial design experiments used in the process map presented in section 4.5 in chapter 4. The table is presented in three sections with a total number of experiments of 27.

Test No.	Laser power (W)	Scanning speed (mm/min)	Powder feed rate (g/min)	Linear energy density (J/mm)	Effective energy density (J/mm^2)	Powder deposition density (g/mm^2)	Observation
1	200	180	4	66.6	66.6	0.005	Weak deposition
2	200	180	6	66.6	66.6	0.008	Weak deposition
3	200	180	10	66.6	66.6	0.013	Weak deposition
4	200	240	4	50	50	0.004	Weak deposition
5	200	240	6	50	50	0.006	Weak deposition
6	200	240	10	50	50	0.01	Weak deposition
7	200	360	4	33.3	33.3	0.002	Weak deposition
8	200	360	6	33.3	33.3	0.004	Weak deposition
9	200	360	10	33.3	33.3	0.007	Weak deposition

Test No.	Laser power (W)	Scanning speed (mm/min)	Powder feed rate (g/min)	Linear energy density (J/mm)	Effective energy density (J/mm^2)	Powder deposition density (g/mm^2)	Observation
10	350	180	4	116.6	116.6	0.005	Good bonding
11	350	180	6	116.6	116.6	0.008	Good bonding
12	350	180	10	116.6	116.6	0.013	Good bonding
13	350	240	4	87.5	87.5	0.004	Good bonding
14	350	240	6	87.5	87.5	0.006	Good bonding
15	350	240	10	87.5	87.5	0.0104	Good bonding
16	350	360	4	58.3	58.3	0.002	High dilution
17	350	360	6	58.3	58.3	0.004	High dilution
18	350	360	10	58.3	58.3	0.007	High dilution

Test No.	Laser power (W)	Scanning speed (mm/min)	Powder feed rate (g/min)	Linear energy density (J/mm)	Effective energy density (J/mm^2)	Powder deposition density (g/mm^2)	Observation
19	500	180	4	166.6	166.6	0.005	High dilution
20	500	180	6	166.6	166.6	0.008	Good bonding
21	500	180	10	166.6	166.6	0.013	Good bonding
22	500	240	4	125	125	0.004	High dilution
23	500	240	6	125	125	0.006	Good bonding
24	500	240	10	125	125	0.01	Good bonding
25	500	360	4	83.3	83.3	0.002	High dilution
26	500	360	6	83.3	83.3	0.004	High dilution
27	500	360	10	83.3	83.3	0.007	Good bonding

Table B.2: Specific sets of process parameters and corresponding clads qualities used in the process map presented in section 4.5 in chapter 4: tests 1 and 2 were performed at the same powder feed rate and energy density (linear and effective): tests 3 and 4 were performed at the same powder feed rate and energy density (linear and effective).

Test No.	Laser power (W)	Scanning speed (mm/min)	Powder feed rate (g/min)	Linear energy density (J/mm)	Effective energy density (J/mm^2)	Powder deposition density (g/mm^2)	Observation
1	300	180	10	100	100	0.013	Good bonding
2	400	240	10	100	100	0.01	Cracking
3	450	180	4	150	150	0.005	High dilution
4	600	240	4	150	150	0.004	High dilution

Appendix C

C.1: Calculation of WC_M dissolution ratio in section 4.3.1.5 – chapter 4

The dissolution ratio of WC_M was determined from the difference between the original WC_M volume fraction in the feedstock and the retained WC_M volume fraction in the clad and then dividing this by the original WC_M volume fraction in the feedstock. The results were built on the following assumptions:

- The flow of powder is consistent throughout the deposition process.
- The melt pool consistently accommodates the impinging powder (bouncing of relatively large WC_M particles is neglected).
- The total volume fraction of WC_M in the clad (including the dissolved portion) is equal to that in the feedstock.

The step-by-step calculation is presented below.

(1) Original WC_M volume fraction: The feedstock composition is WC_M-Co (88-12 wt.%). The densities of WC_M and Co are 15800 Kg/m³ and 8900 Kg/m³, respectively. This gives that the WC_M volume fraction (V_o) in the feedstock is 80%.

(2) The retained volume fraction: The clad area above substrate surface (A_c) was determined. The total retained (undissolved) WC_M area (A_r) from all captured WC_M particles was calculated. Then, the retained WC_M volume fraction per unit clad length (V_r) is calculated: $V_r = A_r/A_c$.

(3) The dissolved fraction: The difference between WC_M volume fraction in the feedstock and WC_M volume fraction in the clad determines the dissolved fraction (V_f) as given in Eq.C.1 [86]:

$$V_f = V_o - V_r \quad \text{(C.1)}$$

(4) The dissolution ratio: The WC_M dissolution ratio (V_{dis}) is determined from Eq.C.2.

$$V_{dis} = \frac{V_f}{V_o} \times 100\% \quad \text{(C.2)}$$

Appendix D

D.1: DED-L X-ray Diffraction Standards

This section shows the diffraction standards of phases in the Spherotene® powder, Co powder, mild steel substrate, and DED-L selected clads presented in Figure 3.2 – chapter 3 and Figure 4.20 – chapter 4. The phases' files were taken from the 2015 JCPDS-International Centre for Diffraction Data. The JCPDS files of W_2C (hcp), WC (hcp), WC_{1-x} (fcc), Co (fcc), Co (hcp), Fe (bcc), and Co_3W_3C (fcc) phases are given in the tables below.

W_2C Tungsten Carbide		**2θ (°)**	**d (Å)**	**Intensity**	**h**	**k**	**l**
System	Hexagonal	34.589	2.59115	220	1	0	0
S.G.	P63/mmc (194)	38.059	2.36250	238	0	0	2
a (Å)	2.992	39.638	2.27195	1000	1	0	1
c (Å)	4.725	52.365	1.74579	146	1	0	2
Radiation	CuKa1λ	61.982	1.49600	152	1	1	0
Standard no.	01-071-6322	69.828	1.34587	138	1	0	3
		72.963	1.29557	19	2	0	0
		75.101	1.26391	135	1	1	2
		76.123	1.24946	101	2	0	1
		81.401	1.18125	19	0	0	4
		85.391	1.13597	25	2	0	2
		91.561	1.07483	17	1	0	4
		100.684	1.00056	42	2	0	3
		103.725	0.97936	12	2	1	0
		106.883	0.95898	71	2	1	1
		112.380	0.92708	46	1	1	4
		116.736	0.90471	23	2	1	2
		120.373	0.88780	30	1	0	5
		123.883	0.87290	10	2	0	4
		126.212	0.86372	20	3	0	0
		135.698	0.83169	53	2	1	3
		143.455	0.81120	33	3	0	2

WC Tungsten Carbide		**2θ (°)**	**d (Å)**	**Intensity**	**h**	**k**	**l**
System	Hexagonal	31.555	2.83300	48	0	0	1
S.G.	P-6m2 (187)	35.729	2.51100	101	1	0	0
a (Å)	2.902	48.437	1.87780	97	1	0	1
c (Å)	2.831	64.228	1.44900	28	1	1	0
Radiation	CuKa1λ	65.965	1.41500	10	0	0	2
Standard no.	00-061-0244	73.263	1.29100	39	1	1	1
		75.586	1.25700	13	2	0	0
		77.326	1.23300	24	1	0	2
		84.197	1.14900	25	2	0	1
		98.869	1.01400	18	1	1	2
		117.548	0.90080	25	2	1	1

WC_{1-x} Tungsten carbide		**2θ (°)**	**d (Å)**	**Intensity**	**h**	**k**	**l**
System	Cubic	36.978	2.42900	41	1	1	1
S.G.	Fm-3m (225)	42.888	2.10700	100	2	0	0
a (Å)	4.2355	62.028	1.49500	30	2	2	0
Radiation	CuKa1λ	74.200	1.27700	50	3	1	1
Standard no.	00-020-1316	78.230	1.22100	11	2	2	2
		93.106	1.06100	15	4	0	0
		104.685	0.97300	41	3	3	1
		108.692	0.94800	41	4	2	0

Co Cobalt		**2θ (°)**	**d (Å)**	**Intensity**	**h**	**k**	**l**
System	Cubic	44.217	2.04670	101	1	1	1
S.G.	Fm-3m (225)	51.524	1.77230	41	2	0	0
a (Å)	3.5447	75.855	1.25320	26	2	2	0
Radiation	CuKa1λ	92.227	1.06880	31	3	1	1
Standard no.	00-015-0806	97.660	1.02330	13	2	2	2

Co Cobalt		**2θ (°)**	**d (Å)**	**Intensity**	**h**	**k**	**l**
System	Hexagonal	41.579	2.17026	267	1	0	0
S.G.	P63/mmc (194)	44.496	2.03450	279	0	0	2
a (Å)	2.506	47.440	1.91491	1000	1	0	1
c (Å)	4.069	62.527	1.48428	113	1	0	2
Radiation	CuKa1λ	75.870	1.25300	100	1	1	0
Standard no.	01-071-4239	84.090	1.15019	99	1	0	3
		90.448	1.08513	13	2	0	0
		92.441	1.06689	92	1	1	2
		94.560	1.04849	64	2	0	1
		98.443	1.01725	13	0	0	4
		107.130	0.95746	16	2	0	2
		113.502	0.92109	14	1	0	4
		130.762	0.84733	32	2	0	3
		139.791	0.82028	11	2	1	0
		146.655	0.80411	57	2	1	1

Fe Iron		**2θ (°)**	**d (Å)**	**Intensity**	**h**	**k**	**l**
System	Cubic	44.674	2.0268	101	1	1	0
S.G.	Im-3m (229)	65.023	1.43320	21	2	0	0
a (Å)	2.8664	82.335	1.17020	31	2	1	1
Radiation	CuKa1λ	98.949	1.01340	11	2	2	0
Standard no.	00-006-0696	116.390	0.90640	13	3	1	0
		137.144	0.82750	7	2	2	2

Co_3W_3C Cobalt Tungsten Carbide		2θ (°)	d (Å)	Intensity	h	k	l
System	Cubic	13.904	6.36413	54	1	1	1
S.G.	Fd-3m (227)	22.800	3.89722	228	2	2	0
a (Å)	11.023	26.803	3.32356	16	3	1	1
Radiation	CuKa1λ	28.018	3.18207	2	2	2	2
Standard no.	01-078-3750	32.464	2.75575	454	4	0	0
		35.469	2.52885	267	3	3	1
		40.040	2.25006	596	4	2	2
		42.583	2.12138	1000	5	1	1
		46.570	1.94861	621	4	4	0
		48.840	1.86323	6	5	3	1
		49.579	1.83717	30	4	4	2
		52.459	1.74289	2	6	2	0
		54.547	1.68099	2	5	3	3
		55.231	1.66178	16	6	2	2
		57.914	1.59103	29	4	4	4
		59.874	1.54353	126	5	5	1
		63.060	1.47301	5	6	4	2
		64.928	1.43507	169	7	3	1
		67.980	1.37787	29	8	0	0
		69.780	1.34667	125	7	3	3
		72.735	1.29907	287	8	2	2
		74.485	1.27283	81	5	5	5
		75.065	1.26442	6	6	6	2
		77.370	1.23241	16	8	4	0
		79.085	1.20993	42	9	1	1
		79.654	1.20271	10	8	4	2
		81.921	1.17506	4	6	6	4
		83.614	1.15552	10	9	3	1
		86.423	1.12503	9	8	4	4
		88.104	1.10785	87	7	7	1
		90.902	1.08089	84	10	2	0
		92.582	1.06563	124	9	5	1
		93.142	1.06069	10	10	2	2
		97.075	1.02790	16	9	5	3
		99.904	1.00626	7	10	4	2
		101.614	0.99391	2	11	1	1
		104.486	0.97431	2	8	8	0
		106.227	0.96308	44	11	3	1
		106.811	0.95943	4	8	8	2
		109.164	0.94521	41	10	6	0
		110.952	0.93496	14	11	3	3
		111.552	0.93161	3	10	6	2
		113.980	0.91858	18	12	0	0
		115.831	0.90916	33	11	5	1
		118.983	0.89408	120	12	2	2
		120.920	0.88539	6	9	7	5
		124.241	0.87145	4	12	4	0
		126.298	0.86339	14	9	9	1
		129.853	0.85044	7	10	8	2
		132.076	0.84295	15	11	5	5
		132.834	0.84050	2	10	6	6
		135.968	0.83089	2	12	4	4
		138.439	0.82390	61	11	7	3
		139.290	0.82161	4	10	8	4
		142.853	0.81263	72	12	6	2
		145.729	0.80608	40	9	9	5

D.2: X-ray diffraction patterns of Spherotene® powder, Co powder, satelliting WC_M-12 wt.% Co powder, mild steel substrate, DED-L sample 1, and DED-L sample 2 presented in Figure 3.2 – chapter 3 and Figure 4.20 – chapter 4.

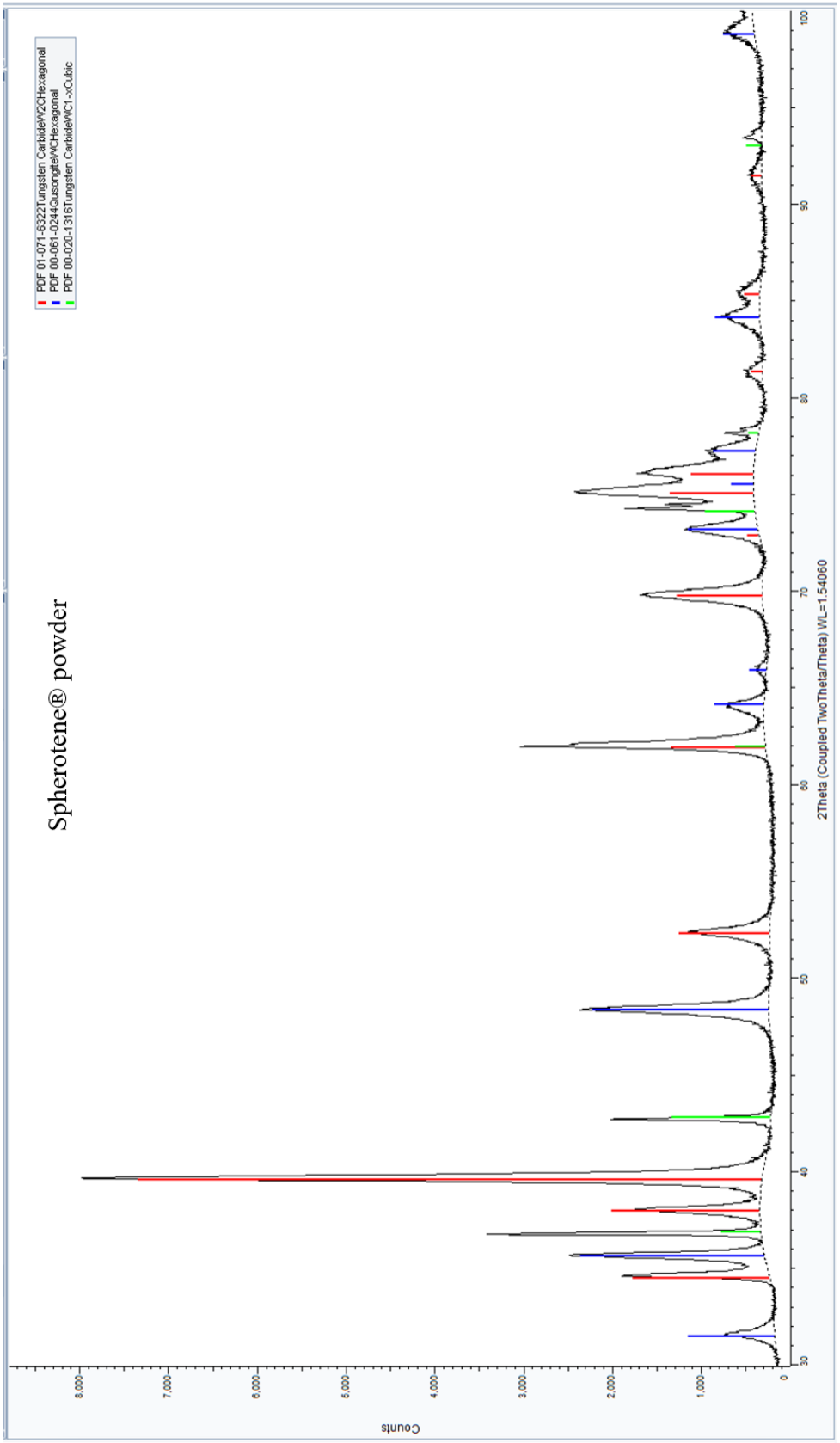

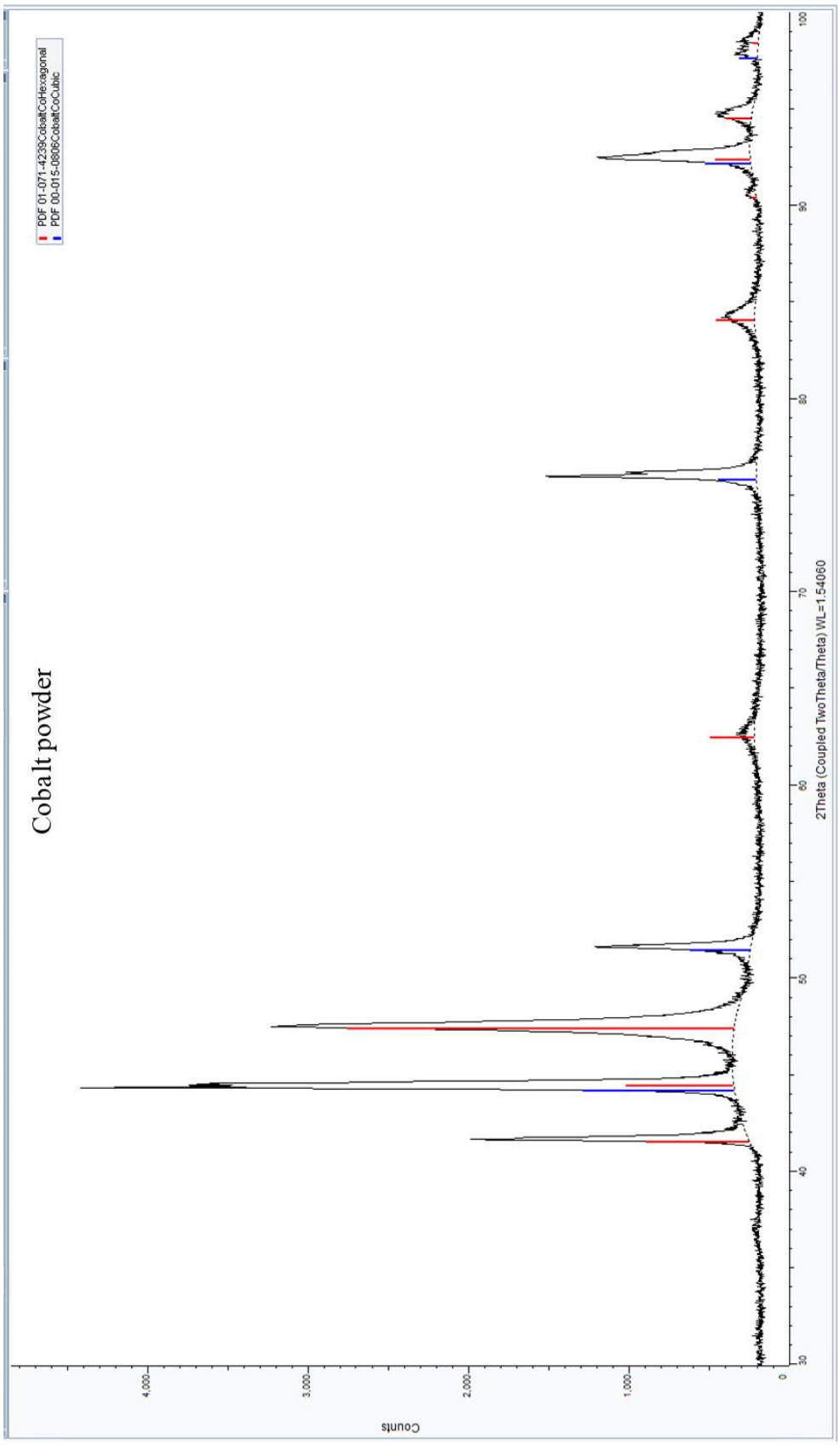
Cobalt powder
PDF 01-071-4239 Cobalt CoHexagonal
PDF 00-015-0806 Cobalt CoCubic
Counts
4,000
3,000
2,000
1,000
0
30
40
50
60
70
80
90
100
2Theta (Coupled TwoTheta/Theta) WL=1.54060

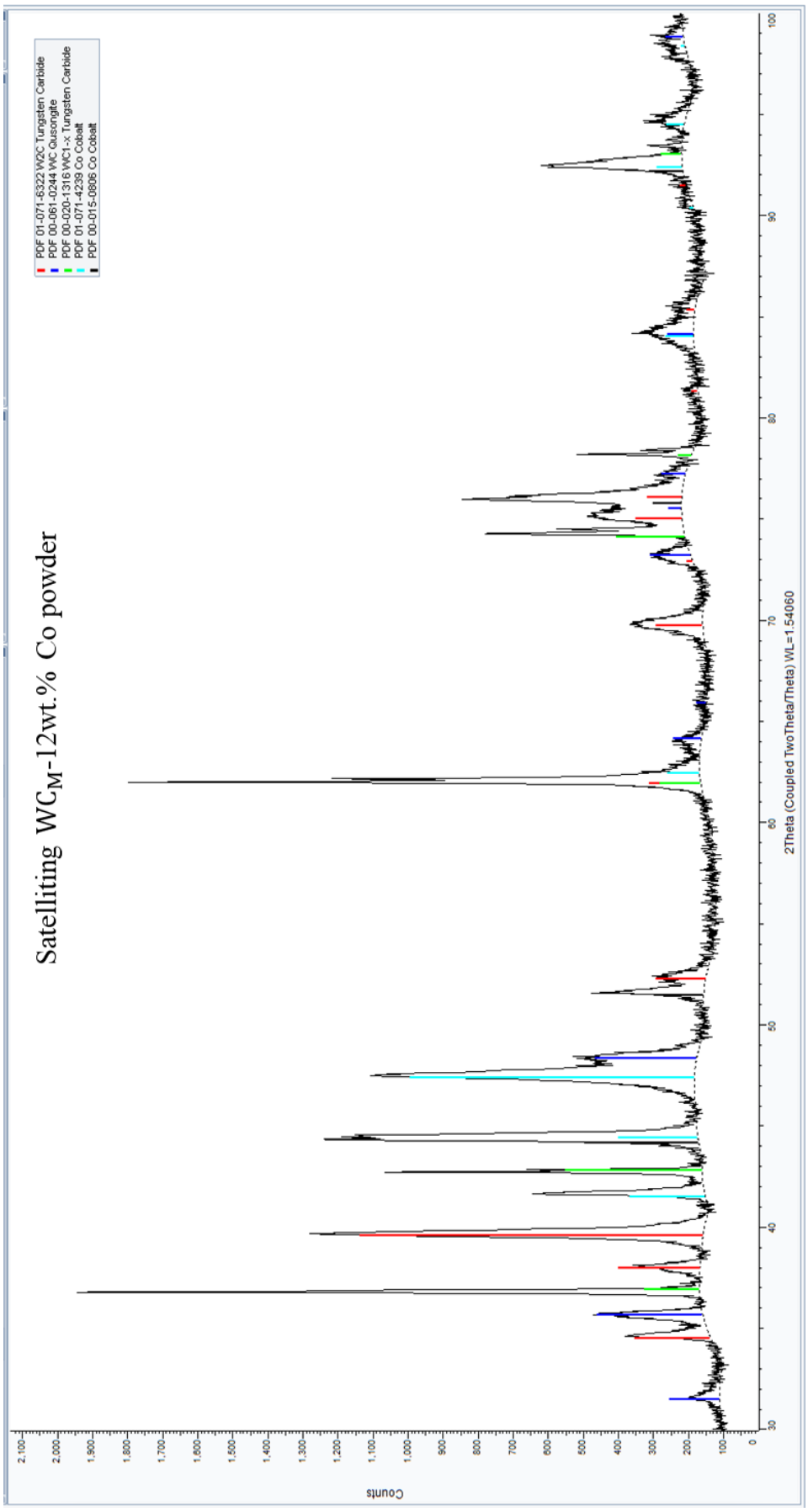
Satelliting WCм-12wt.% Co powder
PDF 01-071-6322 W2C Tungsten Carbide
PDF 00-061-0244 WC Qusongite
PDF 00-020-1316 WC1-x Tungsten Carbide
PDF 01-071-4239 Co Cobalt
PDF 00-015-0806 Co Cobalt
Counts
2Theta (Coupled TwoTheta/Theta) WL=1.54060

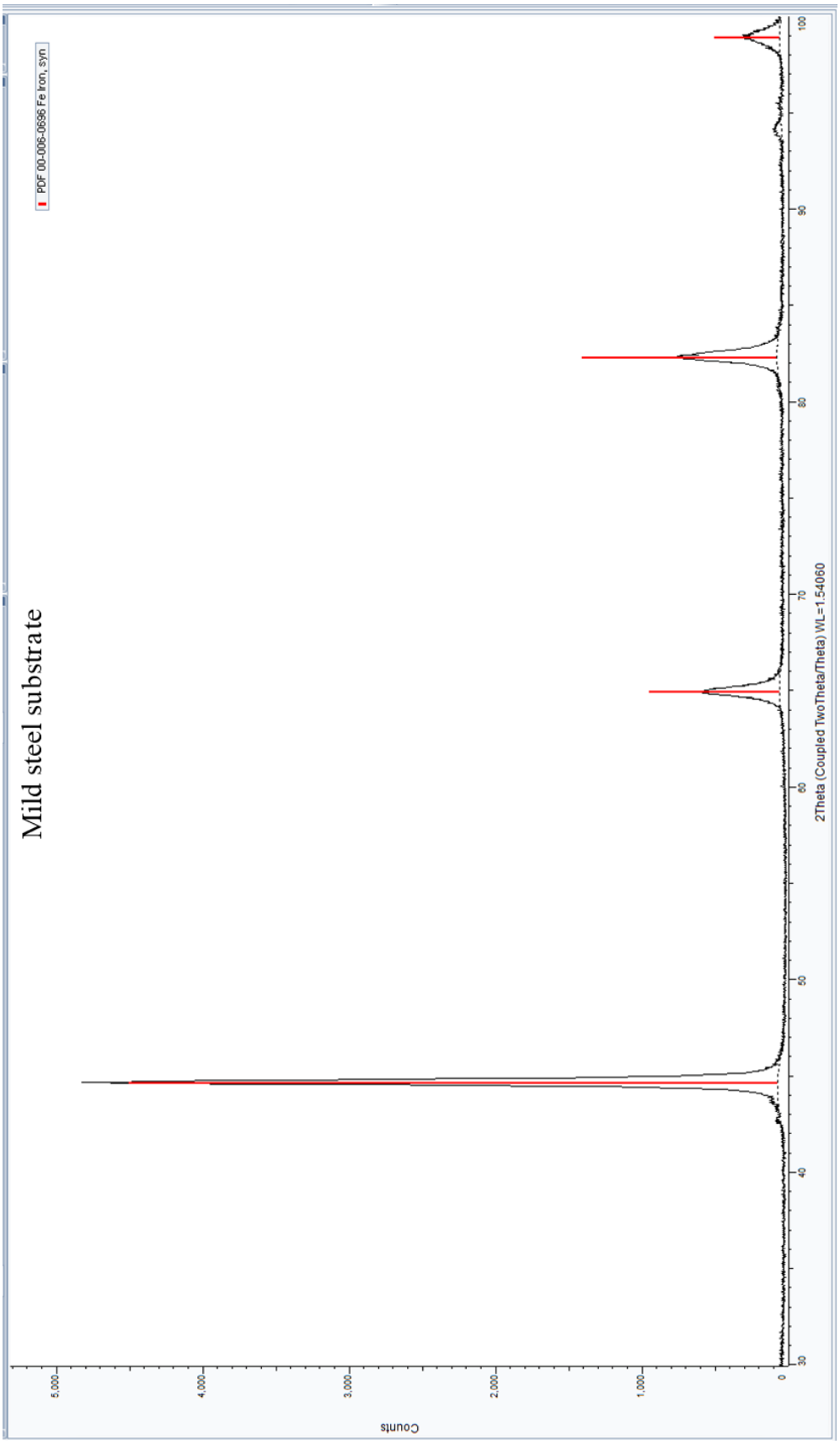
Mild steel substrate
PDF 00-006-0696 Fe Iron, syn
Counts
5.000
4.000
3.000
2.000
1.000
0
30
40
50
60
70
80
90
100
2Theta (Coupled TwoTheta/Theta) WL=1.54060

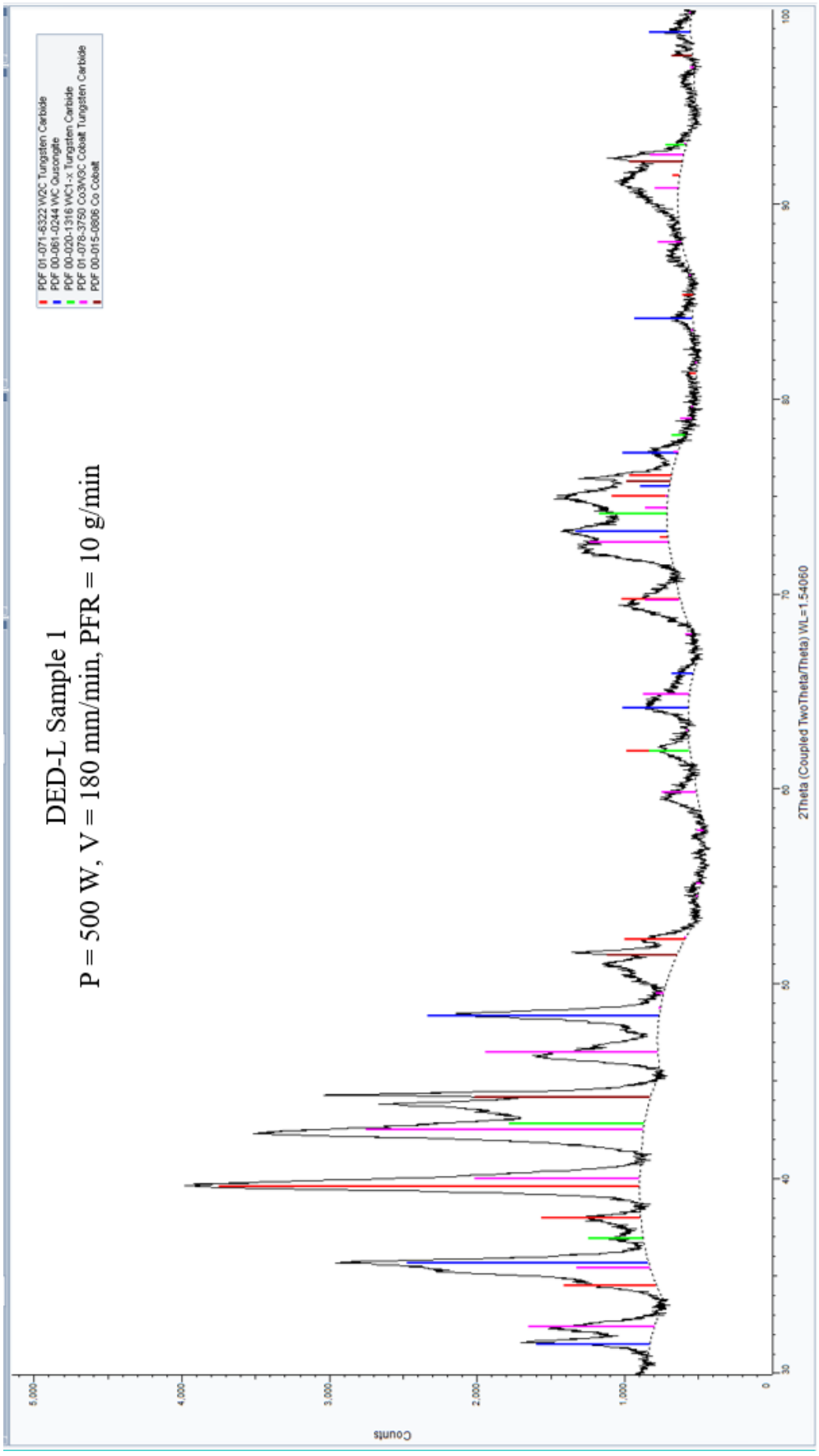
DED-L Sample 1
P = 500 W, V = 180 mm/min, PFR = 10 g/min
PDF 01-071-6322 W2C Tungsten Carbide
PDF 00-061-0244 WC Qusongite
PDF 00-020-1316 WC1-x Tungsten Carbide
PDF 01-078-3750 Co3W3C Cobalt Tungsten Carbide
PDF 00-015-0806 Co Cobalt
Counts
2Theta (Coupled TwoTheta/Theta) WL=1.54060

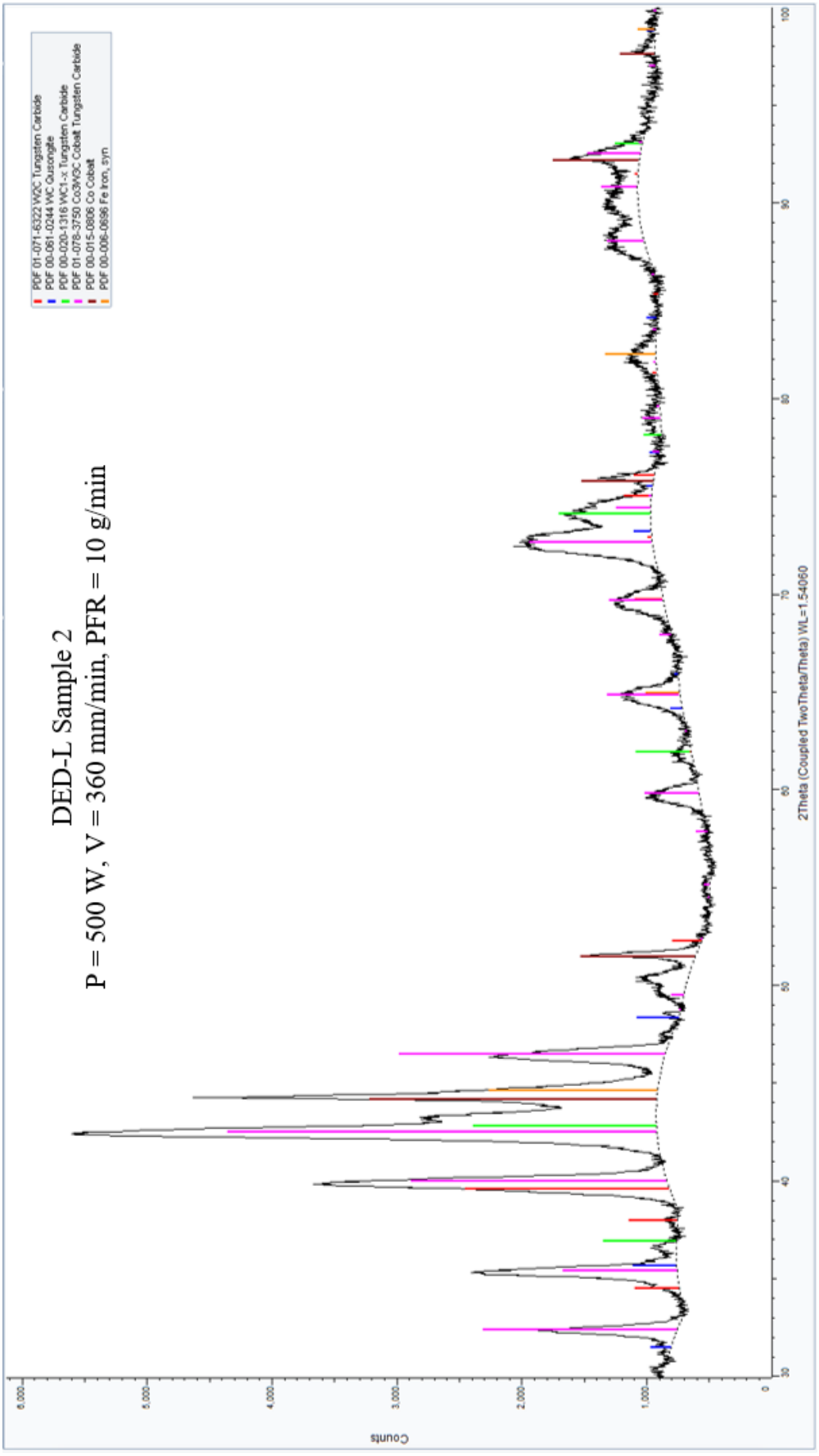
DED-L Sample 2
P = 500 W, V = 360 mm/min, PFR = 10 g/min
PDF 01-071-6322 W2C Tungsten Carbide
PDF 00-061-0244 WC Qusongite
PDF 00-020-1316 WC1-x Tungsten Carbide
PDF 01-078-3750 Co3W3C Cobalt Tungsten Carbide
PDF 00-015-0806 Co Cobalt
PDF 00-006-0696 Fe Iron, syn
Counts
2Theta (Coupled TwoTheta/Theta) WL=1.54060

D.3: L-PBF X-ray diffraction standards

This section shows the ICDD files of plasma densified WC-17 wt.% Co powder and L-PBF sample presented in Figure 5.31-chapter 5. The phases' files were taken from the 2015 JCPDS-International Centre for Diffraction Data. The JCPDS files of WC (hcp), Co (fcc), Co_6W_6C (fcc), and W_2C (hcp) phases are given in the tables below.

WC Tungsten Carbide		**2θ (°)**	**d (Å)**	**Intensity**	**h**	**k**	**l**
System	Hexagonal	31.555	2.83300	48	0	0	1
S.G.	P-6m2 (187)	35.729	2.51100	101	1	0	0
a (Å)	2.902	48.437	1.87780	97	1	0	1
c (Å)	2.831	64.228	1.44900	28	1	1	0
Radiation	CuKa1λ	65.965	1.41500	10	0	0	2
Standard no.	00-061-0244	73.263	1.29100	39	1	1	1
		75.586	1.25700	13	2	0	0
		77.326	1.23300	24	1	0	2
		84.197	1.14900	25	2	0	1
		98.869	1.01400	18	1	1	2
		117.548	0.90080	25	2	1	1

Co_6W_6C Cobalt Tungsten Carbide		**2θ (°)**	**d (Å)**	**Intensity**	**h**	**k**	**l**
System	Cubic	32.840	2.72500	31	4	0	0
S.G.	Fd-3m (227)	35.892	2.50000	31	3	3	1
a (Å)	10.898	40.453	2.22800	5	4	2	2
Radiation	CuKa1λ	43.081	2.09800	100	5	1	1
Standard no.	00-022-0597	47.124	1.92700	35	4	4	0
		60.634	1.52600	16	7	1	1
		65.755	1.41900	16	7	3	1
		70.785	1.33000	20	7	3	3
		73.595	1.28600	50	8	2	2

Co Cobalt		**2θ (°)**	**d (Å)**	**Intensity**	**h**	**k**	**l**
System	Cubic	44.217	2.04670	101	1	1	1
S.G.	Fm-3m (225)	51.524	1.77230	41	2	0	0
a (Å)	3.5447	75.855	1.25320	26	2	2	0
Radiation	CuKa1λ	92.227	1.06880	31	3	1	1
Standard no.	00-015-0806	97.660	1.02330	13	2	2	2

W_2C Tungsten Carbide		**2θ (°)**	**d (Å)**	**Intensity**	**h**	**k**	**l**
System	Hexagonal	18.756	4.72730	1	0	0	1
S.G.	P-31m (162)	19.744	4.49294	1	1	0	0
a (Å)	5.188	27.363	3.25669	1	1	0	1
c (Å)	4.7273	34.550	2.59400	214	1	1	0
Radiation	CuKa1λ	38.040	2.36365	235	0	0	2
Standard no.	01-076-7103	39.598	2.27412	999	-1	-1	1
		43.214	2.09184	1	1	0	2
		44.623	2.02902	1	2	0	1
		52.322	1.74713	156	-1	-1	2
		53.951	1.69817	1	2	1	0
		56.466	1.62834	1	2	0	2
		57.630	1.59818	1	-2	-1	1
		58.529	1.57577	1	0	0	3
		61.907	1.49765	169	3	0	0
		65.304	1.42771	1	3	0	1
		69.775	1.34675	160	-1	-1	3
		72.870	1.29700	21	2	2	0
		75.019	1.26508	163	3	0	2
		76.028	1.25078	123	-2	-2	1
		79.475	1.20496	1	-3	-1	1
		81.353	1.18183	23	0	0	4
		83.653	1.15509	1	-2	-1	3
		85.289	1.13706	31	-2	-2	2
		86.596	1.12323	1	4	0	0
		88.662	1.10231	1	-3	-1	2
		89.640	1.09281	1	4	0	1
		90.403	1.08556	1	3	0	3
		91.491	1.07547	22	-1	-1	4
		94.865	1.04592	1	2	0	4
		96.717	1.03075	1	3	2	0
		98.802	1.01451	1	4	0	2
		99.792	1.00709	1	-3	-2	1
		100.567	1.00141	59	-2	-2	3
		103.565	0.98044	17	4	1	0
		106.717	0.96001	106	-4	-1	1
Line with multiple indexes		109.123	0.94546	1	0	0	5
		109.123	0.94546	1	-3	-2	2
		112.256	0.92775	69	3	0	4
		114.743	0.91465	1	4	0	3
		116.549	0.90562	35	-4	-1	2
		118.015	0.89859	1	5	0	0
		120.262	0.88830	48	-1	-1	5
		123.718	0.87356	14	-2	-2	4
		125.964	0.86467	32	3	3	0
		127.872	0.85751	1	-3	-1	4
		129.820	0.85056	1	-3	-3	1
		130.245	0.84909	1	4	2	0
		133.009	0.83994	1	5	0	2
		134.360	0.83571	1	-4	-2	1
		135.437	0.83246	91	-4	-1	3
		137.655	0.82606	1	-2	-1	5
		143.100	0.81204	58	-3	-3	2
		145.328	0.80696	1	5	1	0
Line with multiple indexes		148.946	0.79948	1	-4	-2	2
		148.946	0.79948	1	3	0	5

D.4: X-ray diffraction patterns of plasma densified WC-17 wt.% Co powder and L-PBF sample presented in Figure 5.31- chapter 5.

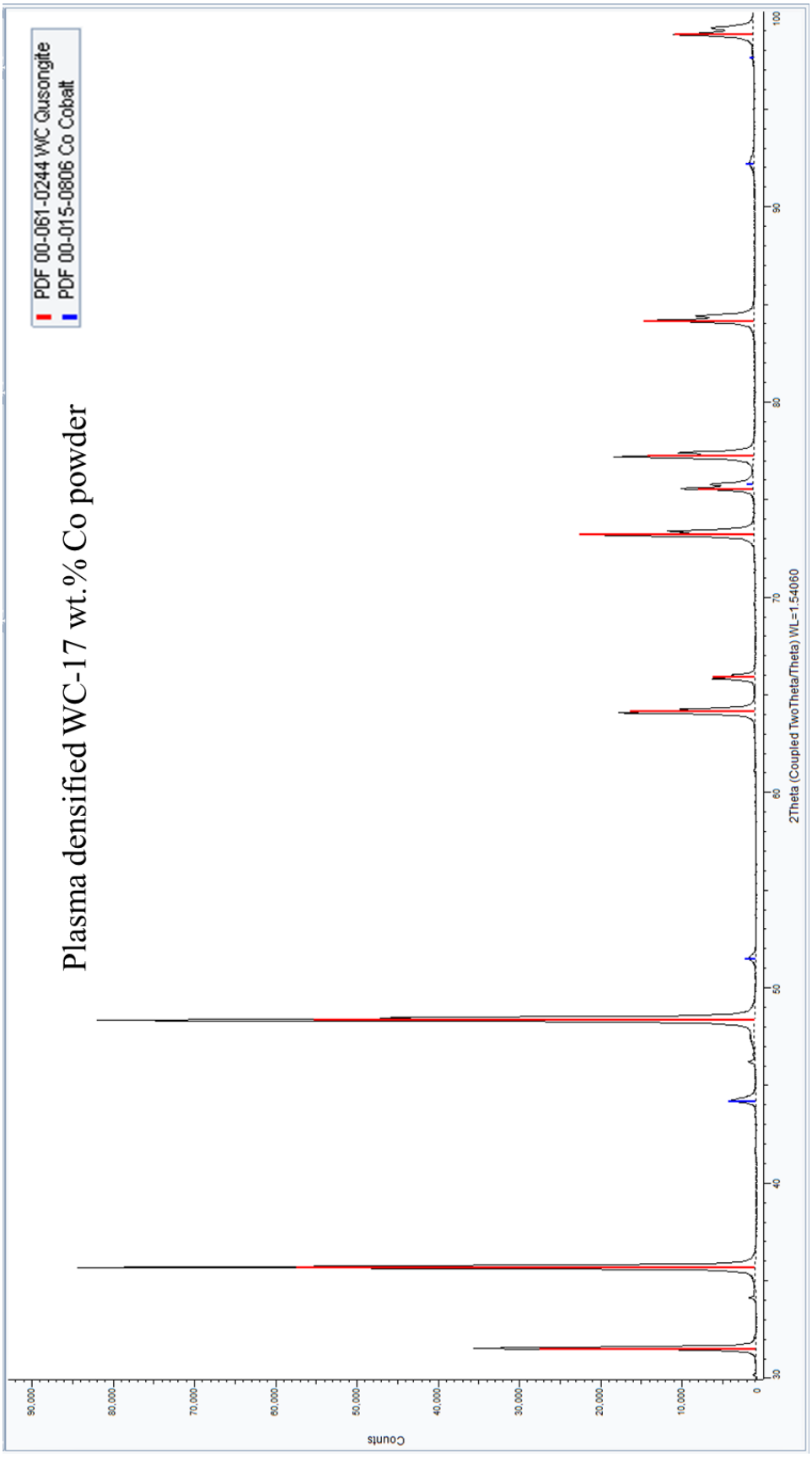

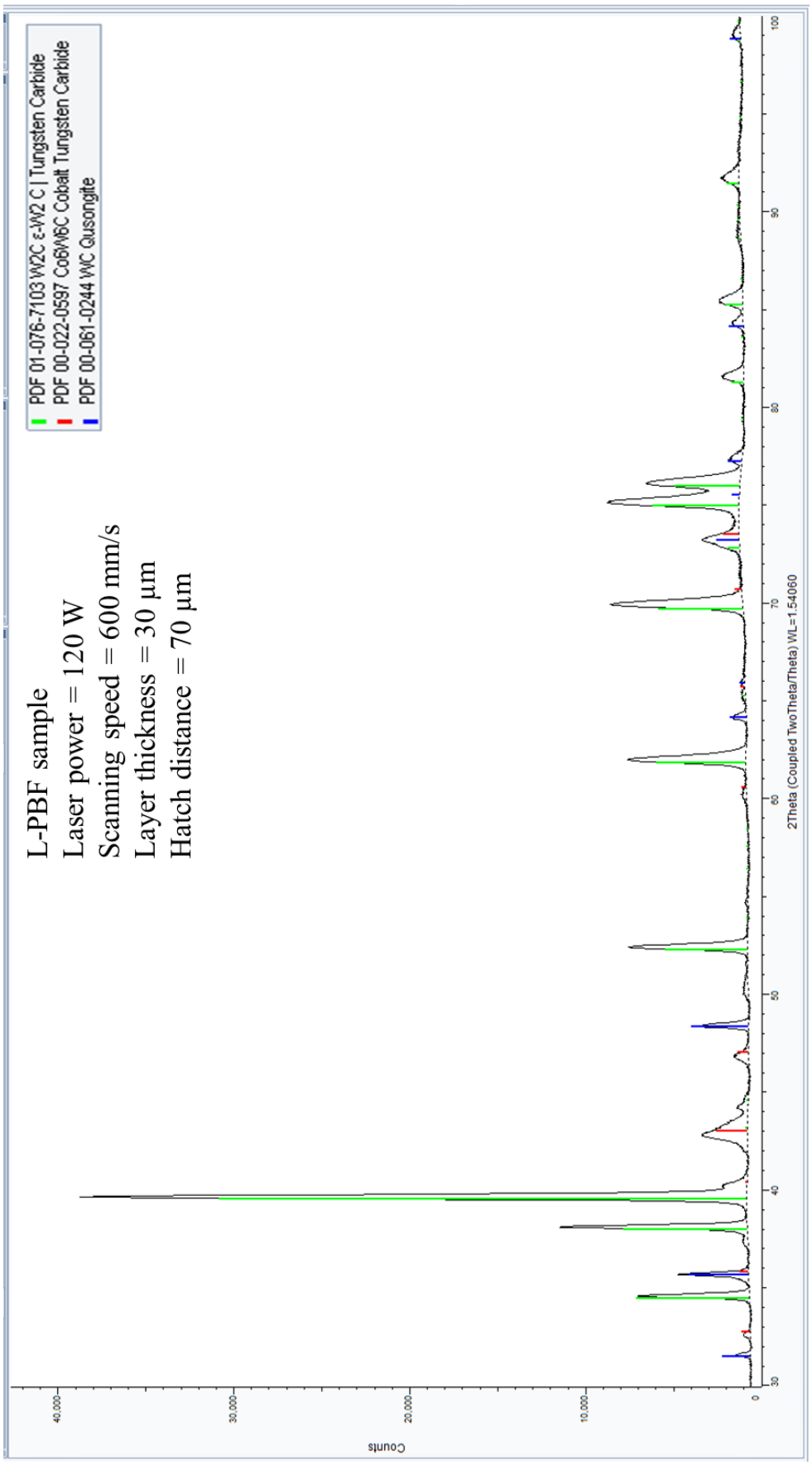
PDF 01-076-7103 W2C ε-W2 C | Tungsten Carbide
PDF 00-022-0597 Co6W6C Cobalt Tungsten Carbide
PDF 00-061-0244 WC Qusongite
L-PBF sample
Laser power = 120 W
Scanning speed = 600 mm/s
Layer thickness = 30 µm
Hatch distance = 70 µm
Counts
40,000
30,000
20,000
10,000
0
30
40
50
60
70
80
90
100
2Theta (Coupled TwoTheta/Theta) WL=1.54060

Appendix E

E.1: To simplify the Rosenthal equation (Eq.3.8 in section 3.1.2-chapter 3), auxiliary constants M and N have been defined as given in Eq.E.1 and Eq.E.2, respectively [117].

$$M = \frac{v}{2\alpha_e} \qquad [m^{-1}] \tag{E.1}$$

$$N = \frac{2\pi \lambda_e (T_m - T_o)}{\eta_e P} \qquad [m^{-1}] \tag{E.2}$$

Using the above constants, the Rosenthal equation can be re-written as:

$$\ln (Nr) + M (\xi + r) = 0 \tag{E.3}$$

By expressing the equation in cylindrical coordinates ($\xi = r \cos \theta$, and $y = r \sin \theta$), it gives the following expression:

$$\ln (Nr) + Mr (\cos \theta + 1) = 0 \tag{E.4}$$

This can be put as:

$$Nr = \exp^{-Mr (\cos\theta+1)} \tag{E.5}$$

The later equation was solved using MATLAB software to find out the melt pool radius (r) as a function of θ as given below.

```
>> syms M N r theta;
>> eq1=exp(-M*r*(cos(theta) + 1)) == N*r;
>> isolate (eq1,r)
ans =
r == lambertw(0, (M*(cos(theta) + 1))/N)/(M*(cos(theta) + 1))
```
(E.6)

The process parameters and the values of M and N for the satellited WC_M-12 wt.% Co and plasma densified WC-17 wt.% Co powders are given in Table E.1.

Table E.1: Process parameters and the values of $M=V/2\alpha_e$, and $N=2\pi\lambda_e(T_m- T_0)/(\eta_e P)$ used to calculate the melt pool size of the satellited WC_M-12 wt.% Co and plasma densified WC-17 wt.% Co powders in L-PBF using Rosenthal equation.

Powder	Process parameters		Rosenthal constants	
	Laser power (W)	Scanning speed (m/s)	M (m^{-1})	N (m^{-1})
Satellited WC_M-12 wt.% Co	100	0.14	1166	9377
Plasma densified WC-17 wt.% Co	120	0.6	6000	8136

E.2: MATLAB code to find out the theoretical melt pool size of the satellited WC_M-12 wt.% Co powder in section 5.2.1.1 – chapter 5 using the Rosenthal equation E.6 and corresponding constants in Table E.1.

```
clear
clc
theta=0:0.05:6.25;
M=1166;
N=9377;
for i=1:length(theta)
r(i) = lambertw(0, (M*(cos(theta(i)) + 1))/N)/(M*(cos(theta(i)) +
1));
end
```

E.3: MATLAB code to find out the theoretical melt pool size of the plasma densified WC-17 wt.% Co powder in section 5.2.2.1 – chapter 5 using the Rosenthal equation E.6 and corresponding constants in Table E.1.

```
clear
clc
theta=0:0.05:6.25;
M=6000;
N=8136;
for i=1:length(theta)
r(i) = lambertw(0, (M*(cos(theta(i)) + 1))/N)/(M*(cos(theta(i)) +
1));
end
```

References

[1] D. Kotoban, A. Nazarov, I. Shishkovsky, Comparative study of selective laser melting and direct laser metal deposition of Ni3Al intermetallic alloy, Procedia IUTAM 23 (2017) 138-146.

[2] D. Gu, Laser additive manufacturing of high-performance materials, book, Springer, 2015.

[3] B. Nagarajan, Z. Hu, X. Song, W. Zhai, J. Wei, Development of micro selective laser melting: The state of the art and future perspectives, Engineering 5(4) (2019) 702-720.

[4] S. Dong, X. Zhang, F. Ma, J. Jiang, W. Yang, Z. Lin, Research on metallurgical bonding of selective laser melted AlSi10Mg alloy, Materials Research Express 7(2) (2020) 025801.

[5] D. Gu, H. Wang, F. Chang, D. Dai, P. Yuan, Y.-C. Hagedorn, W. Meiners, Selective laser melting additive manufacturing of TiC/AlSi10Mg bulk-form nanocomposites with tailored microstructures and properties, Physics Procedia 56 (2014) 108-116.

[6] J. Zhang, F. Li, Q. Zhu, H. Zhang, Preparation of Silicon Carbide Reinforced Aluminium Matrix Composites (SiC/Al) by Selective Laser Melting, IOP Publishing, p. 012015.

[7] Z. Fan, H. Feng, Study on selective laser melting and heat treatment of Ti-6Al-4V alloy, Results in Physics 10 (2018) 660-664.

[8] W. Xu, E.W. Lui, A. Pateras, M. Qian, M. Brandt, In situ tailoring microstructure in additively manufactured Ti-6Al-4V for superior mechanical performance, Acta Materialia 125 (2017) 390-400.

References

[9] W. Xu, M. Brandt, S. Sun, J. Elambasseril, Q. Liu, K. Latham, K. Xia, M. Qian, Additive manufacturing of strong and ductile Ti–6Al–4V by selective laser melting via in situ martensite decomposition, Acta Materialia 85 (2015) 74-84.

[10] S.S. Babu, N. Raghavan, J. Raplee, S.J. Foster, C. Frederick, M. Haines, R. Dinwiddie, M.K. Kirka, A. Plotkowski, Y. Lee, Additive manufacturing of nickel superalloys: opportunities for innovation and challenges related to qualification, Metallurgical and Materials Transactions A 49(9) (2018) 3764-3780.

[11] H. Zhang, D. Gu, L. Xi, H. Zhang, M. Xia, C. Ma, Anisotropic corrosion resistance of TiC reinforced Ni-based composites fabricated by selective laser melting, Journal of Materials Science & Technology 35(6) (2019) 1128-1136.

[12] S. Cacace, A.G. Demir, Q. Semeraro, Densification mechanism for different types of stainless steel powders in selective laser melting, Procedia Cirp 62 (2017) 475-480.

[13] E. Liverani, S. Toschi, L. Ceschini, A. Fortunato, Effect of selective laser melting (SLM) process parameters on microstructure and mechanical properties of 316L austenitic stainless steel, Journal of Materials Processing Technology 249 (2017) 255-263.

[14] R. Zahiri, R. Sundaramoorthy, P. Lysz, C. Subramanian, Hardfacing using ferro-alloy powder mixtures by submerged arc welding, Surface and Coatings Technology 260 (2014) 220-229.

[15] C. Cui, Z. Guo, Y. Liu, Q. Xie, Z. Wang, J. Hu, Y. Yao, Characteristics of cobalt-based alloy coating on tool steel prepared by powder feeding laser cladding, Optics & Laser Technology 39(8) (2007) 1544-1550.

[16] F. Arias-González, J. Del Val, R. Comesaña, J. Penide, F. Lusquiños, F. Quintero, A. Riveiro, M. Boutinguiza, J. Pou, Fiber laser cladding of nickel-based alloy on cast iron, Applied Surface Science 374 (2016) 197-205.

[17] J.-m. Chen, G. Chun, J.-s. Zhou, Microstructure and tribological properties of laser cladding Fe-based coating on pure Ti substrate, Transactions of Nonferrous Metals Society of China 22(9) (2012) 2171-2178.

[18] L. Song, G. Zeng, H. Xiao, X. Xiao, S. Li, Repair of 304 stainless steel by laser cladding with 316L stainless steel powders followed by laser surface alloying with WC powders, Journal of Manufacturing Processes 24 (2016) 116-124.

[19] A. Riveiro, A. Mejías, F. Lusquiños, J. Del Val, R. Comesaña, J. Pardo, J. Pou, Laser cladding of aluminium on AISI 304 stainless steel with high-power diode lasers, Surface and Coatings Technology 253 (2014) 214-220.

[20] J. Leunda, V.G. Navas, C. Soriano, C. Sanz, Effect of laser tempering of high alloy powder metallurgical tool steels after laser cladding, Surface and Coatings Technology 259 (2014) 570-576.

[21] M. Zhong, W. Liu, Laser surface cladding: the state of the art and challenges, Proceedings of the Institution of Mechanical Engineers, Part C: Journal of Mechanical Engineering Science 224(5) (2010) 1041-1060.

[22] B.G. Park, A.G. Crosky, A.K. Hellier, Material characterisation and mechanical properties of Al2O3-Al metal matrix composites, Journal of materials science 36(10) (2001) 2417-2426.

[23] S. Catchpole-Smith, A.T. Clare, In-situ synthesis of titanium aluminides by direct metal deposition, Journal of Materials Processing Technology 239 (2017) 230-239.

[24] M. Zhong, X. Xu, W. Liu, H. Sun, Laser synthesizing NiAl intermetallic and TiC reinforced NiAl intermetallic matrix composite, Journal of Laser Applications 16(3) (2004) 160-166.

[25] J. Liang, X. Yin, Z. Lin, S. Chen, C. Liu, C. Wang, Microstructure and wear behaviors of laser cladding in-situ synthetic (TiBx+ TiC)/(Ti2Ni+ TiNi) gradient composite coatings, Vacuum (2020) 109305.

[26] H. Zhang, Y. Zou, Z. Zou, W. Zhao, Comparative study on continuous and pulsed wave fiber laser cladding in-situ titanium–vanadium carbides reinforced Fe-based composite layer, Materials Letters 139 (2015) 255-257.

[27] F. Wang, J. Mei, X. Wu, Direct laser fabrication of Ti6Al4V/TiB, Journal of materials processing technology 195(1-3) (2008) 321-326.

[28] T. Chen, F. Wu, H. Wang, D. Liu, Laser cladding in-situ Ti (C, N) particles reinforced Ni-based composite coatings modified with CeO2 nanoparticles, Metals 8(8) (2018) 601.

[29] H.X. Zhang, H.J. Yu, C.Z. Chen, In-situ forming composite coating by laser cladding C/B4C, Materials and Manufacturing Processes 30(6) (2015) 743-747.

[30] D. Shu, Z. Li, K. Zhang, C. Yao, D. Li, Y. Yuan, Z. Dai, Phase constituents and growth mechanism of laser in situ synthesized WC reinforced composite coating with WC-Ni system, Journal of Materials Research 32(3) (2017) 557.

[31] M. Yu, W.Y. Li, X.K. Suo, H.L. Liao, Effects of gas temperature and ceramic particle content on microstructure and microhardness of cold sprayed SiCp/Al 5056 composite coatings, Surface and Coatings Technology 220 (2013) 102-106.

[32] M.H. Enayati, G.R. Aryanpour, A. Ebnonnasir, Production of nanostructured WC–Co powder by ball milling, International Journal of Refractory Metals and Hard Materials 27(1) (2009) 159-163.

[33] M. Yandouzi, L. Ajdelsztajn, B. Jodoin, WC-based composite coatings prepared by the pulsed gas dynamic spraying process: Effect of the feedstock powders, Surface and coatings technology 202(16) (2008) 3866-3877.

[34] M. He, J. Wang, R. He, H. Yang, J. Ruan, Effect of cobalt content on the microstructure and mechanical properties of coarse grained WC-Co cemented carbides fabricated from chemically coated composite powder, Journal of Alloys and Compounds 766 (2018) 556-563.

[35] D.E. Wolfe, T.J. Eden, J.K. Potter, A.P. Jaroh, Investigation and characterization of Cr 3 C 2-based wear-resistant coatings applied by the cold spray process, Journal of thermal spray technology 15(3) (2006) 400-412.

[36] S.W. Huang, M. Samandi, M. Brandt, Abrasive wear performance and microstructure of laser clad WC/Ni layers, Wear 256(11-12) (2004) 1095-1105.

[37] A. Riquelme, P. Rodrigo, M.D. Escalera-Rodríguez, J. Rams, Corrosion Resistance of Al/SiC Laser Cladding Coatings on AA6082, Coatings 10(7) (2020) 673.

[38] P. Xu, C. Lin, C. Zhou, X. Yi, Wear and corrosion resistance of laser cladding AISI 304 stainless steel/Al2O3 composite coatings, Surface and Coatings Technology 238 (2014) 9-14.

[39] P.K. Farayibi, Laser cladding of Ti-6Al-4V with carbide and boride reinforcements using wire and powder feedstock, PhD thesis, University of Nottingham, UK, 2014.

[40] A. Mthisi, A.P.I. Popoola, D.I. Adebiyi, O.M. Popoola, Laser Cladding of Ti-6Al-4V Alloy with Ti-Al2O3 Coating for Biomedical Applications, IOP: Materials Science and Engineering 350 (2018) 012005.

[41] K.S. Al-Hamdani, J.W. Murray, T. Hussain, A.T. Clare, Controlling ceramic-reinforcement distribution in laser cladding of MMCs, Surface and Coatings Technology 381 (2020) 125128.

[42] J.D. Majumdar, A. Kumar, L. Li, Direct laser cladding of SiC dispersed AISI 316L stainless steel, Tribology International 42(5) (2009) 750-753.

[43] T.E. Abioye, Laser deposition of Inconel 625/tungsten carbide composite coatings by powder and wire feedstock, PhD thesis, University of Nottingham, UK, 2014.

[44] S. Sun, Y. Durandet, M. Brandt, Correlation between melt pool temperature and clad formation in pulsed and continuous wave Nd: YAG laser cladding of Stellite 6, Proceedings of the 1st Pacific International Conference on Application of Lasers and Optics. Laser Institute of America, 2004.

[45] L. Wang, P. Pratt, S.D. Felicelli, H. El Kadiri, J.T. Berry, P.T. Wang, M.F. Horstemeyer, Pore formation in laser-assisted powder deposition process, Journal of manufacturing science and engineering 131(5) (2009).

[46] H. Qi, J. Mazumder, H. Ki, Numerical simulation of heat transfer and fluid flow in coaxial laser cladding process for direct metal deposition, Journal of applied physics 100(2) (2006) 024903.

[47] U. De Oliveira, V. Ocelik, J.T.M. De Hosson, Analysis of coaxial laser cladding processing conditions, Surface and Coatings Technology 197(2-3) (2005) 127-136.

[48] I. Tabernero, A. Lamikiz, S. Martínez, E. Ukar, L.N.L. De Lacalle, Modelling of energy attenuation due to powder flow-laser beam interaction during laser cladding process, Journal of materials processing technology 212(2) (2012) 516-522.

[49] J. Lin, Laser attenuation of the focused powder streams in coaxial laser cladding, Journal of laser applications 12(1) (2000) 28-33.

[50] W. Ya, Laser materials interactions during cladding: analyses on clad formation, thermal cycles, residual stress and defects, PhD thesis, University of Twente, Netherlands, 2015.

[51] G. Piscopo, E. Atzeni, A. Salmi, A Hybrid Modeling of the Physics-Driven Evolution of Material Addition and Track Generation in Laser Powder Directed Energy Deposition, Materials 12(17) (2019) 2819.

[52] S. Zanzarin, Laser cladding with metallic powders, PhD thesis, University of Trento, Italy, 2015.

[53] J. Ibarra-Medina, M. Vogel, A.J. Pinkerton, A CFD model of laser cladding: from deposition head to melt pool dynamics, International Congress on Applications of Lasers & Electro-Optics. Laser Institute of America, 2011.

[54] D. Triantafyllidis, L. Li, H. Stott, Modeling of Boundary Porosity Formation in Laser Melting and Re-Solidification of Ceramics, Journal of the American Ceramic Society 89(4) (2006) 1286-1294.

[55] H.J. Niu, I.H. Chang, Selective laser sintering of gas and water atomized high speed steel powders, Scripta Materialia 41(1) (1999) 25-30.

[56] B. Song, T. Hussain, K.T. Voisey, Laser cladding of Ni50Cr: A parametric and dilution study, Physics Procedia 83 (2016) 706-715.

[57] M. Thomas, G.J. Baxter, I. Todd, Normalised model-based processing diagrams for additive layer manufacture of engineering alloys, Acta Materialia 108 (2016) 26-35.

[58] M. Erfanmanesh, H. Abdollah-Pour, H. Mohammadian-Semnani, R. Shoja-Razavi, An empirical-statistical model for laser cladding of WC-12Co powder on AISI 321 stainless steel, Optics & Laser Technology 97 (2017) 180-186.

[59] J. Liu, Y. Song, C. Chen, X. Wang, H. Li, J. Wang, K. Guo, J. Sun, Effect of scanning speed on the microstructure and mechanical behavior of 316L stainless steel fabricated by selective laser melting, Materials & Design 186 (2020) 108355.

[60] A. Dass, A. Moridi, State of the art in directed energy deposition: From additive manufacturing to materials design, Coatings 9(7) (2019) 418.

[61] B. Bax, R. Rajput, R. Kellet, M. Reisacher, Systematic evaluation of process parameter maps for laser cladding and directed energy deposition, Additive Manufacturing 21 (2018) 487-494.

[62] A. Emamian, S.F. Corbin, A. Khajepour, Effect of laser cladding process parameters on clad quality and in-situ formed microstructure of Fe–TiC composite coatings, Surface and Coatings Technology 205(7) (2010) 2007-2015.

[63] D.M. Goodarzi, J. Pekkarinen, A. Salminen, Effect of process parameters in laser cladding on substrate melted areas and the substrate melted shape, J. Laser Appl 27(S2) (2015) S29201.

[64] D.J. Corbin, A.R. Nassar, E.W. Reutzel, A.M. Beese, N.A. Kistler, Effect of directed energy deposition processing parameters on laser deposited Inconel® 718: External morphology, J. Laser Appl 29(2) (2017).

[65] S. Shi, A. Xu, J. Fan, H. Wei, Study of cobalt-free, Fe-based alloy powder used for sealing surfaces of nuclear valves by laser cladding, Nuclear engineering and design 245 (2012) 8-12.

[66] Z. Zhou, L. Huang, Y. Shang, Y. Li, L. Jiang, Q. Lei, Causes analysis on cracks in nickel-based single crystal superalloy fabricated by laser powder deposition additive manufacturing, Materials & Design 160 (2018) 1238-1249.

[67] Y. Korobov, Y. Khudorozhkova, H. Hillig, A. Vopneruk, A. Kotelnikov, S. Burov, P. Balu, A. Makarov, A. Chernov, The effect of thickness on the properties of laser-deposited NiBSi-WC coating on a Cu-Cr-Zr substrate, Photonics. Vol. 6. No. 4. Multidisciplinary Digital Publishing Institute, 2019.

[68] X. Luo, Z. Yao, P. Zhang, D. Gu, Al2O3 nanoparticles reinforced Fe-Al laser cladding coatings with enhanced mechanical properties, Journal of Alloys and Compounds 755 (2018) 41-54.

[69] J.M. Amado, M.J. Tobar, J.C. Alvarez, J. Lamas, A. Yáñez, Laser cladding of tungsten carbides (Spherotene®) hardfacing alloys for the mining and mineral industry, Applied Surface Science 255(10) (2009) 5553-5556.

[70] G.K.L. Ng, A.E.W. Jarfors, G. Bi, H.Y. Zheng, Porosity formation and gas bubble retention in laser metal deposition, Applied Physics A 97(3) (2009) 641.

[71] A.A.A. Younis, Microstructure, mechanical properties and sliding wear behaviour of thermally sprayed cermet coatings, PhD thesis, University of Nottingham, UK, 2016.

[72] R.J.K. Wood, Tribology of thermal sprayed WC–Co coatings, International Journal of Refractory Metals and Hard Materials 28(1) (2010) 82-94.

[73] G. Bolelli, A. Colella, L. Lusvarghi, S. Morelli, P. Puddu, E. Righetti, P. Sassatelli, V. Testa, TiC–NiCr thermal spray coatings as an alternative to WC-CoCr and Cr3C2–NiCr, Wear (2020) 203273.

[74] J. Sampedro, I. Pérez, B. Carcel, J.A. Ramos, V. Amigó, Laser cladding of TiC for better titanium components, Physics Procedia 12 (2011) 313-322.

[75] W. Chen, B. Liu, L. Chen, J. Xu, Y. Zhu, Effect of Laser Cladding Stellite 6-Cr3C2-WS2 Self-Lubricating Composite Coating on Wear Resistance and Microstructure of H13, Metals 10(6) (2020) 785.

[76] M. Cadenas, R. Vijande, H. Montes, J. Sierra, Wear behaviour of laser cladded and plasma sprayed WC-Co coatings, Wear 212(2) (1997) 244-253.

[77] J. Picas, Y. Xiong, M. Punset, L. Ajdelsztajn, A. Forn, J. Schoenung, Microstructure and wear resistance of WC–Co by three consolidation processing techniques, International Journal of Refractory Metals and Hard Materials 27(2) (2009) 344-349.

[78] H. Wang, T. Webb, J.W. Bitler, Study of thermal expansion and thermal conductivity of cemented WC–Co composite, International Journal of Refractory Metals and Hard Materials 49 (2015) 170-177.

[79] Y. Xiong, J.E. Smugeresky, J.M. Schoenung, The influence of working distance on laser deposited WC–Co, Journal of Materials Processing Technology 209(10) (2009) 4935-4941.

[80] W.D. Kaplan, D. Chatain, P. Wynblatt, W.C. Carter, A review of wetting versus adsorption, complexions, and related phenomena: the rosetta stone of wetting, Journal of Materials Science 48(17) (2013) 5681-5717.

[81] Z. Roulon, Effect of binder on sintering and microstructure of cemented carbides, PhD thesis, Grenoble Alpes University**,** France, 2019.

[82] S. Adjam, D. Mari, T. LaGrange, Strain glass transition of cobalt phase in a cemented carbide, International Journal of Refractory Metals and Hard Materials 87 (2020) 105161.

[83] C. Paul, H. Alemohammad, E. Toyserkani, A. Khajepour, S. Corbin, Cladding of WC–12 Co on low carbon steel using a pulsed Nd: YAG laser, Materials Science and Engineering: A 464(1-2) (2007) 170-176.

[84] Y. Xiong, J.E. Smugeresky, L. Ajdelsztajn, J.M. Schoenung, Fabrication of WC–Co cermets by laser engineered net shaping, Materials Science and Engineering: A 493(1-2) (2008) 261-266.

[85] V.K. Balla, S. Bose, A. Bandyopadhyay, Microstructure and wear properties of laser deposited WC–12%Co composites, Materials Science and Engineering: A 527(24-25) (2010) 6677-6682.

[86] S. Zanzarin, S. Bengtsson, A. Molinari, Study of carbide dissolution into the matrix during laser cladding of carbon steel plate with tungsten carbides-stellite powders, Journal of Laser Applications 27(S2) (2015) S29209.

[87] D. Janicki, J. Górka, A. Kotarska, Laser cladding of Inconel 625-based composite coatings, Welding Technology Review 90(9) (2018).

[88] J. Leunda, C. Soriano, C. Sanz, Inner walls laser cladding of WC reinforced Ni coatings, Lasers in Manufacturing Conference, Munich, Germany, 2015.

[89] J.M. Amado, M.J. Tobar, A. Yáñez, V. Amigó, J.J. Candel, Crack free tungsten carbide reinforced Ni (Cr) layers obtained by laser cladding, Physics Procedia 12 (2011) 338-344.

[90] E. Uhlmann, A. Bergmann, W. Gridin, Investigation on additive manufacturing of tungsten carbide-cobalt by selective laser melting, Procedia CIRP 35 (2015) 8-15.

[91] T. Schwanekamp, M. Reuber, Additive Manufacturing of application optimized tungsten carbide precision tools, Proceedings of 6th International Conference on Additive Technologies, Additive Manufacturing of Metals presented at the 6th International Conference on Additive Technologies iCAT, Nurnberg, Germany, 2016.

[92] S.L. Campanelli, N. Contuzzi, P. Posa, A. Angelastro, Printability and Microstructure of Selective Laser Melting of WC/Co/Cr Powder, Materials 12(15) (2019) 2397.

[93] A. Domashenkov, A. Borbély, I. Smurov, Structural modifications of WC/Co nanophased and conventional powders processed by selective laser melting, Materials and Manufacturing Processes 32(1) (2017) 93-100.

[94] R.S. Khmyrov, A.P. Shevchukov, A.V. Gusarov, T.V. Tarasova, Phase composition and microstructure of WC–Co alloys obtained by selective laser melting, Mechanics & Industry 18(7) (2017) 714.

[95] R.S. Khmyrov, V.A. Safronov, A.V. Gusarov, Obtaining crack-free WC-Co alloys by selective laser melting, Physics Procedia 83 (2016) 874-881.

[96] A. Fortunato, G. Valli, E. Liverani, A. Ascari, Additive Manufacturing of WC-Co Cutting Tools for Gear Production, Lasers in Manufacturing and Materials Processing 6(3) (2019) 247-262.

[97] S. Grigoriev, T. Tarasova, A. Gusarov, R. Khmyrov, S. Egorov, Possibilities of Manufacturing Products from Cermet Compositions Using Nanoscale Powders by Additive Manufacturing Methods, Materials 12(20) (2019) 3425.

[98] J. Chen, M. Huang, Z.Z. Fang, M. Koopman, W. Liu, X. Deng, Z. Zhao, S. Chen, S. Wu, J. Liu, Microstructure analysis of high density WC-Co composite prepared by one step selective laser melting, International Journal of Refractory Metals and Hard Materials 84 (2019) 104980.

[99] T. DebRoy, H.L. Wei, J.S. Zuback, T. Mukherjee, J.W. Elmer, J.O. Milewski, A.M. Beese, A. Wilson-Heid, A. De, W. Zhang, Additive manufacturing of metallic components–process, structure and properties, Progress in Materials Science 92 (2018) 112-224.

[100] H. Ali, H. Ghadbeigi, K. Mumtaz, Effect of scanning strategies on residual stress and mechanical properties of Selective Laser Melted Ti6Al4V, Materials Science and Engineering: A 712 (2018) 175-187.

[101] S. Fries, S. Genilke, M.B. Wilms, M. Seimann, A. Weisheit, A. Kaletsch, T. Bergs, J.H. Schleifenbaum, C. Broeckmann, Laser-Based Additive Manufacturing of WC–Co with High-Temperature Powder Bed Preheating, steel research international (2020) 1900511.

[102] D. Woo, B. Sneed, F. Peerally, F. Heer, L. Brewer, J. Hooper, S. Osswald, Synthesis of nanodiamond-reinforced aluminum metal composite powders and coatings using high-energy ball milling and cold spray, Carbon 63 (2013) 404-415.

[103] W. Li, H. Assadi, F. Gaertner, S. Yin, A Review of Advanced Composite and Nanostructured Coatings by Solid-State Cold Spraying Process, Critical Reviews in Solid State and Materials Sciences (2018) 1-48.

[104] D. Zhang, Processing of advanced materials using high-energy mechanical milling, Progress in Materials Science 49(3-4) (2004) 537-560.

[105] F.L. Zhang, C.Y. Wang, M. Zhu, Nanostructured WC/Co composite powder prepared by high energy ball milling, Scripta materialia 49(11) (2003) 1123-1128.

[106] P. Fauchais, G. Montavon, G. Bertrand, From powders to thermally sprayed coatings, Journal of thermal spray technology 19(1-2) (2010) 56-80.

[107] L.-M. Berger, Hardmetals as thermal spray coatings, Powder Metallurgy 50(3) (2007) 205-214.

[108] H. Zhong, Y. Ouyang, G. Yu, B. Hu, D. Yan, Preparation of core-shell structured cobalt coated tungsten carbide composite powders by intermittent electrodeposition, Journal of Materials Science & Technology 32(11) (2016) 1171-1178.

[109] J.P. Kruth, P. Mercelis, J. Van Vaerenbergh, L. Froyen, M. Rombouts, Binding mechanisms in selective laser sintering and selective laser melting, Rapid prototyping journal (2005).

[110] K. Al-Hamdani, J. Murray, T. Hussain, A. Kennedy, A. Clare, Cold sprayed metal-ceramic coatings using satellited powders, Materials Letters 198 (2017) 184-187.

[111] H. Tan, D. Hao, K. Al-Hamdani, F. Zhang, Z. Xu, A.T. Clare, Direct metal deposition of TiB2/AlSi10Mg composites using satellited powders, Materials Letters 214 (2018) 123-126.

[112] F. Zhang, M. Mei, K. Al-Hamdani, H. Tan, A.T. Clare, Novel nucleation mechanisms through satelliting in direct metal deposition of Ti-15Mo, Materials Letters 213 (2018) 197-200.

[113] M. Simonelli, N.T. Aboulkhair, P. Cohen, J.W. Murray, A.T. Clare, C. Tuck, R.J. Hague, A comparison of Ti-6Al-4V in-situ alloying in Selective Laser Melting using simply-mixed and satellited powder blend feedstocks, Materials Characterization (2018).

[114] Technogenia, Spherotene, [cited in 06/04/2020]. http://www.technogenia.com/product/spherotene/.

[115] C. Guo, J. Zhou, J. Chen, J. Zhao, Y. Yu, H. Zhou, High temperature wear resistance of laser cladding NiCrBSi and NiCrBSi/WC-Ni composite coatings, Wear 270(7-8) (2011) 492-498.

[116] L. Idoughi, X. Mininger, F. Bouillault, L. Bernard, E. Hoang, Thermal model with winding homogenization and FIT discretization for stator slot, IEEE Transactions on Magnetics 47(12) (2011) 4822-4826.

[117] M. Tang, P.C. Pistorius, J.L. Beuth, Prediction of lack-of-fusion porosity for powder bed fusion, Additive Manufacturing 14 (2017) 39-48.

[118] J. Yang, S. Sun, M. Brandt, W. Yan, Experimental investigation and 3D finite element prediction of the heat affected zone during laser assisted machining of Ti6Al4V alloy, Journal of Materials Processing Technology 210(15) (2010) 2215-2222.

[119] F. Fulchini, U. Zafar, C. Hare, M. Ghadiri, H. Tantawy, H. Ahmadian, M. Poletto, Relationship between surface area coverage of flow-aids and flowability of cohesive particles, Powder technology 322 (2017) 417-427.

[120] T. Kojima, J.A. Elliott, Effect of silica nanoparticles on the bulk flow properties of fine cohesive powders, Chemical Engineering Science 101 (2013) 315-328.

[121] J.M. Park, J.-H. Yu, T.G. Kang, S.J. Kim, S.J. Park, Particle size effect on the magneto-rheological behavior of powder injection molding feedstock, Materials Characterization 94 (2014) 19-25.

[122] K.I. Popov, S.B. Krstić, M.Č. Obradović, M.G. Pavlović, L.J. Pavlović, E.R. Ivanović, The effect of the particle shape and structure on the flowability of electrolytic copper powder I: Modeling of a representative powder particle, Journal of the Serbian Chemical Society 68(10) (2003) 771-778.

[123] Z. Liu, H.-C. Zhang, S. Peng, H. Kim, D. Du, W. Cong, Analytical modeling and experimental validation of powder stream distribution during direct energy deposition, Additive Manufacturing 30 (2019) 100848.

[124] D.V. Sergachev, A.A. Mikhal'chenko, O.B. Kovalev, V.I. Kuz'min, G.N. Grachev, P.A. Pinaev, Laser-optic measurements of velocity of particles in the powder stream at coaxial laser cladding, Physics Procedia 56 (2014) 193-203.

[125] A.J. Pinkerton, An analytical model of beam attenuation and powder heating during coaxial laser direct metal deposition, Journal of Physics D: Applied Physics 40(23) (2007) 7323.

[126] D. Janicki, High power direct diode laser cladding of stellite 6+ WC coatings, MTM virtual journal (7) (2012) 57.

[127] S. Wen, Y.C. Shin, Modeling of transport phenomena during the coaxial laser direct deposition process, Journal of Applied Physics 108(4) (2010) 044908.

[128] R.R. Unocic, J.N. DuPont, Process efficiency measurements in the laser engineered net shaping process, Metallurgical and materials transactions B 35(1) (2004) 143-152.

[129] A. Frenk, M. Vandyoussefi, J.D. Wagniere, W. Kurz, A. Zryd, Analysis of the laser-cladding process for stellite on steel, Metallurgical and Materials transactions B 28(3) (1997) 501-508.

[130] J. Pekkarinen, V. Kujanpää, A. Salminen, Laser cladding with scanning optics: Effect of power adjustment, Journal of Laser Applications 24(3) (2012) 7.

[131] J. Liu, J. Li, X. Cheng, H. Wang, Effect of dilution and macrosegregation on corrosion resistance of laser clad AerMet100 steel coating on 300M steel substrate, Surface and Coatings Technology 325 (2017) 352-359.

[132] P. Wu, H.M. Du, X.L. Chen, Z.Q. Li, H.L. Bai, E.Y. Jiang, Influence of WC particle behavior on the wear resistance properties of Ni–WC composite coatings, Wear 257(1-2) (2004) 142-147.

[133] S.V. Meschel, O.J. Kleppa, Standard enthalpies of formation of some 3d transition metal carbides by high temperature reaction calorimetry, Journal of alloys and compounds 257(1-2) (1997) 227-233.

[134] M. Zhong, W. Liu, Y. Zhang, X. Zhu, Formation of WC/Ni hard alloy coating by laser cladding of W/C/Ni pure element powder blend, International Journal of Refractory Metals and Hard Materials 24(6) (2006) 453-460.

[135] M. Rombouts, R. Persoons, E. Geerinckx, R. Kemps, M. Mertens, W. Hendrix, H. Chen, Development and characterization of nickel based tungsten carbide laser cladded coatings, Physics Procedia 5 (2010) 333-339.

[136] P. Wu, C. Zhou, X. Tang, Laser alloying of a gradient metal-ceramic layer to enhance wear properties, Surface and Coatings Technology 73(1-2) (1995) 111-114.

[137] T.E. Abioye, P.K. Farayibi, D.G. McCartney, A.T. Clare, Effect of carbide dissolution on the corrosion performance of tungsten carbide reinforced Inconel 625 wire laser coating, Journal of Materials Processing Technology 231 (2016) 89-99.

[138] Y. Lee, M. Nordin, S.S. Babu, D.F. Farson, Effect of fluid convection on dendrite arm spacing in laser deposition, Metallurgical and Materials Transactions B 45(4) (2014) 1520-1529.

[139] H.U. Miao, J.-c. Tang, X.-g. Chen, Y.E. Nan, X.-y. Zhao, M.-m. Xu, Microstructure and properties of WC-12Co composite coatings prepared by laser cladding, Transactions of Nonferrous Metals Society of China 30(4) (2020) 1017-1030.

[140] P.K. Farayibi, J. Folkes, A. Clare, O. Oyelola, Cladding of pre-blended Ti–6Al–4V and WC powder for wear resistant applications, Surface and Coatings Technology 206(2-3) (2011) 372-377.

[141] S. Zhou, X. Dai, T. Zhang, Effect of binder metals on structure and properties of WC ceramic-metal composite coatings by laser-induction hybrid rapid cladding, Journal of composite materials 47(12) (2013) 1549-1559.

[142] Y. Yang, D. Gu, D. Dai, C. Ma, Laser energy absorption behavior of powder particles using ray tracing method during selective laser melting additive manufacturing of aluminum alloy, Materials & Design 143 (2018) 12-19.

[143] X. Shi, S. Ma, C. Liu, C. Chen, Q. Wu, X. Chen, J. Lu, Performance of high layer thickness in selective laser melting of Ti6Al4V, Materials 9(12) (2016) 975.

[144] L. Reddy, S.P. Preston, P.H. Shipway, C. Davis, T. Hussain, Process parameter optimisation of laser clad iron based alloy: Predictive models of deposition efficiency, porosity and dilution, Surface and Coatings Technology 349 (2018) 198-207.

[145] Y.-c. Zhu, K. Yukimura, C.-x. Ding, P.-y. Zhang, Tribological properties of nanostructured and conventional WC–Co coatings deposited by plasma spraying, Thin solid films 388(1-2) (2001) 277-282.

[146] A. Bahari, Investigation into Tribological Performance of Vegetable Oils as Biolubricants at Severe Contact Conditions, PhD thesis, University of Sheffield, UK, 2017.

[147] D. Gu, W. Meiners, Microstructure characteristics and formation mechanisms of in situ WC cemented carbide based hardmetals prepared by Selective Laser Melting, Materials Science and Engineering: A 527(29-30) (2010) 7585-7592.

[148] U.S. Bertoli, A.J. Wolfer, M.J. Matthews, J.-P.R. Delplanque, J.M. Schoenung, On the limitations of volumetric energy density as a design parameter for selective laser melting, Materials & Design 113 (2017) 331-340.

[149] P. Gao, Z. Wang, X. Zeng, Effect of process parameters on morphology, sectional characteristics and crack sensitivity of Ti-40Al-9V-0.5Y alloy single tracks produced by selective laser melting, International Journal of Lightweight Materials and Manufacture (2019).

[150] W.E. King, H.D. Barth, V.M. Castillo, G.F. Gallegos, J.W. Gibbs, D.E. Hahn, C. Kamath, A.M. Rubenchik, Observation of keyhole-mode laser melting in laser powder-bed fusion additive manufacturing, Journal of Materials Processing Technology 214(12) (2014) 2915-2925.

[151] B. Zhang, H. Liao, C. Coddet, Microstructure evolution and density behavior of CP Ti parts elaborated by self-developed vacuum selective laser melting system, Applied Surface Science 279 (2013) 310-316.

[152] R. Baitimerov, P. Lykov, D. Zherebtsov, L. Radionova, A. Shultc, K.G. Prashanth, Influence of powder characteristics on processability of AlSi12 alloy fabricated by selective laser melting, Materials 11(5) (2018) 742.

[153] K. Wei, Z. Wang, X. Zeng, Preliminary investigation on selective laser melting of Ti-5Al-2.5 Sn α-Ti alloy: From single tracks to bulk 3D components, Journal of Materials Processing Technology 244 (2017) 73-85.

[154] A. Gusarov, I. Smurov, Modeling the interaction of laser radiation with powder bed at selective laser melting, Physics Procedia 5 (2010) 381-394.

[155] E. Mirkoohi, D.E. Seivers, H. Garmestani, S.Y. Liang, Heat source modeling in selective laser melting, Materials 12(13) (2019) 2052.

[156] I. Yadroitsev, A. Gusarov, I. Yadroitsava, I. Smurov, Single track formation in selective laser melting of metal powders, Journal of Materials Processing Technology 210(12) (2010) 1624-1631.

[157] B. Song, S. Dong, S. Deng, H. Liao, C. Coddet, Microstructure and tensile properties of iron parts fabricated by selective laser melting, Optics & Laser Technology 56 (2014) 451-460.

[158] D. Wang, W. Dou, Y. Yang, Research on selective laser melting of Ti6Al4V: Surface morphologies, optimized processing zone, and ductility improvement mechanism, Metals 8(7) (2018) 471.

[159] S. Shrestha, T. Starr, K. Chou, A Study of Keyhole Porosity in Selective Laser Melting: Single-Track Scanning With Micro-CT Analysis, Journal of Manufacturing Science and Engineering 141(7) (2019).

[160] Y. Liu, Y. Yang, S. Mai, D. Wang, C. Song, Investigation into spatter behavior during selective laser melting of AISI 316L stainless steel powder, Materials & Design 87 (2015) 797-806.

[161] V. Gunenthiram, P. Peyre, M. Schneider, M. Dal, F. Coste, I. Koutiri, R. Fabbro, Experimental analysis of spatter generation and melt-pool behavior during the powder bed laser beam melting process, Journal of Materials Processing Technology 251 (2018) 376-386.

[162] Y. Bai, Y. Yang, D. Wang, M. Zhang, Influence mechanism of parameters process and mechanical properties evolution mechanism of maraging steel 300 by selective laser melting, Materials Science and Engineering: A 703 (2017) 116-123.

[163] P. Yuan, D. Gu, Molten pool behaviour and its physical mechanism during selective laser melting of TiC/AlSi10Mg nanocomposites: simulation and experiments, Journal of Physics D: Applied Physics 48(3) (2015) 035303.

[164] C. Qiu, C. Panwisawas, M. Ward, H.C. Basoalto, J.W. Brooks, M.M. Attallah, On the role of melt flow into the surface structure and porosity development during selective laser melting, Acta Materialia 96 (2015) 72-79.

[165] N. Ku, J.J. Pittari, S. Kilczewski, A. Kudzal, Additive Manufacturing of Cemented Tungsten Carbide with a Cobalt-Free Alloy Binder by Selective Laser Melting for High-Hardness Applications, JOM 71(4) (2019) 1535-1542.

[166] Z. Wang, J. Jia, B. Wang, Y. Wang, Two-Step Spark Plasma Sintering Process of Ultrafine Grained WC-12Co-0.2VC Cemented Carbide, Materials 12(15) (2019) 2443.

[167] Q. Zhan, L. Yu, F. Ye, Q. Xue, H. Li, Quantitative evaluation of the decarburization and microstructure evolution of WC–Co during plasma spraying, Surface and Coatings Technology 206(19-20) (2012) 4068-4074.

[168] C. Li, Z.Y. Liu, X.Y. Fang, Y.B. Guo, Residual stress in metal additive manufacturing, Procedia Cirp 71 (2018) 348-353.

[169] T. Simson, A. Emmel, A. Dwars, J. Böhm, Residual stress measurements on AISI 316L samples manufactured by selective laser melting, Additive Manufacturing 17 (2017) 183-189.

[170] M. Grasso, B.M. Colosimo, Process defects and in situ monitoring methods in metal powder bed fusion: a review, Measurement Science and Technology 28(4) (2017) 044005.

[171] P. Bian, X. Shao, J. Du, Finite Element Analysis of Thermal Stress and Thermal Deformation in Typical Part during SLM, Applied Sciences 9(11) (2019) 2231.

[172] W. Xing, D. Ouyang, N. Li, L. Liu, Estimation of residual stress in selective laser melting of a zr-based amorphous alloy, Materials 11(8) (2018) 1480.

[173] N.J. Harrison, I. Todd, K. Mumtaz, Reduction of micro-cracking in nickel superalloys processed by Selective Laser Melting: A fundamental alloy design approach, Acta Materialia 94 (2015) 59-68.

[174] B. Song, S. Dong, Q. Liu, H. Liao, C. Coddet, Vacuum heat treatment of iron parts produced by selective laser melting: microstructure, residual stress and tensile behavior, Materials & Design (1980-2015) 54 (2014) 727-733.

[175] S.S. Al-Bermani, An investigation into microstructure and microstructural control of additive layer manufactured Ti-6Al-4V by electron beam melting, PhD thesis, University of Sheffield, UK, 2011.

[176] Y. He, C. Montgomery, J. Beuth, B. Webler, Melt pool geometry and microstructure of Ti6Al4V with B additions processed by selective laser melting additive manufacturing, Materials & Design 183 (2019) 108126.

[177] P. Promoppatum, S.-C. Yao, P.C. Pistorius, A.D. Rollett, A comprehensive comparison of the analytical and numerical prediction of the thermal history and

solidification microstructure of Inconel 718 products made by laser powder-bed fusion, Engineering 3(5) (2017) 685-694.

[178] H. Hekmatjou, Z. Zeng, J. Shen, J.P. Oliveira, H. Naffakh-Moosavy, A Comparative Study of Analytical Rosenthal, Finite Element, and Experimental Approaches in Laser Welding of AA5456 Alloy, Metals 10(4) (2020) 436.

[179] I. Yadroitsev, I. Smurov, Selective laser melting technology: from the single laser melted track stability to 3D parts of complex shape, Physics Procedia 5 (2010) 551-560.

[180] A.H. Maamoun, Y.F. Xue, M.A. Elbestawi, S.C. Veldhuis, Effect of selective laser melting process parameters on the quality of Al alloy parts: Powder characterization, density, surface roughness, and dimensional accuracy, Materials 11(12) (2018) 2343.

[181] J.H. Tan, W.L.E. Wong, K.W. Dalgarno, An overview of powder granulometry on feedstock and part performance in the selective laser melting process, Additive Manufacturing 18 (2017) 228-255.

[182] J. Zhang, D. Gu, Y. Yang, H. Zhang, H. Chen, D. Dai, K. Lin, Influence of Particle Size on Laser Absorption and Scanning Track Formation Mechanisms of Pure Tungsten Powder During Selective Laser Melting, Engineering 5(4) (2019) 736-745.